

**Nanostructured thermoelectrics:
Bi₂Te₃ / Sb₂Te₃ based superlattice systems
fabricated by MBE and sputtering**

Dissertation

der Mathematisch-Naturwissenschaftlichen Fakultät
der Eberhard Karls Universität Tübingen
zur Erlangung des Grades eines
Doktors der Naturwissenschaften
(Dr. rer. nat.)

vorgelegt von
Dipl. Phys. Markus Winkler
aus Müllheim

Tübingen
2014

Gedruckt mit Genehmigung der Mathematisch-Naturwissenschaftlichen Fakultät der Eberhard Karls Universität Tübingen.

Tag der mündlichen Qualifikation:	29.01.2015
Dekan:	Prof. Dr. Wolfgang Rosenstiel
1. Berichterstatter:	Prof. Dr. Oliver Eibl
2. Berichterstatter:	Prof. Dr. Reinhold Kleiner

Eidesstattliche Versicherung

Ich erkläre hiermit, dass ich die zur Promotion eingereichte Arbeit mit dem Titel „Nanostructured thermoelectrics Bi_2Te_3 / Sb_2Te_3 - based superlattice systems fabricated by MBE and sputtering“ selbständig verfasst, nur die angegebenen Quellen und Hilfsmittel benutzt und wörtlich oder inhaltlich übernommene Stellen als solche gekennzeichnet habe. Ich versichere an Eides statt, dass diese Angaben wahr sind und dass ich nichts verschwiegen habe. Mir ist bekannt, dass die falsche Abgabe einer Versicherung an Eides statt mit Freiheitsstrafen bis zu drei Jahren oder mit Geldstrafe bestraft wird. Weiterhin erkläre ich, dass bisher kein Promotionsversuch unternommen wurde.

Freiburg, den _____, _____ (Markus Winkler)

Zusammenfassung

Thermoelektrische Materialien wandeln basierend auf dem Seebeck- und Peltiereffekt wechselseitig thermische Energie in elektrische Energie um. Für hohe Wirkungsgrade werden extrinsische Halbleiter mit bestimmten Eigenschaften benötigt, d.h. typischerweise einer Ladungsträgerkonzentration n im Bereich von 10^{19} cm^{-3} , einer elektrischen Leitfähigkeit σ von ca. 1000 S/cm , einer Thermokraft S von ca. $200 \text{ } \mu\text{V/K}$, einem Powerfaktor $S^2\sigma$ von ca. $40 \text{ } \mu\text{W/cmK}^2$, einer Wärmeleitfähigkeit λ von ca. 1 W/mK und folglich einer thermoelektrischen Gütezahl $ZT = T S^2\sigma / \lambda$ von etwa 1. Für Raumtemperaturanwendungen werden Bi_2Te_3 und insbesondere die Mischkristalle bzw. Festlösungen dieser Verbindung mit Sb_2Te_3 und Bi_2Se_3 verwendet. Seit einigen Jahren finden umfangreiche Forschungsaktivitäten statt mit dem Ziel, die thermoelektrische Gütezahl ZT auf Werte deutlich über 1 zu steigern und so den Wirkungsgrad der thermoelektrischen Energiekonversion zu erhöhen. Hierzu sollen Effekte genutzt werden, die sich durch eine Nanostrukturierung des thermoelektrischen Materials ergeben. Hier sind vor allem Übergitter – Strukturen [superlattice (SL)] von Interesse.

Die chemische Zusammensetzung hat bei Bi_2Te_3 -basierten Materialien einen sehr starken Einfluss auf die Dichte der Antisite-Defekte und hierdurch auf die Ladungsträgerdichte. Die Herstellung von elektronenleitenden (n-leitenden) Bi_2Te_3 -basierten Dünnschichten durch Molekularstrahlepitaxie (engl. MBE) und durch Sputtern auf heißen Substraten ist mit Problemen behaftet: Die temperaturabhängige Re-Evaporation des relativ flüchtigen Te ist problematisch und erfordert die Anpassung des Te-Flusses an die jeweilige Substrattemperatur. Eine gezielte Stöchiometrie-Kontrolle ist hier sehr wichtig, um eine Kontrolle über die Ladungsträgerkonzentration und die damit verknüpften elektrischen Eigenschaften zu erzielen. Aufgrund ihrer pseudo-hexagonalen Kristallstruktur weisen Bi_2Te_3 -basierte Materialien eine Anisotropie der elektrischen und phononischen Transporteigenschaften und Diffusionskoeffizienten auf. Die elektrischen und thermischen Eigenschaften sind hierbei stark anisotrop, während die Seebeck-Koeffizienten kaum betroffen sind. Bei der Mehrzahl der dünnfilmbasierten thermoelektrischen Bauteile findet der Ladungsträgertransport senkrecht zur Substratebene statt. Für SL-basierte Bauteile ist es vorteilhaft, wenn die c-Achse senkrecht zur Substratebene, d.h. parallel zur Wachstumsrichtung liegt.

Ein Ziel dieser Arbeit war die Untersuchung neuer Methoden für die Herstellung Bi_2Te_3 -basierter Dünnschichten und SL, wobei gleichzeitig der Herstellungsprozess vereinfacht werden sollte. Hierfür wurde neben epitaktischem Wachstum auch die sogenannte Nanoalloying-Methode angewendet: Nominell stöchiometrische Filme wurden durch eine alternierende Abscheidung von dünnen Elementschichten mit entsprechenden Dicken und einem anschließenden Tempereschritt erhalten. Aufgrund der Abscheidung auf kalten Substraten kann die Re-Evaporation von Te umgangen werden. Ausserdem kann auf die Verwendung von Substraten, die epitaktisches Wachstum gewährleisten würden, verzichtet werden. Die Filme wurden in einer kalibrierten MBE-Anlage und einer Sputteranlage abgeschieden. Die Gesamtschichtdicke betrug etwa $1 \text{ } \mu\text{m}$, während die Elementschichtdicken im Bereich von nm oder darunter lagen. Es wurden verschiedene Substratmaterialien verwendet, d.h. (111)-orientiertes BaF_2 für ein epitaktisches Wachstum und Si/SiO_2 – Wafer, mit denen eine kostengünstige Massenproduktion realisierbar ist. Zur Durchführung des Nanoalloying-Verfahrens wurden die hergestellten Filme und SL einem Niedertemperatur-Temperprozess in Te-reicher Atmosphäre unterzogen. Dieser Prozessschritt ist besonders kritisch: Während des Tempervorganges soll einerseits die Verbindungsbildung aus den Elementen durch eine Festkörperreaktion stattfinden, andererseits soll die nanoskalige SL-Struktur bei der Temperung erhalten bleiben. Eine neue Zweizonen-Temperprozedur in einer Te-reichen Atmosphäre ermöglichte für Filme aus Bi_2Te_3 eine Einstellung der Zusammensetzung und bemerkenswerterweise auch des Ladungsträgertyps.

In dieser Arbeit wurden umfangreiche Probenserien hergestellt und untersucht, d.h. insgesamt ~ 100 binäre Dünnschichten und SL mit der Nanoalloying-Methode auf "kalten" BaF_2 und Si/SiO_2 Substraten und ~ 30 epitaktische binäre Filme und SL durch gleichzeitige Abscheidung der Elemente auf heißen Substraten. (i) Binäre Bi_2Te_3 und Sb_2Te_3 Filme wurden durch Nanoalloying hergestellt, und die Elementschichtdicke, chemische Zusammensetzung und die Temperbedingungen wurden variiert. (ii) $\text{Bi}_2\text{Te}_3/\text{Sb}_2\text{Te}_3$ SL wurden durch Nanoalloying in einer MBE-Anlage hergestellt, und p-leitende Sb_2Te_3 /

$(\text{Bi,Sb})_2\text{Te}_3$ und n-leitende Bi_2Te_3 / $(\text{Bi,Sb})_2\text{Te}_3$ Filme wurden durch Sputtern hergestellt. (iii) Schließlich wurden binäre Bi_2Te_3 und Sb_2Te_3 Filme und Bi_2Te_3 / Sb_2Te_3 SL mit der MBE-Anlage epitaktisch abgeschieden. Bei den SL wurden die Dicken der Bi_2Te_3 und Sb_2Te_3 Einzelschichten bzw. die Periodenlängen bis minimal 6 nm variiert.

Die Ladungsträgerkonzentration und -mobilität, die Thermokraft und die elektrische Leitfähigkeit wurden entlang der Filmebene (in-plane Richtung) gemessen während die Wärmeleitfähigkeit in der senkrecht dazu liegenden Wachstumsrichtung (cross-plane Richtung) gemessen wurde. Diese Vorgehensweise wurde gewählt da (i) die cross-plane Wärmeleitfähigkeit empfindlicher auf die Beschaffenheit der SL-Struktur reagiert und weil (ii) die elektrische in-plane Charakterisierung einfacher durchzuführen ist, da hierfür keine Mikrostrukturierung der Probe erforderlich ist und so eine umfangreichere Anzahl an Proben charakterisiert werden konnte. Alle Messungen wurden bei Raumtemperatur durchgeführt. Aufgrund der Anisotropie der Transporteigenschaften durfte ZT nicht direkt aus den elektrischen und thermischen Transporteigenschaften berechnet werden. Stattdessen wurden unter verschiedenen Annahmen Ober- und Untergrenzen für diesen Wert abgeschätzt. Rasterelektronenmikroskopie und energiedispersive Röntgenspektroskopie wurden genutzt, um die Mikrostruktur und chemische Zusammensetzung der Proben zu untersuchen. Weitere strukturelle Untersuchungen (Röntgenstrukturanalyse, Transmissionselektronenmikroskopie) wurden von Partnerinstituten ausgeführt. Besonderes Augenmerk wurde in dieser Arbeit auf den Zusammenhang der Textur mit der thermischen Stabilität der SL-Struktur, den elektrischen Eigenschaften und der Wärmeleitfähigkeit gelegt. Für die Bi_2Te_3 / Sb_2Te_3 SL wurden zudem Kompensationseffekte, die sich durch das Stapeln von n-leitendem Bi_2Te_3 auf p-leitendes Sb_2Te_3 ergeben untersucht.

Bei den durch Nanoalloying hergestellten binären Filmen konnte gezeigt werden, dass die Ladungsträgerkonzentration und die elektrischen Transportgrößen durch die chemische Zusammensetzung eingestellt werden können. Die Proben wurden hierzu isotherm für typischerweise 2 h bei 250 °C getempert. Auf diese Weise gelang die Synthese von Sb_2Te_3 Dünnschichten mit niedrigen Ladungsträgerkonzentrationen ($\sim 10^{19} \text{ cm}^{-3}$) und hohen -mobilitäten ($> 400 \text{ cm}^2/\text{Vs}$). Im Gegensatz zu Sb_2Te_3 Volumenmaterialien erweisen sich damit Sb_2Te_3 Filme als für thermoelektrische Bauteile geeignet. Bei Tempertemperaturen von 500 °C konnten n-leitende Bi_2Te_3 Filme bemerkenswerterweise in p-leitende Materialien umgewandelt werden. Die Textur der Filme konnte über die Elementschichtdicken eingestellt werden.

Insgesamt erwies sich die Nanoalloying-Methode als sehr gut geeignet für die Herstellung von elektronen- und löcherleitenden Bi_2Te_3 -basierten Filmen und SL. Mit der Methode konnten diese Filme mit kontrollierter chemischer Zusammensetzung, Ladungsträgerkonzentration und elektrischen Eigenschaften hergestellt werden, wodurch eine hohe thermoelektrische Güte erzielt werden konnte. Sowohl n- als auch p-leitende Filme konnten hergestellt werden. Unter praktischen Gesichtspunkten ist die Erkenntnis, dass n-leitendes gesputtertes $(\text{Bi,Sb})_2\text{Te}_3$ anstelle des bekannten $\text{Bi}_2(\text{Te,Se})_3$ verwendet werden kann, von hoher Relevanz. Hierdurch kann die technologisch schwierige Verwendung von Se Sputtertargets umgangen werden. Die Ausrichtung der c-Achse parallel zur Wachstumsrichtung und die sich hierdurch ergebenden optimalen Transporteigenschaften parallel zur Substratebene können sowohl durch epitaktisches MBE-Wachstum auf BaF_2 Substraten als auch durch Sputtern auf Si/SiO_2 Wafern durch entsprechende Wahl der Elementschichtdicken erzielt werden. Die Kontrolle über die Filmtextur spielte auch bei der thermischen Stabilität der Multilagenstruktur eine Schlüsselrolle. Diese ist wichtig, um eine möglichst niedrige Wärmeleitfähigkeit zu erzielen.

Von den mit der Nanoalloying-Methode hergestellten Filmen wiesen insbesondere die p-leitenden gesputterten SL herausragend hohe, mit einkristallinen Volumenmaterialien vergleichbare Powerfaktoren $> 40 \mu\text{W}/\text{cmK}^2$ auf. Die Filme waren stark texturiert und wiesen eine niedrige Wärmeleitfähigkeit auf. Die starke c-Orientierung der Filme führte zu einer erhöhten thermischen Stabilität der SL-Struktur aufgrund verminderter Diffusion entlang der Wachstumsrichtung. Die epitaktisch gewachsenen Übergitter zeigten eine sehr starke Textur und selbst für sehr niedrige Periodenlängen von 6 nm scharf getrennte Einzelschichten. Diese SL wiesen gegenüber den per Nanoalloying hergestellten SL eine deutlich erhöhte thermische Stabilität auf, und die

Gitterwärmeleitfähigkeit konnte gegenüber den binären Filmen um ~60% (d.h. auf 0.28 W/mK) reduziert werden.

Venkatasubramanian erzielte für Bi_2Te_3 / Sb_2Te_3 Übergitter spektakuläre ZT-Werte von 2.4. Diese Ergebnisse konnten allerdings bislang nicht reproduziert werden und werden fortlaufend kontrovers diskutiert. Im Rahmen dieser Arbeit konnten p-leitende gesputterte SL-Systeme mit hohen ZT-Werten im Bereich von schätzungsweise 1.0 (konservative Schätzung) bis 1.9 (optimistische Schätzung) hergestellt werden.

Die in dieser Arbeit gezeigten Ergebnisse zeichnen sich dadurch aus, dass zwei wichtige Abscheidungsverfahren (thermische Verdampfung und Sputtern), zwei verschiedene in-situ Verfahren zur Verbindungsbildung (MBE und Nanoalloying) und zwei verschiedene ex-situ Temperverfahren angewendet wurden. Im Ergebnis erhielt man eine Vielzahl verschiedener Dünnschichten mit maßgeschneidertem Schicht- und Filmaufbau. Auf Si/SiO₂ Substraten abgeschiedene Filme wiesen trotz der amorphen Struktur der Substratoberfläche eine starke Textur auf. Durch MBE-Wachstum auf heißen BaF₂-Substraten konnte epitaktisches Wachstum erzielt werden. Die gewählten Abscheide- und Temperbedingungen ermöglichten eine präzise Einstellung der Dotierung, Textur und Übergitterstruktur und ergaben Filme mit hervorragenden thermoelektrischen Eigenschaften, die so bislang noch nicht publiziert wurden. Die gezeigten Ergebnisse sind auch für andere Forschungsgebiete von Nutzen. Die Verwendung der Nanoalloying-Methode zur Filmherstellung ist insbesondere dann vorteilhaft, wenn die verwendeten Elemente große Unterschiede beim jeweiligen Dampfdruck aufweisen, was die Abscheidung auf heißen Substraten und daher die Kontrolle der Stöchiometrie und der Ladungsträgerkonzentration erschwert, z.B: (i) bei photovoltaischen Anwendungen basierend auf CdTe Dünnschichten mit Sb_2Te_3 Rückseitenkontakten und (ii) für Bi_2Te_3 -basierte topologische Isolatoren, die eine niedrige Ladungsträgerkonzentration erfordern.

Summary

Thermoelectric materials yield mutual conversion of thermal to electrical energy by the Seebeck and Peltier effect. For high efficiencies, extrinsic semiconductors with specific transport properties are required, typically a carrier concentration n of $\sim 10^{19} \text{ cm}^{-3}$, an electrical conductivity σ of $\sim 1000 \text{ S/cm}$, a thermo power S of $\sim 200 \text{ } \mu\text{V/K}$, a power factor $S^2\sigma$ of $\sim 40 \text{ } \mu\text{W/cmK}^2$, a thermal conductivity λ of $\sim 1 \text{ W/mK}$, and in summary a thermoelectric figure of merit $ZT = T S^2\sigma / \lambda \sim 1$. For room temperature applications, Bi_2Te_3 and in particular its hole- and electron conducting solid solutions with Sb_2Te_3 and Bi_2Se_3 are used. Recently, there have been great efforts to increase ZT significantly beyond 1 by exploiting the beneficial effects of nanostructuring thermoelectric materials, particularly by introducing superlattice (SL) structures.

In Bi_2Te_3 -related materials the chemical composition strongly determines the density of antisite defects and thereby the charge carrier density. n -type Bi_2Te_3 -related thin films and SLs deposited by Molecular Beam Epitaxy (MBE) and sputtering on hot substrates revealed several *complications*: temperature-dependent re-evaporation of the volatile Te is a severe problem and requires the re-adjustment of the Te flux for each substrate temperature. Thus, stoichiometry control is critical for controlling the carrier concentration and the related electrical properties. Due to their pseudo-hexagonal crystal structure, Bi_2Te_3 – related materials exhibit an anisotropy of the transport coefficients of electrons and phonons and diffusion coefficients, note that electrical and thermal conductivity are strongly anisotropic while the Seebeck coefficient is hardly affected. For the majority of thin-film based thermoelectric devices carrier transport takes place perpendicular to the substrate plane. For SL-based devices it is favorable if the c axis lies perpendicular to the substrate plane, i.e. parallel to the growth direction.

One aim of this work was to investigate new routes of synthesis of high- ZT Bi_2Te_3 -based thin films and SLs and to facilitate their fabrication. For this, besides epitaxial growth the nanoalloying method was applied: Nominally stoichiometric films can be obtained by alternative deposition of elemental layers with appropriate thicknesses and a subsequent annealing step. Te re-evaporation is avoided by deposition on cold substrates, and epitaxially compatible substrates are not required. Films were deposited in a calibrated MBE system and a sputtering system, film thicknesses were around $1 \text{ } \mu\text{m}$ and the thickness of elemental layers was in the nm to sub-nm range. Different substrate materials were used, i.e. (111)-oriented BaF_2 for epitaxial growth and Si/SiO_2 wafers that are suitable for a mass-production. During the nanoalloying process, the films and SLs were exposed to a low-temperature annealing process in a Te rich atmosphere, this processing step being especially critical: during annealing compound formation should take place via a solid state reaction, however, the nanoscaled SL structure should be retained during annealing. A new two-zone annealing in a Te rich atmosphere yielded a post-deposition control of the composition of as-grown Bi_2Te_3 thin films and, most strikingly, their charge carrier type.

Sample series were deposited, i.e. ~ 100 binary thin films and SLs with the nanoalloying method on cold BaF_2 or Si/SiO_2 substrates and ~ 30 epitaxial binary films and superlattices by co-deposition of the elements on hot BaF_2 substrates. (i) Nanoalloyed binary Bi_2Te_3 and Sb_2Te_3 films were grown and the elemental layer thicknesses, the chemical composition, isothermal annealing conditions, and two-zone annealing conditions were varied for the binary films. (ii) Nanoalloyed $\text{Bi}_2\text{Te}_3 / \text{Sb}_2\text{Te}_3$ SLs were grown in a MBE system and p -type $\text{Sb}_2\text{Te}_3 / (\text{Bi,Sb})_2\text{Te}_3$ and n -type $\text{Bi}_2\text{Te}_3 / (\text{Bi,Sb})_2\text{Te}_3$ SLs were grown by sputtering. (iii) Finally, binary Bi_2Te_3 and Sb_2Te_3 films and $\text{Bi}_2\text{Te}_3 / \text{Sb}_2\text{Te}_3$ SLs were grown epitaxially in the MBE system. For the SLs, the ratios of Bi_2Te_3 and Sb_2Te_3 layer thicknesses and period lengths were varied down to 6 nm .

Carrier concentration and μ -mobility, thermo power and electrical conductivity were measured along the film plane (in-plane direction) while thermal conductivity was measured in the growth direction (cross-plane direction). These measurement directions were chosen (i) because the cross-plane thermal conductivity is more sensitive to the quality of the SL structure and (ii) because in-plane electrical characterization is simpler and does not require microstructuring of the samples. Thus a larger series of samples could be characterized. All measurements were carried out at room temperature. Due to transport anisotropy, electrical and thermal transport properties cannot be directly combined to

calculate ZT, therefore different cases were considered to estimate ZT. Scanning electron microscopy and energy dispersive X-ray spectroscopy were used to investigate the microstructure and chemical composition. Further structural characterization (X-Ray diffraction, transmission electron microscopy) was carried out elsewhere. Special attention was paid to the relation of texture to the electrical properties of the films and SLs. Texture also affected the thermal stability of the SL structure and its thermal conductivity. Also for SLs, carrier compensation effects induced by stacking n-type Bi₂Te₃ on p-type Sb₂Te₃ layers were investigated.

For nanoalloyed binary films it was proven that carrier concentration and electrical properties can be adjusted by the chemical composition via isothermal annealing conditions, typically 250 °C for 2 h. In this way, Sb₂Te₃ thin films with low carrier concentrations ($\sim 10^{19} \text{ cm}^{-3}$) and high mobilities ($> 400 \text{ cm}^2/\text{Vs}$) could be synthesized successfully. It could be shown that Sb₂Te₃ thin films are suitable for thermoelectric devices, in contrast to Sb₂Te₃ bulk materials. Bi₂Te₃ thin films could even be converted from n- into p-type at annealing temperatures of 500 °C and the elemental layer thickness allowed to control film texture.

The nanoalloying synthesis method was successfully applied for the fabrication of electron and hole conducting Bi₂Te₃ related thin films and SLs. Such films were deposited with controlled chemical composition, carrier concentration and electrical properties and yield improved thermoelectric figures of merit. Both n and p-type films could be obtained, it is also of significant practical importance that n-type sputtered (Bi,Sb)₂Te₃ could be used to replace Bi₂(Te,Se)₃ thin films and avoid Se targets, which are difficult to handle. A c axis parallel to the growth direction and thus optimum in-plane transport properties can either be achieved by epitaxial MBE growth on BaF₂ substrates or by sputtering on Si/SiO₂ wafers with appropriate choice of elemental layer thicknesses. The control of texture in the films was also of key importance for the thermal stability of multilayered structures during annealing and hence for retaining a low thermal conductivity.

Record power factors $> 40 \mu\text{W}/\text{cmK}^2$ were obtained for the nanoalloyed SLs, particularly for sputtered p-type films and were similar to bulk single crystals. These films revealed a high degree of texture and a low thermal conductivity. Also, a higher degree of c-orientation in the films resulted in a higher thermal stability of the SL structure due to a reduced diffusion along the growth direction. The epitaxially grown SLs yielded a very strong texture with sharply separated layers even for period lengths as small as 6 nm. These SLs proved to be more thermally stable than nanoalloyed SLs and the lattice thermal conductivity was reduced by up to ~60% (i.e. down to 0.28 W/mK) as compared to binary films.

Venkatasubramanian reported a spectacular ZT value of 2.4 in Bi₂Te₃ / Sb₂Te₃ superlattices, however, these results could not be reproduced and are still under debate. In this work, for the sputtered p-type films a high ZT value was estimated being 1.0 for a conservative estimation and 1.9 under optimistic assumptions.

The results obtained in this study are unique in the sense that two powerful deposition technologies (evaporation and sputtering), two different in-situ compound formation techniques (MBE and nanoalloying) and two ex-situ annealing techniques have been applied yielding a large number of thin films with tailored film architecture. Films deposited on Si/SiO₂ substrates reported in this study were strongly textured, despite the amorphous structure of the substrate top layer. In case of MBE on hot BaF₂ substrates epitaxial growth was achieved. It could be shown that doping, texture and SL structure can be precisely controlled for all deposition and annealing conditions and yielded outstanding thermoelectric film properties not reported before. Other research fields may also benefit from these results. The nanoalloying method is clearly advantageous when elemental species show large differences in vapor pressure, complicating the deposition on hot substrates and thus control of stoichiometry and charge carriers: (i) in photovoltaic applications for CdTe thin films and Sb₂Te₃ back contacts and (ii) for Bi₂Te₃ based topological insulators that require low charge carrier concentrations.

Chapter preview and overview over deposited films

The first 4 chapters serve as introduction and description of experimental details.

Chapter 1 is a phenomenological introduction to thermoelectricity.

Chapter 2 shows the interplay of the transport properties and the performance of thermoelectric materials and gives an introduction into (thermoelectric) transport theory for bulk materials and in particular for 2D nanostructured superlattice (SL) systems.

Chapter 3 gives an overview over the examined material system, i.e. Bi_2Te_3 , Sb_2Te_3 and $(\text{Bi}_{1-x}\text{Sb}_x)_2\text{Te}_3$ solid solutions. Properties of bulk as well as thin-film materials are shown. The second part of the chapter is an in-depth review of the record-breaking MOCVD-grown $\text{Bi}_2\text{Te}_3 / \text{Sb}_2\text{Te}_3$ SLs and an analysis of the accompanying phenomena and publications. Their outstanding properties reported in 2001 initiated a boost for synthesis of thermoelectric thin films and many other types of nanomaterials.

In **Chapter 4** the fabrication methods and setups that were used to synthesize the films are described, i.e. the nanoalloying and epitaxial method and the used molecular beam epitaxy and sputtering system. It is pointed out that the nanoalloying method has several advantages over more conventional methods such as co-deposition on a hot substrate. A broad selection of characterization methods was used to characterize the structure and transport properties of the films. The applied methods are elaborated together with the used measurement parameters.

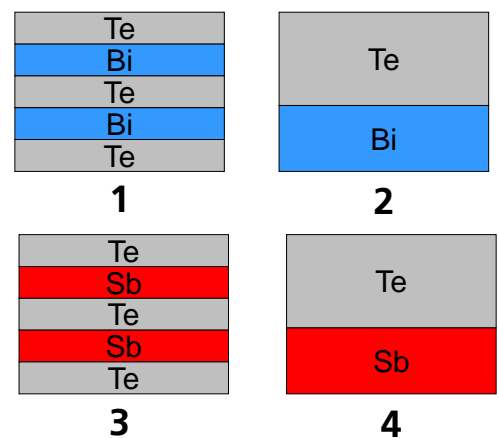
Experimental results are given in **chapters 5 to 9**. An overview over the used deposition patterns and deposited structures is given below. The thicknesses d of the element and compound layers are given as well as the number of deposited periods and the annealing temperature. ρ_{BT} and ρ_{ST} indicate the number of Bi-Te and Sb-Te quintuples in chapter 6.

Chapter 5: Binary MBE nanoalloyed thin films

Chapter 5 shows results for binary Bi_2Te_3 and Sb_2Te_3 thin films grown by MBE. Different deposition and annealing conditions are used and Te content, element thicknesses and annealing methods are varied.

Nr.	d_{Bi} [nm]	d_{Sb} [nm]	d_{Te} [nm]	Periods	Anneal.Temp. [°C]
1	0.2		0.2	999	250, 400, 450, 500
2	0.2-1.7		0.2-2.4	250-999	250
3		0.2	0.2	999	250
4		0.2-1.5	0.2-2.6	250-999	250

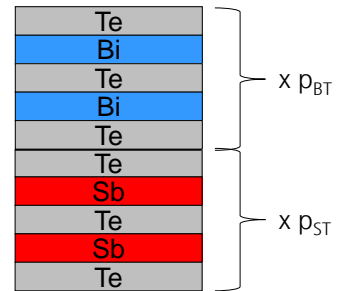
Used substrate materials: BaF_2 and Si/SiO_2 . Only properties determined with BaF_2 as substrate are shown, properties on Si/SiO_2 were similar and are not shown. TEM images were acquired with Si/SiO_2 as substrate.



Chapter 6: Bi₂Te₃ / Sb₂Te₃ superlattice thin films grown by MBE

In chapter 6, Bi₂Te₃ / Sb₂Te₃ SL structures fabricated with a MBE setup with different ratios of Sb₂Te₃:Bi₂Te₃ compound layer thicknesses and annealing temperatures are characterized. The effects of the quality of the SL structure on transport properties (e.g. thermal conductivity and carrier compensation effects) are investigated.

d_{Bi} d_{Te} [nm]	d_{Sb} d_{Te} [nm]	ρ_{BT} = nm Bi ₂ Te ₃	ρ_{ST} = nm Sb ₂ Te ₃	Periods	Anneal.Temp. [°C]
0.2	9	9	9	56	150, 250
0.2	9	3	3	83	150, 250
0.2	15	3	3	56	150, 250
0.2	18	3	3	48	150, 250
0.2	21	3	3	42	150, 250



Used substrate materials: BaF₂ and Si/SiO₂. Most properties were determined with BaF₂ as substrate.

Chapter 7: Sputtered p-type Sb₂Te₃ / (Bi,Sb)₂Te₃ multilayer systems

In Chapter 7 results obtained on p-type nanoalloyed sputtered Sb₂Te₃ / (Bi_{0.2}Sb_{0.8})₂Te₃ SLs with a period length of 50, 25 and 12.5 nm are shown. Annealing temperatures, period length and total film thickness are varied.

Total period [nm]	(Bi,Sb) ₂ Te ₃			Sb ₂ Te ₃		Periods	Anneal.Temp. [°C]
	d_{Bi} [nm]	d_{Sb} [nm]	d_{Te} [nm]	d_{Sb} [nm]	d_{Te} [nm]		
50	2.2	7.5	15.8	9.5	16.1	30, 360	150, 250, 300, 350
25	1.1	3.8	7.9	4.8	8.0	60	150
12.5	0.6	1.9	4.0	2.4	4.0	120	150



Used substrate materials: Si/SiO₂

Chapter 8: Sputtered n-type Bi_2Te_3 / $(\text{Bi,Sb})_2\text{Te}_3$ multilayer systems

In Chapter 8, sputtered n-type nanoalloyed homogeneous compound films of Bi_2Te_3 and $(\text{Bi,Sb})_2\text{Te}_3$ and Bi_2Te_3 / $(\text{Bi}_{0.9}\text{Sb}_{0.1})_2\text{Te}_3$ SL films are investigated. The upper half of the shown deposition pattern is used for the deposition of $(\text{Bi,Sb})_2\text{Te}_3$ and the lower half is used for Bi_2Te_3 . For the homogeneous films, the Sb content is varied. For the SL films, the annealing temperature is varied.

Total period [nm]	$(\text{Bi,Sb})_2\text{Te}_3$			Bi_2Te_3		Periods	Anneal.Temp. [°C]
	d_{Bi} [nm]	d_{Sb} [nm]	d_{Te} [nm]	d_{Bi} [nm]	d_{Te} [nm]		
50	9.5	0.9	15.1	10.5	15.0	30	150, 200, 225, 250

Used substrate materials: Si/SiO₂



Chapter 9: Epitaxial Bi_2Te_3 and Sb_2Te_3 binary films and superlattices

Chapter 9 shows results for epitaxial films grown by MBE, i.e. binary Bi_2Te_3 and Sb_2Te_3 films and SLs. The results are analyzed with regard to the previously published works.

Total period [nm]	d-Sb ₂ Te ₃ [nm]	d-Bi ₂ Te ₃ [nm]	Periods
18	9	9	56
18	15	3	56
12	6	6	83
6	5	1	166

Used substrate materials: BaF₂.

Binary Sb_2Te_3 films were deposited with a substrate temperature of 330, 350 and 370 °C. The deposition temperature used for the superlattices was 350 °C, if not indicated otherwise.



Table of contents

Zusammenfassung	5
Table of contents	15
1 Thermoelectricity	17
1.1 The Seebeck, Peltier and Thomson effect and its applications	18
1.1.1 Thermoelectric devices and the figure of merit ZT	19
2 Thermoelectric transport in bulk and nanoscale materials	21
2.1 Bulk materials	22
2.1.1 Electrical properties	22
2.1.2 Lattice thermal properties, phonon transport: The Debye-Callaway model	25
2.2 Nanoscale materials	28
2.2.1 Electronic aspects, quantum confinement	28
2.2.2 Thermal aspects, reduction of thermal conductivity	30
3 The material system (Bi,Sb)₂Te₃	33
3.1 Overview over general structural properties	33
3.1.1 Suitable substrate materials	33
3.2 Phase diagrams	34
3.3 Transport properties	36
3.4 Thin films	39
3.5 Superlattice thin films	41
3.5.1 Structural properties of MOCVD-grown films	41
3.5.2 Transport properties of MOCVD-grown films	41
4 Experimental details: Deposition and characterization methods	43
4.1 Deposition methods and thin film fabrication	43
4.1.1 The "Nanoalloying" method	43
4.1.2 Calculation of element layer thicknesses	44
4.1.3 Molecular Beam Epitaxy (MBE)	45
4.1.4 Sputtering	48
4.1.5 Annealing system	52
4.2 Transport property characterization – methods and application	54
4.2.1 Van der Pauw method and Hall effect measurements	54
4.2.2 Seebeck coefficient measurement	55
4.2.3 Time Domain Thermal Reflectance (TDTR)	57
4.3 Structural characterization – methods and application	61
4.3.1 X-ray Diffractometry (XRD)	61
4.3.2 Scanning Electron Microscopy (SEM) with Energy-Dispersive X-ray Analysis (EDX)	62
4.3.3 Transmission Electron Microscopy (TEM)	63
4.3.4 Secondary Ion Mass Spectroscopy (SIMS)	64
5 Bi₂Te₃ and Sb₂Te₃ thin films grown with an MBE setup by nanoalloying	65
5.1 Dependence of texture on deposition pattern and initial element layer thickness	65
5.1.1 Bi ₂ Te ₃	65
5.1.2 Sb ₂ Te ₃	68
5.2 Dependence of transport properties on Te content	71
5.2.1 Bi ₂ Te ₃	71

5.2.2	Sb ₂ Te ₃	74
5.3	Electrical and structural properties in dependence on temperature	75
5.4	High-rate deposition experiments	77
5.5	Two-zone high-temperature annealing experiments with Bi ₂ Te ₃	78
5.6	Conclusions	80
6	Bi₂Te₃ / Sb₂Te₃ superlattice thin films grown with a MBE setup by nanoalloying	81
6.1	Structural properties	81
6.1.1	Composition and structure	81
6.1.2	Thermal stability	82
6.2	Transport properties	85
6.2.1	Electrical properties	85
6.2.2	Thermal conductivity	87
6.3	Conclusions	88
7	Sputtered p-type Sb₂Te₃ / (Bi,Sb)₂Te₃ multilayer systems grown by nanoalloying	89
7.1	Structural properties	89
7.2	Electrical properties	93
7.3	Power factor and thermal conductivity	95
7.4	Upscaling of film thickness and cross-plane measurement of electrical conductivity	96
7.4.1	Electrical cross-plane conductivity measurements on thick films	97
7.5	Estimation of <i>ZT</i>	98
7.6	Reduction of period length	99
7.6.1	Structural properties	99
7.6.2	Transport properties	101
7.7	Conclusions	102
8	Sputtered n-type Bi₂Te₃ / (Bi,Sb)₂Te₃ multilayer systems grown by nanoalloying	103
8.1	Optimization of Sb-content in (Bi,Sb) ₂ Te ₃	103
8.2	Bi ₂ Te ₃ / (Bi,Sb) ₂ Te ₃ – SL systems	104
8.2.1	Structural characterization	104
8.2.2	Transport properties	107
8.3	Conclusions	109
9	Epitaxial Bi₂Te₃ / Sb₂Te₃ binary thin films and superlattices	111
9.1	Binary thin films	111
9.1.1	Bi ₂ Te ₃	111
9.1.2	Sb ₂ Te ₃	111
9.2	Bi ₂ Te ₃ / Sb ₂ Te ₃ superlattices	115
9.2.1	Structural characterization	115
9.2.2	Transport properties	118
9.2.3	Thermal stability of SLs with 6 nm period length	119
9.3	Conclusions	122
	List of acronyms and symbols	123
	List of figures and tables	126
	List of publications	129
	Acknowledgement	132
	Bibliography	133

1 Thermoelectricity

Thermoelectric effects are known roughly since the beginning of the 19th century [1]. In 1794-1795, A. Volta conducted the very first experiments investigating this phenomenon. In 1821 T.J. Seebeck reported the magnetic polarization of metals and ores by a temperature difference and published it in 1825 [2,3-p.3]. Oersted stated correctly in 1823 that the effect is of electric rather than magnetic nature, coining the term “thermoelectricity”. The Peltier effect was discovered later in 1834. Altenkirch gave a theoretical analysis of energy conversion using thermocouples in 1911 [4], showing that the performance of thermoelectric materials is governed by the figure of merit ZT . With the introduction of semiconductors in the 1950s and later the introduction of solid solutions as thermoelectric materials [5,6] one was able to obtain sufficient values for ZT and attain appreciable performance of thermoelectric devices. However, the enthusiasm began to wane when since the 1950-1960s no material could be found that actually exceeded a ZT of ~ 1 . Much later, in the mid 1990s, research in the field of thermoelectrics experienced a renaissance due to theoretical predictions that the thermoelectric efficiency could be greatly enhanced through quantum confinement effects induced by nanostructural engineering [7]. However, in practice the reduction of thermal conductivity proved to be the more important effect of nanostructuring as was demonstrated by reports of a path-breaking ZT value of 2.4 for nanoscale $\text{Bi}_2\text{Te}_3 / \text{Sb}_2\text{Te}_3$ superlattices [8]. Currently, most of the activities in thermoelectric materials research is dedicated to the further improvement of the performance of thermoelectric materials by exploiting beneficial effects on the transport properties induced by nanostructuring, extending the range of applications for thermoelectric devices (Figure 1.1).

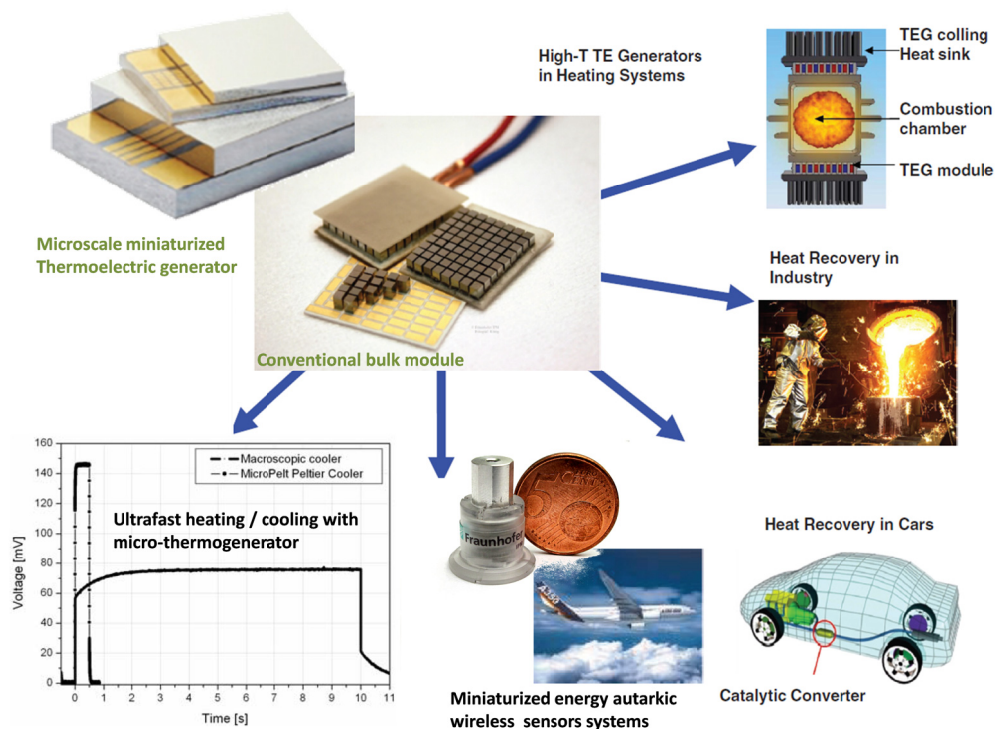


Figure 1.1 Applications of thermoelectricity. Images supplied by Micropelt GmbH and Fraunhofer IPM.

Thermoelectric generators scavenge heat and convert thermal energy to a “more useful” form, electric energy. They can be used in the form of large module arrays to harvest energy from heat sources in industrial processes, plants and automobiles or in the form of small assemblies to power energy autarkic sensor networks. Thermoelectric coolers can be used for the all-purpose space-limited cooling of arbitrary systems such as solid-state lasers or computer processors and are also available in multiple sizes ranging from tens of cm to several hundred micrometers. Advances in micro-electro-mechanical systems

engineering have enabled the fabrication of thin-film based microscale modules, which enable high cooling power densities of several 100 W/cm². Due to their low thermal mass, the desired temperatures can be attained extremely fast, usually within ~100 ms. Their low size allows to integrate them into very small energy harvesting systems that can be attached to a wide range of heat sources, for example to power energy-autarkic sensor systems.

1.1 The Seebeck, Peltier and Thomson effect and its applications

The Seebeck, Peltier and Thomson effect are the basic effects of thermoelectrics (see e.g. [9,10,11]) and can be illustrated with the thermocouple shown in Figure 1.2.

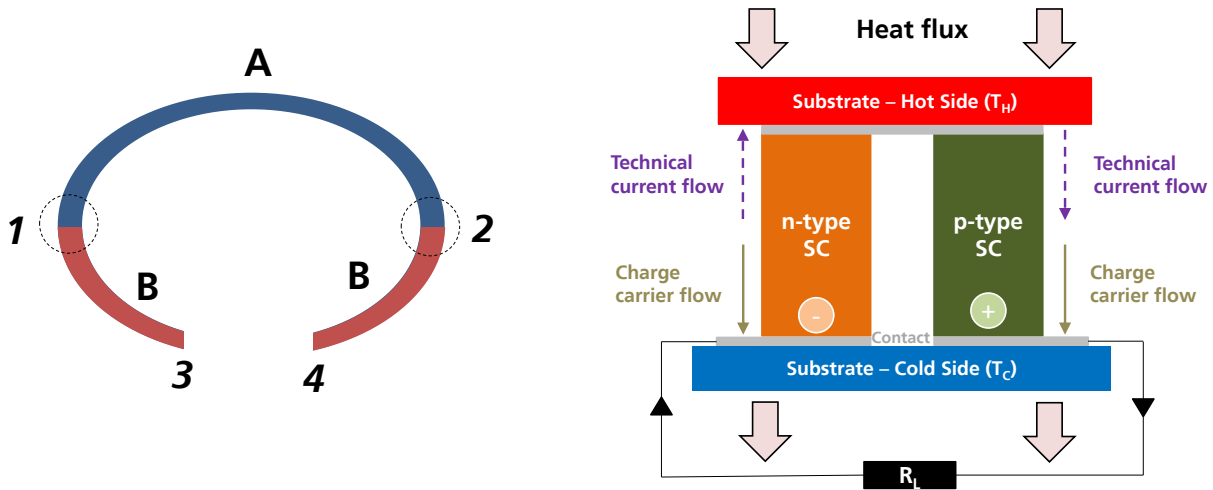


Figure 1.2 Left: Simple thermocouple consisting of materials A and B with junctions 1 and 2 and free ends 3 and 4. Right: Unicouple, representing the working principle of a thermoelectric generator.

Seebeck effect : The Seebeck effect can be seen as a consequence of thermally induced charge carrier diffusion [12]. If a small temperature difference ΔT is established between the material junctions 1 and 2 with junction 1 having a higher temperature than junction 2 and the free ends 3 and 4 of the material B are kept at the same temperature, a potential difference V is established between the free ends. The differential Seebeck coefficient (also referred to as thermopower) S_{AB} is defined as the ratio of this potential and temperature difference by

$$S_{AB} = \frac{V}{\Delta T} = S_A - S_B \tag{1.1}$$

and is given by the difference of the Seebeck coefficients S_A and S_B of the materials. S_{AB} is defined as positive if the potential difference induces a conventional current flow from the hot to the cold junction and negative if the opposite is the case. In practical Seebeck coefficient measurements (see e.g. sect. 4.2.2), always the differential Seebeck coefficient is measured since the material always has to be connected to some kind of conductor (e.g. Cu) in order to determine the Seebeck voltage V . Conveniently, usually the absolute Seebeck coefficient S is given for a single material which is then defined as positive (negative) for p (n)-type conductors.

Peltier effect: The Peltier effect is the phenomenologically reverse effect of the Seebeck effect. If a DC current I flows through materials A and B and junctions 1 and 2, one of the junctions heats up while the other cools down depending on the direction of the current. The differential Peltier coefficient Π_{AB} gives a relation between the current I and the amount of heat Q transported per time:

$$\dot{Q} = \Pi_{AB} \cdot I \tag{1.2}$$

Π_{AB} is defined as positive if current flows from material B to A and junction 1 heats up while junction 2 cools down and defined as negative if the opposite is the case. An absolute Peltier coefficient for each material can be defined in the same fashion as for the Seebeck coefficient.

Thomson effect: Contrary to the Seebeck and Peltier effect, the Thomson effect generally applies to single materials A and B. Suppose the ends of the material are subjected to a temperature difference ΔT while simultaneously an electrical current I flowing in the same direction as the gradient is applied to the material. The material then exchanges heat Q with its surroundings according to

$$\dot{Q} = \beta_T \cdot I \cdot \Delta T \quad (1.3)$$

with the Thomson coefficient β_T . The Thomson effect plays a rather minor role in thermoelectrics and can mostly be neglected.

Kelvin relations: Peltier, Seebeck and Thomson are related to each other via the Kelvin relations:

$$\Pi_{AB} = S_{AB} \cdot T ; \quad \frac{\partial S_{AB}}{\partial T} = \frac{\beta_{T,A} - \beta_{T,B}}{T}; \quad S_{A(B)} = \int_0^T \frac{\beta_{T,A(B)}}{T} dT \quad (1.4)a$$

With these equations, the Peltier and Thomson coefficient can be calculated from the relatively easily obtainable Seebeck coefficient.

1.1.1 Thermoelectric devices and the figure of merit ZT

The working principles behind thermoelectric energy conversion can be well illustrated with a single thermocouple consisting of a leg of n- and p-type semiconductor (SC) material (Figure 1.2). A basic derivation of device performances is outlined in [10].

The thermoelectric cooler: In this and the next section, an index p (n) will mark the transport property of the p (n) – type leg. The hot and cold side temperatures will be given by T_H and T_C , respectively.

The most important property of a thermoelectric cooler is the coefficient of performance (COP) ϕ , which is defined as the ratio of the heat extracted from the source to the expenditure of electrical energy.

The maximum COP ϕ_{max} that can be reached under optimum current conditions is:

$$\phi_{max} = \frac{T_C}{(T_H - T_C)} \cdot \frac{\sqrt{1 + ZT_m} - (T_H/T_C)}{\sqrt{1 + ZT_m} + 1} \quad (1.5)$$

with the mean temperature $T_m = (T_H + T_C)/2$. Expressed with the maximum COP $\phi_c = T_C / (T_H - T_C)$ that can be reached in a Carnot cycle it can be seen that eq. 1.5 is the Carnot COP multiplied with a loss factor depending on the material parameters and hot and cold side temperature. The influence of all material parameters is summarized in the figure of merit Z. Under optimal leg geometry, Z is given by

$$Z = \frac{(S_p - S_n)^2}{(\sqrt{\lambda_p \rho_p} + \sqrt{\lambda_n \rho_n})^2} \quad (1.6)$$

In the search for improved materials, a variant of Z that characterizes the performance of a single thermoelectric material would be convenient. With the material's (total) thermal conductivity λ , electrical conductivity σ and Seebeck coefficient S one can define a figure of merit z for a single material by

$$z_{n,p} = \frac{S^2}{\lambda \cdot \rho} = \frac{S^2 \cdot \sigma}{\lambda} = \frac{S^2}{\frac{\lambda_l}{\mu e} + LT} \quad (1.7)$$

where the numerator that characterizes the electrical transport properties of the material is commonly called the power factor ($PF=S^2\sigma$). In literature on thermoelectrics, it is common to denote the quantity z by Z , so Z will be used instead of z for the following sections of this work. Multiplying z or Z with T yields ZT , a dimensionless form of the figure of merit which is commonly used to characterize the thermoelectric performance of a material. Rewriting ZT with the lattice thermal conductivity λ_l (obtained by subtracting the electronic part of the thermal conductivity, λ_e from λ), the charge carrier mobility and concentration μ and n and Lorentz number L shows that ZT is determined by the ratio of λ_l to μ , which is a key point for material improvement considerations.

The thermoelectric generator: As shown in Figure 1.2, a thermoelectric generator converts thermal energy into electrical energy that it delivers to an application with load resistance R_L . The system can be characterized by the efficiency η , i.e. the ratio of electric output power to the thermal power that is drawing heat from the hot side. For optimized leg properties (load matching etc.), the maximum efficiency η_{max} is given by:

$$\eta_{max} = \frac{T_H - T_C}{T_H} \cdot \frac{\sqrt{1 + ZT_m} - 1}{\sqrt{1 + ZT_m} + T_C/T_H} \tag{1.8}$$

The definition of Z is analogous to the case of thermoelectric cooling as well as the structure of η_{max} compared to ϕ_{max} . The maximum efficiency is given by the Carnot efficiency η_c that applies to a reversible process multiplied with a loss factor induced by the irreversible processes due to irreversible losses (Joule heating, thermal conduction). η_{max} in dependence on ZT_m is plotted in Figure 1.3 for different hot side temperatures and is far below the maximum values that can be achieved in an ideal Carnot process. Increasing ZT to a value of 2 (a perhaps realistic goal) would yield significant improvements, significantly expanding the application field for thermoelectric energy conversion. The ZT values of the most important state-of-the-art-thermoelectric p-type materials for bulk and thin films are given in Figure 1.3 in dependence on temperature. Clearly, a significant improvement in performance was achieved by the introduction of nanostructured materials (indicated by an asterisk in the figure).

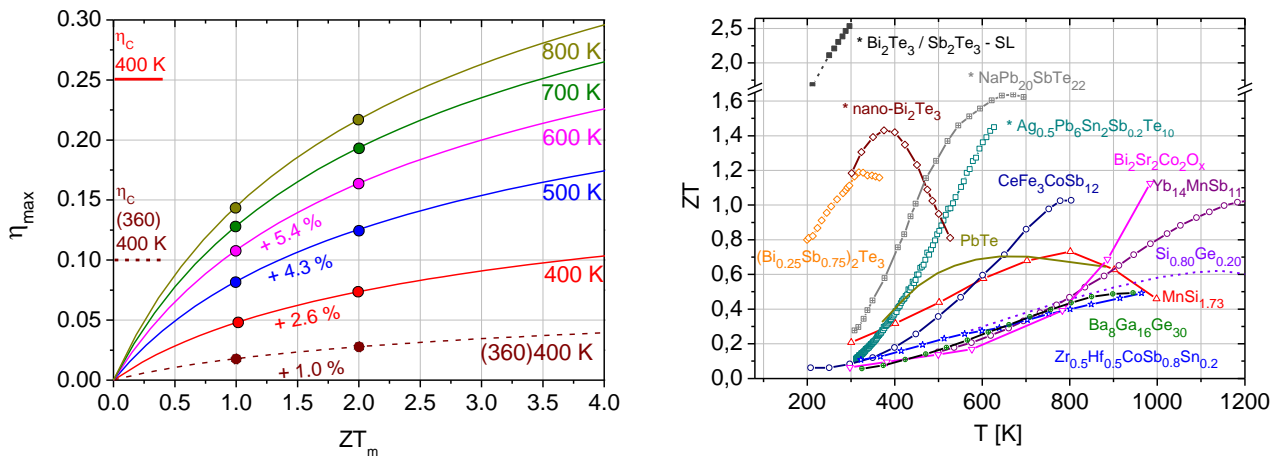


Figure 1.3 Left: Thermoelectric generator, plot of η_{max} vs. ZT_m (eq. 1.8) for different hot side temperatures. Solid lines: Cold side kept at 300 K, Brown dashed line: Cold side kept at 360 K (typical application case). Efficiency gains by increasing ZT from the classic value of 1 to a higher value of 2 are indicated for some temperatures. The Carnot efficiency η_c for selected temperatures is indicated on the left. Right: Current data for ZT of the currently most important p-type state-of-the-art thermoelectric materials. Asterisks indicate nanostructured materials. References: [8,13,14,15,16,17,18, 19,20,21,22,23,24,25].

2 Thermoelectric transport in bulk and nanoscale materials

The thermoelectric energy conversion is determined by the ratios of the transport coefficients and thus fundamental parameters of the electron and phonon systems. In the first part of this chapter the interrelations of the transport properties is explained for bulk materials based on the band theory for crystalline solids and solution of the linearized Boltzmann transport equations. It is further sketched how thermal conductivity can be described by the Debye-Callaway model. Electron and phonon scattering mechanisms are discussed and electron and phonon-related criteria for good thermoelectric materials are given. As a summary, in bulk materials best efficiencies are obtained for extrinsic semiconductors (i.e. semiconductors with enhanced electrical conductivity caused by additional dopand species). Specific values of the transport properties are necessary to yield a high efficiency. Typical values are $n \sim 10^{19} \text{ cm}^{-3}$, $\sigma \sim 1000 \text{ S/cm}$, $S \sim 200 \text{ } \mu\text{V/K}$ and a power factor $S^2\sigma$ of $\sim 40 \text{ } \mu\text{W/cmK}^2$. In addition to that, a low thermal conductivity λ is required, typically $\lambda = \lambda_e + \lambda_l$ is around 1 W/mK . The transport parameters σ , S and λ_e involved in the definition of ZT all depend sensitively in a different manner on the position of the chemical potential with respect to the band edges and thus carrier concentration (Figure 2.1), complicating materials optimization.

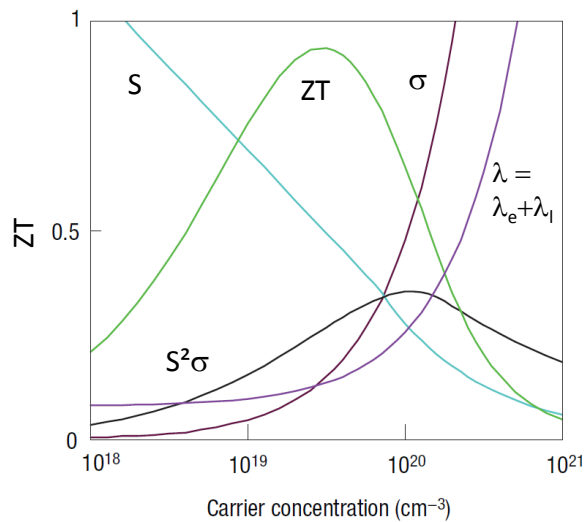


Figure 2.1 Interconnection of electrical conductivity, Seebeck coefficient, thermal conductivity and ZT on carrier concentration for Bi_2Te_3 [16] (details on crystal structure not given in reference). The optimum carrier concentration for this material is in the range of $10^{19} - 10^{20} \text{ cm}^{-3}$.

The transport parameters and ZT are also dependent on temperature. For thermoelectric applications around room temperature, Bi_2Te_3 and in particular its hole- and electron conducting solid solutions with Sb_2Te_3 and Bi_2Se_3 are used. Material properties of these compounds will be explained and discussed in the next chapter in detail. As a brief introduction for this chapter, these materials are characterized by a pseudo-hexagonal crystal structure. Transport is strongly anisotropic in these materials, i.e. electrical and thermal conductivity and diffusion coefficients are much lower parallel to the c -axis than perpendicular to it. This is why it is always important to consider the texture of the films and the direction in which these properties were measured. The directions referred to as "in-plane" and "cross-plane" direction correspond to the direction parallel and perpendicular to the film plane, respectively. In this work, the electrical properties were characterized in in-plane direction while the thermal conductivity was measured in cross-plane direction.

The second part of the chapter is dedicated to thermoelectric transport theory for nanostructured materials. Note that while there is no theoretical limit on ZT , several authors have dealt with the limits of

ZT of non-nanostructured materials under practical considerations, giving a practical maximum ZT of 1-2 [26] or a value of 2 at room temperature and ~ 4 at 1200 K [27]. It was concluded by the authors that radically different concepts such as nanostructures are required to increase ZT beyond that limit which is why there is a great amount of research activity in that field. The two major mechanisms for ZT improvement are, firstly, an improvement of the product of Seebeck coefficient and carrier concentration (or electrical conductivity) and secondly a reduction of thermal conductivity. Examples for both are given for 2D nanostructured superlattice systems. Recent results directly related to the record-breaking V_2VI_3 SLs are described in detail.

2.1 Bulk materials

2.1.1 Electrical properties

2.1.1.1 Boltzmann transport theory

The following considerations (see e.g. [9,10,11..]) apply to isotropic semiconductors with a single band and parabolic dispersion for electrons. Analogous considerations apply to holes as charge carriers. In the parabolic approximation, the energy $E = E(\mathbf{k})$ of a charge carrier is related to its momentum \mathbf{k} and effective mass m^* by $E = \hbar^2 k^2 / 2m^*$. In the most general case, the effective mass is a tensor with principal values of the effective masses m_1, m_2, m_3 along the crystal axes. The bulk energetic density of states is then given by

$$\rho(E) dE = \frac{\sqrt{2}}{\pi^2 \hbar^3} \cdot m_d^{\frac{3}{2}} \sqrt{E} dE \quad (2.1)$$

with the density of states (DOS) mass $m_d = K^{2/3} (m_1 m_2 m_3)^{1/3}$ that is a geometric mean of m_1, m_2, m_3 multiplied with the number of band extrema K . The Fermi-Dirac distribution for fermions in thermal equilibrium is given by eq. 2.2 with E_F as Fermi energy and k_B as Boltzmann constant. The Fermi distribution can be approximated by the Boltzmann approximation for $(E - E_F) \gg k_B T$, yielding a simple exponential distribution (right-hand side of eq. 2.2) [28].

$$f_0(E) = \frac{1}{\exp\left(\frac{E - E_F}{k_B T}\right) + 1} \approx \exp\left(\frac{E_F - E}{k_B T}\right) \quad (2.2)$$

The carrier concentration n is given by

$$n = \int_0^\infty \rho(E) f_0(E) dE \approx n_0 \cdot \exp\left(\frac{E_F - E_C}{k_B T}\right) \quad \text{with} \quad n_0 = 2 \left(\frac{m_d k_B T}{2\pi \hbar^2}\right)^{\frac{3}{2}}. \quad (2.3)$$

Applying the Boltzmann approximation in eq. 2.3 results in a simple exponential dependence for the carrier concentration on the position of the Fermi level E_F relative to the lower edge of the conduction band E_C . For heavily degenerate semiconductors (E_F moves into the conduction band), the Boltzmann approximation tends to get inaccurate and the integral form of eq. 2.3 has to be used to get accurate results.

Starting with the Boltzmann Transport Equation (BTE) in the relaxation time approximation [29-p.246] and taking into account the definitions of heat and electrical currents, expressions for the electrical conductivity, Seebeck coefficient and Lorentz number L that gives a relation between electrical and electronic thermal conductivity can be derived [9-p.403-417]:

$$\sigma = 2e\mu n_0 \cdot \frac{F_{s+1/2}}{\Gamma(s+3/2)} \quad (2.4)$$

$$\lambda_e = LT\sigma \quad (2.5)$$

$$S = \pm \frac{k_B}{e} \left[\eta - \frac{(s+5/2) \cdot F_{s+3/2}}{(s+3/2) \cdot F_{s+1/2}} \right] \quad (2.6)$$

$$L = \pm \left(\frac{k_B}{e} \right)^2 \left[\frac{(s+7/2) \cdot F_{s+5/2}}{(s+3/2) \cdot F_{s+1/2}} - \left(\frac{(s+5/2) \cdot F_{s+3/2}}{(s+3/2) \cdot F_{s+1/2}} \right)^2 \right] \quad (2.7)$$

Γ represents the Γ -integral and s the scattering parameter. s has a value of $-1/2$ for acoustic phonon and alloy scattering and $3/2$ for scattering on ionized impurities [10-p.59ff]. In the equations, a numerically convenient form of the so-called transport integrals as given in [10-p.35] is used:

$$K_i = \frac{8\pi}{3} \left(\frac{2}{h^2} \right)^{3/2} \sqrt{m_d} T \tau_0 \left(i + s + \frac{3}{2} \right) (kT)^{i+s+3/2} \cdot F_{i+s+1/2}(\eta) \quad (2.8)$$

$$\text{where } \eta = \frac{E_F}{k_B T} \quad \text{and} \quad F_z(\eta) = \int_0^\infty \frac{x^z}{1 + \exp(x - \eta)} dx$$

with the reduced dimensionless Fermi level energy η and the Fermi integral F_z . L for different solid solutions of $(\text{Bi}_{1-x}\text{Sb}_x)_2\text{Te}_3$ is given in Figure 2.2. For metals or generally, materials with very high carrier concentrations, L approaches the value of $\pi^3/3 (k_B/e)^2 = 2.45 \times 10^{-8} \text{ V}^2/\text{K}$.

Different simplifications for the transport equations exist. A very useful and widely used one is the Pisarenko relation, derived for a single carrier type in the Boltzmann approximation [30-p.307] which is, however, not accurate for metals and heavily degenerate semiconductors:

$$S = \frac{k_B}{e} \left[C + \ln \frac{2(2\pi m_d k_B T)^{3/2}}{h^3 n} \right] \quad (2.9)$$

with C as a constant that depends on the electron scattering mechanism. The relation explains why semiconductors in the non- or only slightly degenerate regime have a linear dependence of the Seebeck coefficient on logarithmic charge carrier concentration.

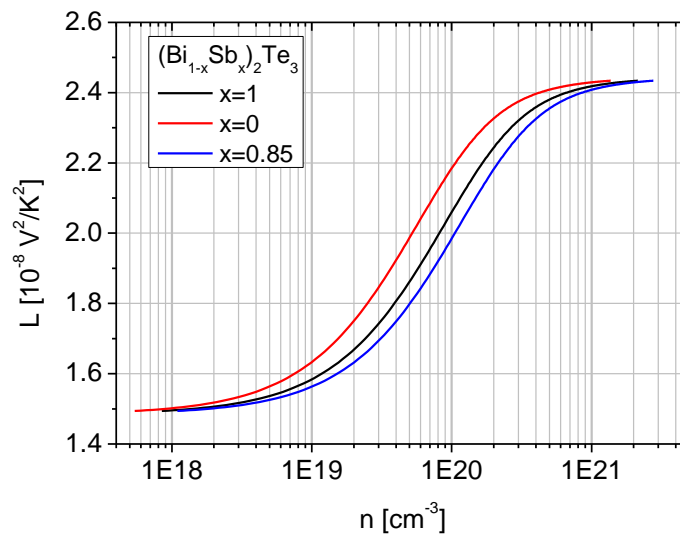


Figure 2.2 Calculated Lorentz number L in dependence of n for single crystalline $(\text{Bi}_{1-x}\text{Sb}_x)_2\text{Te}_3$ for different x (m_d for $x=1$ (n-type) was taken from [11-p.118], for the other values of x (p-type) the values of m_d were taken from Table 3.3 or [31]. The calculated L for $x = 0.75, 0.85$ and 0.9 are nearly identical, thus only L for $x = 0.85$ is shown.

2.1.1.2 Carrier compensation effects on electrical conductivity

For intrinsic and extrinsic semiconductors, the intrinsic carrier concentration n_i is connected to the electron concentration n and the hole concentration p by [28]:

$$n_i = \sqrt{n \cdot p} = \sqrt{n_0 \cdot p_0 \cdot e^{-E_G/(k_B T)}} \quad (2.10)$$

with p_0 for the holes defined analogously to n_0 for the electrons in eq. 2.3. As an example, using the material data for Bi_2Te_3 presented in section 3.3, $n_i = 1.4 \times 10^{18} \text{ cm}^{-3}$ for Bi_2Te_3 can be calculated.

The total carrier concentration n_{tot} determines the electrical conductivity by $\sigma = en_{tot}\mu$ and can be calculated by:

$$n_{tot} = n + p = n_i^2/p + p \quad (2.11)$$

where n and p are electron and hole concentration, respectively. Figure 2.3 shows n_{tot} in dependence of p . This corresponds to a one-band n-conducting semiconductor (n_i is constant) in which charge is partly carried by holes, corresponding to a compensated semiconductor. Evidently, the addition of holes reduces the conductivity until a n_{tot} that corresponds to twice the intrinsic carrier concentration is reached. Since also the Seebeck coefficient is reduced by compensation effects (see eq. 2.17 below), these effects are clearly detrimental for the thermoelectric performance.

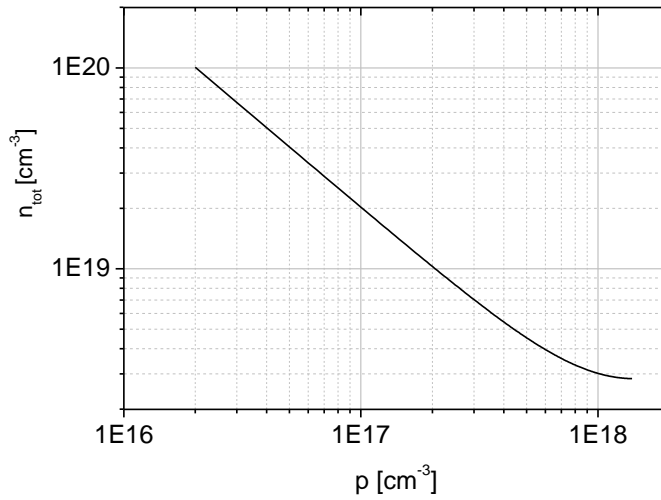


Figure 2.3 Calculated total carrier concentration n_{tot} in dependence of hole concentration p for Bi_2Te_3 .

2.1.1.3 Electronic scattering processes

Scattering by acoustic phonons is the predominant process in the Bi_2Te_3 -based materials at room temperature and above. The carrier mobility under acoustic phonon scattering is limited due to fluctuations of the periodic potential and given by $\mu \propto v^2 \rho \cdot m^{*-5/2} T^{-3/2}$ [32-p.69].

For alloy scattering, no quantitative expression is given in [32] and subrefs. One may consider the scattering on neutral impurities. According to [9-p.409], the mobility due to scattering on neutral impurities is inversely proportional to the concentration of scatterers N_N . Indeed, it appears that for some compounds the decrease of electrical conductivity or mobility is roughly linear to the content of foreign atoms if their concentration is small, e.g. for the alloy $\text{Bi}_2\text{Te}_3\text{-Sb}_2\text{Te}_3$ (p-type), Figure 2.4, $\text{Bi}_2\text{Te}_3\text{-Bi}_2\text{Se}_3$ (n-type) [6] or Cu-Ni [29-p.255].

Electron grain boundary scattering was investigated by a number of authors. The consensus is that the increase of resistivity ρ_{gr} over that of a single crystal due to boundary scattering is proportional to the

2.1 BULK MATERIALS

inverse grain diameter d [33] according to the relation $\rho_{gr} \propto \frac{R_{ref}}{1-R_{ref}} S_V$ where R_{ref} is the reflection coefficient and $S_V \propto d^{-1}$ the total boundary surface per unit volume.

Ionized impurity scattering is not of great importance despite the high number of acceptors and donors in typical highly doped thermoelectric materials, [32-p.70].

The influences of different scattering mechanisms associated with carrier mobilities μ_i on the total mobility μ_{tot} can be combined by Matthiessen's rule, $1/\mu_{tot} = \sum_i 1/\mu_i$.

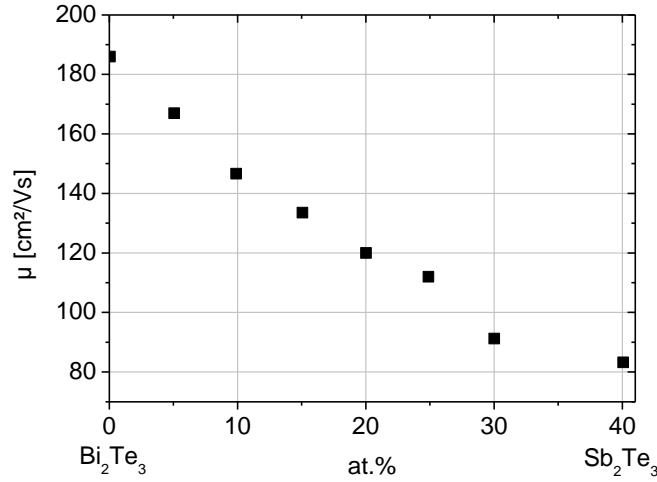


Figure 2.4 Electron mobility in dependence of composition in the Bi_2Te_3 - Sb_2Te_3 system. Data from [6] (details on crystal structure not given in the reference).

2.1.2 Lattice thermal properties, phonon transport: The Debye-Callaway model

After the collision of two phonons with wave vectors \mathbf{k}_1 and \mathbf{k}_2 , the resulting wave vector is given by \mathbf{k}_3 plus a reciprocal lattice vector \mathbf{G} [9-p.328], i.e. $\mathbf{k}_1 + \mathbf{k}_2 = \mathbf{k}_3 + \mathbf{G}$. Here, $\mathbf{G}=0$ characterizes N(normal)-processes during which the total phonon momentum is conserved and heat transport is not impaired, yet phonon momentum is redistributed. U(mklapp)-processes occur for $\mathbf{G} \neq 0$, meaning that the crystal lattice participates in the scattering process and the resulting wave vector \mathbf{k}_3 leads outside the Brillouin zone which is possible if the initial phonon momenta are sufficiently high. U-processes are associated with phonon momentum reversal and tend to restore the phonon distribution towards the equilibrium distribution and thus give rise to thermal resistance.

The Debye-Callaway (DC) model is a sophisticated model for the calculation of the thermal conductivity of elements and compounds. It assumes that collisions change the phonon energy distribution by momentum-conserving N-processes (relaxation time τ_N) and non-momentum conserving processes (relaxation time τ_r) which have to be treated separately. Asen-Palmer et al. [34] and finally Morelli et al. [35] pointed out that the total lattice thermal conductivity λ_l consists of two terms (see eq. 2.13) of which the second one cannot be neglected for very pure, defect-free samples and that good results can be obtained by treating transverse and longitudinal phonons separately. Only acoustic phonons are considered since optical phonons hardly carry any heat due to their low group velocity due to their flat dispersion $\partial\omega/\partial k$ [36]. λ_l is given by adding up longitudinal and transversal phonon thermal conductivity λ_L and λ_T [35]:

$$\lambda_l = \lambda_L + 2\lambda_T \quad \text{with} \quad \lambda_{L,T} = \lambda_{L,T1} + \lambda_{L,T2} \quad (2.12)$$

Here, only the case of longitudinal phonons (indices $L1$ and $L2$) is sketched in eq. 2.13. Expressions for transversal phonons are analogous and C , θ_D , τ , v_s , B and τ_N^{-1} (see below) have to be taken accordingly.

$$\lambda_{L1} = \frac{1}{3} CT^3 \int_0^{\theta_D/T} \tau_C J dx \quad \text{and} \quad \lambda_{L2} = \frac{1}{3} CT^3 \frac{\left[\int_0^{\theta_D/T} \frac{\tau_C}{\tau_N} J dx \right]^2}{\int_0^{\theta_D/T} \frac{\tau_C}{\tau_N \tau_R} J dx} \quad (2.13)$$

where

$$J(x) = \frac{x^4 e^x}{(e^x - 1)^2}, \quad 1/\tau_C = 1/\tau_N + 1/\tau_R, \quad x = \frac{\hbar\omega}{k_B T}, \quad C = \frac{k_B^4}{2\pi^2 \hbar^3 v_S}.$$

According to Matthiessen's Rule, the influence of scattering processes can be combined by adding up the inverses of the relaxation times. In this sense, the relaxation time τ_R sums up all resistive, phonon-momentum changing scattering processes. τ_C sums up all of these scattering processes plus the normal processes with τ_N . The scattering processes associated with the given relaxation times τ are Umklapp scattering (τ_U), mass-fluctuation (point-defect) scattering (τ_I), boundary scattering (τ_B) and normal scattering (τ_N) that are added up by:

$$\tau_R^{-1} = \tau_U^{-1} + \tau_I^{-1} + \tau_B^{-1} \quad \text{and} \quad \tau_C^{-1} = \tau_N^{-1} + \tau_R^{-1}. \quad (2.14)$$

Each τ has a different dependence on phonon frequency ω and temperature T :

$$\tau_U^{-1} = B_U \omega^2 T e^{-\theta_D/3T} \quad ; \quad \tau_I^{-1} = B_I \omega^4 \quad ; \quad \tau_B^{-1} = \frac{v_S}{d} \quad ; \quad \tau_N^{-1} = B_N \omega^2 T^3. \quad (2.15)$$

Here, d is the dimension of the crystal or grain. The prefactors B contain material-specific properties such as the phonon group velocity v_s and are given e.g. in refs. [10-p.71,35]. Specifically, the point-defect scattering prefactor B_I is proportional to the mass disorder, i.e. the sum of the deviations of the i -th unit cell atomic mass M_i (with a concentration x_i) from the average mass per unit cell \overline{M} divided by the number N of unit cells per volume [32-p.78].

$$B_I = \frac{\pi}{2v_S^3 N} \underbrace{\sum_i x_i \left[\frac{M_i - \overline{M}}{\overline{M}} \right]^2}_{\Gamma} \quad (2.16)$$

Figure 2.5 (left) shows schematically the limitation of λ due to different scattering mechanisms [32-p.80]. The upper boundary is given by the ω^2 dependence of U and N processes that occur in every solid. Point defect scattering reduces the thermal conductivity strongly in the high-frequency regime due to the ω^4 dependence. For low frequencies, point defect scattering is negligible and boundary scattering becomes more and more important which was verified in several experiments (sect. 2.1.2.1).

2.1.2.1 Scattering of phonons on grain boundaries in polycrystalline materials

Figure 2.5 (left) explains why boundary scattering by grains can indeed reduce the thermal conductivity although the average phonon MFP is several orders of magnitude lower than the grain size: In a typical (alloyed) thermoelectric material with its high number of point defects due to alloying, the high phonon frequencies are cut off by point defect scattering and only the phonons with long wavelength (much larger than the typical average of 10^{-9} - 10^{-10} m) and MFP remain [32-p.80]. It is concluded that these remaining long-wave phonons can be successfully scattered by the boundaries of nm to μm sized grains, which was experimentally proven on irradiated Si and SiGe [32-p.81] and V_2VI_3 compounds.

Figure 2.5 (right) displays the results of experiments carried out by Boikov et al. [37]. λ_l of $(\text{Bi}_{0.25}\text{Sb}_{0.75})_2\text{Te}_3$ and Bi_2Te_3 deposited on different substrates (at 250-270 °C) with and without annealing (at 370-380 °C) are compared. The thermal conductivity in alloy (i.e. point-defect rich) $(\text{Bi,Sb})_2\text{Te}_3$ films deposited on nylon was found to be strongly reduced (by ~ 40 %) in unannealed films compared to annealed films due to the increased number of grain boundaries. In Bi_2Te_3 , as theoretically predicted the reducing effect on λ_l is lower (~ 20 %). A reduction of λ_l compared to bulk single crystals [11-p.126],

2.1 BULK MATERIALS

Bi_2Te_3 : 1.4 - 1.7 W/mK, $(\text{Bi}_{0.25}\text{Sb}_{0.75})_2\text{Te}_3$: 0.55 - 1.2 W/mK is evident. Since simultaneously the electrical properties remained stable, an improvement of ZT compared to the best room-temperature values of bulk single crystals (~ 1.0 for $(\text{Bi}_{0.25}\text{Sb}_{0.75})_2\text{Te}_3$ [11]) obtained up to the time of the publication is reported.

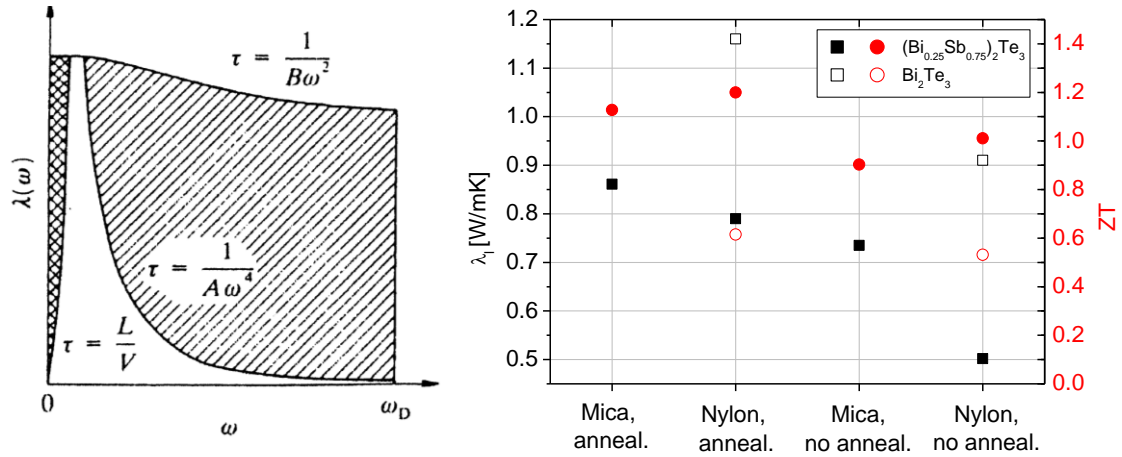


Figure 2.5 Left: Schematic dependence of thermal conductivity on phonon frequency [32-p.80]. Note that the symbols for the prefactors differ from those given in eq. 2.15. Void area: Only Umklapp / Normal scattering is effective. Single hatched area: Thermal conductivity reduction due to alloy scattering in a solid solution. Double-hatched area: Reduction of $\lambda(\omega)$ by boundary scattering for small crystallite sizes. Right: Lattice thermal conductivity (black symbols) and ZT (red symbols) of $(\text{Bi}_{0.25}\text{Sb}_{0.75})_2\text{Te}_3$ and Bi_2Te_3 on different substrates. Data from [37].

In another experiment reported by the groups of D.C. Johnson and D. Cahill, the (total) thermal conductivities of polycrystalline Bi_2Te_3 and $(\text{Bi}_{0.5}\text{Sb}_{0.5})_2\text{Te}_3$ thin films were analysed in dependence on grain size d [38] and compared to the predictions of an extended DC model for the lattice thermal conductivity (Figure 2.6). The parameters and assumptions used to construct the model are described in the reference. For the alloy, point defect scattering was included by estimating $\Gamma = 0.3$.

Similarly, Takashiri et al. measured the cross-plane thermal conductivity of nanocrystalline $(\text{Bi,Sb})_2\text{Te}_3$ films (grain size = 150 nm) and found a thermal conductivity of 0.6 W/mK, which they describe as a 20 % reduction to the corresponding bulk single crystal alloy [39].

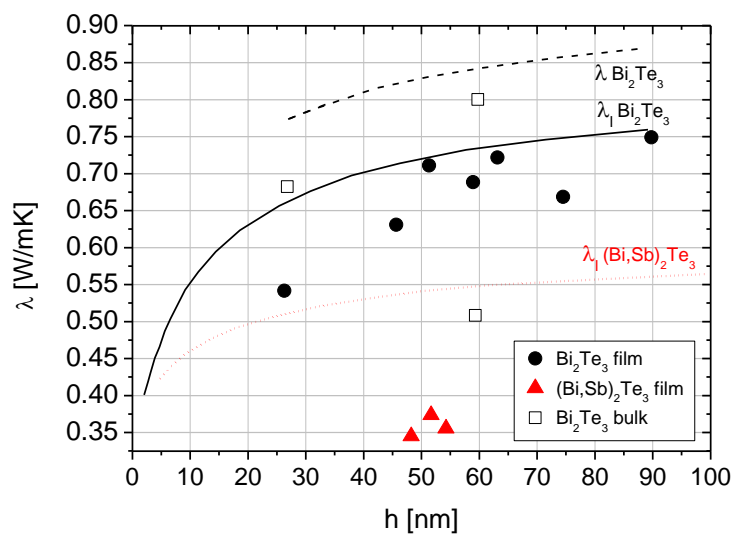


Figure 2.6 Plot of thermal conductivity vs. grain size of Bi_2Te_3 and $(\text{Bi}_{0.5}\text{Sb}_{0.5})_2\text{Te}_3$ thin films [38]. Symbols are described in the key. Black solid line: λ_l derived from DC model for Bi_2Te_3 . Black dashed line: λ_l from DC model plus electronic thermal conductivity for Bi_2Te_3 . Red dotted line: λ_l derived from DC model for $(\text{Bi,Sb})_2\text{Te}_3$.

2.2 Nanoscale materials

2.2.1 Electronic aspects, quantum confinement

Multilayered stacks can be described in a transport matrix formalism [40], treating them as bulk and not taking into account nanoscale effects. Two layers A and B are considered and the transport properties S , σ , λ , γ and thicknesses d are indexed accordingly. In the case of current flow parallel to the layers of the ML system, the transport properties σ_C , S_C , γ_C of the whole layer system are given by [54]

$$\sigma_C = \frac{d_A \sigma_A + d_B \sigma_B}{d_A + d_B} \quad S_C = \frac{d_A \sigma_A S_A + d_B \sigma_B S_B}{d_A \sigma_A + d_B \sigma_B} \quad \gamma_C = \frac{d_A \gamma_A + d_B \gamma_B}{d_A + d_B} \quad (2.17)$$

with $\gamma_C = \lambda_C + T \sigma_C S_C^2$. After further detailed considerations, the authors conclude that $Z_C T$ for a “bulk” ML system is always smaller than that of a single layer. Similar considerations apply for a current flow perpendicular to the MLs, showing that the improvement of $Z_C T$ by synthesizing ML systems is only possible by exploiting nanoscale effects.

The basic idea behind the nanostructuring of thermoelectric materials (presented e.g. by Dresselhaus et al. [7] in the 1990s) was the modification of the electronic dispersion relation and thus the density of states, allowing new opportunities to vary S , σ , and λ quasi-independently for length scales small enough to give rise to quantum-confinement effects. Considering the electronic properties, the main goal for the introduction of nanostructures is the improvement of the *relation of S and σ* , i.e. an increase of the power factor. Here, the focus will be set on thin film materials in the form of 2-dimensional so-called multi(ple) quantum well (MQW) structures. A MQW structure can be defined by a periodic arrangement of quantum wells (Figure 2.7) with a depth of V_b that are separated by barriers. An ideal MQW has an infinite depth, e.g. $V_b = \infty$. The electron wave function $\psi(\mathbf{r})$ must fulfill the Schrödinger equation [29-p.450] for the three components m_i of the effective mass. Separating $\psi(\mathbf{r})$ into a simple plane wave for the electrons that are free in the x and y direction and a function $\phi_n(z)$ that describes the confinement in the z direction allows to separate eq. the Schrödinger equation into two differential equations:

$$\left[-\frac{\hbar^2}{2m_z} \frac{\partial^2}{\partial z^2} - eV(z) \right] \phi_n(z) = E_n \phi_n(z) \quad (2.18)$$

$$\left(-\frac{\hbar^2}{2m_x} \frac{\partial^2}{\partial x^2} - \frac{\hbar^2}{2m_y} \frac{\partial^2}{\partial y^2} \right) e^{ik_x x + ik_y y} = E_{xy} e^{ik_x x + ik_y y}$$

This gives the dispersion relations for the discrete energy levels E_n in each ideal quantum well with $V_b = \infty$ according to eq. 2.19. The dispersion relation can be interpreted as so-called subbands that are continuous along k_x and k_y but discrete for different k_z (Figure 2.7). Each subband has a constant DOS of $m_{\parallel} / \pi \hbar^2$ [29-p.451] and the DOS for the 2D system of all subbands $\rho(E)_{2D}$ is given by a staircase-like function with H as the Heaviside function:

$$E_n(\mathbf{k}) = \frac{\hbar^2 k_x^2}{2m_x} + \frac{\hbar^2 k_y^2}{2m_y} + \frac{n^2 \hbar^2 \pi^2}{2m_z d_A^2} = \frac{\hbar^2 k_{\parallel}^2}{2m_{\parallel}} + \frac{n^2 \hbar^2 \pi^2}{2m_z d_A^2} \implies \rho(E)_{2D} = \frac{m_{\parallel}}{\pi \hbar^2} \sum_n H(E - E_n) \quad (2.19)$$

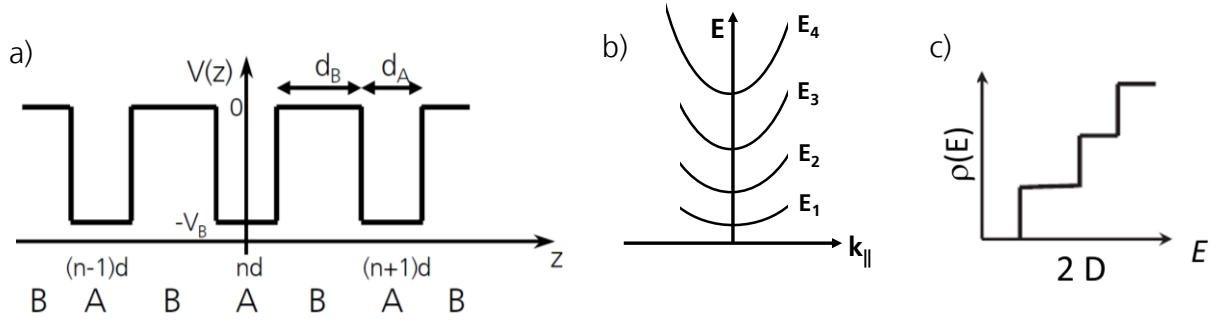


Figure 2.7 a) Schematic of MQW structure, consisting of multiple quantum wells with a width of d_A , spaced apart by the period length $d=d_A+d_B$. b) Schematic of subbands in a single quantum well ($V_B = \infty$) for the discrete energy levels E_n . The energy difference between the subbands is given by eq. 2.19. c) DOS for a two-dimensional nanostructure.

Dresselhaus et al. assumed an ideal quantum well embedded in a wide-bandgap semiconductor i.e. a) the electrons occupy only the lowest ($n=1$) subband, b) no tunneling takes place through the wide-gap semiconductor and c) the wide-gap semiconductor does not conduct [7]. The transport parameters were recalculated under these conditions, yielding under further assumptions a $Z_{2D}T$ that depends also on the well width d_A . Altogether, a significant improvement of $Z_{2D}T$ over the bulk ZT value was evident depending on d_A . An experimental proof, refinement and extension of the concept discussed above was later presented in [41]. However, in a more realistic scenario the transport properties of the whole system (wells *and* barriers) must be taken into account. Furthermore, in a real SL structure the barriers are not infinitely high and the well wave function penetrates into the barriers, where it decays exponentially and “leaks” into the other wells. By this well interaction, minibands form and the DOS is no more a sharp step function but “smears out”, becoming more and more similar to a 3D dispersion relation [42-p.35]. Altogether, it is not surprising that in more realistic models a much lower effective ZT than given by the first simplified calculations is obtained [43]. In conclusion, it is evident that under realistic conditions, electronic effects induced by 2D nanostructuring *play a rather minor role in directly improving ZT* , in particular for Bi_2Te_3 -based SLs as treated in this work.

Electron filtering effects: When the Fermi level moves deeply into the band, the so-called differential conductivity $\sigma(E) \propto \rho(E)$ that is related to the electrical conductivity by $\sigma = \int_0^\infty \sigma(E) \left(-\frac{\partial f_0(E)}{\partial E}\right) dE$ becomes more and more symmetric with respect to the Fermi energy E_F due to the flat square-root shape of the bulk DOS [44]. Then, the contributions from electrons below and above E_F cancel out each other in the Seebeck integral [45]

$$S = \frac{k_B}{e} \frac{1}{\sigma} \int_0^\infty \sigma(E) \left(\frac{E - E_F}{k_B T}\right) \left(\frac{\partial f_0(E)}{\partial E}\right) dE \quad (2.20)$$

and a low Seebeck coefficient results, which is the case in a metal or very heavily doped semiconductor. Contrarily, a highly asymmetric differential conductivity in combination with high electron energies should yield a high Seebeck coefficient. Venkatasubramanian proposes the mechanism to lead to high PFs in cross-plane direction of $\text{Bi}_2\text{Te}_3/\text{Sb}_2\text{Te}_3$ - SLs [46] through a filtering effect caused by the valence-conduction band offset due to band gap differences of the binaries.

2.2.1.1 Electrical anisotropy in Bi_2Te_3 / Sb_2Te_3 SLs

The Mertig group in Halle recently published a series of results dealing with the electrical properties of $\text{Bi}_2\text{Te}_3/\text{Sb}_2\text{Te}_3$ stacks with special focus on the severe reduction of transport anisotropy in the SLs as proposed in [8] (see Figure 3.6) for cross-plane/in-plane electrical conductivity, an unexpected phenomenon that is still not well understood. Transport properties of Bi_2Te_3 and Sb_2Te_3 under strain [47] and the anisotropy of Bi_2Te_3 and Sb_2Te_3 in a stack arrangement in a nanoscale heterostructure [48] were examined. Interestingly in the case of p-conduction, the heterostructure showed an electrical conductivity anisotropy comparable to bulk material [48]. A clear preference for the in-plane transport

direction was obtained. The results are of high interest with respect to experimental results where an elimination of the electrical conductivity anisotropy was found for SLs at distinct period lengths [8]. No such effects could be confirmed by the mentioned theoretical calculations.

Recently, the ab initio calculations were further improved and extended to a SL with 3 nm period consisting of different proportions x of Bi_2Te_3 and Sb_2Te_3 [49]. In the calculations, quantum confinement effects due to the band-gap differences of the two compounds and band-structure effects were also taken into account. Most importantly, the authors *still did not* find a significant reduction of conductivity anisotropy $\sigma_{\parallel}/\sigma_{\perp}$ but rather a monotonous variation between the values for the binaries (Figure 2.8,d). The cross-plane PF showed no improvement over both binaries for the SL structure (b) and thus, even assuming the most optimistic value for the thermal cross-plane lattice conductivity (0.22 W/mK), a maximum cross-plane ZT of only 0.9 was obtained at room temperature and 1.3 at elevated temperature (c). The latter is only roughly half the value reported for the SLs with 6 nm period in [8].

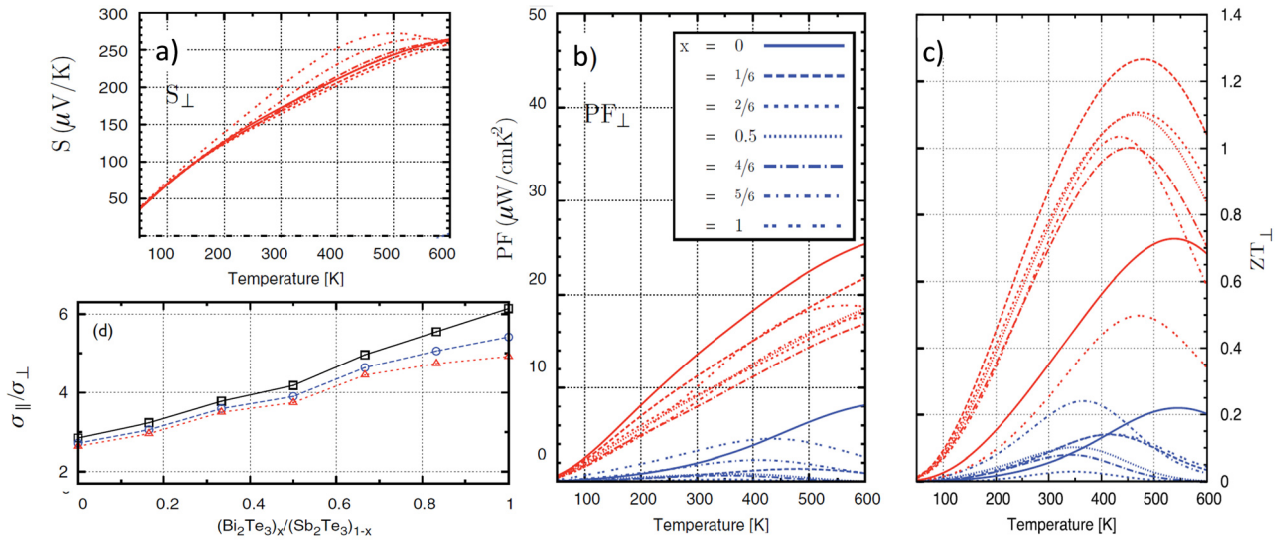


Figure 2.8 a) Calculated cross-plane Seebeck coefficient in $\text{Bi}_2\text{Te}_3/\text{Sb}_2\text{Te}_3$ SL stacks [49]. b) Cross-plane power factors in SLs. c) Cross-plane ZT in SLs under assumption of $\lambda_{\perp} = 0.22 \text{ W/mK}$. Red lines refer to hole doping, blue lines refer to electron doping (not relevant for this work). d) Variation of anisotropy ratio in dependence of the thickness proportion in $(\text{Bi}_2\text{Te}_3)_x/(\text{Sb}_2\text{Te}_3)_{1-x}$ SLs. x is 0 for pure Bi_2Te_3 , 1 for pure Sb_2Te_3 and 0.5 for a $\text{Bi}_2\text{Te}_3/\text{Sb}_2\text{Te}_3$ SL with a compound layer thickness of 1.5 nm each. Black, blue and red lines refer to carrier concentrations of 3 , 6 and $9 \times 10^{19} \text{ cm}^{-3}$.

2.2.2 Thermal aspects, reduction of thermal conductivity

In this section, some exemplaric works on the theoretical and experimental understanding of thermal conductivity reduction in SL structures are shown. It is noted that further research in this direction was carried out by authors such as Hyldgaard and Mahan [50] (phonon confinement due to Si and Ge mode mismatch), Ren et al. [51] (mini-Umklapp processes in SLs), Touzalbaev et al. [52] (consideration of interface roughness) and Takahashi et al. [53] (description of one-dimensional heat transport by a matrix formalism for sharp and diffuse interfaces).

Bragg reflection of phonons and phonon stop bands: Electrons traveling through a periodic SL structure consisting of layers A and B undergo Bragg reflection if the condition $m\lambda_p = 2D\cos\theta$ is fulfilled [54]. Here, λ_p is the phonon wavelength, $D = d_A + d_B$ the superlattice period and θ the angle of the phonon incidence vector with the SL normal. The Bragg reflection produces band gaps or “stop bands” at the boundaries and centers of the Brillouin zone, similar to the electron band gap in semiconductors and isolators. At the frequencies corresponding to the stop bands, the phonon transmission rate (calculated for a finite SL with 15 periods) is strongly reduced. Experimental proof of the phonon stop bands was found by Narayanamurti et al. [55] who determined the phonon transmission rate of a GaAs / GaAlAs SL. Dips in the transmission rates were found and their positions corresponded well to energies calculated under the assumption of Bragg reflection (0.93 meV). In analogy to optical dielectric photon filters, the authors coin the term of “dielectric phonon filters” for their SLs.

Specular and diffusive scattering of phonons at interfaces: Chen considered interface roughness in SLs by taking into account a certain proportion of diffuse scattering mixing with specular scattering [56]. Several models were presented, including the elastic acoustic mismatch model that gives interface reflectivity as

$$R_{am} = r_{am}^2 = \left(\frac{Z_A \cos \theta_A - Z_B \cos \theta_B}{Z_A \cos \theta_A + Z_B \cos \theta_B} \right)^2 \quad (2.21)$$

with θ as normal angle and $Z = \rho v_s$ as acoustic impedance of the material which is the product of density ρ and speed of sound v_s . It was found that especially for SLs thinner than the phonon MFP, the effective λ is to a large degree controlled by the interfaces and not the bulk scattering processes in the single layers. Thus, the authors conclude that many good thermal conductors (such as Si or Ge) can be engineered to yield low- λ structures. As expected, λ_l is strongly dependent on the period thickness and also on the value of the specularity.

Diffusive transport and phonon localization: Based on the thermal conductivity data on MOCVD-grown $\text{Bi}_2\text{Te}_3/\text{Sb}_2\text{Te}_3$ SLs (Figure 2.9), Venkatasubramanian explained the interconnection of thermal conductivity and SL period with simple models based on diffusive transport analysis and Bragg reflection at the interfaces [57]. It is concluded that a low-frequency cutoff $\omega_{cut} \propto (l_{mfp})^{-1}$ exists that is directly related to the phonon mean free path l_{mfp} . The proposed near-complete transmission of high-frequency phonons and lossy transmission of low-frequency phonons is in agreement with previous observations on GaAs / (Al,Ga)As SLs [55]. The frequency cutoff increases for smaller l_{mfp} and less phonons can participate in heat transfer, leading to lower thermal conductivity. Furthermore, acoustic mismatch is considered to explain the drop in λ_l with decreasing period length. To explain the following rise of λ_l for very small period lengths < 5 nm it is proposed that the two layers get coupled when the cutoff wavelength approaches the thickness of both layers, reducing the effect of acoustic mismatch and enabling phonon transport across the interface.

Additionally, localization criteria known from the analysis of electron and photon scattering in media with substructural features such as SL are applied to explain the data. Generally, the argument is that localization occurs if $kl_{mfp} < 1$ [58]. Then, the phonon MFP is so small in comparison to the wavelength that the wave cannot execute one single oscillation before being scattered again [59]. Consequently, a small kl_{mfp} product indicates strong transmission blocking and localization. In [8] the kl_{mfp} products of holes and phonons are calculated and compared. kl_{mfp} for holes is 7.6 while that of the phonons is only 0.5, which illustrates the phonon-blocking / electron-transmitting nature (Figure 2.9) of the MOCVD-grown SLs.

Specular and diffusive scattering of phonons at interfaces: Pattamatta and Madnia adopt the features of Chen's model [56] to model the heat transfer in $\text{Bi}_2\text{Te}_3 / \text{Sb}_2\text{Te}_3$ SLs [61]. Results of calculations are shown in Figure 2.9 in comparison with experimental data. A ρ of 0.8 – 1 fits the experimental data appropriately for period lengths down to 5 nm. The model fails to predict the rise of thermal conductivity k with small period lengths $L\rho$. The authors reason that this rise is due to the wave nature of phonons [57] while the presented model treats them as particles.

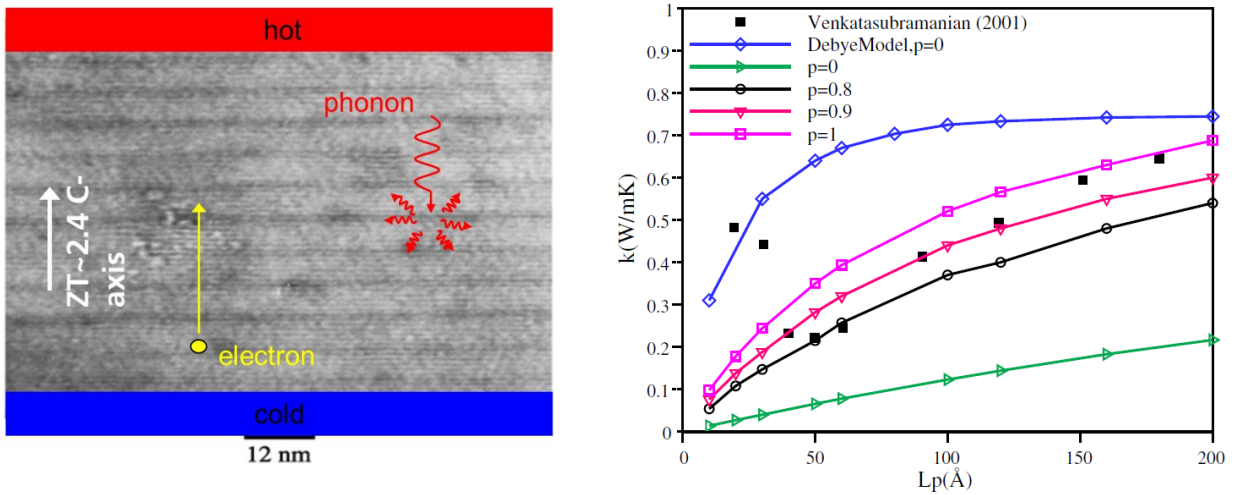


Figure 2.9 Left: TEM image of a SL with 60 Å (6 nm) period length [60], representing a so-called Phonon Glass Electron Crystal (PGEC) structure. Dark lines = Bi_2Te_3 , bright sections = Sb_2Te_3 . Right: Variation of lattice thermal conductivity (here, k) with period length L_p for $\text{Bi}_2\text{Te}_3 / \text{Sb}_2\text{Te}_3$ SLs (black squares, data from [57]) together with model data from Pattamatta et al. [61] (description below).

Analysis of optical and acoustic phonons in SLs by ultrafast time-resolved pump-probe methods and transport modeling: Wang et al. carried out measurements of phonon lifetimes in MOCVD – grown SLs [8] by time-resolved pump-probe experiments. Both optical [62] and acoustic [63] phonons were examined. The oscillations of certain optical phonon modes can be directly made visible in the oscillatory change of reflectivity. The reflectivity change signal decays exponentially with a time constant corresponding to the scattering rate. In comparison it was found that the signal for $\text{Bi}_2\text{Te}_3 / \text{Sb}_2\text{Te}_3$ SLs decayed noticeably faster than that of single Bi_2Te_3 and Sb_2Te_3 , showing that the phonon lifetime in SLs is shorter and suggesting phonon-interface interactions.

Likewise, acoustic phonon scattering was examined for long-wavelength phonons [63] by examining the reflectivity signals (Figure 2.10). The change in reflectivity is proportional to the phonon amplitude after traveling forth and back through the film with acoustic reflections at the film/substrate (binary) or film/buffer (SLs) interfaces. The authors found that upon increasing the film thickness, the phonon signal amplitude was hardly diminished for Bi_2Te_3 but reduced by 40-50 % for the SLs while simultaneously the speed of sound derived from the from the reflectivity signal time delay was also found to decrease. To conclude, the experiments reveal that both phonon reflectivity amplitude and sound velocity are reduced by the nanostructuring, effectively resulting in a lower thermal conductivity.

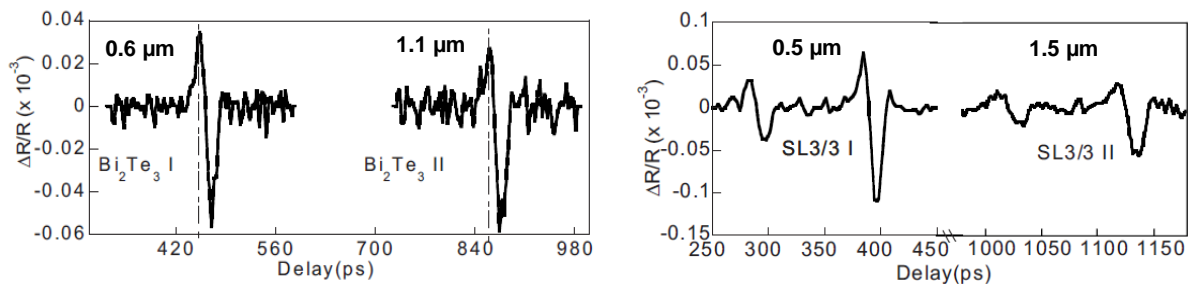


Figure 2.10 Coherent acoustic phonon signal for Bi_2Te_3 and a SL with 3nm $\text{Bi}_2\text{Te}_3 / 3\text{nm} \text{Sb}_2\text{Te}_3$. Film thicknesses are indicated. For increased thickness, the phonon reflectivity signal amplitude decreases significantly faster in the SL [63].

To conclude this sections it is noted that a broad multitude of physical models was used to explain the reduction of thermal conductivity in different SLs. Some of the models are validated by experimental data and/or phonon frequency probe methods. Finally, a single universal theory that describes the phononic aspects of all SLs has not yet been presented.

3 The material system $(\text{Bi,Sb})_2\text{Te}_3$

3.1 Overview over general structural properties

Bi_2Te_3 and Sb_2Te_3 and its solid solutions belong to the space group $R\bar{3}m$. The hexagonal representation of the unit cell is shown in Figure 3.1. The stacking order ABCABC... of the single atomic layers corresponds to a cubic close-packed structure. The unit cell consists of so-called quintuples which are merely held together by van der Waals force, meaning that covalent, ionic-covalent and van der Waals bonds alternate in the direction of the c-axis. In contrast to this, only covalent bonds exist between the atoms perpendicular to the c-axis, i.e. parallel to the so-called basal plane of the unit cell. The particular structure of the unit cell leads to a strongly expressed anisotropy of the crystal that manifests itself in three important properties which apply to all compounds from the $(\text{Bi,Sb})_2\text{Te}_3$ subgroup.

Mechanical properties: The crystals cleave much easier along the basal plane of the unit cell than parallel to the c-axis and the thermal expansion coefficient is larger in the direction parallel to the c-axis.

Diffusion processes: the diffusion coefficient parallel to the c-axis is by orders of magnitude lower than parallel to the basal plane [64].

Transport properties: Electronic and thermal transport are strongly favored parallel to the basal plane (section 3.3).

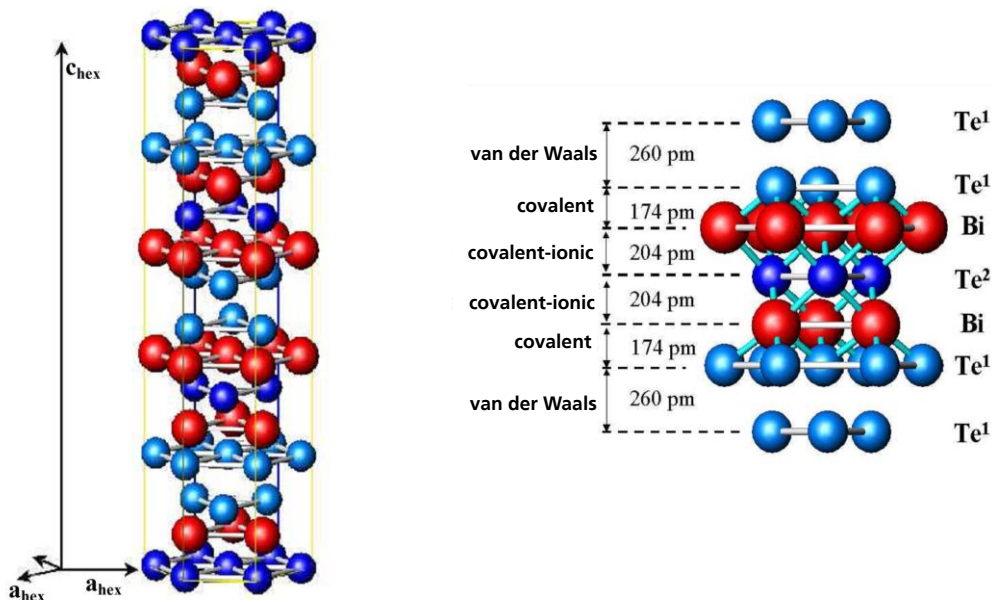


Figure 3.1 Left: Complete Bi_2Te_3 unit cell, hexagonal representation. Right: Detail image of one quintuple with interlayer spacings between the atomic layers, bond types are indicated and alternate along the c-axis. Images from [42-p.47].

3.1.1 Suitable substrate materials

Barium fluoride: An overview of low-mismatch materials that may serve as substrates for the epitaxial growth of $(\text{Bi,Sb})_2(\text{Se,Te})_3$ based materials was recently given in ref. [65]. Si, GaAs, BaF_2 , Bi, CdTe and Al_2O_3 are more or less suitable candidates. Among those are many cubic materials on which films can be grown on the (111) surface as described below exemplarily for BaF_2 . The insulator BaF_2 crystallizes in the CaF_2 structure ($Fm\bar{3}m$) and is well cleavable parallel to the (111) plane. Along the [111] direction, layers of Ba and F alternate and the atoms are arranged hexagonally, meaning that the surfaces of (111)-oriented BaF_2 and $(00.l)\text{-V}_2\text{VI}_3$ material are well-matched (Figure 3.2). The "hexagonal lattice constant" a_h that is associated with the cubic lattice constant a_c by $a_h = a_c/\sqrt{2}$ for (111)- BaF_2 (Table 4.1) clearly shows a very low mismatch of 0.1 % for Bi_2Te_3 and -2.7 % for Sb_2Te_3 . Another great advantage of this

substrate material is the very good match of the thermal expansion coefficient to that of Bi₂Te₃ and Sb₂Te₃ which is a necessary prerequisite for the fabrication of films with a thickness greater than a few μm (there is tendency for thicker films to develop cracks on nonmatched substrates). For all these reasons, BaF₂ is used in our work group since discovered by J. Nurnus roughly 15 years ago at Fraunhofer IPM as a very good substrate for the growth of high-quality V₂VI₃ and IV-VI films.

Silicon / silicon dioxide: The other substrate material that is used in this work is oxidized silicon. Though amorphous, it can be used as a cheap and readily available substrate for nanoalloyed polycrystalline films. However, due to the very large difference in thermal expansion coefficient the film thickness must be kept within few μm, otherwise cracks will occur in the film. Sputtered films with a thickness of 1.5 μm showed no signs of thermal stress while 6 μm thick films were found to exhibit a significant amount of microcracks.

Table 3.1 Relevant structural properties of thin film materials and used substrate materials. Given are the densities ρ [66-p.189], lattice constants a,c,a_c,a_h [67,68,65], linear thermal expansion coefficients perpendicular to the c-axis α [69,70,71,72,73], specific heat capacities per volume c_v [53] and melting points T_M [66-p.197]. a_c and the associated “hexagonal” lattice constant a_h are defined below. Values that are not of relevance here are omitted.

Material	ρ [g/cm ³]	Lattice constants [Å]	α [10 ⁻⁶ / K]	c _v [J / cm ³ K]	T _M [°C]
Bi ₂ Te ₃	7.86	a: 4.386, c: 30.497	14.4	1.29	585
Sb ₂ Te ₃	6.57	a: 4.264, c: 30.458	18.0	1.31	621
BaF ₂		a _c : 6.196, a _h : 4.381	18.7		
Si		a _c : 5.430, a _h : 3.840	2.6		
SiO ₂		amorphous	0.56		

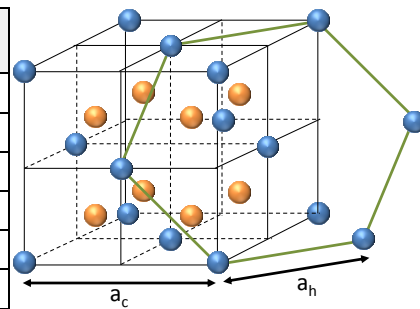


Figure 3.2 Crystal structure of BaF₂. Blue = Ba, Orange = F atoms. Along the [111]-direction, the Ba and F atoms are hexagonally arranged (green outline) with a distance corresponding to the hexagonal lattice constant a_h, allowing the growth of (Bi,Sb)₂Te₃ thin films on BaF₂.

3.2 Phase diagrams

The Bi-Te system: Note that different phase diagrams have been published for the system [74] and possibly not all of the numerous Bi-Te phases have been discovered or characterized yet. A well-described phase diagram was published by Abrikosov et al. [66-p.173] and shows three peritectic reactions at 312, 420 and 540 °C as evident from Figure 3.3. The homogeneity range of the Bi₂Te₃ phase (~ 0.2 at % to both the Te and Bi-rich side) was described by Brebrick et al. [75] and other authors. Literature values for the homogeneity range differ somewhat as pointed out in the reference. Bi₂Te₃ pulled from a stoichiometric melt is always strongly p-type since the maximum melting point is not exactly at 60 at. % Te but slightly shifted towards Bi, which generates Bi_{Te} antistructure defects.

The Sb-Te system: The phase diagram of Sb-Te around the composition Sb₂Te₃ displays a wide range of solid solutions from 0 – 60 at. % Te [66-p.165]. Three peritectic reactions occur at 548, 550 and 558 °C. Above a Te content of 60 at.%, an eutectic of Te and Sb₂Te₃ forms. Strictly stoichiometric Sb₂Te₃ exists only at temperatures close to the liquidus curve (Figure 3.3). If not straightly quenched from the melt, the composition of the δ-phase phase shifts in the direction of excess antimony and the compound is inherently unstoichiometric.

3.2 PHASE DIAGRAMS

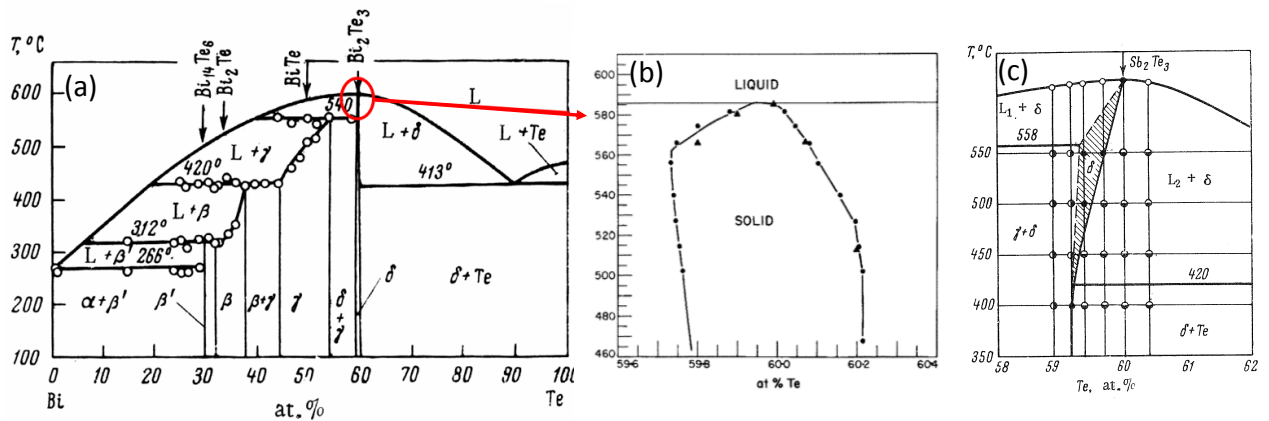


Figure 3.3 a) Bi_2Te_3 phase diagram [66-p.173]. b) Homogeneity range of the Bi_2Te_3 phase [75]. c) Sb_2Te_3 phase diagram [66-p.165].

In the Bi-Te system, all other binary phases besides Bi_2Te_3 were found to be members of the homologous series $(\text{Bi}_2)_m(\text{Bi}_2\text{Te}_3)_n$ [76]. Nine phases of this type were reported which consist of stacked Te-Bi-Te-Bi-Te quintuples (Q) with Bi_2 bilayers (B) in between. These phases can be p- or n-type and have widely varying Seebeck coefficients (Figure 3.4 a). Most of them have metal-like characteristics [76]. As an example, the BiTe phase with the sequence Q-B-Q-Q-B-Q is reported as n-type with a low S of around -30 to $-50 \mu\text{V}/\text{K}$ at 300 K, in contrast to the high Seebeck coefficient of the semiconducting Bi_2Te_3 phase. In analogy to the Bi-Te system, the Sb-Te system also forms homologous series $(\text{Sb}_2\text{Te}_3)_m(\text{Sb}_2)_n$. In [77] structural data are given on five members of the series that have been found.

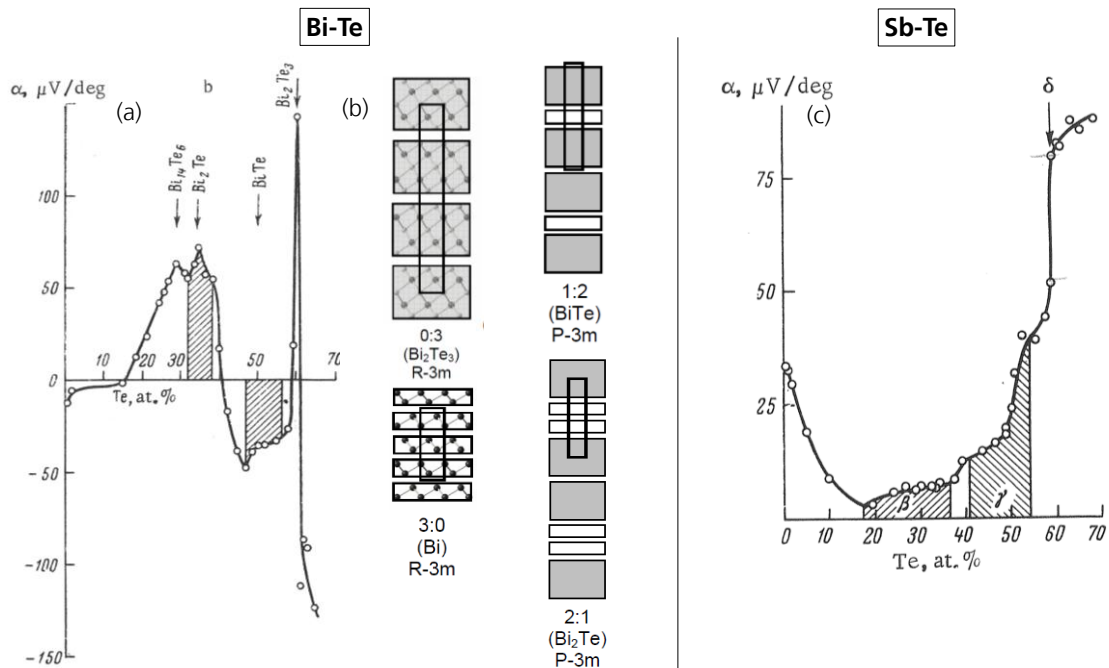


Figure 3.4 a+c) Comparison of the connection of Seebeck coefficient and Te content, corresponding to the phase diagrams shown in Figure 3.3 [66-p.174 and 165]. The dependence of S on Te content is clearly different in the Bi-Te and Sb-Te system. b) Examples of phases of the homologous series $(\text{Bi}_2)_m(\text{Bi}_2\text{Te}_3)_n$ [76]. Gray blocks = Te-Bi-Te-Bi-Te quintuples, white blocks = Bi bilayers.

The solid solution of Bi_2Te_3 with Sb_2Te_3 : A careful and recent analysis of the phase diagram was carried out by differential scanning calorimetry by Caillat et al. [78]. Between 580 and 620 °C, Bi_2Te_3 and Sb_2Te_3 form a continuous range of solid solutions. With increasing Sb_2Te_3 content, Bi_2Te_3 - Sb_2Te_3 solid solutions tend to deviate from stoichiometric lines towards Bi and Sb which has a direct impact on

defect chemistry and transport properties. Furthermore, it was observed that the lattice constant a decreases upon increasing the content of Sb_2Te_3 while c remains almost constant [66-p.208].

3.3 Transport properties

Note that newer results of other authors indicate that the “single crystalline” ingots described here may actually contain other phases due to their deviations from stoichiometry [76]. Doping experiments carried out by several groups with foreign dopands including several halogens, metals, germanium and others will not be described here.

Binary compounds

Bismuth telluride, Bi_2Te_3 : The transport properties of Bi_2Te_3 are governed by its defect chemistry and much research was devoted to this matter. There is a general agreement that in Bi_2Te_3 the hole and electron generating antistructure defects Bi_{Te} and Te_{Bi} (Bi on Te site and Te on Bi site, respectively) and the vacancy defects V_{Bi} and V_{Te} exist [79] and that defects of the antistructure type play the clearly dominant role. Generally, antisite defects are prominent in materials with low differences in electronegativity such as Bi_2Te_3 . In this case, the formation energy for such defects is low, i.e. ~ 0.4 eV in contrast to ~ 1 eV for vacancy defects [80]. The presence of antisite defects was first postulated by Harman et al. [81] and later proven experimentally by Miller et al. by precision density measurements [80] under the assumption that each antisite defect generates one charge carrier. Corresponding to this assumption, tight binding studies of Pecheur et al. reveal that Bi_{Te} and Te_{Bi} each give one hole and electron, respectively [82]. Kröger postulated that the ratios of current carriers to excess bismuth and tellurium are 3/5 and 2/5 respectively [83]. It is noted that some authors claim that besides antisite defects also vacancy defects play a role for carrier generation. A very good overview and calculations were recently given by Hashibon et al. [84]. The calculations show that Bi_{Te} and Te_{Bi} have the lowest formation energies of all mentioned defects and are thus clearly dominating the transport properties of Bi_2Te_3 . Recently, first experiments with high accuracy chemical analysis using Wavelength-dispersive X-Ray Spectrometry (WDX) [85] allowed to quantitative inference about the Te_{Bi} antisite defect concentration in Te-rich thin films, assuming that non-stoichiometry is only compensated by this type of point defect.

The band structure of Bi_2Te_3 is commonly described by a six-valley model for both conduction and valence band extrema [11-p.115], although newer calculations [86] indicate that the conduction band minimum may be a two-valley minimum. In any case, the effective masses were found to be strongly anisotropic, resulting in the known anisotropy for the electrical conductivity [87]. The bandgap of Bi_2Te_3 is indirect and values from 130 - 200 meV are reported [88,91]. The DOS effective mass m_d is given as $0.58m_e$ for electrons and $1.07m_e$ for holes (m_e = electron mass) at 300 K under the assumption of acoustic phonon scattering [11-p.118]. From these parameters, an intrinsic carrier concentration of $1.4 \times 10^{18} \text{ cm}^{-3}$ can be calculated using eq. 2.10. It is noted that Austin reports a n-type Bi_2Te_3 sample with a carrier concentration of $1.7 \times 10^{18} \text{ cm}^{-3}$ as extrinsic and one with a measured n of $1.7 \times 10^{17} \text{ cm}^{-3}$ as intrinsic [89]. As has been recently confirmed by calculations [84], donor and acceptor levels (caused by antistructure defects) lie extremely close to the conduction and valence band edges, respectively, meaning that carriers are never frozen out even at very low temperatures [11-p.117]. In order to achieve a high ZT , the Seebeck coefficient should be around 200 $\mu\text{V/K}$. This is the case at temperatures not too far away from room temperature due to the small bandgap of the material. The lattice thermal conductivities at 300 K are 1.5 (0.7) W/mK perpendicular (parallel) to the c -axis, respectively [11-p.118].

Exemplaric transport properties of selected n-type samples of Bi_2Te_3 grown with the Traveling Heater Method (THM) are given in Table 3.2. The Seebeck coefficient is reasonably isotropic within 10 % in contrast to the other properties that exhibit a pronounced anisotropy. The material changes from p to n-type above a (liquidus) Te content of slightly lower than 63 at. % Te as demonstrated on THM grown crystals [90] and crystals pulled from the melt [91]. A liquid with this Te content is in equilibrium with stoichiometric Bi_2Te_3 . The maximum melting point is nonstoichiometric and contains a slight Bi excess,

leading to p-type conduction. Generally, deviations from stoichiometry increase n and lower the absolute value of S . The ZT value is not a monotonous function of the Te content and is very sharply peaked, making accurate stoichiometry control very critical. The alloys of Bi_2Te_3 with Bi_2Se_3 and Sb_2Te_3 extend the range of optimum compositions somewhat, which is why they are preferred over the pure compound for the fabrication of thermoelectric devices.

Antimony Telluride, Sb_2Te_3 : For the defect chemistry of Sb_2Te_3 , similar considerations as for Bi_2Te_3 apply. However, the inherent nonstoichiometry of the compound leads to a high number of Sb_{Te} antisite defects and the bulk compound is always p-type with carrier concentrations in the 10^{20} to 10^{21} cm^{-3} range. Figure 3.4 c) shows the Seebeck coefficient in dependence on Te content. Interestingly, upon entering the existence range of the Sb_2Te_3 phase, the Seebeck coefficient (α in the figure) climbs very steeply by $\sim 50\%$ and adding Te to Sb_2Te_3 , thus exceeding the stoichiometric composition increases the Seebeck coefficient even more. Nevertheless, it has never been achieved to yield n-conduction in Sb_2Te_3 either by adding Te or foreign dopands. The valence band structure can be described by a six-valley band model. The valence band structure is complex since with increasing carrier concentration two subbands which correspond to different effective mass values are occupied progressively [90]. The maximum Seebeck coefficient achieved for bulk material is $133 \mu\text{V/K}$ at room temperature [11-p.122]. For the lattice thermal conductivity, values ranging from 1.0 to more than 2.0 W/mK were reported in the a direction [11-p.122]. Optical measurements of the band gap gave a value of 290 meV [92] whereas electrical measurements yielded 190 meV [93]. Transport properties of selected samples are given in Table 3.2.

With the low Seebeck coefficients and high thermal conductivities, only low ZT values can be attained with bulk Sb_2Te_3 . Compared to Sb-rich compositions, Te-rich ones show clearly higher S , μ and lower λ and thus yield higher ZT s. Contrarily to Bi_2Te_3 , ZT is higher parallel to the c -axis. The Seebeck coefficient in this compound is evidently anisotropic which can be explained by assuming an anisotropic relaxation time for the carrier scattering that is a mixed scattering on acoustical phonons and also ionized impurities [92]. The impurity scattering is associated with the large n in contrast to Bi_2Te_3 where clearly acoustical scattering dominates.

Table 3.2 Selected transport properties of Traveling Heater Method (THM)-grown and annealed binaries Bi_2Te_3 (n-type), Sb_2Te_3 and $(\text{Bi}_{0.2}\text{Sb}_{0.8})_2\text{Te}_3$ [90]. Anisotropy factors are given in red columns. Units: Te concentration c_{Te} in at. % (liquidus composition), electrical conductivity σ in S/cm , carrier mobility μ in cm^2/Vs , carrier concentration n in cm^{-3} , Seebeck coefficient S in $\mu\text{V/K}$, power factor PF in $\mu\text{W/cmK}^2$, thermal conductivity λ in W/mK . Subindex 11 and 33: Property measured perpendicular / parallel to c -axis. For $(\text{Bi}_{0.2}\text{Sb}_{0.8})_2\text{Te}_3$, no c_{Te} was given in the reference and the annealing temperature is given instead.

Material	c_{Te}	S_{11}	$\frac{S_{11}}{S_{33}}$	σ_{11}	$\frac{\sigma_{11}}{\sigma_{33}}$	PF_{11}	$\frac{PF_{11}}{PF_{33}}$	λ_{11}	λ_{33}	$\frac{\lambda_{11}}{\lambda_{33}}$	μ_{11}	$n \times 10^{19}$	ZT_{11}	$\frac{ZT_{11}}{ZT_{33}}$
Bi_2Te_3	63.5 - 70.5	-115 - -224	isotr.	559 - 3846	4.2 - 6.7	28 - 58	4.2 - 6.7	1.92 - 3.24	1.0 - 1.3	2.0 - 2.5	152 - 227	0.7 - 14.6	0.35 - 0.87	2.0 - 2.7
Sb_2Te_3	44.2 - 82.0	37 - 83	0.7 - 1.2	5263 - 9346	2.6 - 4.9	8 - 37	1.2 - 6.6	5.01 - 7.52	0.85 - 1.63	3.8 - 7.1	31 - 313	10.6 - 106	0.04 - 0.20	0.3 - 1.1
$(\text{Bi}_{0.2}\text{Sb}_{0.8})_2\text{Te}_3$	510 - 570	172 - 194	0.88 - 0.96	1005 - 1715	2.6 - 3.0	37 - 51	2.1 - 2.7	1.26 - 2.15	0.68 - 0.88	2.1 - 2.4	146 - 176	4.8 - 7.5	0.69 - 0.89	0.9 - 1.1

The solid solution of Bi_2Te_3 and Sb_2Te_3 , $(\text{Bi}_{1-x}\text{Sb}_x)_2\text{Te}_3$

Champness et al. and a series of other authors have carried out systematic investigations of the transport properties of $(\text{Bi}_{1-x}\text{Sb}_x)_2\text{Te}_3$ in dependence of x . The results are summarized in ref. [122] and shown in Figure 3.5. If n-type Bi_2Te_3 is alloyed with small amounts of Sb_2Te_3 the Seebeck coefficient increases at first, followed by a sharp drop and a change of sign at $x \sim 0.5$ where the proportions of Bi_2Te_3 and Sb_2Te_3 are roughly equal. Simultaneously, the electrical conductivity has a minimum at this concentration since carrier compensation minimizes the number of extrinsic carriers. Consequently, the power factor also has a minimum in the compensation regime and the figure of merit will become very small. For higher Sb_2Te_3 contents, ZT rises again up to the well-known high values at $x \sim 0.75$. The lattice thermal conductivity is minimal at 70 mol % of Sb_2Te_3 . The electron mobility of n-type

(Bi_{1-x}Sb_x)₂Te₃ solid solutions for small x was examined in another work and a decrease of μ for increasing Sb₂Te₃ content was reported ([6], Figure 2.4).

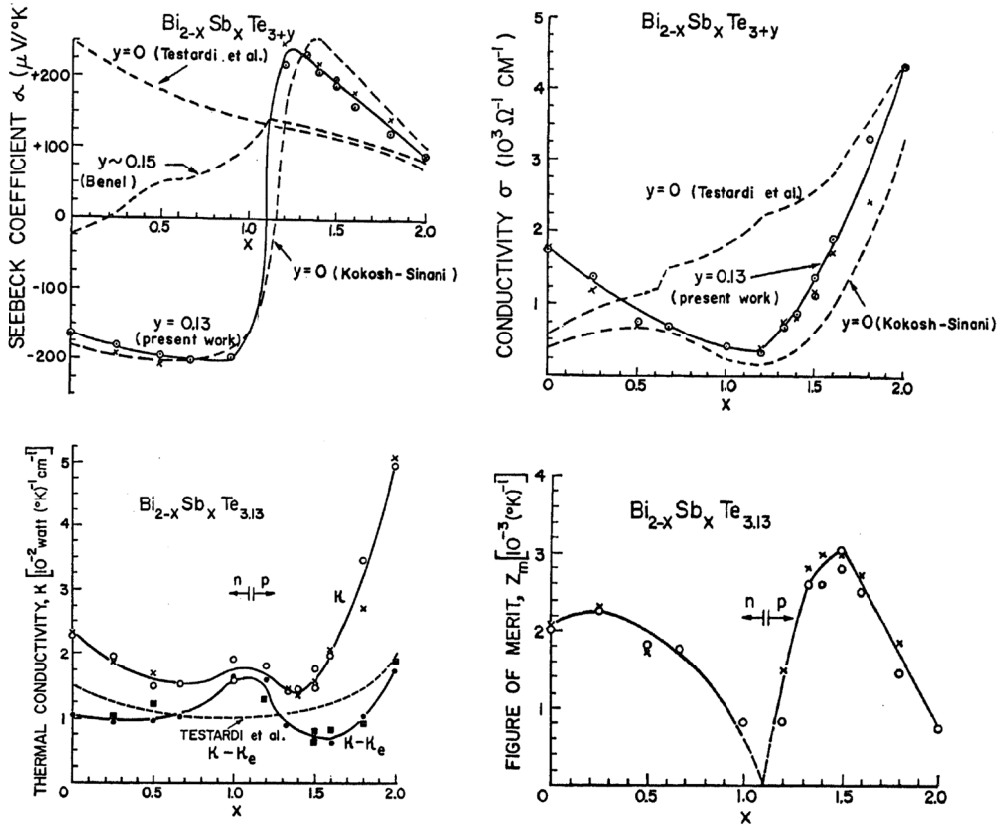


Figure 3.5 Transport properties of (Bi_{1-x}Sb_x)₂Te₃ in dependence of x [122]. Note that the authors describe the composition with Bi_{2-x}Sb_xTe_{3+y} instead of the more common (Bi_{1-x}Sb_x)₂Te₃, leading to different values for x than given in the text.

Furthermore, it was found that the band gap in the Bi₂Te₃ – Sb₂Te₃ system varies linearly between the values of the binaries up to a concentration of 80 mol % of Sb₂Te₃ [66]. The effective DOS masses m_d for different solid solutions of p-type (Bi_{1-x}Sb_x)₂Te₃ are given in Table 3.3.

Table 3.3 Some effective DOS masses m_d for different x in p-type (Bi_{1-x}Sb_x)₂Te₃. Data from [31].

x	0.5	0.75	0.8	0.85	0.9	1
m_d/m_e	0.735	0.922	1.01	0.926	0.927	0.781

P-type Sb₂Te₃ – rich compositions: P-type Sb-rich solid solutions of the binaries Bi₂Te₃ with Sb₂Te₃ still show unmatched thermoelectrical properties (i.e. ZT values around unity) at room temperature (Table 3.2). The compositions (Bi_{0.2}Sb_{0.8})₂Te₃ or (Bi_{0.25}Sb_{0.75})₂Te₃ were examined closely, both having high figures of merit. The compound (Bi_{0.225}Sb_{0.775})₂Te₃ was reported to yield the highest figure of merit (~1) of all examined solid solutions [90]. Since all used p-type compounds are distinctly Sb-rich and thus similar to Sb₂Te₃, the defect chemistry and electrical properties are also similar to the binary. This means that the Sb-rich solutions have a strong tendency to form Sb_{Te} and Bi_{Te} antistructure defects and are purely p-conducting, yet by far not as strong as the pure binary. The highest room-temperature ZT values of 1.2 for non-nanostructured bulk material were published in another work [13] for Bridgman-grown Te-enriched annealed polycrystalline samples of (Bi_{0.25}Sb_{0.75})₂Te₃.

N-type Bi₂Te₃ – rich compositions: There are hardly any reports on Bi₂Te₃-rich n-conducting (Bi_{1-x}Sb_x)₂Te₃ solid solutions since better figures of merit were achieved by alloying Bi₂Te₃ with small amounts of Bi₂Se₃, leading to the establishment of Bi₂(Te_{1-x}Se_x)₃ solutions as standard n-type material in

thermoelectric applications. However, the maximum ZT of 0.69 reported by Champness et al. for $(\text{Bi}_{0.875}\text{Sb}_{0.125})_2\text{Te}_3$, Figure 3.5, is not much smaller than that of the best Se-based materials $\text{Bi}_2(\text{Te}_{0.975}\text{Se}_{0.025})_3$ and $\text{Bi}_2(\text{Te}_{0.95}\text{Se}_{0.05})_3$ with a ZT of 0.87 [90]. Under certain conditions the use of $(\text{Bi}_{1-x}\text{Sb}_x)_2\text{Te}_3$ instead of $\text{Bi}_2(\text{Te}_{1-x}\text{Se}_x)_3$ based solutions may be advantageous, as was pointed out by Scherrer et al. due to various problems with accurately maintaining small Se concentrations and achieving homogeneity [94]. They fabricated $(\text{Bi}_{1-x}\text{Sb}_x)_2\text{Te}_3$ with varying x by mechanical alloying and found n-conduction if the Sb_2Te_3 content was below 50 wt. %. Carrier concentrations in the favorable range of 10^{19} cm^{-3} were observed for the n-type compositions, showing their potential for thermoelectric applications. Also in sputtering technology, the replacement of problematic Se (see section 4.1.4.4) could be beneficial.

3.4 Thin films

There are many reports on thin films of $(\text{Bi}_{1-x}\text{Sb}_x)_2\text{Te}_3$ grown by a wide variety of methods like MOCVD, MBE, Sputtering, Pulsed Laser Deposition (PLD), Co-, flash- and mono-evaporation, Hot-Wall epitaxy (HWE). The most important works together with obtained results are summarized in Table 3.4 and serve as a comparison base to the film properties obtained in this work. In general the best films (highest carrier mobilities and power factors) are obtained around the stoichiometric composition. Precise stoichiometry control is usually an issue since a part of the Te impinging on the substrate re-evaporates, depending on substrate temperature. The atomic flux ratio of Te to Sb is therefore larger than unity (mostly around 2-3 : 1). If not deposited epitaxially, V_2VI_3 films are usually polycrystalline and have a distinct tendency to grow with a more or less distinct c-texture with the exception of electrodeposited films. The grain size as well as the degree of c-orientation typically grows with increasing annealing temperature.

A very interesting and mostly not directly addressed phenomenon is the defect chemistry of the V_2VI_3 thin films that is distinctly different from bulk material. Regardless of Te content, thin film Bi_2Te_3 seems to be n-type in the very most cases, see e.g. refs. [130,114,95] save for a few exceptional cases where high substrate temperatures were used. For instance, Zou managed to deposit p-type Bi_2Te_3 (albeit with low Seebeck coefficient) by significantly increasing the substrate temperature above the optimum temperature for n- Bi_2Te_3 and a large Bi/Te flux ratio [111]. Uher et al. found a high-temperature growth regime for MBE growth where any excess Te evaporates during growth and only stoichiometric / Bi-rich Bi_2Te_3 results which is always p-type ([96], unpublished information). The hole-generating antisite defect Bi_{Te} seems to be significantly less dominant in thin films. This issue will be detailed in chapter 5, sect. 5.2.1.

Generally, there are significantly more reports on Bi_2Te_3 than on Sb_2Te_3 . Also Sb_2Te_3 in thin film form seems to be “less strongly p-conducting” (i.e. has lower carrier concentration / higher Seebeck coefficient) than its bulk counterpart, indicating that also in this material the Sb_{Te} antisite defect plays a less dominant role in thin films. Carrier concentrations in the range of $10^{18} - 10^{19} \text{ cm}^{-3}$ can be easily obtained in contrast to bulk.

Table 3.4 Properties overview of (Bi,Sb)₂Te₃ alloy and binary thin films grown with different methods. If not otherwise stated, the transport properties were obtained at room temperature. Values for the films with highest ZT or PF are given. If the films were fabricated using a range of growth or annealing temperatures, the substrate temperature T_{sub} which yielded the best PF is given as growth temperature. If not indicated otherwise with *, the electrical properties were measured in in-plane and thermal conductivity in cross-plane direction (standard procedure). ** Thermal conductivity of 1.5 W/mK was assumed. Symbols: – information not provided, a) from ref. [97] b) annealing temperature c) co-sputtering d) compound target e) Bi / Te element multilayers, f) annealed material, g) significant impurities (Te and TeO₂) present in the film. h) study on multiple substrates: glass, mica, MgO, Pt, Al₂O₃. i) Properties of films deposited on different substrates differ strongly. j) Overview article. Results for many different substrate types are reported. k) A heat shield was used in the sputtering apparatus. l) Best properties were not obtained at room temperature x) Thermoelectric properties not measured on same sample. The film orientation (or.) is given by: n = no distinct or only slight crystalline orientation, c = slightly, cc = strongly, cc(c) = almost exclusively (minor other reflexes,), ccc = exclusively c-oriented, (a) = tendency towards a-orientation. Units as previously defined. If not directly given, the PF was calculated from given σ and S values. If σ was not given it was calculated from $\sigma = en\mu$ for the PF calculation.

Method	Film	Substrate	T_{sub}	Or.	c_{Te}	d	μ	$n \times 10^{19}$	σ	S	PF	λ	ZT	Ref.
MOCVD	Sb ₂ Te ₃	GaAs,Al ₂ O ₃	-	ccc	-	-	-	-	-	115	-	-	-	98
MOCVD	(Bi _{0.25} Sb _{0.75}) ₂ Te ₃	GaAs,Al ₂ O ₃	-	ccc	-	-	384	-	-	186	-	1.65	-	98
MOCVD	Bi ₂ Te ₃	GaAs	225	ccc	-	-	145	1	-	-	-	-	-	60
MOCVD	Sb ₂ Te ₃	GaAs	225	ccc	-	-	350	1	-	-	-	-	-	60
MOCVD	Bi ₂ Te ₃	Pyrex	-	-	-	0.6	52	10	909	-213	41	-	-	99
MOCVD	Sb ₂ Te ₃	Pyrex	-	-	-	0.6	50	30	2500	110	30	-	-	99
MOCVD	(Bi _{0.27} Sb _{0.73}) ₂ Te ₃	Pyrex	-	-	-	0.6	67	5	476	240	27	-	-	99
MBE ^{x)}	Bi ₂ Te ₃	BaF ₂	290	ccc	-	-	150	4	960	(~200)	-	1.8*	0.6*	100
MBE	Bi ₂ Te ₃	CdTe	250	ccc	-	5	670	0.6	1000	-190	36	-	-	101
MBE	Sb ₂ Te ₃	CdTe	200	ccc	-	2.5-3.5	279	0.8	-	126	5	-	-	102
MBE	(Bi _{0.2} Sb _{0.8}) ₂ Te ₃	CdTe	200	ccc	-	3	64	4.5	~500	184	16	-	-	103
MBE ^{x)}	Sb ₂ Te ₃	Al ₂ O ₃	350	ccc	-	0.07 ^{a)}	680	1.2	1250	-	-	-	-	65
Sputtering ^{c),f)}	Bi ₂ Te ₃	Si/SiO ₂	300 ^{b)}	n	-	~20	-	-	-	-160	16	-	-	104
Sputtering ^{c),f)}	(Bi _{0.25} Sb _{0.75}) ₂ Te ₃	Si/SiO ₂	300 ^{b)}	n	-	~20	-	-	-	180	25	-	-	104
Sputtering ^{d),f)}	(Bi _{0.15} Sb _{0.85}) ₂ Te ₃	Kapton	250 ^{k)}	cc(c)	-	1-2	360	-	1140	182	38	-	-	105
Sputtering ^{f)}	(Bi _{0.15} Sb _{0.85}) ₂ Te ₃	Polyimide	-	-	-	1	-	-	-	~200	36	-	-	106
Sputtering ^{e),f)}	Bi ₂ Te ₃	Si/SiO ₂	200 ^{b)}	n ^{g)}	-	~0.5	-	-	435	-202	18	0.71	-	107
PLD	Bi ₂ Te ₃	Si, Mica	250	cc(c)	-	0.5 - 2	90	10	~700	-184	24 ^{l)}	-	-	108
PLD ^{f)}	Bi ₂ Te ₃	Glass	190	cc	-	-	-	-	690	-195	26	0.34	-	109
PLD ^{f)}	(Bi _{0.15} Sb _{0.85}) ₂ Te ₃	Glass	240	-	-	-	-	-	950	198	37	-	-	109
Co-evapor.	Bi ₂ Te ₃	^{h)}	260	cc(c)	60.1	1	125	1.8	345	-228	18	-	-	110
Co-evapor.	Sb ₂ Te ₃	^{h)}	270	cc	60.5	1.1	-	-	810	149	18	-	-	110
Co-evapor.	Bi ₂ Te ₃	Glass	314	cc	58.8	0.7	15	160	3125	81	21	-	-	111
Co-evapor.	Bi ₂ Te ₃	Glass	260	cc	-	~0.7	75	6.5	770	-228	40	**	0.3	112
Co-evapor.	Sb ₂ Te ₃	Glass	230	cc(c)	-	~0.7	173	3.4	960	171	28	**	0.3	112
Co-evapor.	Bi ₂ Te ₃	Polyimide	270	cc	62.0	~1	-	-	794	-248	49	~1.3	-	113
Electroch. ^{f),j)}	Bi ₂ Te ₃	^{j)}	RT	(a)	-	200	-	-	-	-100	18	-	-	114
Electroch. ^{f)}	(Bi _{0.38} Sb _{0.62}) ₂ Te ₃	Si/Cr/Pt	RT	n(a)	59.6	~23	35	7	400	182	13	1	0.4	115

3.5 Superlattice thin films

This section gives a review of the outstanding properties of MOCVD-grown SL structures reported by Venkatasubramanian that still have not been reproduced, despite significant synthetic efforts undertaken by many groups with growth methods such as MOCVD, MBE, (Co)-sputtering and Co-evaporation, electrochemical deposition and Pulsed Layer Deposition (PLD). For details on results achieved with these methods the author refers to his overview article [116].

3.5.1 Structural properties of MOCVD-grown films

The structural results reported for the SLs deposited on (100) GaAs are quite astonishing. It is known that the V_2VI_3 compounds with threefold symmetry can be grown on cubic (111) surfaces that are also characterized by threefold symmetry, see section 3.1.1. There are several reports of successful epitaxial growth of Bi_2Te_3 -based materials on cubic substrates such as BaF_2 or $CdTe$ [65] resulting in films with high structural quality [42,100]. However, these considerations do not apply to cubic (100) surfaces with fourfold symmetry such as GaAs. The problem of symmetry mismatch was not addressed specifically in the associated publication(s), where instead a lattice mismatch of 22 % was stated [60] that was apparently derived with the lattice constants $a_h = 4.386 \text{ \AA}$ of Bi_2Te_3 and $a_c = 5.653 \text{ \AA}$ of the GaAs substrate. Despite these obvious obstacles, the authors report to have obtained "single crystalline" films though it seems that rotational order was not verified, e.g. by showing an XRD pole figure measurement. The XRD results presented are restricted to the (00.15) reflection of a Bi_2Te_3 film deposited on Al_2O_3 [117]. In conclusion, it must be emphasized that there remains significant doubt if the reported film growth of V_2VI_3 compounds on (100)-GaAs can be really considered as "epitaxial".

Due to the high crystalline quality, the samples produced by MOCVD are purported to exhibit a low intermixing between the Bi_2Te_3 and Sb_2Te_3 layers. TEM micrographs show a sharply defined SL structure which was also confirmed by the presence of satellite peaks in the double-crystal XRD pattern [60] and in-situ spectroscopic ellipsometry that confirmed "perfect superlattice growth with an abrupt interface between the two constituent films" [118].

3.5.2 Transport properties of MOCVD-grown films

Already the first transport data for the short-periodic (period length $\leq 10 \text{ nm}$) Bi_2Te_3/Sb_2Te_3 SLs published in 1996 were extremely promising [98]. For asymmetric SL structures varying in period length with Bi_2Te_3 thickness fixed at 15 \AA , very high in-plane carrier mobilities of more than $600 \text{ cm}^2/Vs$ were reported combined with very high in-plane Seebeck coefficients of $\sim 200 - 270 \text{ \mu V/K}$, leading to an outstanding PF of 59 \mu W/cmK^2 , even exceeding that of state of the art p-type bulk alloy. Remarkably, these electrical properties were achieved while simultaneously the cross-plane thermal conductivity (minimum value of 0.22 W/mK) was a factor of 4-7 smaller than that of bulk material. The high quality of the SL structure is the predominant reason for the significant reduction of the thermal conductivity. Furthermore, low contact resistances in the range of $10^{-8} \text{ \Omega cm}^2$ are apparently possible with the displayed technique, enabling the fabrication of high-performance thermoelectric coolers.

The carrier mobility and Seebeck coefficient for SLs were also studied in more detail, but unfortunately the thickness of the single binary layers was not clearly mentioned [117]. The values reported in this publication are slightly lower than for the asymmetrical SLs mentioned above.

Remarkably, it was also stated that the binary MOCVD-grown Bi_2Te_3 is always n-conducting while the binary Sb_2Te_3 is always p-conducting. This is puzzling since usually, stacking a p-conductor on a n-conductor evokes compensation effects as observed in this work on nanoalloyed and also epitaxial SLs fabricated by a MBE system, see sections 6.2.1, 9.2 as well as refs. [119,120,121]. The Seebeck coefficients S_A and S_B of compounds A and B with their opposite signs theoretically cancel out each other according to eq. 2.17. In contrast, the Seebeck coefficients of the MOCVD grown SLs are very high and exceed 250 \mu V/K . This particular phenomenon is subject to further debate. For instance, it is possible that the interfaces are not exactly atomically abrupt (this cannot be determined from the TEM image shown later in [60]). If this is the case for asymmetric SLs where the Sb_2Te_3 layer is thicker than the Bi_2Te_3 layer, significant Sb interdiffusion into Bi_2Te_3 may have occurred, yielding the ternary phase

$(\text{Bi}_{1-x}\text{Sb}_x)_2\text{Te}_3$ which becomes p-conducting for $x \gtrsim 0.5$ [122]. An alternative explanation may be the SL structure itself: The outstanding ZT value of 2.4 was obtained for an “asymmetric” SL structure with very low dimensions, i.e. 1 nm of Bi_2Te_3 deposited on 5 nm of Sb_2Te_3 [8]. Consequently, each nanometer thick stack of Bi_2Te_3 is surrounded by 2 nm of Sb_2Te_3 , forming a full 3 nm unit cell (see also Figure 6.8) with the stacking order Te-Sb-Te-Sb-Te • Te-Bi-Te-Bi-Te • Te-Sb-Te-Sb-Te (• = van der Waals type bonds) that can be interpreted as an “ordered alloy” (a term coined by Venkat. in [46]) of $(\text{Bi}_{0.33}\text{Sb}_{0.67})_2\text{Te}_3$ which is p-type. Thus, the p-conducting compound $(\text{Bi}_{0.33}\text{Sb}_{0.67})_2\text{Te}_3$ would be stacked on p-type Sb_2Te_3 , eliminating the compensation effects and yielding high Seebeck coefficients. Another possibility is that external p-type dopants were introduced in the Bi_2Te_3 layers, however none of this was mentioned explicitly. Interestingly, for the symmetric SLs examined no Seebeck coefficients were reported [60]. Compensation effects may be strongly expressed for the symmetric SLs since the single layer thicknesses are identical, leading to pronounced carrier compensation according to eq. 2.17, thus significantly reducing the Seebeck coefficient. Furthermore, the in-plane carrier mobilities for symmetric SLs were lower than for asymmetric SLs. Nevertheless, the mobilities are significantly higher than that of reference ternary alloys and range between that of the binaries. This finding indicates that layer interface charge carrier scattering is significantly weaker than alloy scattering.

In the major subsequent publication, the electrical conductivity anisotropy in the SLs was examined [8]. The ratio σ_{33}/σ_{11} with σ_{33} as conductivity parallel to the c -axis, corresponding to the cross-plane direction in the exclusively c -textured films, and σ_{11} perpendicular to the c -axis corresponding to the film in-plane direction is around 0.2-0.4 for bulk Bi_2Te_3 and Sb_2Te_3 binaries and alloys [90]. In contrast to this, the anisotropy ratio for short-periodic $\text{Bi}_2\text{Te}_3/\text{Sb}_2\text{Te}_3$ SLs was, astonishingly, reported to be around 1, Figure 3.6 a) and even higher for asymmetric films (not shown here). It was argued that in the SLs very small band offsets between Bi_2Te_3 and Sb_2Te_3 , resulting in only weak confinement effects, are responsible for the disappearance of the conductivity anisotropy [8]. However, as was pointed out in [15], this argument leads to the conclusion that in pure Bi_2Te_3 and Sb_2Te_3 the cross-plane and in-plane conductivity should also be identical since the valence-band offsets between the quintuples forming the unit cell of these compounds are zero. Recently, theoretical calculations were presented dealing with this phenomenon (see section 2.2.1.1). The calculations could not confirm the measured strong anisotropy reduction in the SLs.

Finally, it is important to note that the high ZT values of 2.4/1.5 for p/n SLs were determined with the Harman method for varying SL thicknesses. Irregularities in the measurements are notable [8]. A distinct voltage spike was observed in the associated measurements (Figure 3.6 b)) that “prevents reliable determination of residual V_0 for $t < 1 \mu\text{s}$ ”. As the “thermoelectric” part of the voltage that is induced by the Seebeck effect and decays with the thermal constant, V_0 is an important measurement parameter and was used for the determination of ZT . In the plots shown for different thicknesses (Figure 3.6 c)) some scattering of the data points is evident that may be associated with the difficulty of determining V_0 . From the fit it is not entirely clear which data points were included into the fit to determine ZT . The measurements of the different electric values to estimate the value of ZT and conductivity anisotropy were validated by measurements on reference materials with known properties.

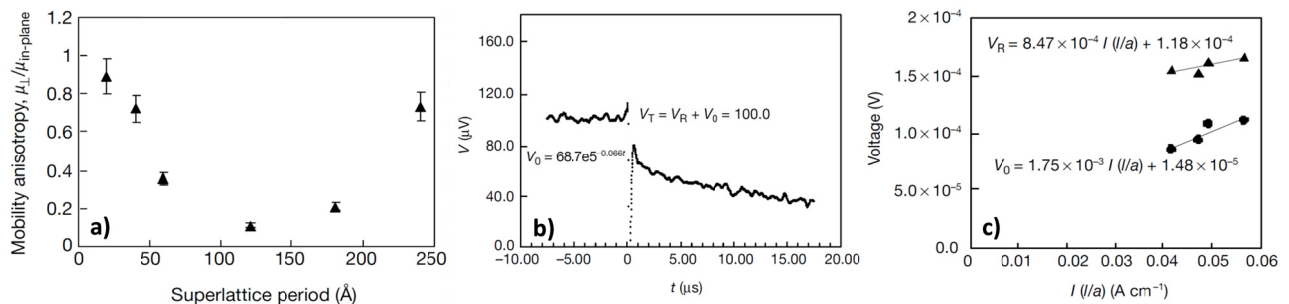


Figure 3.6 a) Mobility (=conductivity) anisotropy in symmetric SLs with different periods. b) Harman method: Voltage spike at $t=0 \mu\text{s}$, complicating the extraction of the “thermoelectric” part of the measured voltage. c) Scattering of data points used to determine ZT . It is not entirely clear which data points were included.

4 Experimental details: Deposition and characterization methods

4.1 Deposition methods and thin film fabrication

4.1.1 The “Nanoalloying” method

The “nanoalloying” method is based on the 1.) (nominally) stoichiometric deposition of element layers with a thickness in the nm range on a cold substrate and 2.) the application of a low-temperature annealing process. In this process, the compound formation takes place in a solid-state reaction. For the examined compounds in most cases annealing temperatures between 150 – 350 °C were used. The process is schematically illustrated in Figure 4.1. In actual deposition processes more complex patterns are used as will be shown in the respective sections of the following chapters. The method is closely related to the Method of Elemental Reactants (MER) introduced by D.C. Johnson et al. [123].

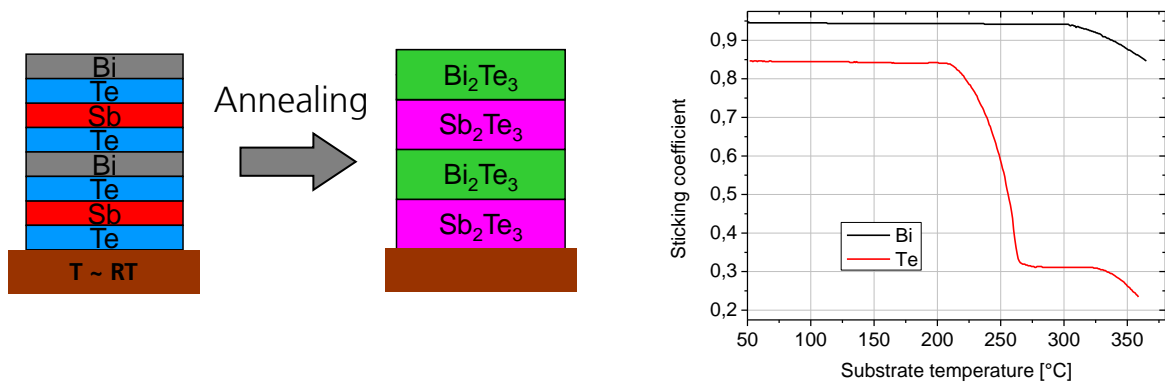


Figure 4.1 Left: Schematic illustration of the nanoalloying process for a Bi₂Te₃ / Sb₂Te₃ SL. Note that the boundaries between the compounds in reality are not sharp as suggested by the schematic but smeared out by interdiffusion. Right: Dependence of sticking coefficient on substrate temperature for Bi and Te [124].

Nanoalloying offers several advantages compared to “conventional” growth by the deposition on a heated substrate:

- The crystal growth is **not** epitaxial and starts at the interfaces of the element layers. No epitaxial relation to the substrate is needed, allowing the use of a much wider (and likely cheaper) range of substrate materials compared to epitaxial growth.
- In contrast to co-deposited material, the films exhibit a strong texture that can be influenced by the element deposition pattern (section 5.1).
- The sticking coefficient is strongly dependent on substrate temperature which aggravates accurate stoichiometry control for films co-deposited on heated substrates (Figure 4.1). The deposition on a substrate at ambient temperature facilitates stoichiometry control and enables a fast composition screening.
- Deposition is carried out in a setup without integrated heater (including sputtering systems) which is easier and less expensive to accomplish.
- The compound formation takes place at very low temperatures and starts at ~ 100 °C for (Bi,Sb)₂Te₃ (section 5.3) allowing the use of temperature-sensitive substrates such as polymer foils for film fabrication.
- The nanoalloyed films (when annealed at moderate temperatures) are very smooth compared to hot co-deposited thin films, which tend to exhibit a significant roughness [42,p. 62].
- High deposition rates are possible (section 5.4).

- When the element thicknesses are chosen such that a (near-)stoichiometric V_2VI_3 compound results, generally no other phases besides the V_2VI_3 phase were observed on the films grown in this work.

However, some disadvantages must be taken into account:

Grain growth: The fabricated V_2VI_3 films are all polycrystalline since crystal growth starts practically everywhere at the chalcogen-(semi)metal interface at once.

Grain growth during the annealing process can be seen as Ostwald ripening or competitive growth, i.e. the growth of larger particles at the expense of smaller particles [125, p.1ff][126]. According to a calculation by Lifshitz, Slyozov and Wagner, the growth rate of the average particle radius \bar{R} is related to temperature T , time t and diffusion coefficient D where E_A is the activation energy and R the gas constant by [127]: $\bar{R} \propto \left(\frac{D}{T} \cdot t\right)^{1/3} \propto \left(D_0 \cdot \exp\left(-\frac{E_A}{RT}\right) \cdot \frac{t}{T}\right)^{1/3}$. This explains why increasing the annealing temperature should have a much stronger effect on the crystalline structure than increasing annealing time due to the exponential dependence.

Interdiffusion takes place in the films before crystallization, e.g. in the (partially) amorphous as-grown precursor state [128] which is detrimental to the formation of sharp SL interfaces. Since interdiffusion softens out the boundaries between compound layers, the resulting SLs are referred to as “soft superlattices”.

Generally, diffusion in the case of a non-infinite source can be described by a Gaussian profile. With $D = D_0 \cdot \exp\left(-\frac{E_A}{RT}\right)$ as the diffusion coefficient containing the activation energy E_A it is useful to define a diffusion length, given by $x = 2\sqrt{Dt}$. Literature data on diffusion coefficients D in the Bi_2Te_3 - Sb_2Te_3 system are scarce. There is one report of Boltaks on D of Sb in Bi_2Te_3 [129-p.298f.] stating that $D = 10^{-13} \text{ cm}^2/\text{s}$ at 250 °C, however it was not stated along which crystal direction D was measured and how the crystal structure of the material was. For a 2 h annealing procedure this D yields a diffusion length as large as 537 nm, which can certainly not apply to diffusion along the c-axis of the SLs deposited in this work.

4.1.2 Calculation of element layer thicknesses

The following material properties are necessary to calculate the required element thicknesses for the fabrication of the desired compound:

A_S :	sample surface area	d_{BST} :	thickness of layer of compound $(Bi_{1-x}Sb_x)_2Te_3$
n_{BST} :	number of moles of compound $(Bi_{1-x}Sb_x)_2Te_3$	n_Z :	total number of moles of element Z
M_{BST} :	molar mass of compound $(Bi_{1-x}Sb_x)_2Te_3$	M_Z :	molar mass of element Z
ρ_{BST} :	density of compound $(Bi_{1-x}Sb_x)_2Te_3$	m_Z :	number of moles of elem. Z in compound
ρ_{BT} :	density of Bi_2Te_3	ρ_Z :	density of element Z
ρ_{ST} :	density of Sb_2Te_3	d_Z :	thickness of layer of element Z

All required material properties are listed in Table 4.1.

Table 4.1 Material properties of used elements and compounds. Data for Te,Bi,Sb taken from [28-p.621], compound data taken from [66-p.189].

Element	Molar mass M [g/mol]	Density ρ [g/cm ³]
Te	127.66	6.25
Bi	208.90	9.79
Sb	121.75	6.69
Bi_2Te_3	800.80	7.86
Sb_2Te_3	626.32	6.57

A desired compound layer thickness d_{BST} corresponds to

$$n_{BST} = \frac{A_S \cdot \rho_{BST} \cdot d_{BST}}{M_{BST}} \quad (4.1)$$

moles of the compound, where ρ_{BST} is given by

$$\rho_{BST} = (1 - x) \cdot \rho_{BT} + x \cdot \rho_{ST} \quad (4.2)$$

which means that the density of $(\text{Bi}_{1-x}\text{Sb}_x)_2\text{Te}_3$ is linearly interpolated between the densities of Bi_2Te_3 and Sb_2Te_3 . From n_{BST} , the number n_Z of moles of element Z can be calculated by

$$n_Z = n_{BST} \cdot m_Z \text{ where } m_Z = \begin{cases} 2(1 - x) & \text{for Bi} \\ 2x & \text{for Sb} \\ 3 & \text{for Te} \end{cases} \quad (4.3)$$

which yields the necessary element layer thickness of each element:

$$d_Z = \frac{n_Z \cdot M_Z}{\rho_Z \cdot A_S} \quad (4.4)$$

Examples for calculated thicknesses are given in the following chapters. The numbers of periods was chosen such that a total film thickness of 1 μm for the MBE films and 1.5 μm for the sputtered films is obtained. A film thickness in the range of μm increases transport property measurement accuracy and facilitates structural characterization.

Often, the deposition rate of the elements has to be readjusted. In most cases this applies to Te, either due to the constant decay of the deposition rate during sputtering or the fabrication of films with different Te content (section 5.2). If the current Te content is given as C and the desired content is given as D, then the content has to be corrected by an amount x_c to achieve the desired content according to

$$D = \frac{C + x_c}{1 + x_c} \rightarrow x_c = \frac{C - D}{D - 1}. \quad (4.5)$$

The deposition rate R_0 then has to be corrected as follows to give the new rate R_c :

$$R_c = R_0 \cdot \left(1 + \frac{x_c}{C}\right) = R_0 \cdot \left(1 + \frac{1}{C} \cdot \frac{C - D}{D - 1}\right) \quad (4.6)$$

4.1.3 Molecular Beam Epitaxy (MBE)

4.1.3.1 Description of setup and growth process

Molecular beam epitaxy (MBE) is an evaporation-based deposition method used to deposit films with high purity and crystalline quality. Typical features of a MBE system are the ultra high vacuum in the growth chamber (to prevent a large amount of gaseous contaminants from entering the grown film), a heatable substrate holder (to supply the impinging atoms with enough thermal energy to arrange to crystalline layers) and substrate shutters to be able to select the deposited species with high accuracy. The method and its features are described e.g. in [131]. Three growth modes can be observed in MBE growth: 1.) Van der Merwe growth during which films grow layer by layer and a new layer is started only if one layer is complete. 2.) Volmer-Weber growth that is characterized by island-like growth and 3.) Stranski-Krastanov mode where the film grows as a layer at first but later changes to island growth.

In this work, the MBE system EPI 930 fabricated by Veeco Instruments Inc. was used. The system is equipped with nine effusion cells and a beam flux monitor (BFM) to monitor and adjust cell effusion beam-equivalent pressures (BEP). The cell-shutters are fast-acting with open/close operating times around 0.1 s. The bakeout station allows to bake out substrates at temperatures of up to 1000 °C. A cooling shroud is installed that can be filled with liquid nitrogen. The substrate holder can be rotated to ensure rotational uniformity of the thin films. The setup is shown in Figure 4.2. The molybdenum substrate holders have a diameter of three inches, allowing the accommodation of over a dozen single 10 x 10 mm² substrates. The substrates are bonded to the holders by an InGa eutectic which has a very low vapor pressure and thus does not interfere with typical growth processes. During the growth process, the cooling shroud was always kept filled with liquid nitrogen and the background pressure was in the range of 10⁻⁹ Torr (note that all gauges in the MBE system display pressure values in Torr, so this unit will be used in this subsection).

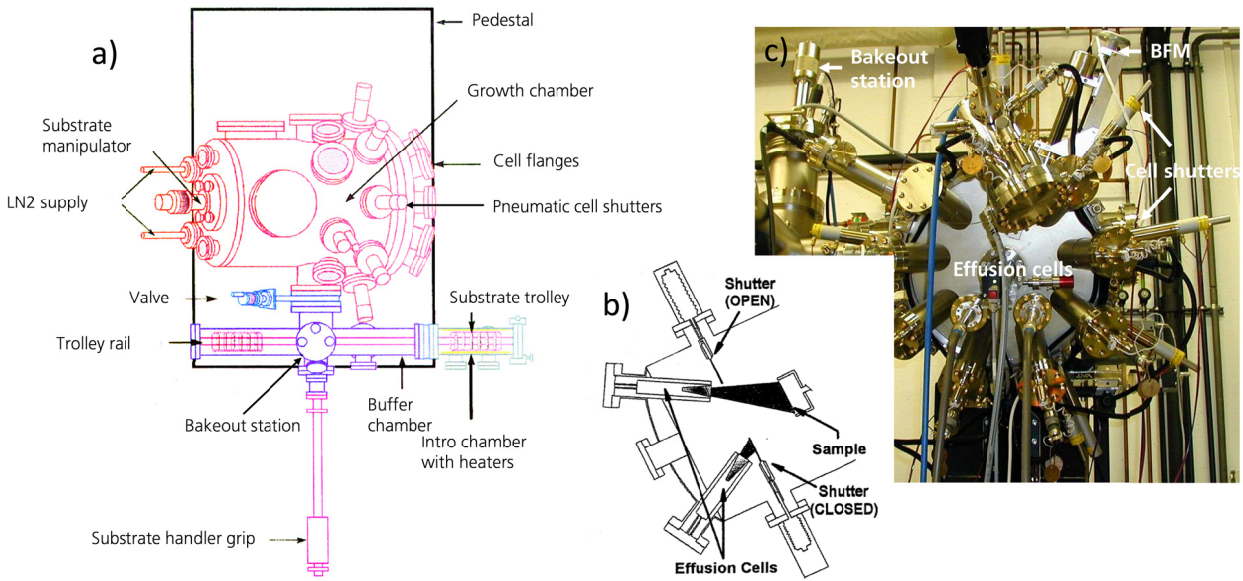


Figure 4.2 MBE setup EPI 930 by Veeco/Epi Inc. a) top view. b) schematic of growth chamber. c) frontal photograph.

4.1.3.2 Element deposition and calibration

Bi, Sb and Te were supplied by: Chempur (Te pieces low oxygen, 99.999 % purity, Item # 009440), Koch chemicals (Bi granules, 99.9999 % purity, Item # 1027) and Sb (Chempur, Sb pieces, 99.9999 % purity, Item # 009022). The V₂VI₃ compounds treated in this work evaporate incongruently [130,84] therefore the element sources were also used for the co-deposition of epitaxial films.

All elements are evaporated from standard thermal Knudsen-type effusion cells. The effusion rate Γ_e (emitted molecules per second) from an effusion cell is described by the Knudsen effusion equation and depends on orifice area A_e , vapor pressure p_{eq} , molecular weight M of the atomic species of the evaporant and the Avogadro constant N_a [131-p.31f] with the vapor pressure being derived from the Clausius-Clapeyron equation [132,133-p.80] with A and B as material-specific constants:

$$\Gamma_e = A_e p_{eq} \sqrt{\frac{N_a}{2 \pi M k_B T}} \quad \text{where} \quad p_{eq} = \exp\left(-\frac{A}{T} + B\right). \quad (4.7)$$

The effusion rates and thus the growth rates of films are in direct proportion to p_{eq} which are proportional to the beam equivalent pressures (BEPs) displayed by the BFM. Figure 4.3 shows measured BEPs in dependence on effusion cell temperature with the BFM. The data were collected from many different growth runs. A simplified fit of the form

$$p_{BEP} = C_{BEP} \cdot \frac{\exp\left(-\frac{A}{T}\right)}{\sqrt{T}} \quad (4.8)$$

where the parameter $\exp(B)$ and all other parameters given in the above equations are summarised into a variable parameter C_{BEP} shows a good agreement with the recorded data. The data from the fit can be used to adjust the BEP via the growth temperature such that the desired growth rate is attained. The standard BEPs were chosen to give a good compromise between deposition rate and sub-nm accuracy and are given in Table 4.2 together with cell temperatures and growth rates.

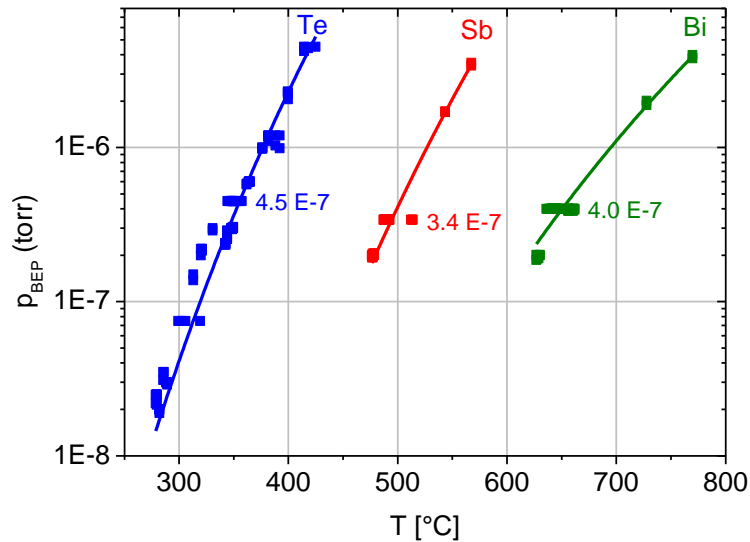


Figure 4.3 BEP in dependence of effusion cell temperature with fit after eq. 4.8. The growth rates are directly proportional to the BEP for each element. The standard BEPs used in this work are indicated in the plot (in units of Torr).

Table 4.2 Used effusion cell parameters during growth. The approximate growth rate was determined from single element films. The cell temperature needed to sustain a certain p_{BEP} varies slightly from run to run by up to ~ 5 °C.

Element	Typical cell temperature [°C]	p_{BEP} [Torr]	Approximate growth rate [nm/min]	Melting point [K / °C] [72]
Te	355	4.5×10^{-7}	13.9	723 / 450
Bi	645	4.0×10^{-7}	6.8	514 / 271
Sb	490	3.4×10^{-7}	4.0	904 / 631

However, the Knudsen equation is fully valid only as long as the evaporating surface (e.g., the surface of the source material inside the cell) is large compared to the orifice, which is not the case in the effusion cells used inside the shown MBE system with their relatively large orifices. Under these circumstances, the pressure becomes dependent on the evaporating surface to some degree [133-p.78ff.]. The evaporation surface is changing during evaporation of the source material and therefore, the molecular cell fluxes have a tendency to drift during growth. This is also evident from Figure 4.3, where the temperature required for setting the standard BEP varied significantly between growth runs. During one single growth run, the effusion cell pressures were found to vary by up to 5-10 %. Flux stability could be improved by keeping the effusion cells at their working temperature for ca. 1 hour before starting growth and by re-adjusting cell pressures once in the middle of each run. Overall due to the mentioned fluctuations, the desired elemental composition could be attained with a precision of about 0.5 - 1 at. %.

The element layer thickness was controlled by the shutter opening time while the molecular beam flux from each cell was maintained at a constant value. The growth rate that has to be known for setting the shutter opening time was determined by SEM from single element films as shown in Figure 4.4. The

Bi and Sb films showed a Frank-van der Merwe-like growth and were relatively smooth and dense and had a specular appearance. In contrast to this, the Te films exhibited a more island-like (Volmer-Weber) growth, were rough, porous and looked dull black, resembling soot. Thus, the growth rate is overestimated when taking the Te element layer thickness as observed in the cross section and as a consequence, first compound films had a lower Te content than intended. A re-calibration using EDX to determine the actual layer composition and re-adjusting shutter opening times was necessary to achieve stoichiometry. For the element layer deposition with the MBE setup, two different deposition patterns (quintuple and bilayer pattern) were applied. Details are given in section 5.1. The standard growth rate of the compound films was $\sim 0.3 \mu\text{m/h}$ for Sb_2Te_3 and $\sim 0.4 \mu\text{m/h}$ for Bi_2Te_3 .

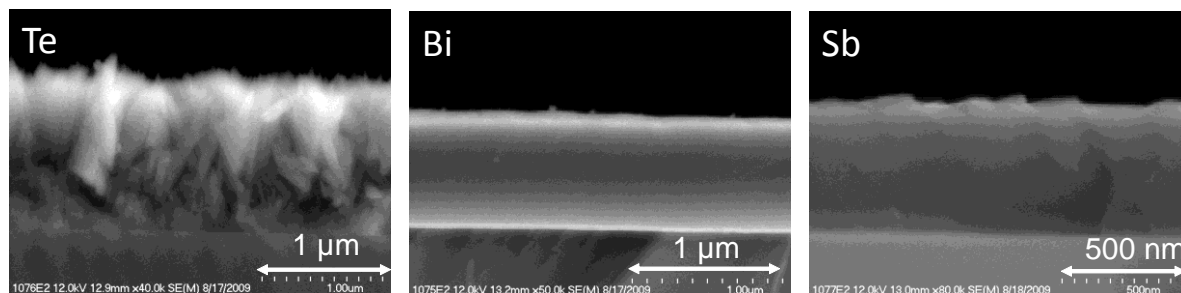


Figure 4.4 Cross sections of element single layer thin films. The Te film is rough and not fully dense.

4.1.3.3 Preparation of substrate materials

Barium fluoride (BaF_2): Single crystalline (111)-oriented BaF_2 platelets with a thickness of around 700-1000 μm were used. The platelets were hand-cleaved right before growth from $10 \times 10 \times 25 \text{ mm}^3$ bars using a trapezoidal blade and a hammer. The bars were supplied by Crystec GmbH, Berlin, Germany.

Oxidized Silicon (Si/SiO_2 wafers): 4 inch wafers of (100)-oriented Czochralski-grown dry-oxidized silicon (100 nm oxide thickness) were supplied by Siegert Consulting e.K., Aachen, Germany. This type of substrate was only used for the nanoalloying experiments. Before deposition, the so called "base piranha" pre-cleaning procedure consisting of baths in 1. HCL and 2. $\text{NH}_4\text{OH} / \text{H}_2\text{O}_2$ was applied to the samples in order to remove organic and metallic surface contaminants. At the end, the wafers were cleaved into $10 \times 10 \text{ mm}^2$ substrates suitable for MBE growth using a diamond scribe, model RV-125 supplied by ATV Technologie GmbH, Vaterstetten, Germany.

Nanoalloying: After a pre-bake step at 180 °C for 18 min in the introduction chamber under a vacuum in the 10^{-7} to 10^{-8} Torr range to desorb the biggest part of water and atmospheric contaminants, the substrate holders were transferred to the buffer chamber. Here, the final bakeout at 300 °C for 1 hour took place under vacuum in the 10^{-9} to 10^{-10} Torr range. After cooling down, the holders were transferred to the growth chamber.

Epitaxial growth: Only BaF_2 freshly cleaved before growth was used as substrate. Prior to growth, the substrate was heated at 425 °C in the growth chamber for 25 minutes to desorb residual water and gases. Further details concerning epitaxial growth are given in chapter 9.

4.1.4 Sputtering

4.1.4.1 Magnetron sputtering

Sputtering is a process where atoms are ejected from a target surface due to momentum exchange by bombarding ions [134-p.7ff], Figure 4.5. The process takes place under vacuum and a sputter gas pressure mostly between 10^{-4} and 10^{-2} mbar. The bombarding ions are typically formed by a glow discharge process where an inert gas (in most cases, Argon) is ionized by an electric discharge to form a

plasma. The target is negatively biased and works as the cathode, attracting the positively charged ions. Behind the target a permanent magnet is mounted that forces the electrons in the plasma on cyclic trajectories, increasing the plasma density by a decade and resulting in an increase in the flux of sputtered atoms. The highest sputtering rate is observed when the magnetic field is parallel to the target since the electron confinement is most effective there and a typical circular sputter trench develops which has a width of a few cm (in our setup, $\sim 1.5 - 2$ cm).

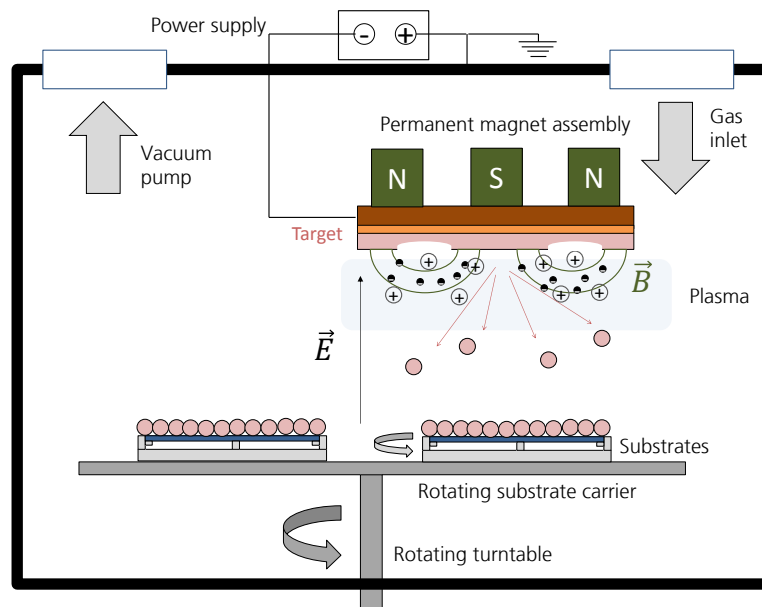


Figure 4.5 Principles of magnetron sputtering. Argon ions impinge on the target, leading to the ejection of target atoms and molecules (pink).

For the sputtering of low-conductivity and insulating materials a HF voltage with a frequency in the MHz range is applied to the target, preventing the buildup of a positive surface charge and a resulting repulsion of Ar ions. Se and Te have low electrical conductivity and must thus be deposited by HF sputtering, while DC sputtering is sufficient for Bi and Sb.

4.1.4.2 The sputtering system FHR MS150x4 and deposition parameters

All sputtered films shown in this work were deposited by the sputtering system MS150x4 assembled by FHR Anlagenbau, Ottendorf-Okrilla, Germany. The setup consists of a turntable with six substrate carriers. A homogeneous deposition on 4" and 6" wafers is achieved by a double-rotation scheme, where the turntable as well as every single substrate holder is rotating continuously. The system was calibrated such that for all elements a very homogeneous deposition results with an inhomogeneity span between 1 and 2 %.

An advanced programming and automatization language is integrated into the control software. Each period consisted approximately of 40 single operation steps, resulting in a total of ca. 4800 single steps for a SL with a period of 12.5 nm and a total thickness of $\sim 1.5 \mu\text{m}$. The whole setup and a screenshot of the user interface software are shown in Figure 4.6. The setup in its original state had several flaws (timing inaccuracies, mechanical problems etc.) that were fixed with several upgrades and modifications during this thesis. The modifications allow the accurate deposition of the nanometer – thin element layers and guarantee the stability of the deposition process.

The background pressure in the setup was always around $2-3 \times 10^{-7}$ mbar. The Ar sputter gas pressure was kept at 5×10^{-3} mbar during growth. The target bias voltages were around 250 V for DC sputtering and 600 V for HF sputtering. In most cases, whole 4" Si/SiO₂ wafers (see section 4.1.3.3) are used as substrates. For a few exceptional cases, i.e. film thicknesses $> 2 \mu\text{m}$, cleaved BaF₂ is additionally used. For the removal of residual atmospheric contamination (e.g. water vapor) from the substrates the inverse sputter etching chamber was used. Here, the substrate instead of the target is bombarded by ions, resulting in an effective "scrubbing action" of the substrate surface [135-p.127].

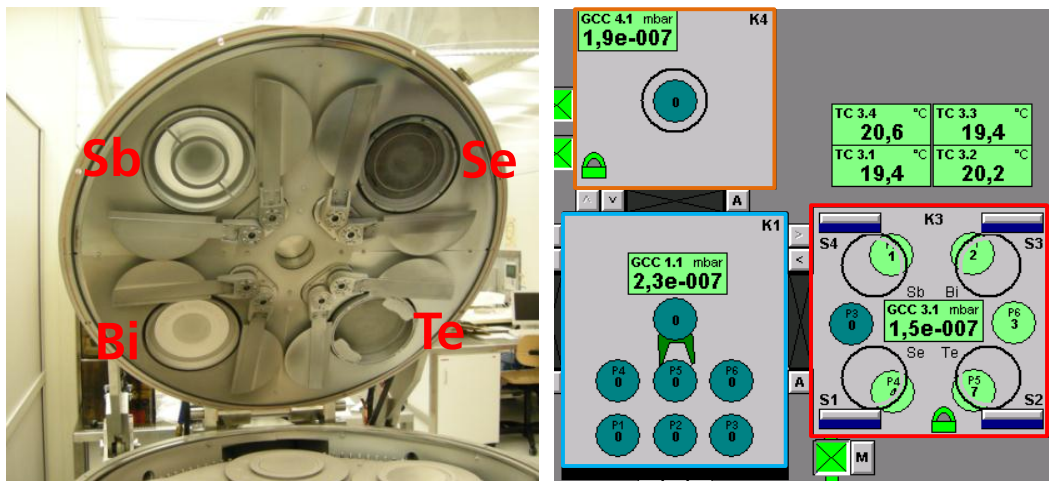


Figure 4.6 Left: Main sputtering chamber with targets inserted. Right: Screenshot of controlling software. Red = main sputter chamber, orange = sputter etching chamber, blue = intro chamber.

4.1.4.3 Morphology of sputtered element films and thickness calibration

A widely accepted and popular description of microstructural growth during sputtering was given by Thornton [136] who presented the Thornton zone model (TZM, Figure 4.7) several decades ago. According to the model, the two parameters that influence growth are given by the ratio of substrate temperature to melting temperature, T/T_M and the sputter gas pressure. In Zone I ($T/T_M < 0.3$) the low adatom mobility results in a morphology that is characterized by the growth of large dome-shaped and loosely bound crystallites. In Zone II ($0.3 < T/T_M < 0.5$) deposited films show large faceted columnar grains with dense boundaries (leading to a rough surface), changing to a recrystallized grain structure in zone III for $T/T_M < 0.5$ where bulk diffusion starts to set in. In transition zone T between zone I and II, densely packed small-scale fibrous grains, leading to a smooth morphology are reported.

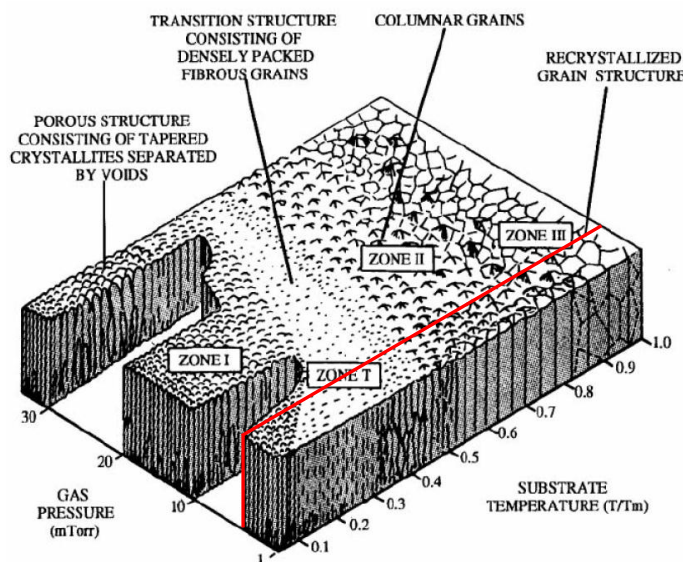


Figure 4.7 Thornton Zone model for sputtered films. Several growth zones are obtained for different gas pressures and substrate temperatures. Red line: Used sputtering gas pressure of 3.8 mTorr = 5×10^{-3} mbar.

The used sputtering Ar pressure of 5×10^{-3} mbar corresponds to 3.8 mTorr in the diagram. A correspondence between the TZM and sputtered elementary thin films was found as demonstrated by

Figure 4.8. The T/T_M ratios of Te, Sb and Bi are 0.4, 0.3 and 0.5 respectively (see Table 4.2). Sb falls fully into zone T and exhibits a very smooth growth (mirror-like surface) with very small grains that are not distinctly visible at 20 k magnification. The Te surface is closer to zone II and slightly larger, distinguishable grains form. Nevertheless, the surface is still smooth and mirror-like. Bismuth with its higher T/T_M ratio lies in the transition zone between zone T and II and clearly exhibits distinct features from zone II. Single large faceted columnar grains are evident and the films appear opaque. The roughness of sputtered Bi was also noted by other authors [107] and leads to a higher roughness of nanoalloyed films with a high Bi content such as the Bi_2Te_3 -based films shown in chapter 8.

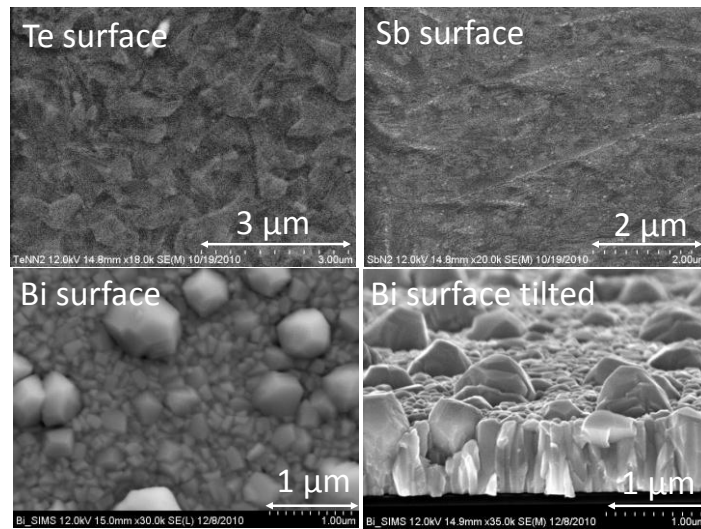


Figure 4.8 Surface morphology of sputtered element thin films. The morphology corresponds to the prediction by the TZM.

4.1.4.4 Thickness calibration of sputtering system

The thickness of sputtered films was determined with a lift-off technique. Analyzing the film remaining after the lift-off process with a profilometer (model Veeco Dektak 6M) yields the layer thickness and thus the growth rate if the deposition time is considered. Understandably, this approach is not fully applicable to the very rough Bi films. The profilometer needle has a diameter of 10 μm while the grains on the Bi film surface are spaced apart by only few μm . Thus, instead of probing the surface, the needle “hops” from grain to grain and a film thickness higher than actually present is determined. From EDX measurement, it was found out that a correction factor of roughly 0.55 has to be applied to the measured film thickness to get the “mole-equivalent” full-density thickness.

The accuracy of the calibration can be increased by determining the growth rate for different sputtering powers and applying a linear fit. A plot of growth rate vs. power shows a linear relationship for lower power ranges (Figure 4.9). At higher powers, the top target surface tends to melt up partially, generating droplets in the process and the rate vs. power relationship is no more linear. In this case, a part of the energy brought into the target by the impinging ions is not used to knock atoms out of the target but instead is lost to supply the latent heat needed to melt up the material, which results in a lower sputtering rate than anticipated from the extrapolation. It is strongly advisable not to operate in this high power range due to the detrimental effect of the droplets. The sputtering powers of Sb and Te were kept below 170 W and 300 W, respectively to avoid droplet formation.

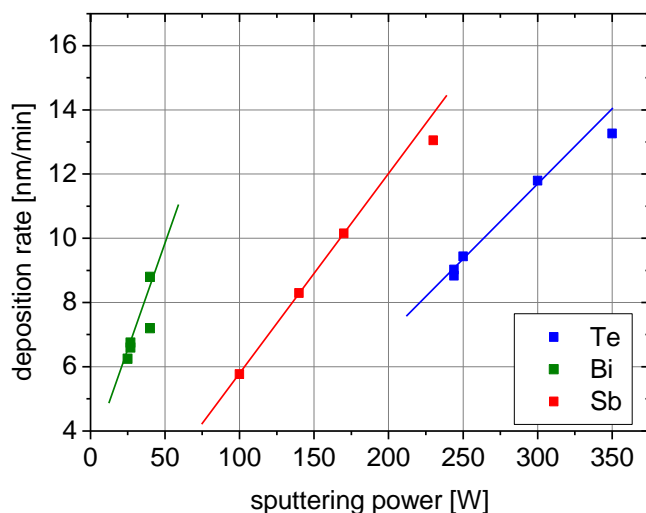


Figure 4.9 Sputtering rate vs. power for the elements used in this work determined in calibration runs. At higher power, the target surface partially melts up, the deposition rate drops and the linear relationship is no more valid as can be observed for Te and Sb.

Unfortunately, the sputtering rate is subject to a long-time drift due to changes in target morphology. The large difference in energy between the bombarding species and the sputtered species and the relatively low yield for most target materials means that as much as 80-90 % of the impinging ions energy is converted to heat which has to be transported away by cooling [134-p.16]. While the deposition rate drift of Bi and Sb is rather slow, Te is problematic since it has a low thermal conductivity of $\sim 2\text{-}3$ W/mK [72]. This means that a relatively large temperature gradient between surface and top as well as between sputter trench and the rest of the target is established during continuous sputtering. Since Te is brittle, this leads to a continuous degeneration of the target material. The material becomes rough, porous and tends to develop cracks and thus the thermal conductivity drops even more, further aggravating the situation. Additionally, since a porous surface generates less sputtered atoms [134-p.12], the sputtering power has to be increased to get the same deposition rate as before, accelerating the degeneration even more. The rate usually drops by up to 10 % after the deposition of 5-10 μm compound film which translates to a Te content reduction of around 3 at. % in the film, having a drastic impact on the electrical properties. The amount of deposition rate drift is unpredictable which makes depositing of near - stoichiometric films difficult and requires frequent re-calibration of the sputtering system.

Note that Se is also extremely critical under the mentioned aspects. Due to its very low thermal conductivity of 0.5 – 2.9 W/mK and its low melting point of 221 $^{\circ}\text{C}$ [72-p.4-122], already the application of low sputtering powers (80 W) lead to the partial melting of the target, rendering it unusable, which is why an alternative material system to $\text{Bi}_2(\text{Se},\text{Te})_3$ was developed (chapter 8).

4.1.5 Annealing system

4.1.5.1 Annealing setup

For compound formation by the nanoalloying method, the element layer stacks have to be annealed, preferentially under a defined atmosphere. For this purpose, a special homebuilt annealing system was assembled at Fraunhofer IPM, Figure 4.10. The sample is inserted into a quartz glass ampoule which consists of two parts that can be pushed together to seal the ampoule. The furnaces are calibrated such that the desired annealing temperature is homogeneous throughout the ampoule. For a one-zone isothermal annealing, only one furnace is pulled over a small ampoule that contains both sample and source. For a two-zone annealing (see next section), a longer ampoule is used and source and sample are kept at different temperatures with the two furnaces.

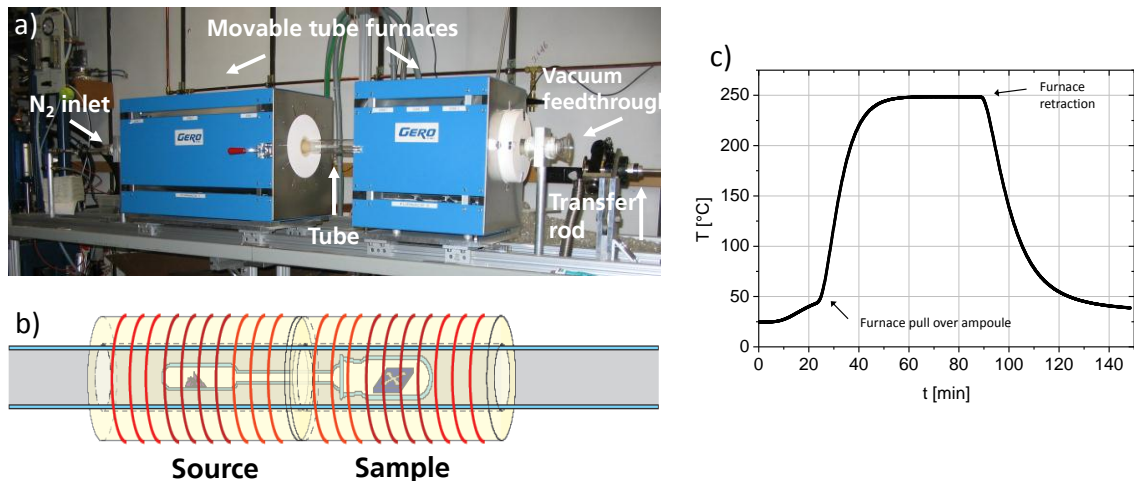


Figure 4.10 a) Annealing system used in this work. The setup is also capable of two-zone annealing experiments. b) Schematic drawing of ampoule and furnace position for two-zone annealing. c) Heating / cooling curves for an annealing temperature of 250 °C.

Firstly, the furnace tube together with the open ampoule is evacuated down to pressures in the range of 10^{-6} mbar after several nitrogen purging steps. Under this vacuum, the ampoule is sealed by pushing the two parts together via the transfer rod. Then, nitrogen is flowing through the furnace tube, acting as a purging gas and simultaneously leading to a pressure on the evacuated ampoule and keeping it tightly sealed. During the whole procedure, the furnace is heated up to the desired temperature without the ampoule inserted. After the ampoule evacuation procedure was carried out and the purge gas is flowing, the hot furnace is finally moved over the ampoule. After the desired annealing time has expired, the furnace is retracted from the ampoule, leaving it to cool down quickly. The heating / cooling curves are shown exemplarily for a temperature of 250 °C. After pulling the furnace over the ampoule it takes roughly 20 minutes to thermally equilibrate the ampoule and the sample with the furnace, i.e. to reach the desired annealing temperature within 10 °C. Upon removing the furnace, the temperature drops below 100 °C within 15 minutes. It is not likely the samples will change much below this temperature, so the properties, i.e. the annealed sample can be considered as quenched and the defect structure as “frozen in”. Annealing times given in this work specify the time between the points where the furnace is pulled over the ampoule and where it is removed again.

Save for the high-temperature two-zone experiments described in 4.1.5.2, the annealing runs in this work were carried out under a Te atmosphere and isothermal one-zone annealing, meaning that a small amount of Te was inserted into the ampoule and the temperature in the ampoule was homogeneous. The function of Te was mainly to provide a safety against Te loss from the sample if the ampoule was not sealed entirely tight. From previous experiments with polycrystalline thin films annealed under Te atmosphere (unpublished work, Fraunhofer IPM) it was found that the presence of Te in the ampoule does not lead to a Te enrichment in the sample up to 400 °C. Additionally in this work, it was tested whether the Te source influences the sample at an annealing temperature of 250 °C. A long annealing time of 8 h was chosen and the samples were annealed with a Te source, under vacuum and under nitrogen inert atmosphere in the ampoule. No difference in composition, morphology or transport properties was observed between the variations of annealing conditions.

4.1.5.2 Two-zone annealing

The theoretical basics for the two-zone annealing were described in ref. [75]. For Bi_2Te_3 samples, Brebrick determined the dependence of the Te partial pressure on temperature and the Te content in the samples. The results are given in Figure 4.11 together with the vapor pressure of pure Te. As expected, a sample with higher Te content will generate a higher Te pressure at the same temperature.

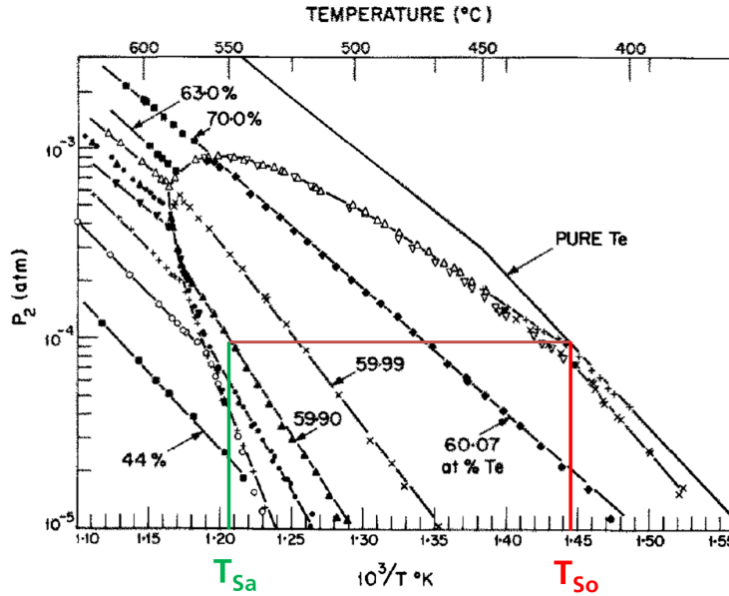


Figure 4.11 Partial pressure of Te and Bi_2Te_3 samples with different Te content versus temperature [75].

On the other hand, the information provided in the diagram can also be utilized to adjust the Te content. The equi-compositional areas are given by lines. If, for instance, a composition of 59.9 at. % of Te is desired and the sample is to be annealed at $T_{\text{Sa}} = 550 \text{ }^\circ\text{C}$, a Te partial pressure of about 10^{-4} atmospheres (0.1 mbars) has to be provided. This can be done by setting the temperature of a pure Te source such that said vapor pressure is established. As can be taken from the diagram, this source temperature is $T_{\text{So}} = 419 \text{ }^\circ\text{C}$.

The whole process can be interpreted with regard to Gibbs' phase rule, which states that

$$P + F = K + 2 \tag{4.9}$$

where P is the possible number of phases, F the possible degrees of freedom and K the number of components. As components, Te and Bi are present. If the considerations are limited to the homogeneity range of Bi_2Te_3 , then only the gas and solid phase are present. Two degrees of freedom remain: The sample temperature and the vapor pressure around the sample, which can be set by adjusting the Te source temperature.

However, the method only works for sufficient annealing temperatures and annealing times. In earlier annealing experiments with polycrystalline sputtered Bi_2Te_3 films (unpublished), the sample was kept at an annealing temperature of $350 \text{ }^\circ\text{C}$ for 2 hours and no influence on sample properties was seen when changing the source temperatures. From the experiments shown in this work a minimum temperature / annealing time of $400 \text{ }^\circ\text{C} / 2 \text{ h}$ are anticipated in order to be able to see an effect.

4.2 Transport property characterization – methods and application

4.2.1 Van der Pauw method and Hall effect measurements

For the determination of the electrical conductivity, charge carrier concentration and –mobility, a measurement setup that makes use of the standard van der Pauw Method as derived and described in ref. [137] and [138] is used here. Two measurements with different contact configurations are carried out, yielding two resistance values that can be used to calculate the specific resistivity ρ_{el} or its reciprocal value, the electrical conductivity σ . For getting accurate results, there are requirements on the film properties and the contacts, which must be sufficiently small and located at the circumference of the

sample. Carrier concentration and –mobility are determined by making use of the Hall effect. If a current I is applied to opposite contacts of a sample with thickness d while a magnetic field with strength B perpendicular to the current is active, the Lorentz force drives the charge carriers away perpendicularly to the flow direction. This results in the buildup of an electric field and a Hall voltage U_H that is given by $U_H = R_H \cdot (IB/d)$ with the Hall coefficient R_H . In the most general case where electrons and holes are simultaneously present as carrier types, the Hall coefficient is given by

$$R_H = \frac{F_H}{e} \cdot \frac{p\mu_p^2 - n\mu_n^2}{(p\mu_p - n\mu_n)^2} \quad (4.10)$$

where p , μ_p and n , μ_n are the carrier concentration and –mobility for holes and electrons, respectively. For the typical case of extrinsic conduction, acoustic scattering and a distinct anisotropy of longitudinal and parallel effective masses which obviously also applies to the materials examined in this work [139], the Hall prefactor F_H can be assumed as unity [140-p.114].

If one carrier type clearly dominates, i.e. $n \gg p$ (n-type electron conduction) or $p \gg n$ (p-type hole conduction), equation 4.10 simplifies to:

$$\text{n – type: } R_H = -\frac{1}{en} \qquad \text{p – type: } R_H = +\frac{1}{ep} \quad (4.11)$$

and the charge carrier concentration can be easily determined. Finally, the charge carrier mobility μ is determined by dividing the obtained electrical conductivity by the carrier concentration.

Contact to the samples is made by pressed contact pins with a pointed end, minimizing contact diameter as required by the van der Pauw Method. The pins are plated with gold which has been known for some time to form ohmic low resistance contacts with many thermoelectric materials, including $(\text{Bi}_{1-x}\text{Sb}_x)_2\text{Te}_3$ [141]. The applied magnetic field is 0.9 Tesla. Currents of typically 5 mA, 2.5 mA, -2.5 mA and -5 mA are applied to the sample while the voltage is simultaneously measured.

The measurement error in the van der Pauw method is systematic, i.e. too low values for resistivity and carrier concentration and too high values for the mobility are determined because of a violation of the contact idealizations that are assumed for the derivation of the relations shown above. The error can be estimated by the relations given by van der Pauw [137]. Under the assumption of realistic values for the contact circumference, diameter and displacement from the sample boundary, the error of the electrical resistivity is around 1 % and can be neglected in comparison to the uncertainty of the film thickness which is assumed as ~ 5 %, leading to an error of ~ 5 % for the electrical resistivity. For carrier concentration and mobility an error of about 10 % can be estimated. The errors in the measurement of voltage, current and magnetic field strength are negligible in comparison to the errors caused by the contact nonideality.

4.2.2 Seebeck coefficient measurement

Room temperature setup

The Seebeck coefficient at room temperature is determined by a setup constructed at Fraunhofer IPM, Figure 4.12. The sample is laid on two copper blocks that are heated and cooled using thermoelectric modules. Two probes consisting of two type T copper-constantan (Cu-CuNi) thermocouples each are applied to the sample. They allow the simultaneous measurement of the two sample temperatures T_H and T_C and the Seebeck voltage U_S caused by the temperature gradient ($\Delta T = T_H - T_C$) between the two different Cu-CuNi junctions that are in contact with the sample. This yields the Seebeck coefficient S of the sample:

$$S = \frac{U_S}{T_H - T_C} \quad (4.12)$$

In our implementation of the setup, the measurement is repeated with reversed temperature gradient and the two obtained results are averaged.

It is noted that an international standardized calibration procedure for Seebeck measurement setups has not yet been established. To avoid errors during measurement, during this thesis a validation procedure taking place every one or two weeks was introduced: 1.) Validation with a Ni sample with known S and 2.) Measurement of one or more V_2Vl_3 reference samples with high S and comparison with previous results obtained on the samples. Special care was taken to ensure proper junctions and good contact to the film. The junctions are inspected by eye prior to the measurement. Faulty junctions will yield too large Seebeck coefficients, leading to their immediate replacement. It is altogether difficult to give a measurement error for this setup. If the values obtained on the reference sample do not deviate by more than 5 % from the reference value, the setup is considered as validated. Thus, the measurement error can be roughly estimated as 5 % and has a systematic character due to the mentioned reasons.

Temperature-dependent measurement of Seebeck coefficient and electrical resistivity with the SRX setup

S and σ are measured in dependence on temperature with the homebuilt setup „IPM-SRX“. The measurement setup is based on a prototype set up at the Ioffe Institute of Physics in Sankt Petersburg in the early 1990s [142] and additional ideas from the MLU Halle [143]. A description of the setup is given in ref. [144]. A type K thermocouple consisting of the alloys chromel and alumel is used in the setup. The sample holder is shown in Figure 4.12 together with a wiring diagram. The chromel/alumel thermocouples are pressed to the bottom of the sample by spiral springs. The sample holder is surrounded by a radiation heat shield. For the measurement of the Seebeck coefficient, a linear regression method proposed by Boffoué et al. is used [144], eliminating undesired residual voltages in the electric circuit that are present due to various reasons.

Prior to the measurement, the samples were cut into stripes with a length of 10 mm and width of 2-3 mm to increase the temperature gradient and thus measurement accuracy. Typical maximum temperature gradients are between 2 and 6 K. The sample chamber was evacuated and then kept under a nitrogen pressure of 100 mbar to protect the sample against evaporation and to achieve good thermal contact between sample and copper block. For each sample, several incremental heating/cooling cycles were carried out. The maximum temperature was increased stepwise in each heating/cooling cycle. If no stabilization of the electrical properties was observed on cooling, further heating/cooling cycles were carried out. A measurement uncertainty of 7 % is estimated.

The simultaneous measurement of the electrical conductivity is done with a standard 4-point probe method. A current I is injected into the sample with length l . The resistance R is measured by using the Alumel branches as the voltage probe to determine the voltage drop U on the sample with a cross section of A (corresponding to a thickness of d and a width of w). For rectangular samples such as the ones characterized in this work, the electrical conductivity of the sample is then given by

$$\sigma = \frac{l}{R \cdot A} = \frac{I \cdot l}{U \cdot d \cdot w} \quad (4.13)$$

The measurement is carried out with 3 different voltages and currents. The obtained resistances are averaged. Residual voltages are determined prior to the measurement of the electrical resistivity and subtracted from the measured voltage. A measurement uncertainty of ~ 10 % is estimated. Often, the measured stripes show an irregular shape or cracks. In this case, the obtained σ have to be normalized to values obtained at room temperature by van der Pauw measurements (section 5.3).

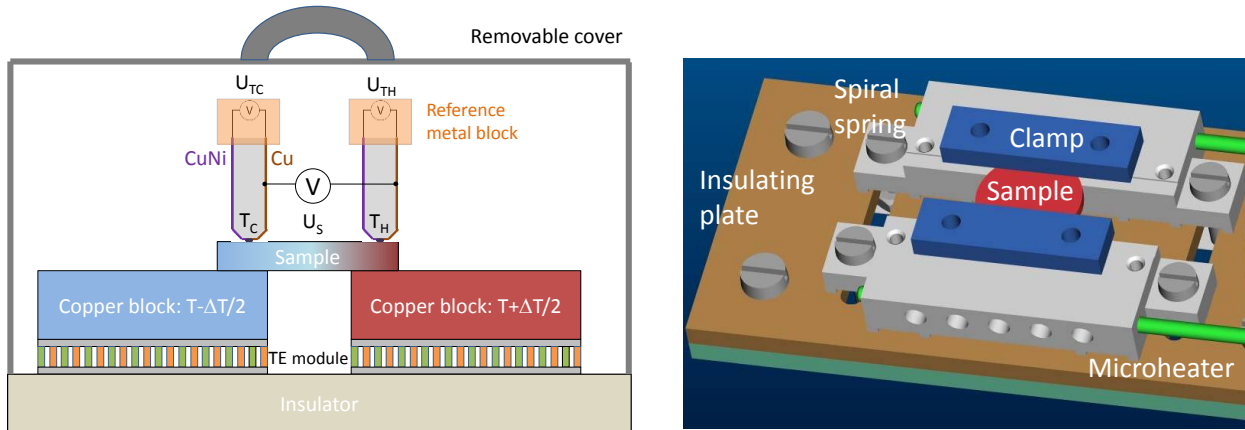


Figure 4.12 Left: Room temperature measurement setup for Seebeck coefficient. Right: Sample holder of SRX measurement setup (CAD drawing).

4.2.3 Time Domain Thermal Reflectance (TDTR)

4.2.3.1 Description and setup

The method of time domain thermal reflectance (TDTR) [145] that is used in this work to determine the cross-plane thermal conductivity is basically a pump-probe experiment. A “pump” laser beam impacts on a sample and causes a local heating and a certain temperature distribution on the sample surface. The subsequently arriving probe beam “probes” the temperature rise caused by the pump beam by analyzing the change in reflectivity ΔR_{th} caused by the temperature rise ΔT . Both are connected through the relation

$$\Delta R_{th} = \frac{\partial R_{th}}{\partial T} \Delta T \quad (4.14)$$

with $\partial R_{th}/\partial T$ as material-specific thermoreflectivity. The analysis of the temperature rise, i.e. reflectivity change yields the thermal conductivity of the characterized thin film. The measurement principle for a multilayered system is sketched in Figure 4.13.

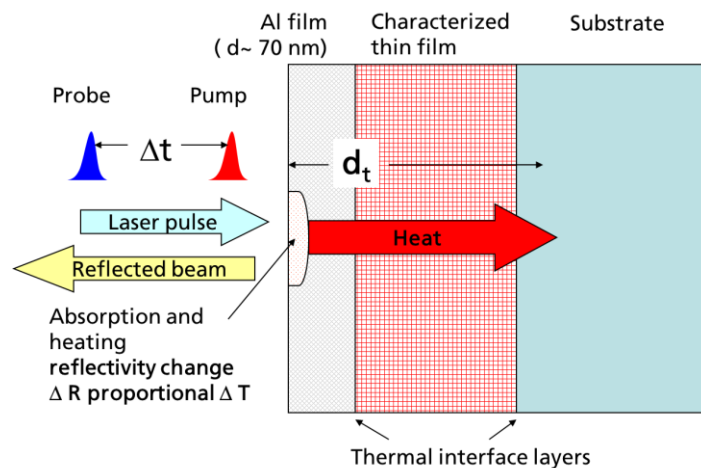


Figure 4.13 TDTR measurement principle. A laser pump beam heats the sample surface, causing a change in reflectivity that is “probed” by the probe beam. The reflected probe beam signal can be evaluated in dependence on delay time Δt to obtain the thermal conductivity of the characterized thin film.

A schematic of the measurement setup is shown in Figure 4.14. The laser beam, generated by a Ti:Sapphire solid state laser is pulsed with a frequency of 80 MHz and has a wavelength of 775 nm. The

laser beam is split up by a polarizing beam splitter into pump (vertically polarized) and probe beam (horizontally polarized) after the optical isolator. The pump beam is modulated with a frequency of 10.7 MHz by an electro-optic modulator. The delay stage that is passed by the pump beam allows one to set a variable time delay between pump and probe beam. Both beams are directed to the sample by a pair of beam splitters and focused on the sample by an objective. The focused laser spots have a diameter of 16-18 μm in our experiment. One of the beam splitters is polarizing, blocking the pump beam from reaching the photodetector. An additional aperture is blocking out any residues of the pump beam that leak through the polarizing beam splitter. The reflected probe signal is picked up by two lock-in amplifiers. The first one is locking on the modulation frequency of 10.7 MHz of the pump beam, while the second one is locking on a frequency of 220 Hz that the probe beam is chopped with (not shown in Figure 4.14). The CCD camera is used to observe the sample surface and position the laser beam. For the actual measurement, the corresponding beam splitter is removed in order to get a higher probe beam intensity and signal. Long pass and short pass filters were introduced to reduce measurement uncertainties due to sample roughness [146].

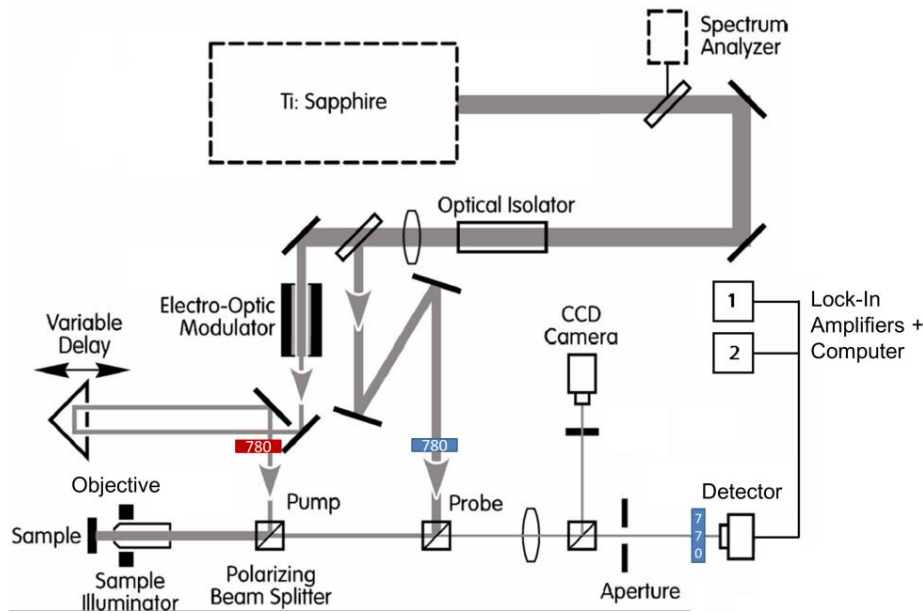


Figure 4.14 Time domain thermal reflectance measurement setup. Red block = long pass wavelength filter, blue block = short pass wavelength filter.

A derivation of the theoretical basics of the TDTR method and the relations shown here is given in ref. [145]. The temperature distribution caused by the modulated pump beam can be described by a point source oscillating with frequency ω on a semi-infinite solid. In the z -direction, the thermal penetration depth of the heat wave is limited to the thermal penetration depth d_t , similar to an electromagnetic wave penetrating an electrical conductor (skin effect). d_t can thus be considered as the “depth of information” of the measurement.

$$d_t = \sqrt{\frac{2D_t}{\omega}} \quad (4.15)$$

The thermal diffusivity $D_t = \lambda/c_v$ is a means to quantify how quickly a solid body assumes the temperature of the environment. As shown in Figure 4.13, each sample consist of multiple layers, including phonon-scattering interfaces between the layers. The mathematical model can be generalized to a layered geometry by an iterative matrix algorithm which is similar to matrix methods used in fields such as electrical engineering or optics [145]. It is important to note that using this algorithm each layer can be fully modeled by taking its thermal conductivity λ , thermal diffusivity D (i.e. c_v) and thickness L_n . Phonon-scattering interface layers between different materials are modeled by a layer with small thermal conductivity and small thickness.

For the selection of an appropriate laser power, one also has to consider the steady-state heating of the substrate and the film. In the film, the heat spreads linearly since the thickness of the films is mostly lower than the laser beam diameter $2w_0$ ($\sim 17 \mu\text{m}$ in our setup). Then, the temperature rise $\Delta\bar{T}_f$ caused by an impinging laser power A_0 can be calculated as given by eq. 4.16 for a film with a thickness of d with thermal conductivity λ . For estimating the heat rise in the substrate (the heat spreading here is three-dimensional), the low frequency limit, $\omega < D / w_0^2$ is considered. Then, one can derive a useful relation that can be used to estimate the steady-state substrate temperature rise $\Delta\bar{T}_s$ in the substrate [145]. For calculating the total sample temperature rise $\Delta\bar{T}_{tot}$, the contributions of film and substrate have to be added according to eq. 4.16. It is noted that the absorbed laser power is only 13 % of the incident laser power since only 15% of the incident power are absorbed by the Al film (the rest is reflected) and the transmission of the optical elements of the setup is 85%.

$$\Delta\bar{T}_{tot} = \Delta\bar{T}_f + \Delta\bar{T}_s = \frac{A_0 \cdot d}{\pi \cdot w_0^2 \cdot \lambda} + \frac{A_0}{2\sqrt{\pi}w_0\lambda} \quad (4.16)$$

For the analysis of V_2VI_3 films the laser power has to be kept low enough to ensure no significant steady-state heating occurs during the analysis. Using eq. 4.16 to calculate the steady-state heat rise in film and substrate with a chosen total incident laser power of 27 mW, one obtains an acceptable total steady heating of 16 K for a V_2VI_3 thin film of $1.5 \mu\text{m}$ thickness with a low thermal conductivity of $\lambda = 0.45 \text{ W/mK}$ on a BaF_2 substrate with $\lambda = 10.9 \text{ W/mK}$ [72-p.12-212].

4.2.3.2 Measurement details

Sample preparation

The sample preparation for the TDTR method is simple. Only an unstructured metal layer as transducer and reflector layer is necessary. Due to its high thermorefectivity $\partial R/\partial T$ and other advantages (easy deposition, well-known properties etc.) Al was chosen. A thickness of 70 nm is optimal for films with low thermal conductivity as can be inferred by exemplaric data modeling.

Measurement procedure

The probe beam signal can be divided into a real and imaginary part, corresponding to the in-phase and out-of-phase signal voltages V_{in} and V_{out} picked up by the lock-in amplifier. Since both real and imaginary part of the signal are analogously affected by frequently occurring nonidealities in the experiment (beam defocus, incomplete overlap of probe and pump beam) taking the ratio of both as measurement signal makes the method more robust to perturbations and increases measurement accuracy [147]. The actual measurement procedure is carried out by varying the time delay t between pump and probe beam and measuring the signal voltages V_{in} and V_{out} for each t . Plotting the ratio of these vs. the time delay yields the ratio-time transient, to which the model data calculated by the procedure described above is fitted. Some examples are given in refs. [145,148,147].

The thermal penetration depth for this film, calculated by eq. 4.15 is only around 100 nm and the total film thickness is around $1.5 \mu\text{m}$. Hence, the substrate can be neglected in the model calculation which was the case for all films analysed in this work. The complete layer system consists of 3 layers including a thermal interface layer between Al and V_2VI_3 material. Each layer is described by thickness, heat capacity and thermal conductivity, resulting in a total of 9 parameters in the model. For the Al and the V_2VI_3 film, the heat capacity values c_v are taken from refs. [72-p.4-124][53] and the thermal conductivity of Al was calculated from the electrical conductivity with the Wiedemann-Franz law, eq. 2.5. The determination of the local thickness of the Al layer is possible through acoustic impedance effects (eq. 2.21), which can be observed due to the picosecond timescale of the experiment as described nicely e.g. in [148].

With all data, two parameters that are varied to fit the model to the data remain: The thermal conductivity of the V_2VI_3 film and the interface thermal conductance. Since the variation of these two

parameters affects the fits differently the variation of one parameter does not influence the other. A good fit yielding a thermal conductivity of 0.45 W/mK can be obtained assuming an Al-V₂VI₃ interface thermal conductance of 32 MW/m²K. This value is rather low since, inevitably, a thin oxide layer has formed on the V₂VI₃ film, acting as a thermal resistance. All V₂VI₃ thin films examined in this work could be modeled with a similar interface resistance.

Measurement uncertainty

The measurement uncertainty can be estimated by the time-dependent sensitivities of the mathematical model to the parameters. The dependence of the sensitivity S_y of the ratio $R(y)$ on a certain parameter y is given by taking the logarithmic derivatives [147,149-p.17].

$$S_y = \frac{\partial \ln R(y)}{\partial \ln y} \Rightarrow R(y) \propto y^{S_y} \quad (4.17)$$

The sensitivity is generally dependent on the delay time. With the definition of the sensitivity as given in eq. 4.17, the ratio depends exponentially on the sensitivity. A small sensitivity value S_y means that the model is not very sensitive to the respective parameter y , resulting in a high uncertainty for the parameter.

The uncertainty for any parameter s_i with sensitivity S_i propagates to the measurement uncertainty s_λ^{V-VI} of the thermal conductivity λ_{V-VI} of the V₂VI₃ film by eq. 4.18 [149-p.17]. In the data modeling range between 40 and 3600 ps the sensitivity on the Al thickness $S_d^{Al} = -0.37$ overwhelms all others, making only this parameter relevant for the determination of s_λ^{V-VI} :

$$s_\lambda^{V-VI} = s_i \cdot \frac{S_i}{S_\lambda^{V-VI}} \xrightarrow{\text{Max}(S_i)=S_d^{Al}} s_\lambda^{V-VI} = s_d^{Al} \cdot \frac{S_d^{Al}}{S_\lambda^{V-VI}} \quad (4.18)$$

The ratio of the sensitivities $|S_d^{Al}/S_\lambda^{V-VI}|$ for the analysed thin films is around 1.75 - 1.9. The uncertainty s_d^{Al} of the Al thickness determination by the acoustic reflexes is estimated as 5 %, meaning that s_λ^{V-VI} is roughly 9-10 %. This can be seen as a lower limit for the measurement uncertainty since other parameters such as surface oxides, nonideal beam overlap and shape etc. also influence the measurement signal. An additional uncertainty is caused by sample roughness which causes the measurement data to get distorted by a long-range oscillation-like pattern. This phenomenon was restricted to the slightly rough samples shown in chapter 8. The uncertainty range can be estimated by giving an upper and lower limit for the fit. Typically, an additional uncertainty on λ_{V-VI} of roughly 10 % is observed which adds up to the uncertainty due to the Al thickness as given above.

The system was validated after installation using a Si/SiO₂ wafer test sample (oxide thickness of 500 nm). A thermal conductivity of 1.30 W/mK for the SiO₂ was determined in very good agreement with the literature value of 1.33 W/mK [150]. The test measurement was repeated on each measurement day to ensure that correct results are obtained.

Comparison and validation of thermal conductivity obtained with TDTR measurements and the 3 ω method

An extended validation of the TDTR setup specifically for V₂VI₃ thin films was carried out by comparing measurement results to results obtained with the well-established and technically completely different 3 ω method (setup in Fraunhofer IPM). Results on several sputtered homogeneous and multilayered thin films annealed at different temperatures are compared in Table 4.3.

Table 4.3 Comparison of thermal conductivity values λ obtained with the TDTR and 3ω method for different nanoalloyed thin films.

Film	Annealing temperature [°C]	λ - TDTR [W/mK]	λ - 3ω [W/mK]
Bi ₂ Te ₃	200	0.65 ± 0.07	0.59 ± 0.06
(Bi _{0.95} Sb _{0.05}) ₂ Te ₃	200	0.50 ± 0.05	0.45 ± 0.05
Bi ₂ Te ₃ / (Bi _{0.95} Sb _{0.05}) ₂ Te ₃ – SL	150	0.57 ± 0.06	0.53 ± 0.05
(Bi _{0.2} Sb _{0.8}) ₂ Te ₃	200	0.57 ± 0.06	0.46 ± 0.05

4.3 Structural characterization – methods and application

4.3.1 X-ray Diffractometry (XRD)

Crystals represent three dimensional diffraction gratings. At certain incidence angles θ depending on the distance between two lattice planes d_{hkl} , constructive interference of the X-rays with wavelength λ_{XRD} occurs according to the Bragg-equation

$$2d_{hkl} \cdot \sin\theta = n \cdot \lambda_{XRD} \quad (4.19)$$

with n as diffraction order. For cubic and hexagonal systems, d_{hkl} is given by

$$\text{cubic: } d_{hkl} = \sqrt{\frac{a_c^2}{h^2 + k^2 + l^2}} \quad \text{hexagonal: } d_{hkl} = \left(\frac{4(h^2 + k^2 + hk)}{3a_h^2} + \frac{l^2}{c^2} \right)^{-\frac{1}{2}} \quad (4.20)$$

where a_c = cubic lattice constant, a_h and c = hexagonal lattice constants. For calculating the positions of the reflexes, the lattice constants for Bi, Sb, Te, Bi₂Te₃ and Sb₂Te₃ were taken from refs. [151], [152], [153], [67], [68], respectively.

For some samples, the grain size p was calculated using the Debye-Scherrer equation:

$$w_{FWHM}(2\theta) = \frac{K_S \cdot \lambda_{XRD}}{p \cdot \cos\theta} \quad (4.21)$$

w_{FWHM} is the full width at half maximum of the reflex at the angle 2θ and K_S the Scherrer constant. The value of K depends on the crystal shape. Usually (and also in this work) a value of 0.9 is used going back to first calculations by Scherrer as mentioned in [154].

In this work, all XRD scans were carried out in Bragg-Brentano geometry (θ - 2θ scan) except for some scans as indicated in section 5.1.2 and 5.3. For the latter, the grazing incidence geometry was used. Details on the XRD apparatus are given in [155]. Additionally, in chapter 9 a PANalytical Empyrean 2 with a 2x Ge 220 Monochromator was used to acquire the XRD data.

4.3.1.1 Superlattice XRD satellites and pole figures

Superlattices correspond to artificial period structures superimposed on the crystal lattice. If there is a SL structure with sufficient quality (sharpness, periodicity) present in the sample, so-called SL satellites are centered equidistantly around the zeroth-order peak which corresponds to the average lattice constant of the SL structure. The period of the SL d_{SL} can be calculated from the angles of the satellites by subtracting the Bragg equation for two different SL reflexes indexed with their order m and n . The intensity of the SL reflexes decays with increasing order. A high intensity at high orders is indicating a good long-range order, i.e. a high quality of the SL structure.

$$d_{SL} = \frac{(m - n) \cdot \lambda_{XRD}}{2(\sin\theta_m - \sin\theta_n)} \quad (4.22)$$

A pole figure provides information about the orientation of the crystallites present in a sample. It can be interpreted by considering the intersections of the normal of the selected (hkl) -planes with an imaginary hemisphere situated above the sample surface. The two-dimensional projection of this hemisphere results in a pole figure. The intensity in each point is proportional to the number of grains in the film that have their normal to the selected (hkl) -planes and point to the respective coordinates on the hemisphere. Pole figures of the V_2VI_3 materials are constructed by first setting the angle 2θ to the strong Sb_2Te_3 (01.5) reflex at 28.2° [42-p.68]. The pole figure is given by the angle χ , representing the "radius" of the pole figure and ϕ , representing the rotational angle of the figure. In order to be able to obtain a reflection, χ and ϕ must be such that the reflection condition is fulfilled. Since (01.5) and (00.l) enclose an angle of $\chi=59^\circ$ in Sb_2Te_3 , (00.l) reflections occur on a circle defined by this angle. During rotation around the sample normal by ϕ , a certain amount of reflexes will appear in dependence on crystal symmetry. The [00.l] direction in the V_2VI_3 materials exhibits a threefold rotational symmetry, so three reflexes should appear if there is perfect rotational order in the crystal. The pole figures were recorded with a PANalytical Empyrean 2 with Cu- $K_{\alpha 1}$ and - $K_{\alpha 2}$ radiation.

4.3.1.2 Rietveld refinement

Most Rietveld refinements of the diffraction data obtained at room temperature were carried out using the GSAS Suite of Programs [156] together with the graphical user interface EXPGUI. The peak profiles were refined using the Pseudo-Voigt function described in the GSAS manual [156-p.156ff]. Spherical harmonics were used to model the texture level in the samples. The orientation index was also determined from the Rietveld refinements and can be used to judge the degree of texture. For a randomly oriented crystal, the index is 1 and increases without boundary for an increasing degree of texture [156-p.139]. The grain size p was calculated from the parameter L_x that describes particle size broadening in the Pseudo-Voigt model as given in [156-p.164]. This calculation is similar to eq. 4.21 but takes into account the broadening of *all* reflexes in the pattern and thus represents an average grain size.

All refinements were carried out with GSAS save for chapter 8 where the program TOPAS Academics [157] was used with the March Dollase Model [158] to refine the strongly preferred orientation parallel to the c -axis. The effect of the surface roughness was corrected using an approach by Suortti [159].

4.3.2 Scanning Electron Microscopy (SEM) with Energy-Dispersive X-ray Analysis (EDX)

Scanning Electron Microscopy (SEM): A scanning electron microscope (SEM) uses a focused electron beam to scan over the surface or the area of interest and forms an image from the collected backscattered and secondary electrons. In this work, the method was used to examine the sample morphology and cross-sections of the film. Two SEM systems were used: 1.) The Hitachi S-4700, a Cold Field Emission Scanning Electron Microscope (FE-SEM) with a secondary electron (SE) detector, a standard back scattered electron (BSE) detector and an additional ring-shaped BSE detector that can be moved into the sample chamber if needed, yielding a superior element contrast. 2.) The Hitachi SU-70, a FE-SEM with a Schottky electron gun that provides high beam currents. It is equipped with the same detectors as the S-4700.

For both SEMs an acceleration voltage of 12 kV was applied. The samples were electrically contacted using silver paint. The measurement of film thicknesses was carried out by analyzing the film cross-section in fast-scan mode to prevent distortion effects by image shifting which occurred during slow-scan mode. The film thickness measurement was carried out on 3-4 different parts of the cross section and averaged. The measurement uncertainty for the film thickness is estimated as $\sim 5\%$. For analyzing the cross-section, the samples were cleaved using a diamond cutter.

The imaging of the cross-section via SEM can be used at room temperature to visualize the nanostructuring. The scattering probability $\sigma_e(\beta)$ for electron scattering for angles $> \beta$ is related to the relativistically corrected wavelength λ_{el} and the atomic number Z by $\sigma_e(\beta) \propto \lambda_{el}^2 Z^{1.3}$ [161-p.378]. Elementary Bi has a higher atomic number than the elements Sb and Te, a larger backscattering coefficient and thus shows up as a bright line in the cross-section image. However, the capability of the BSE detector to distinguish between the elements was only sufficient for unannealed films.

Energy-Dispersive X-ray Analysis (EDX): Energy-Dispersive X-ray Analysis (EDX) was used to analyse the chemical composition in the films. The sample is irradiated by the electron beam, causing the ejection of inner shell electrons. The empty electron shells are occupied with electrons from outer shells with higher energies under emission of characteristic X-ray radiation. The intensity of the X-ray radiation generated by each element is measured and, after a ZAF correction (backscattering and energy loss dependent on atomic number, absorption and fluorescence) the element concentration can be determined. Two EDX systems were used in this work. The S-4700 is equipped with an EDAX Phoenix EDX detector controlled by the Genesis software package. The SU-70 is equipped with an Oxford X-Max EDX System with an INCA detection unit and the INCA software package. The incident electron count rate was set to yield a deadtime of ~ 30 - 35 % in both detectors, yielding a count rate of ~ 1 kcps and ~ 3 - 4 kcps in the EDAX and Oxford system, respectively. The voltage was chosen as 12 kV, which fulfills the requirement that the overvoltage should be at 2-5 x of the respective X-ray line [160]. For Bi, Sb and Te the M, L, and L line were used with α -line energies of 2.42, 3.61 and 3.77 keV, respectively.

The measurement error caused by the overlap of the L lines of Sb and Te can be somewhat compensated by using element standards that also serve for regular calibration of the EDX system. For this, near-stoichiometric element standards for Bi_2Te_3 , Sb_2Te_3 and $(\text{Bi}_{0.25}\text{Sb}_{0.75})_2\text{Te}_3$ with known compositions were used. They were provided by the Martin-Luther University in Halle-Wittenberg by Dr. Matthias Stölzer and consist of Bridgman-grown material synthesized by H.-T. Langhammer during his PhD thesis. For the calibration, three measurements were carried out on the standards and averaged. The correction factor, giving the deviation between measured and nominal element composition was determined from the experiment and applied to subsequent measurements on samples to yield the “true” element composition. The $(\text{Bi}_{0.25}\text{Sb}_{0.75})_2\text{Te}_3$ standard was used for all samples consisting of $(\text{Bi}_{1-x}\text{Sb}_x)_2\text{Te}_3$ with $x \geq 0.5$. It is noted that for lower Sb concentrations, it is not certain that using the standard yields correct results. It is also not guaranteed that the application of the calibration data obtained from a homogeneous standard measurement to layered films yields fully accurate results. For each determination of chemical composition, three measurements with an acquisition lifetime of 100 live seconds were carried out and averaged. The uncertainty of the obtained atomic concentrations is estimated as ~ 0.3 - 0.5 at. % (see also [42]).

4.3.3 Transmission Electron Microscopy (TEM)

In a transmission electron microscope (TEM) the electron beam travels through a thin material slice. By using a system of electromagnetic lenses, a two-dimensional projection that represents sample structure on a screen is possible. TEM analysis of thin film samples was carried out at the University of Tübingen by the Eibl group (mainly by Dr. Nicola Peranio) and the University of Kiel by the Kienle group (mainly by Dr. Ulrich Schürmann and Torben Dankwort).

The instrumental details for the TEM analysis by the Eibl group are given in [166]. For analysis in the Kienle group for most imaging tasks the TEM Tecnai G² F30 with the S-TWIN objective lens and an acceleration voltage of 300 kV was used. The spherical aberration coefficient C_s is 1.2 mm. The system is also capable of High-Resolution TEM (HRTEM). Also, integrated high-resolution Scanning Transmission Electron Microscopy (STEM) is possible. The STEM is a “hybrid” of the TEM and SEM, which uses deflection coils to scan a finely focused converged electron beam across the surface of a thin specimen, each point on the sample creates a corresponding point contrast on the screen. In the system, a High Angle Annular Dark Field (HAADF) detector is used. This type of detector is centered on the optic axis of the STEM and has a hole in the middle. Only electrons with an off-axis angle of > 50 mrad ($\sim 3^\circ$) are acquired, blocking out the “background” of Bragg-diffracted electrons and enabling the acquisition of Z-

contrast images [161-p.379f.] Thus, element distributions such as chemical variations accompanying superlattice structures can be clearly imaged. EDX elemental mapping was performed in the STEM mode using the M-line and the K-Line for Bi and Sb, respectively. For EDX analysis a Si/Li detector (EDAX System) was used.

For imaging in dependence on temperature and in-situ annealing of multilayered films, a 652 Double Tilt Heating Holder by Gatan was used. The temperature was increased stepwise with a heating rate of 5-7 K and held for 20 minutes at the respective temperature with roughly 10-15 minutes of imaging time each. The sample preparation at Kiel was carried out by Focused-Ion Beam (FIB) [161-p.188f.]

The HAADF-HRSTEM images shown in chapter 9 were acquired at the CAMCOR lab at the University of Oregon, Eugene, using an FEI Titan 30-800 with an acceleration voltage of 300 kV, corresponding to a resolution of 1.4 Angstrom as specified by the manufacturer.

4.3.4 Secondary Ion Mass Spectroscopy (SIMS)

Depth profiles of the chemical composition of SLs are determined with dynamic secondary ion mass spectroscopy (SIMS). The sample is irradiated with a primary ion beam whose intensity is so high that the atoms of the film are sputtered away as secondary ions that can be analysed in a mass spectrometer. This procedure yields a depth profile of the thin film. SIMS has been used for several years in our group to evaluate the quality of SL structure. A clear correlation between SL quality and sharpness of the depth profile was evident, e.g. from annealing experiments as shown in [162-p.176ff]. The Johnson group is also working with this method to evaluate nanostructured MLs [128].

In this work, the secondary ion mass spectrometry (SIMS) depth profiles were recorded using a Cameca SIMS 4500 with Caesium (Cs^+) primary ions at an impinging angle of 45° and detecting secondary ions of MCs^+ (with $M = \text{Bi, Sb, Te}$). Using Cs^+ ions results in a high secondary ion yield for the elements Bi, Sb and Te. For all sputtered SLs, the standard Cs^+ ion energy of 5 keV was used. For the strongly interdiffused ML structures shown in chapter 6, the ion energy was reduced to 1 keV to improve the visibility of the element oscillations. A way to check for validity of the results is the direct comparison of the ion signals. If there really is a ML structures in which the Bi and Sb contents vary, then the two ion signal intensities must behave complementary, e.g. a dip of one signal must be accompanied by a peak of the other. This was always the case for the observed nanostructures.

5 Bi₂Te₃ and Sb₂Te₃ thin films grown with an MBE setup by nanoalloying

The binaries Bi₂Te₃ and Sb₂Te₃ form the basic building blocks of the high-performance p-conducting SLs. Therefore, as a starting point comprehensive studies were carried out on the nanoalloying approach for compound binary films. Unless otherwise stated, all characterized films in this chapter were grown on BaF₂ substrates. The films characterized by TEM were grown on Si/SiO₂ substrates. Films grown on BaF₂ and Si/SiO₂ exhibit no significant differences in structural and transport properties [121].

5.1 Dependence of texture on deposition pattern and initial element layer thickness

The results reported in ref. [8] and the impact of the crystal orientation on the thermal stability of nanoscale multilayer structures [64] suggest that a strong degree of *c*-orientation seems to be a necessary prerequisite for creating V₂VI₃ ML structures with sufficiently sharp interfaces, low thermal conductivity and high ZT values. Experiments on sputtered nanoalloyed layers revealed a dependence of the degree of *c*-orientation on the initial element layer thickness [163]. To examine the influence of the thickness of the initial element layers on the crystalline orientation after annealing, thin films with different deposition patterns and element layer thicknesses were prepared and characterized. Two deposition patterns with different initial layer thicknesses were used (Figure 5.1). For the quintuple pattern, the element layer thicknesses were chosen to mimic the unit cells of Bi₂Te₃ and Sb₂Te₃ (space group: *R* $\bar{3}m$) with lattice parameter *c* of ~ 3 nm for Bi₂Te₃ and Sb₂Te₃ [67, 68]. Since Bi₂Te₃ and Sb₂Te₃ crystallize in a rhombohedral layered structure with three quintuple stacks with the sequence Te-M-Te-M-Te (M = Bi or Sb), an analogous quintuple deposition pattern corresponding to this structure was chosen. The exact thicknesses were adjusted such that three quintuples correspond to one unit cell of Bi₂Te₃ or Sb₂Te₃, resulting in individual element layer thicknesses of ~ 0.2 nm. Additionally, a simpler bilayer pattern was used where the elements were stacked in an alternating fashion with an element layer thickness ratio of 2:3 for M:Te. All element layer thicknesses were deposited to maintain the stoichiometric 40:60 ratio for M:Te of the respective compound. All films shown in this chapter were annealed isothermally at 250 °C for two hours.

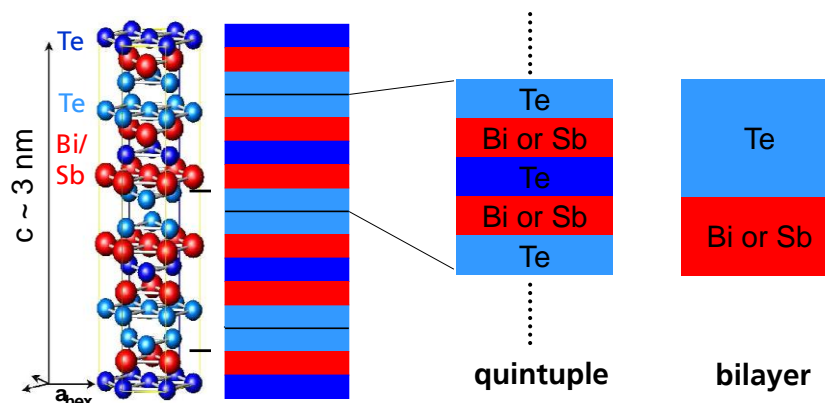


Figure 5.1 Quintuple and bilayer pattern used to deposit the initial element layers.

5.1.1 Bi₂Te₃

The nominal element layer thicknesses, chemical composition and in-plane transport properties are summarized in Table 5.1. The Te content deviated slightly from the intended 60 at. % due to

fluctuations of the effusion cell fluxes during growth (section 4.1.3.2). The total film thickness d of sample BT-Q determined from the SEM cross section after annealing was slightly larger than the thickness calculated from the nominal initial element layer thickness and the number of deposition periods.

Table 5.1 Bi-Te samples: Nominal element initial layer thickness for deposition patterns shown in Figure 5.1, chemical composition and room-temperature in-plane transport properties after annealing at 250 °C for 2 hours. Units: Te concentration c_{Te} in at. %, electrical conductivity σ in S/cm, carrier mobility μ in cm^2/Vs , carrier concentration n in cm^{-3} , Seebeck coefficient S in $\mu\text{V}/\text{K}$, power factor PF in $\mu\text{W}/\text{cmK}^2$, thermal conductivity λ in W/mK . d_{Te} : nominal thickness of Te initial layer in nm, d_{Bi} : nominal thickness of Bi initial layer in nm, d_{per} : total thickness of deposition pattern = period length in nm, N_{per} : total number of periods. d : total thin film thickness as determined by SEM cross sections in μm . A negative sign for n indicates electron conduction.

Deposition pattern (sample name)	d_{Bi}	d_{Te}	d_{per}	N_{per}	c_{Te}	d	μ	n	σ	S	PF
Quintuple (BT-Q)	0.2	0.2	1.0	999	59.1	1.17	77	-2.4×10^{19}	303	-168	9
Bilayer 1 (BT-B1)	0.4	0.6	1.0	999	60.6	1.03	58	-6.5×10^{19}	597	-140	12
Bilayer 2 (BT-B2)	0.9	1.2	2.1	500	61.5	1.04	39	-1.2×10^{20}	745	-113	10
Bilayer 3 (BT-B3)	1.7	2.4	4.1	250	60.9	0.95	81	-8.6×10^{19}	1105	-127	18

Bi_2Te_3 with the quintuple pattern showed the highest value for S of all samples. However, the conductivity was relatively low leading to small values for the PF . The highest PF ($18 \mu\text{W}/\text{cmK}^2$) was observed for the film with “thickest” initial layers that also exhibited the highest mobility and conductivity.

Figure 5.2 shows the XRD patterns of annealed Bi_2Te_3 samples. Rietveld analysis was carried out and the XRD data could all be fitted well using the Bi_2Te_3 structural model [67]. The refined lattice parameters and texture index are summarized in Table 5.2. The sizes of coherent scattering domains, i.e. the crystallite sizes (Table 5.2) do not increase with increasing element layer thickness. Diffuse scattering observed underneath the intensive Bragg peaks particularly in the samples BT-Q, BT-B1 and BT-B2 indicates disorder which was treated as modulated background during the fitting procedure. This local disorder may be due to small variations of chemical composition and/or strain. In this context, we note that an impurity nanoscaled Bi-rich phase was identified in nanoalloyed Bi_2Te_3 samples [164].

For sputtered nanoalloyed Bi_2Te_3 -based thin films with higher initial element layer thicknesses, it is known that the level of preferred c -orientation increases with decreasing element layer thickness [163]. However, the XRD data indicate that the present Bi_2Te_3 samples do not follow this fashion, which is apparent from the intensities observed for the (00.3), (00.6) and (00.15) Bragg reflections. The annealed Bi_2Te_3 film with the thinnest initial element layers exhibits the lowest level of preferred c -orientation. The calculated texture index implies that the preferred orientation level increases slightly when the initial layer thickness increases up to 0.9 nm/1.2 nm (Bi/Te) and increases sharply when the thickness is roughly doubled. Changing the deposition pattern from quintuple pattern to the bi-layer pattern while keeping the period unit of the deposition pattern constant at nominally 1 nm seems to have no influence on the texture of the thin films.

The formation of strongly c -oriented thin films can be achieved if the formation of the covalent/ionic Bi-Te or Sb-Te bonds takes place along the substrate normal such that layers of the same atoms are lying in parallel to the substrate plane. In this case, the basal plane of the unit cell is also lying parallel to the substrate plane. The observations made here indicate that, besides an upper limit observed on sputtering such films [163], there may exist a lower limit of the individual layer thickness below which a strong c -texture cannot be established. Johnson et al. have discussed the critical thickness of the initial element layers, stating that there exists a critical layer thickness below which diffusion of the elements is finished before interfacial reaction (i.e. crystallization) occurs [123]. In this situation, the interfaces between the elements serving as nucleation centers are absent and cannot act as a starting point for the growth of crystallites with the c -axis perpendicular to the element interfaces.

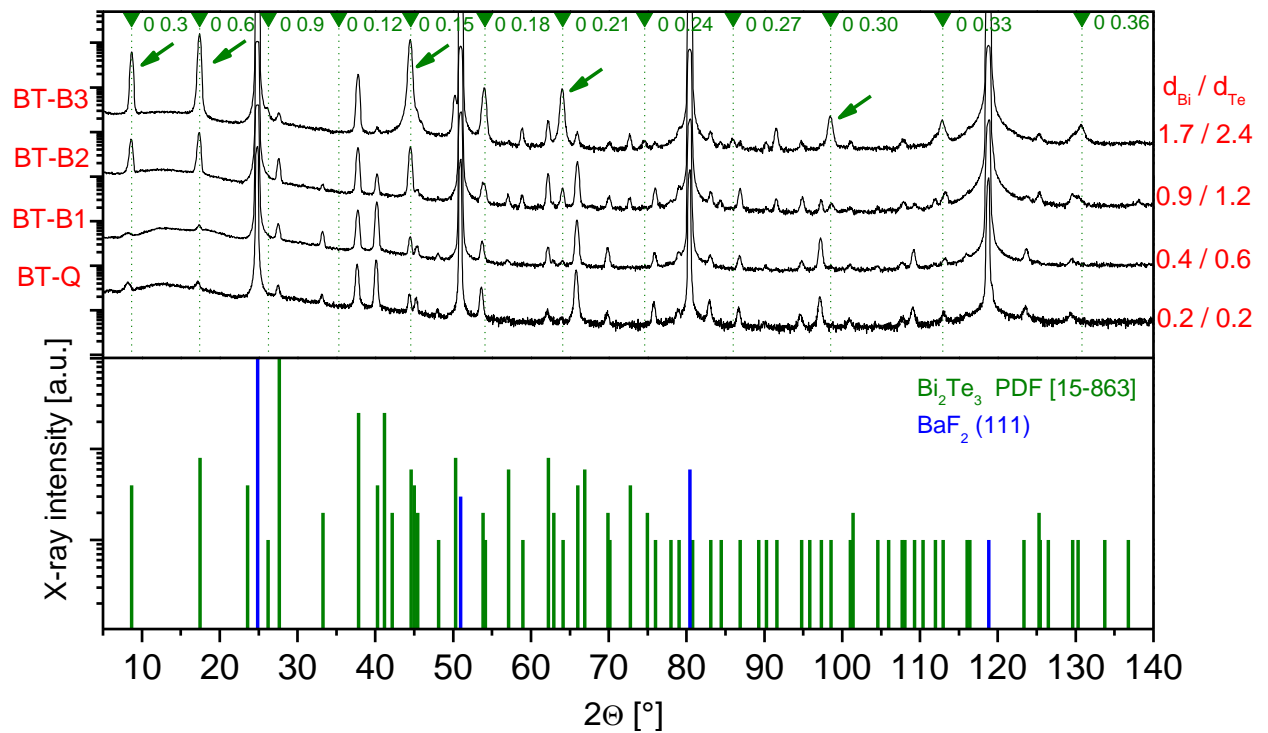


Figure 5.2 Diffraction patterns of annealed Bi_2Te_3 film samples. In order to deal with the intensive reflections from the BaF_2 single crystal substrate, the intensities are shown in logarithmic scale. The element layer thickness d_{Bi} and d_{Te} are given in nm and increase from bottom to top. (00.*l*)-reflections are indexed and indicated by dashed lines. Green arrows point to reflections that most clearly indicate the difference of film orientation. For comparison, a powder diffractogram (JCPDS database) is shown as vertical bars below the experimental patterns.

Table 5.2 Refined lattice parameters, orientation index from Rietveld analysis and the crystallite size of Bi-Te samples. Estimated standard deviations are given in parentheses. The crystallite size was calculated from the width of the (00.18) reflex (indicated by W) and through the Rietveld refinement (section 4.3.1.2, indicated by R).

Sample	a, b [Å]	c [Å]	Orientation Index	Crystallite size W / R [nm]
BT-Q	4.3894(5)	30.5693(10)	5(3)	27 / 110
BT-B1	4.3908(4)	30.5468(14)	6(2)	30 / 180
BT-B2	4.3862(3)	30.4908(14)	7(3)	25 / 170
BT-B3	4.3855(4)	30.5293(12)	14(3)	20 / 170

The change of orientation is also clearly seen in SEM cross-section images of cleaved edges of the samples (Figure 5.3). With increasing c -orientation, the grains tend to show a shape which resembles horizontal bars. These horizontal bars correspond to the typical appearance of Bi_2Te_3 crystallites (hexagonal platelets [42-p.62,165]) viewed perpendicular to the c -axis, i.e. parallel to the basal a - b plane (see also Figure 7.5). The sample with the highest degree of c -orientation shows the highest in-plane charge carrier mobility and the highest in-plane electrical conductivity (Table 5.1) as expected from the reported behavior of anisotropic bulk material whose electrical conductivity is higher perpendicular to the c -axis, section 3.3.

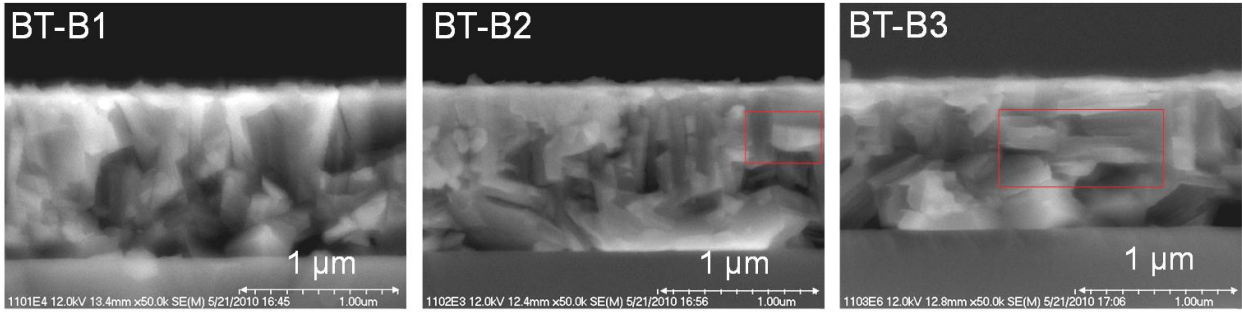


Figure 5.3 SEM cross sections of cleaving edge of annealed Bi_2Te_3 samples. Horizontal bar-shaped grains corresponding to hexagonal platelet shaped crystallites viewed parallel to the a - b plane (red boxes) can be observed in the samples with the highest degree of c -orientation (BT-B3).

A thorough texture analysis by high-energy XRD experiments carried out at the 6-ID-D high-energy station, APS, Chicago, on samples analogous to BT-Q revealed that the c -axis of the crystallites is tilted by up to 30° with respect to the growth direction, i.e. there is a preferential texture [166]. No epitaxial relation to the substrate was found.

One could speculate that the adaption of the total thickness of the element film deposition pattern to the unit cell length (lattice parameter c) might increase the c -orientation of the crystal. Thus, films with period lengths of 3.1 and 6.3 nm, corresponding to a whole and double unit cell length were grown. In comparison to the best c -oriented film BT-B3, no clear trend towards a stronger preferential orientation could be observed and reflexes different from $(00.l)$ were still strongly expressed. Increasing the rotation speed of the substrate rotator could potentially improve element layer homogeneity, providing a better base for c -oriented growth to start at the element layer interfaces. In fact, increasing the rotator speed from 10 to 25 rpm led to slightly more pronounced c -reflexes but the effect was small. Consequently, the transport properties of the films with adapted thickness and increased rotator speed did not differ significantly from the ones shown in Table 5.1.

5.1.2 Sb_2Te_3

For Sb_2Te_3 (ST) samples the element initial layer thickness, deposition pattern, chemical composition and transport properties are listed in Table 5.3. Figure 5.4 shows the corresponding XRD patterns.

Table 5.3 Sample properties of Sb-Te samples: Nominal element initial layer thickness for deposition patterns shown in Figure 5.1 together with chemical composition and room temperature in-plane transport properties after annealing at 250°C for 2 hours. Units as previously defined in Table 5.1. d_{Sb} = Sb initial element layer thickness in nm.

Deposition pattern (sample name)	d_{Sb}	d_{Te}	d_{per}	N_{per}	c_{Te}	d	μ	n	σ	S	PF
Quintuple (ST-Q)	0.2	0.2	1.0	999	61.1	1.11	402	3.0×10^{19}	1933	125	30
Bilayer 1 (ST-B1)	0.4	0.6	1.0	999	61.7	1.04	444	2.6×10^{19}	1815	129	30
Bilayer 2 (ST-B2)	0.8	1.3	2.1	500	58.5	0.98	119	9.7×10^{19}	1857	104	20
Bilayer 3 (ST-B3)	1.5	2.6	4.1	250	59.9	0.99	373	2.4×10^{19}	1450	142	29

The ST samples prepared in the current study via the nanoalloying approach are clearly among the best Sb-Te thermoelectric films reported (Table 3.4) even though the Seebeck coefficients are still lower than for films prepared via ion beam sputtering and co-evaporation.

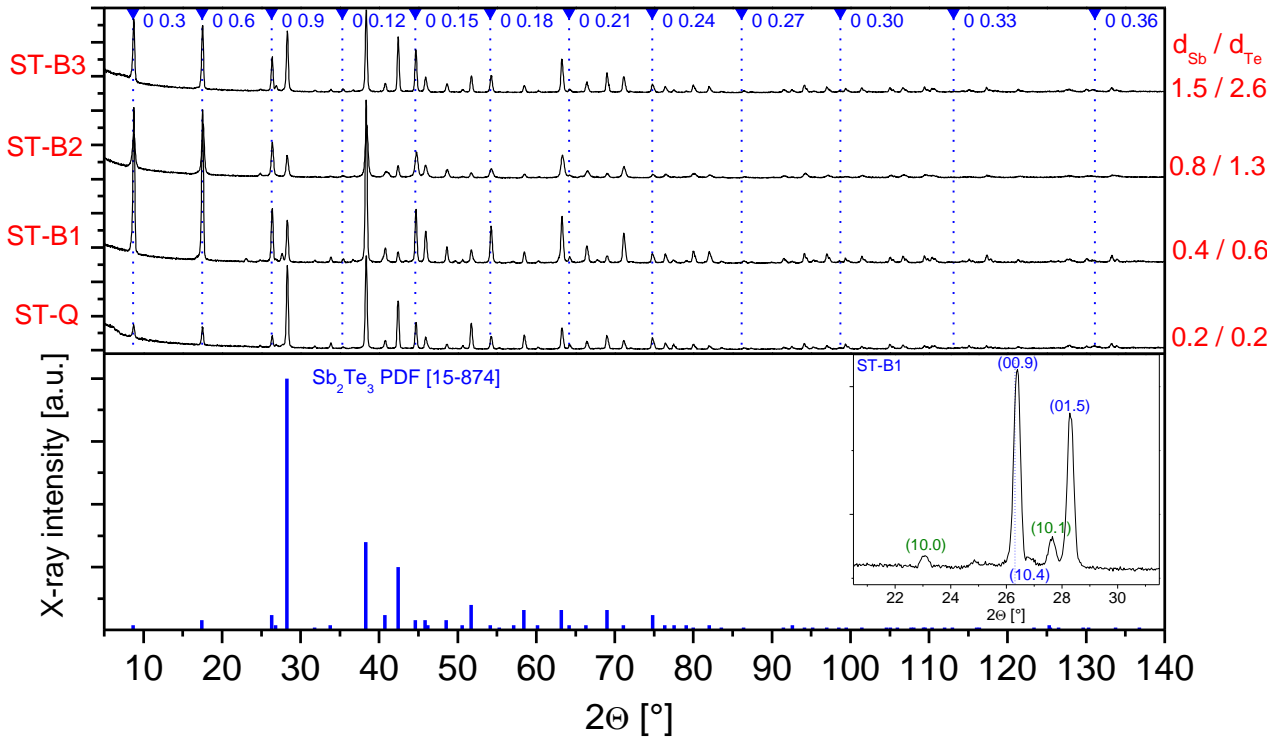


Figure 5.4 Diffraction patterns of Sb_2Te_3 for different deposition patterns and element initial layer thicknesses after annealing. The element layer thicknesses d_{Sb} and d_{Te} are given in nm and increase from bottom to top. (00.*l*)-reflections are indexed [68] and indicated by dashed lines. For comparison, a powder diffractogram (JCPDS database) is shown as vertical bars below the experimental patterns. Inset: Magnified section around $2\theta = 27^\circ$, sample ST-B1. Sb_2Te_3 reflexes indexed in blue, Te reflexes indexed in green.

Table 5.4 Refined lattice parameters, orientation index from Rietveld analysis and the crystallite size of Sb-Te samples. The crystallite size was calculated from the width of the (00.18) reflex (indicated by W) and through the Rietveld refinement (section 4.3.1.2, indicated by R). For unknown reasons, the mathematical calculation routine for the Rietveld refinement did not converge to reasonable values for sample ST-B2.

Sample	a, b [Å]	c [Å]	Orientation Index	Crystallite size W / R [nm]
ST-Q	4.26536(9)	30.4382(8)	61(11)	32 / 140
ST-B1	4.2638(2)	30.736(2)	2978(11)	32 / 130
ST-B2	-	-	-	21 / -
ST-B3	4.2640(1)	30.438(1)	1085(70)	29 / 120

All patterns expect for those obtained on Te-rich samples could be fitted with the Sb_2Te_3 structural model [66-p.179ff.] with refined cell parameters, texture indices and crystallite sizes being summarized in Table 5.4. All four samples exhibited a preferred c-orientation with sample ST-Q showing the lowest level of preferred orientation that was however still more pronounced than that of BT-Q. Using a bi-layer pattern with larger element initial layer thicknesses further increased the degree of c-orientation (sample ST-B1). However, the degree of c-orientation apparently does not depend on the initial element layer thickness in a monotonous fashion.

Concerning grain size, it is not sure if the Debye-Scherrer formula based calculation can be used here since grain sizes up to 100-200 nm are already at the upper limit for the application of the formula. Values obtained from the (00.18) reflex and the Rietveld refinement differ strongly since the crystallites formed by nanoalloying appear to be smaller along the c-direction (see also Figure 7.15 and Figure 5.5). Altogether, TEM cross sections taken on the samples should yield more accurate results and indicate that the grain size in Sb_2Te_3 (350-650 nm) is larger than in Bi_2Te_3 (150-350 nm) and no foreign phases are present [167], Figure 5.5). The Te concentration in the shown Sb_2Te_3 and Bi_2Te_3 film was 59.7 and 59.6 at. %, respectively.

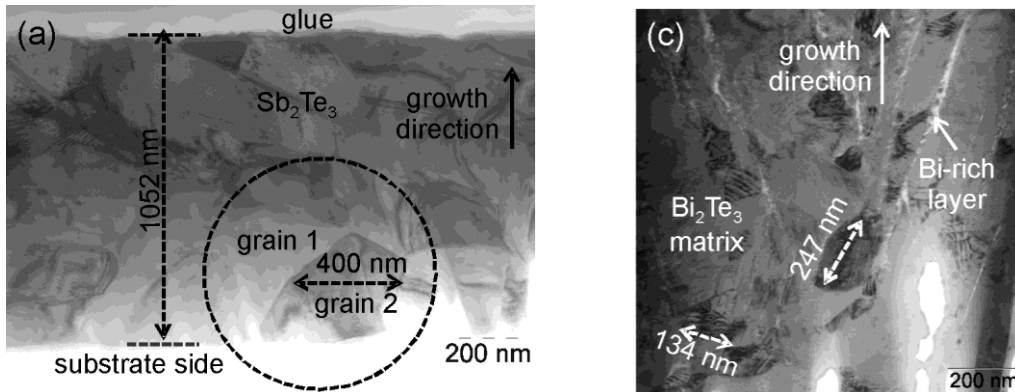


Figure 5.5 TEM images of nanoalloyed annealed Sb_2Te_3 (left) and Bi_2Te_3 (right) grown with the quintuple pattern.

The pronounced texture can also be observed in SEM cross-sections (Figure 5.6). Grains with a hexagonal shape lying parallel to the basal plane are most pronounced in sample ST-B1 with the highest degree of *c*-orientation. Comparable to Bi_2Te_3 , the sample with the highest degree of *c*-orientation has the highest charge carrier mobility. However, the samples cannot be compared straightforwardly as their compositions are slightly different. Extended texture analysis on a film analogous to ST-Q revealed that the *c*-axis is almost parallel to the growth direction with a maximum deviation of 10° [166]. No epitaxial relation to the substrate was found.

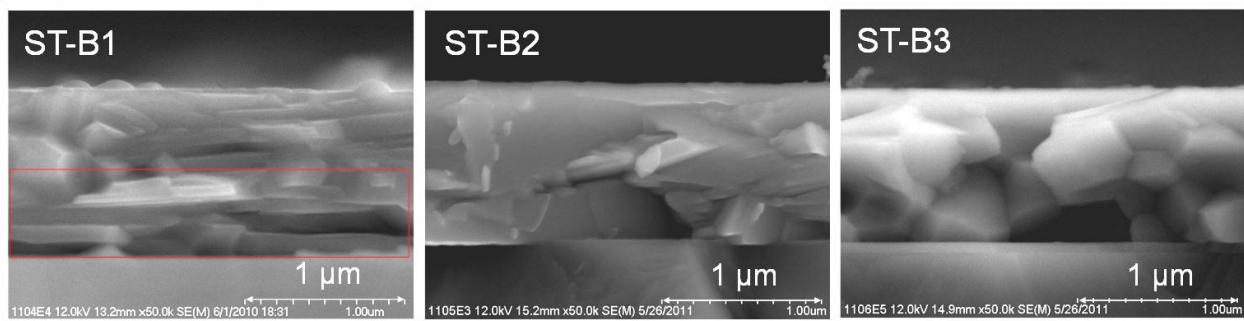


Figure 5.6 SEM images of Sb_2Te_3 cross sections. Horizontal bar-shaped grains corresponding to hexagonal platelet-shaped crystallites viewed parallel to the *a*-*b* plane (red boxes) can be observed in the samples with the highest degree of *c*-orientation (ST-B1).

In samples with Te excess reflexes that could be assigned to Te were found, for example on sample ST-B1. This is in agreement with the phase diagram of Sb-Te displayed in Figure 3.3 that shows that exceeding a Te content of 60 at. % results in a two-phase region where the phase Sb_2Te_3 and pure Te coexist. From the FWHM of the (10.1) reflex at $2\theta = 27.6^\circ$ and using eq. 4.21, a Te grain size of ca. 30 nm is estimated.

Finally, similar experiments as described for Bi_2Te_3 (matching element layer thicknesses to multiples of unit cell length and increasing substrate rotator speed) were carried out for Sb_2Te_3 . Adapting the total stack thickness to the unit cell length did not improve *c*-orientation. Increasing the substrate rotator speed led to a slight increase in *c*-orientation, yet the effect was weak. Overall, the results were similar to the ones obtained for Bi_2Te_3 .

5.2 Dependence of transport properties on Te content

5.2.1 Bi_2Te_3

The dependence of the electrical properties on the Te content of the nanoalloyed film samples is presented in Figure 5.7. Data from films fabricated with the quintuple deposition pattern as well as with the binary pattern with different initial layer thicknesses are shown.

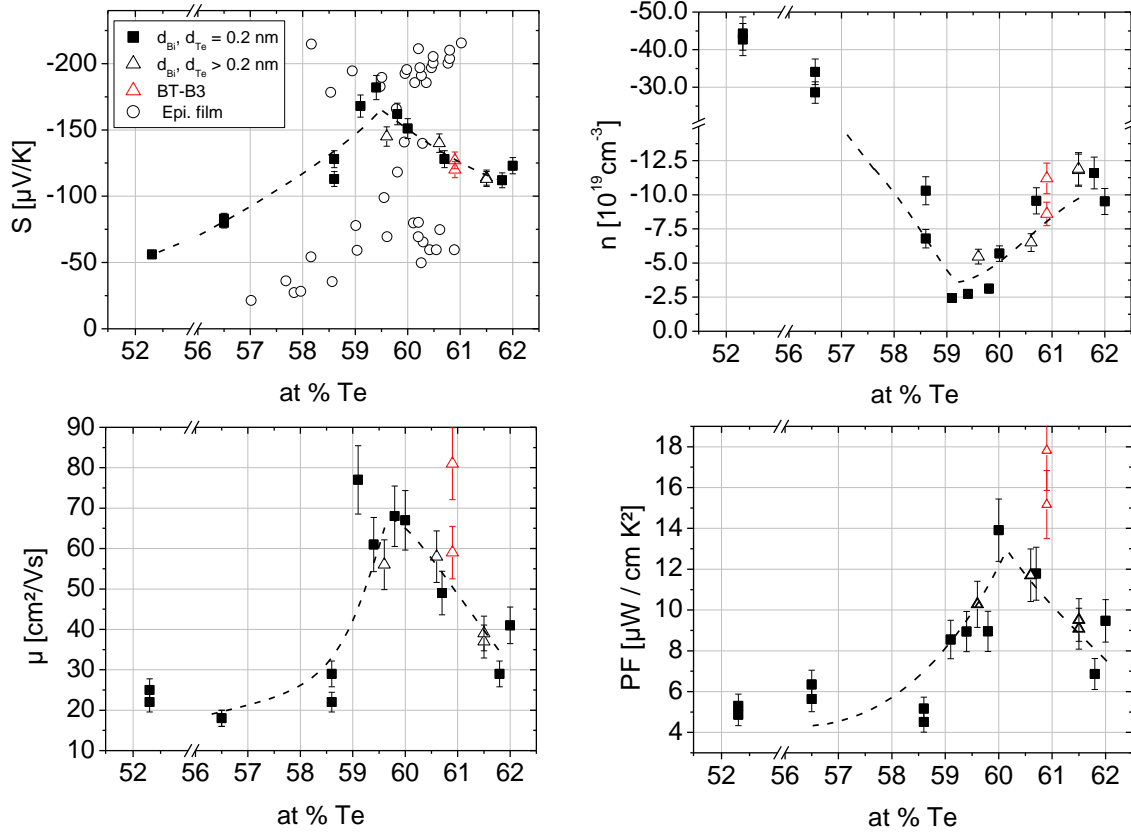
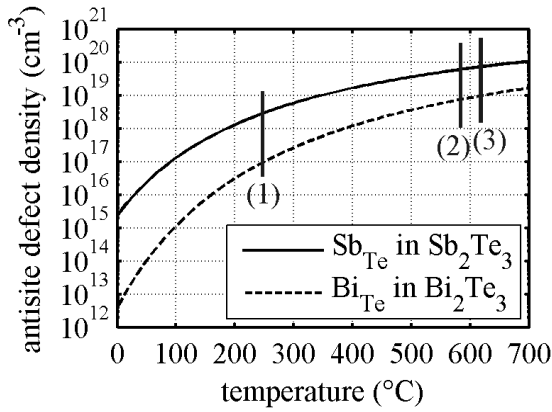


Figure 5.7 Electrical properties of nanoalloyed annealed Bi_2Te_3 in dependence of Te content. Full black squares: Nanoalloyed thin films with element initial thickness of 0.2 nm (quintuple pattern). Empty triangles: Nanoalloyed thin films with element initial thickness $> 0.2\text{nm}$ (bi-layer pattern). Note that the data represented by red triangles cannot be directly compared to the data on the other films since the associated films (BT-B3) exhibit a significantly stronger c-orientation, affecting mainly μ and PF. Empty circles: Data from ref. [95] for MBE epitaxial thin films. A negative sign of n indicates electron conduction. Dashed line: Eyeguide.

All films exhibit n -type conductivity even for an excess of Bi in contrast to bulk materials where an excess of Bi generally leads to p -type conduction. The majority of publications on Bi_2Te_3 thin films also reports that only n -type conducting Bi_2Te_3 could be observed, details are given in section 3.4 and Table 3.4.

As was pointed out in [166,167] there are strong indications that the point defect physics is governed by deposition temperature. Generally, thin film growth processes occur at much lower temperatures than bulk crystal growth processes. It may be concluded that besides antistructure defects which are usually seen as the main cause for the generation of electrons, other defect mechanisms may play a role in determining the sample properties. To illustrate this fact, Figure 5.8 shows a plot of Bi_{Te} and Sb_{Te} antisite defect density in Bi_2Te_3 and Sb_2Te_3 vs. deposition temperature.



$$\mu_{Bi_{Te}} \approx -k_B T_M \left[\ln \left(\frac{n_{Bi_{Te}}}{N_{Te}} \right) + 1 \right] \quad (5.1)$$

where

$\mu_{Bi_{Te}}$ = formation energy of antisite defect

T_M = Melting temperature

$n_{Bi_{Te}}$ = Antisite defect density

N_{Te} = Concentration of Te atoms per unit volume

Figure 5.8 and eq. 5.1 Left: Antisite defect densities of Bi₂Te₃ and Sb₂Te₃ in dependence on temperature [167]. The vertical lines indicate (1) the annealing temperature of 250 °C for nanoalloying, (2) the congruent melting point of Bi₂Te₃ at 585 °C, and (3) the congruent melting point of Sb₂Te₃ at 617 °C. Right: Relation given in [80] used for calculation.

Lower temperatures yield significantly lower densities of antisite defects and thus reduced carrier densities. An experimental confirmation is given by the low antisite density in low-temperature fabricated (i.e. thin film) Sb₂Te₃ compared to bulk material [167], section 5.2.2. The carrier concentrations of $\sim 3\text{-}4 \times 10^{18} \text{ cm}^{-3}$ predicted by eq. 5.1 are close to the experimentally obtained minimum values of $\sim 1\text{-}2 \times 10^{19} \text{ cm}^{-3}$ (Figure 5.10). For Bi₂Te₃, the antisite defect density at the growth temperature of 250 °C likely is so low that other electron-generating defects not included in the "antisite only" model overwhelm the effects of the antisites. These effects could be of the following nature: When deviating from the stoichiometric composition towards higher Bi contents, from the phase diagram of Bi-Te it can be assumed that in addition to Bi₂Te₃, the formation of Bi and the phase BiTe (layered phase consisting of Bi-Te quintuples and Bi₂ layers, see section 3.2 takes place. Both phases are strongly n-conducting with low Seebeck coefficients (BiTe: $\sim -50 \mu\text{V/K}$, Bi: -20 to $-70 \mu\text{V/K}$ according to Figure 3.4 and [11]). It is well possible that these n-type phases are formed instead of the hole-generating point defects. This suggestion is in conformance with TEM experiments [166]: For a sample with 40.5 at. % Bi grown with a quintuple pattern analogous to BT-Q, a nanoscale Bi-rich secondary phase was found at the grain boundaries (Figure 5.9). Altogether, the TEM experiments indicate that grain boundaries act as sinks for point defects.

Plotting the obtained Seebeck coefficients vs. the logarithm of the carrier concentration provides useful information. If a linear relationship exists, one can conclude from the Pisarenko relation (eq. 2.9) that the basic transport parameters such as effective (DOS) mass, scattering type etc. remain the same for all samples, i.e. there is no change in sample composition that leads to another compound dominating the transport property measurement. Evidently, this is the case for the samples examined here (Figure 5.9), the data points agree well with a linear fit of S vs. the logarithm of n . At high carrier concentrations $> 2 \times 10^{20} \text{ cm}^{-3}$ (films with strong Bi excess) there appears to be a slight deviation from the straight line, meaning that other compounds besides Bi₂Te₃ may start to influence the transport properties.

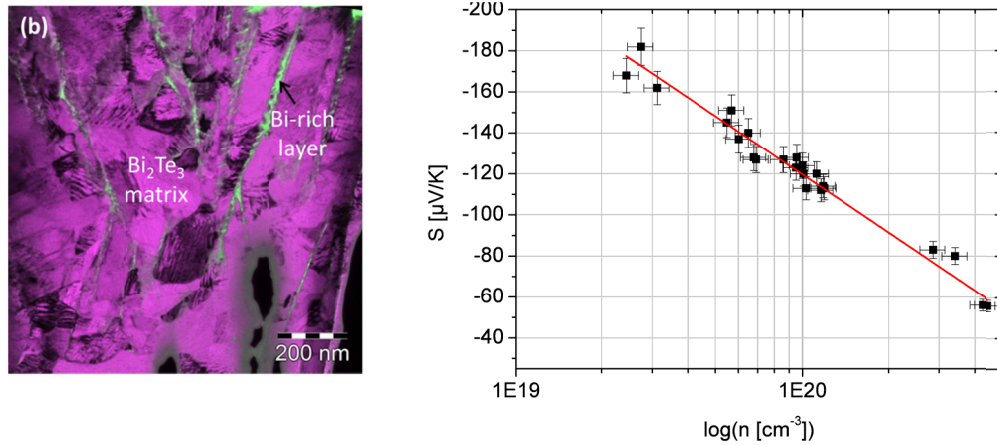


Figure 5.9 Left: TEM image of Bi-rich layers in a nanoalloyed annealed Bi₂Te₃ thin film (Si/SiO₂ substrate) [166]. Right: Seebeck coefficient in dependence of the logarithm of carrier concentration together with Pisarenko fit (red line).

The variations of the Seebeck coefficients of the films (Figure 5.7) as function of Te content are compared with data for thin films [95-p.60] grown on BaF₂ by MBE at different substrate temperatures. Especially in the concentration range of 60-61 at. % Te a pronounced scattering of the epitaxial film data is observed. The Te sticking coefficient strongly depends on the substrate temperature (Figure 4.1). In contrast, the nanoalloyed layers are grown on cold substrates around room temperature while the actual compound formation takes place in a controlled annealing environment after deposition with a negligible evaporation of Te, allowing an easier control of stoichiometry and properties.

Comparing films with similar orientation one finds that generally the highest charge carrier mobilities, Seebeck coefficients and power factors and the lowest charge carrier concentrations are achieved at around ~59-60.5 at. % Te, close to stoichiometric Bi₂Te₃. The mobilities are lower than for epitaxial Bi₂Te₃ films grown on BaF₂ by MBE [100,95]. One reason for the reduced μ may be the presence of the mentioned secondary phase at the grain boundaries which has not been observed in TEM images on epitaxially grown samples [168]. In the latter, μ is as high as ~150 cm²/Vs up to n of ~ 5.5×10^{19} cm⁻³.

The cross-plane thermal conductivity of sample BT-Q was found as low as 0.4 W/mK, which is among the lowest value ever reported for Bi₂Te₃ and significantly lower than in single crystalline bulk material ($\lambda \sim 1$ W/mK parallel and 2-3 W/mK perpendicular to c -axis, section 3.3). A reasonable explanation for the low λ is the presence of the mentioned nanoscale secondary phase at the grain boundaries.

The cross-plane ZT value of sample BT-Q can be estimated by combining the electrical in-plane electrical properties and the cross-plane thermal conductivity taking into account the anisotropy present in the material for the electrical conductivity while the Seebeck coefficient is assumed to be isotropic (section 3.3). Hence, an upper limit for ZT of 0.7 is estimated assuming an anisotropy factor of 1, i.e. the electrical conductivity in in-plane/cross plane direction is identical which would be the case for random crystal orientation. A lower limit for ZT of 0.17 is obtained if the films are assumed to be exclusively c -oriented, resulting in an anisotropy factor of 4 (this is the value for n -type bulk material with a Te concentration that lies closest to that of the films [90]). The real value of ZT is expected to be between these two values. A more accurate definition of the cross-plane ZT for the thin films requires the determination of the Seebeck coefficient and electrical conductivity in cross-plane direction. Further efforts are under way to enable this type of sophisticated characterization.

A comparison of the data of the off-stoichiometric Bi₂Te₃ samples with those reported in literature is not straightforward because different deposition techniques, film thicknesses and substrate deposition temperatures were used in the different studies. The data are summarized in section 3.4. In comparison to other deposition methods, particularly epitaxy, the best achieved power factor of ~ 18 $\mu\text{W/cmK}^2$ is quite low. The main reason for this is the relatively low carrier mobility. Additionally, the Seebeck coefficient of the nanoalloyed films has a sharp maximum of ~ -180 $\mu\text{V/K}$ at 59.5 at. % Te and is very sensitive to deviation from stoichiometry. A deviation of stoichiometry of only ~ 1 at. % from 59.5 at. % Te results in a sharp drop of S to ca. -130 $\mu\text{V/K}$. The films deposited with other methods seem to be more tolerant to compositional deviations from stoichiometry, see e.g. Table 3.4 and some of the epitaxial films shown in Figure 5.7.

5.2.2 Sb₂Te₃

The electrical properties of Sb₂Te₃ films as a function of Te content are shown in Figure 5.10. As expected, all Sb₂Te₃ films exhibited *p*-type conduction. The Seebeck coefficient rises up to 60 at. % Te and remains roughly constant with a slightly rising tendency for higher Te contents, significantly exceeding typical values for bulk materials (maximum ~ 110 $\mu\text{V}/\text{K}$ according to [90], Table 3.2). The obtained values are similar to films synthesized by co-deposition on a hot substrate [110]. The rise of *S* with increasing Te content was also reported for bulk materials, albeit with generally lower values of *S* (Figure 3.4). Correspondingly to the Seebeck coefficient, the charge carrier concentration drops sharply at ~ 60 at. % Te and in contrast to Bi₂Te₃ also remains at the same level for larger Te contents.

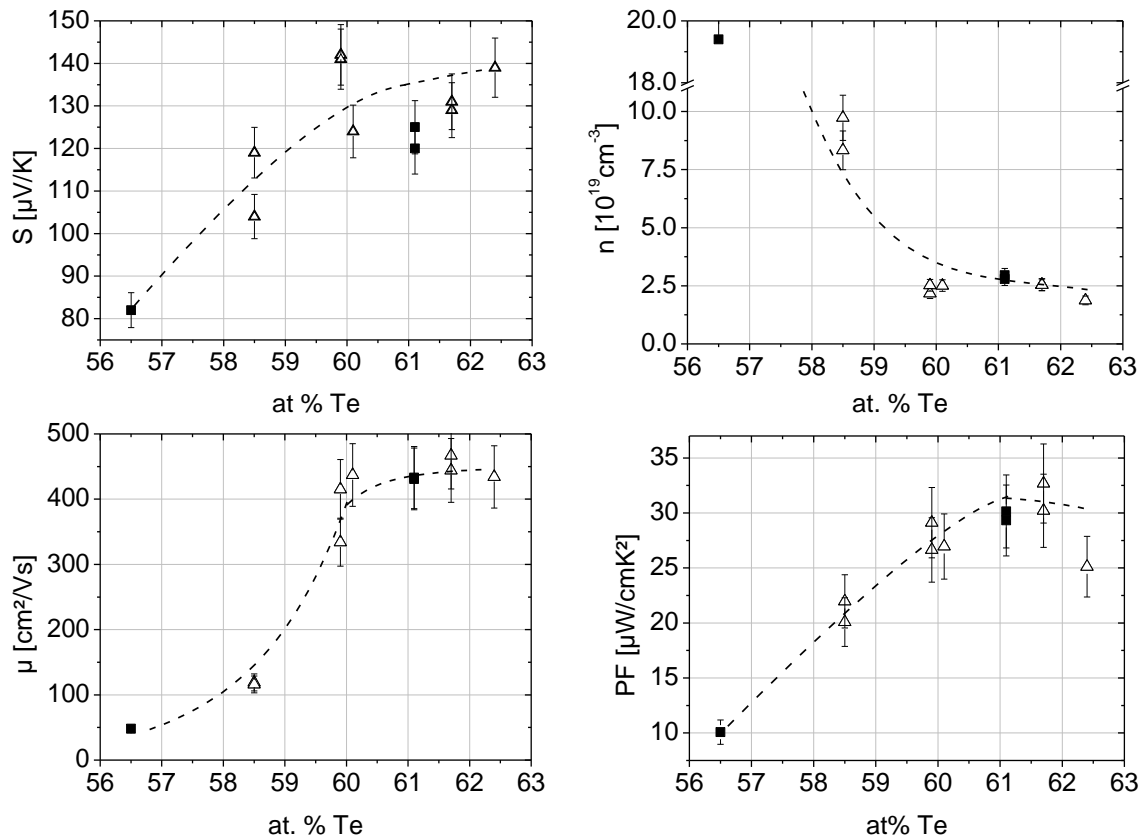


Figure 5.10 Electrical properties of nanoalloyed annealed Sb₂Te₃ films as function of Te content. Full squares: Nanoalloyed thin films with element initial thickness of 0.2 nm (quintuple pattern). Empty triangles: Nanoalloyed thin films with element initial thickness > 0.2nm (bi-layer pattern). Dashed lines: Eyeguide.

From the appearance of Te reflexes in the XRD patterns (Figure 5.4), one may conclude that the excess Te (in contrast to Bi₂Te₃) does not form electron-generating Te_{sb} antisites but instead precipitates into relatively large crystallites. Te as an element is an intrinsic semiconductor with low electrical conductivity (2-3 S/cm [169]). The Te excess has a small, but noticeable effect on the transport properties, as can be inferred from the Pisarenko plot presented in Figure 5.11: Films with a Te excess show a different *S/n* relationship than films with a Te deficit.

The drastic change of the electrical transport properties for Te contents ≥ 60 at. % is also observed in the pronounced increase of carrier mobility. Strikingly high μ of more than 400 cm^2/Vs were achieved despite the polycrystalline nature of the film, exceeding typical μ reported for thin films and even that of single crystalline bulk materials of 313 cm^2/Vs , Table 3.2. It is noted that only very recently higher room temperature carrier mobilities of ~680 cm^2/Vs were published by Wang et al. [65] while for decades the record for epitaxially grown films was at 350 cm^2/Vs , Table 3.4. The high μ compared to bulk material can be explained as follows: Due to the presence of a large number of Sb_{Te} antistructure defects, for Sb₂Te₃ bulk materials the minimal *n* is usually much larger than that attained in this work for Te

contents beyond 60 at. %. Hence, the relatively low carrier concentration in the nanoalloyed samples is likely associated with a lower number of Sb_{Te} antistructure defects and as a consequence a reduced defect scattering of carriers compared to bulk materials. Additionally, carrier-carrier scattering is reduced due to the lower n . With increasing Te content, the high μ accompanied by the large S translates to high PFs of about $30 \mu\text{W}/\text{cmK}^2$ in the nanoalloyed samples with a Te content ≥ 60 at. % which is not much lower than the values of single crystals. The electrical conductivity is generally high and does not show a clear dependence on Te content (Figure 5.11).

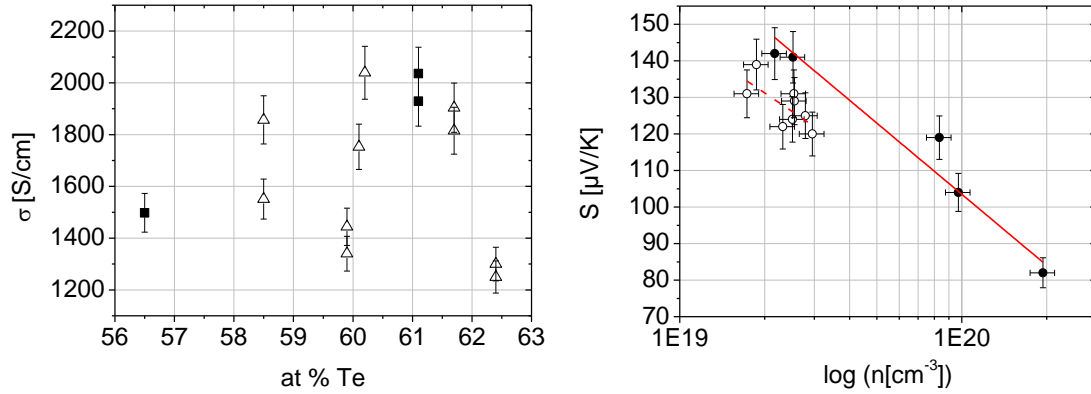


Figure 5.11 Left: Electrical conductivity in dependence on Te content of Sb_2Te_3 . Right: Seebeck coefficient in dependence of the logarithm of carrier concentration together with Pisarenko fit (red lines). Empty squares, dashed line: samples with Te excess. Full circles and full lines: Samples with Te deficiency.

For sample ST-Q, a thermal conductivity of $1.6 \text{ W}/\text{mK}$ was determined. This value is between the λ obtained for single crystalline bulk material of about $0.9\text{-}1.4 \text{ W}/\text{mK}$ parallel and ca. $5\text{-}7 \text{ W}/\text{mK}$ perpendicular to the c -axis (Table 3.2). The similarity to the λ of bulk material can be explained by the fact that 1.) nanoalloyed Sb_2Te_3 with its large grains (size of $350\text{-}650 \text{ nm}$ determined by TEM, Figure 5.5 from [164]) exhibits a low degree of grain boundary scattering and electrical conductivity that is close to bulk single crystalline material and 2.) in the analysed near-stoichiometric sample no foreign phases were found in the TEM analysis. ZT can be estimated with the same assumptions used for Bi_2Te_3 . An upper and lower limit for cross-plane ZT of 0.6 and 0.14 were obtained for an anisotropy ratio of 1 and 4 , respectively.

5.3 Electrical and structural properties in dependence on temperature

To monitor annealing effects on the properties of Bi_2Te_3 and Sb_2Te_3 films fabricated by nanoalloying, the electrical conductivity and Seebeck coefficient of two binary thin films deposited using the quintuple pattern (sample sets BT-Q and ST-Q) were determined in the un-annealed state as a function of temperature for several “incremental” heating/cooling cycles in combination with a temperature-dependent XRD analysis. The results obtained by this combined approach can also be used for finding the optimum annealing conditions for each respective compound.

Temperature-dependent XRD patterns (Figure 5.12) show that crystallization of both compounds starts and finishes at similar temperatures of around $100 - 120 \text{ }^\circ\text{C}$, evidenced by the disappearance of element-related reflexes and the appearance of compound reflexes. This is also reflected in the electrical properties (Figure 5.14). In the as grown state, the Bi-Te sample consists of a mixture of Bi_2Te_3 , Bi and Te (Figure 5.12 and Figure 5.13). The sample has metallic properties due to the presence of n -conducting Bi which dominates the electrical properties due to its high metal-like conductivity. At $\sim 100 \text{ }^\circ\text{C}$, S exhibits a drastic increase while the conductivity drops sharply. After the first heating/cooling cycle no further changes can be observed for the following heating/cooling cycles. The early stabilization of the properties is in accordance with results obtained by standard isothermal annealing (section 5.2). In a long-time annealing experiment, an annealing time of 72 h yielded no significantly different results

compared to a standard annealing time of 2 h (with only the mobility being higher by about 40 %), indicating that a general stabilisation of properties should take place in under 2 h.

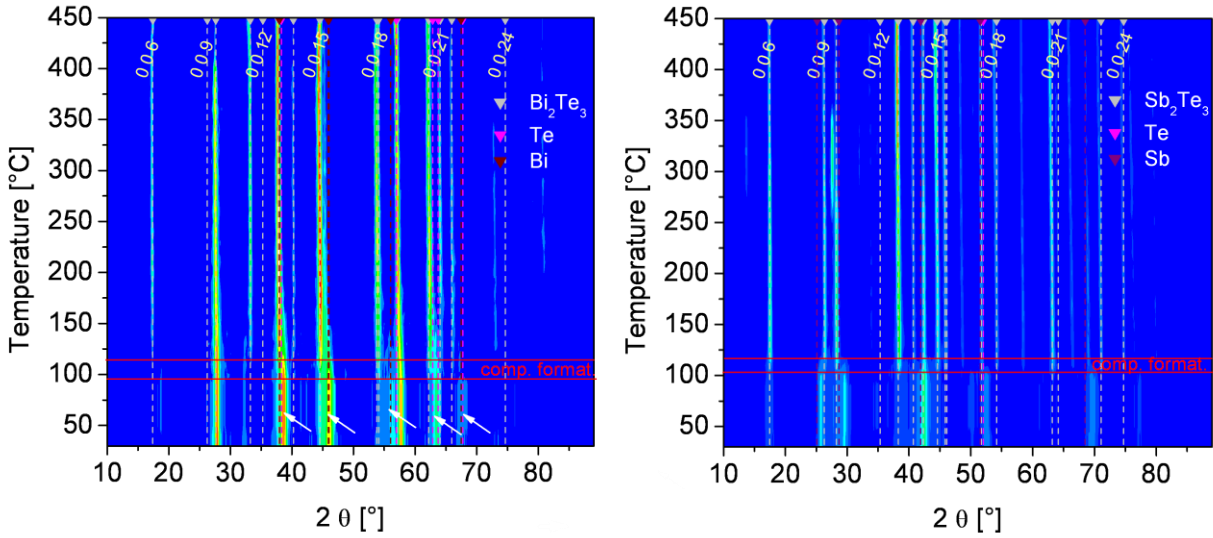


Figure 5.12 Temperature resolved XRD patterns of Bi_2Te_3 (left) and Sb_2Te_3 (right), quintuple deposition pattern. The X-ray intensity is color-coded (going from low to high: blue, green, yellow, orange, red). The temperature regime at which the compound formation starts and is completed is indicated by red horizontal bars. Further increase of the temperature results in a narrowing of the reflections. White arrows indicate element reflexes. Reflections that can be assigned to certain elements or compounds are indicated by dashed vertical bars. For the sake of clarity, only compound (00.l) reflections are indexed.

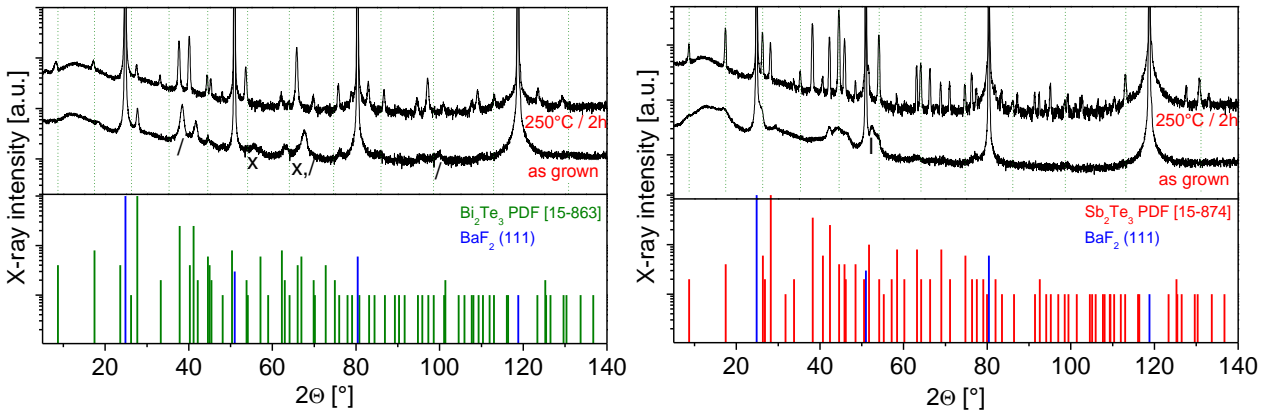


Figure 5.13 Room-temperature XRD patterns of Bi_2Te_3 (left) and Sb_2Te_3 (right), as grown and annealed, quintuple deposition pattern. Compound (00.l) reflections are indicated by dashed vertical bars. In as-grown Bi_2Te_3 , compound reflexes as well as additional element reflexes ($x = \text{Bi}$, $l = \text{Te}$) can be identified. As-grown Sb_2Te_3 has a rather amorphous character and broad reflexes make the identification of single elements and the compound difficult. XRD patterns were also recorded for Si/SiO_2 substrates and showed almost exactly the same features [121].

After the first heating cycle, the formation of Bi_2Te_3 is obviously complete and the thin film shows a typical semiconducting behaviour, i.e. the conductivity increases with increasing temperature. A decrease of the Seebeck coefficient for increasing temperature indicates the generation of additional charge carriers which may either be caused by the onset of intrinsic conduction (which is assumed to occur for the decrease of the Seebeck coefficient after reaching the temperature where it is maximal [170]) or defect-generated impurity levels. The “flattening” of the data near room temperature shows that the maximum of S is near room temperature, suggesting that the mentioned carrier generating mechanisms start becoming relevant at this temperature. Similar observations were made on epitaxial Bi_2Te_3 films with comparable n [42-p.75f.]

The Sb-Te sample shows a different behaviour. In the as grown state, the XRD pattern is typical for an amorphous material, which can also be seen in a $\theta/2\theta$ pattern collected at room temperature (Figure

5.13). The reflections are rather broad and an assignment to a specific element is difficult. A pronounced increase of σ is observed at 100 °C, indicating crystallization of the compound while S starts to increase at 120 °C. With each heating/cooling cycle, S decreases, suggesting an increase of n since, generally, $S \propto \ln(1/n)$ (eq. 2.9). This is likely induced by an evaporation of Te from the sample in the measurement setup which, unlike the standard annealing system, does not provide a Te-rich atmosphere. According to EDX analysis the sample contains 60.5 at. % Te in the as grown state. The carrier concentration increases sharply when the Te content drops below 60 at. % (Figure 5.10), indicating that a small evaporation of Te has drastic effects on the electrical properties. σ increases with each heating/cooling cycle which can be partly traced back to this increase of n , but certainly also to an increase in μ due to grain growth. Overall, the temperature dependent behaviour of the Sb-Te sample is influenced by different annealing effects like grain growth, phase formation, and evaporation of Te and shows no stabilization even after the third heating/cooling cycle.

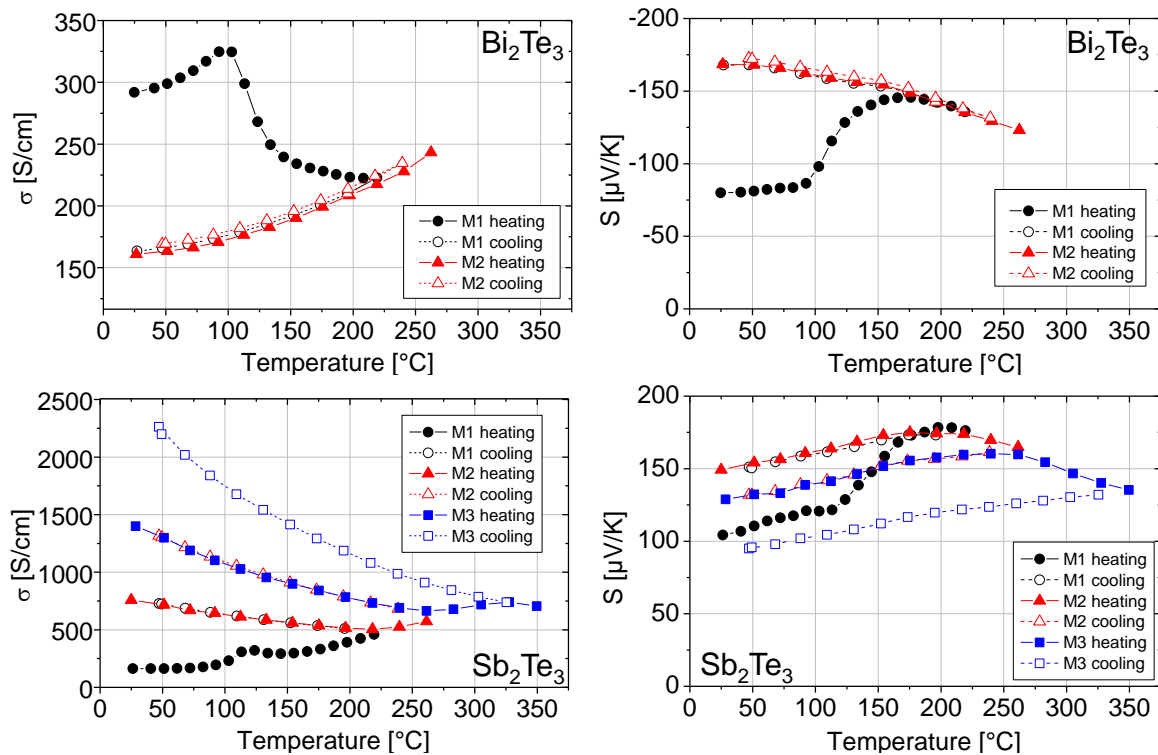


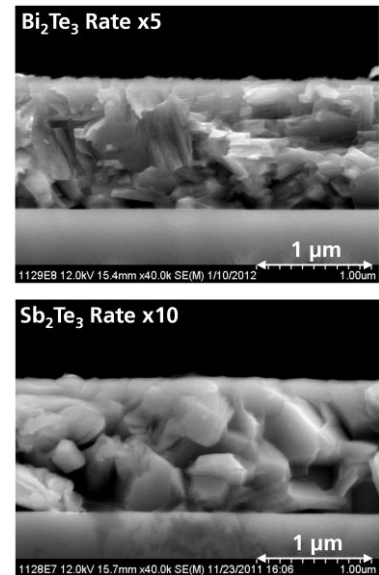
Figure 5.14 Seebeck coefficient and electrical conductivity in dependence on temperature. Top: Bi_2Te_3 , bottom: Sb_2Te_3 . The measurements were carried out for several heating/cooling cycles (M1, M2 and M3).

5.4 High-rate deposition experiments

In order to monitor the influence of deposition rate on film properties, the films with the thickest element layers, i.e. Bi_2Te_3 (Sb_2Te_3) with 2.6 / 3.7 nm Bi/Te (2.3 / 3.9 nm Sb/Te) were regrown with deposition rates increased five- and tenfold (by increasing effusion cell temperatures), resulting in growth rates of $\sim 3 \mu\text{m/h}$ for Sb_2Te_3 and $\sim 4 \mu\text{m/h}$ for Bi_2Te_3 . These rates are quite high in comparison to typical rates reported in literature for co-deposited films, see e.g. [101,105,108,109] - only PLD-grown films exceed growth rates of $\sim 4 \mu\text{m/h}$. Remarkably, the electrical properties of the films did not degrade noticeably upon increasing the growth rate and only a very small increase in film roughness was observed (Table 5.5 with image). This is in contrast to conventional hot co-deposition where a too high deposition rate results in only partial formation of the desired compounds from the elements. Due to the negligible change in transport properties, it is anticipated that the deposition rate can be increased even more, opening a path for cost- and time-efficient film fabrication.

Table 5.5 and **Figure 5.15**: Electrical transport parameters and cross sections of films grown with increased deposition rate. Units as previously defined in Table 5.1. A negative sign of n indicates electron conduction.

Sample	Flux rate	c_{Te}	d	μ	n	σ	S	PF
Bi ₂ Te ₃	1 x	59.9	1.04	-59	-6.0×10^{19}	564	-137	11
Bi ₂ Te ₃	5 x	59.8	1.12	-61	-6.1×10^{19}	599	-142	12
Bi ₂ Te ₃	10 x	60.0	1.24	-49	-5.0×10^{19}	387	-161	10
Sb ₂ Te ₃	1 x	62.4	1.09	434	1.9×10^{19}	1300	139	25
Sb ₂ Te ₃	5 x	61.5	1.11	438	2.0×10^{19}	1400	140	27
Sb ₂ Te ₃	10 x	60.2	1.14	375	2.3×10^{19}	1395	143	29



5.5 Two-zone high-temperature annealing experiments with Bi₂Te₃

As will be shown in chapter 6, compensation effects due to different carrier types of single layers in a Bi₂Te₃ / Sb₂Te₃ ML stack severely degrade the thermoelectric performance of the ML films. The problem originates from the carrier type of Bi₂Te₃ (section 5.2.1). No hole conduction can be achieved under the described experimental conditions. The hypothesis that the defect chemistry is strongly affected by annealing temperature (Figure 5.8) could be confirmed by high-temperature two-zone annealing experiments as described in section 4.1.5.2 using Figure 4.11, carried out on three as-grown Bi-Te samples from different growth runs with different Te contents. The annealings were carried out for 2 h, except for the 500 °C annealing (24 h). Remarkably, the attained Te contents were equal for all samples at 450 °C and 500 °C and corresponded very well (deviation of max. 0.2 at. %, smaller than EDX uncertainty) to the expected content of 59.9 at. %, giving experimental proof that the proposed two-zone annealing method can indeed be used to precisely adjust the Te content in Bi₂Te₃ samples.

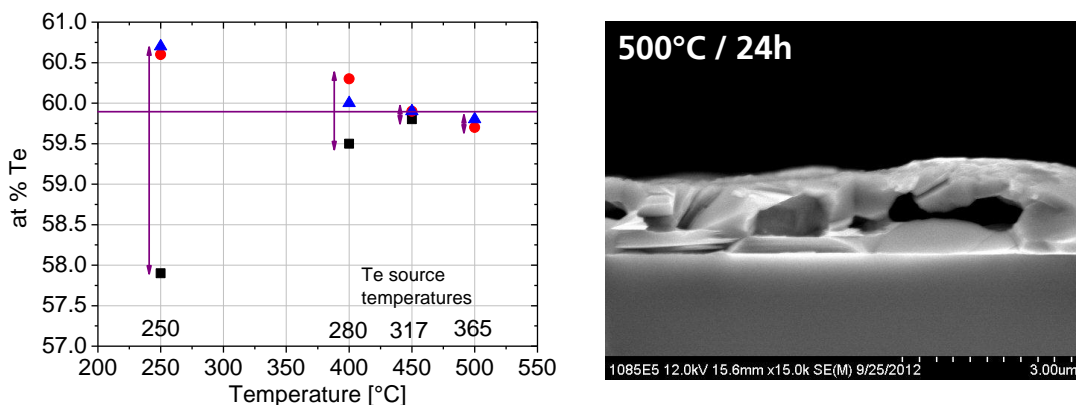


Figure 5.16 Left: Te concentration in dependence on annealing temperature for Bi₂Te₃. With increasing annealing temperature, the Te content of all 3 samples equalizes to the value of 59.9 at. % indicated by the purple horizontal bar and predicted by the two-zone annealing diagram. Black square: Sample 1, red circle: Sample 2, blue triangle: Sample 3. Right: Cross-section of sample 3 after annealing at 500 °C / 24 h.

The transport data (Figure 5.17) reflect the defect structure in dependence on annealing temperature. The samples are strongly n-conducting at 250 °C and then get into the zone of mixed conduction at 400 – 450 °C. This is indicated by the deviation from the Pisarenko line (Figure 5.9), i.e. one or more samples has a low S and a contradicting n . The films finally become clearly and distinctly p-conducting at 500 °C (i.e. a sufficient number of holes was generated as majority charge carriers) with high S over 170 $\mu\text{V/K}$ at n of $4\text{--}5 \times 10^{19} \text{ cm}^{-3}$. However, due to the low carrier mobility, the power factors are low. Using XRD it was verified that the film indeed consisted solely of Bi₂Te₃ so that no other phase could be the reason for the low carrier mobility. Instead, this effect is most likely caused by the rough and porous morphology of the samples induced by solid-state recrystallization induced at this high temperature (Figure 5.16). At 500 °C, film sample 1 was so brittle that no measurement of the electrical properties was possible.

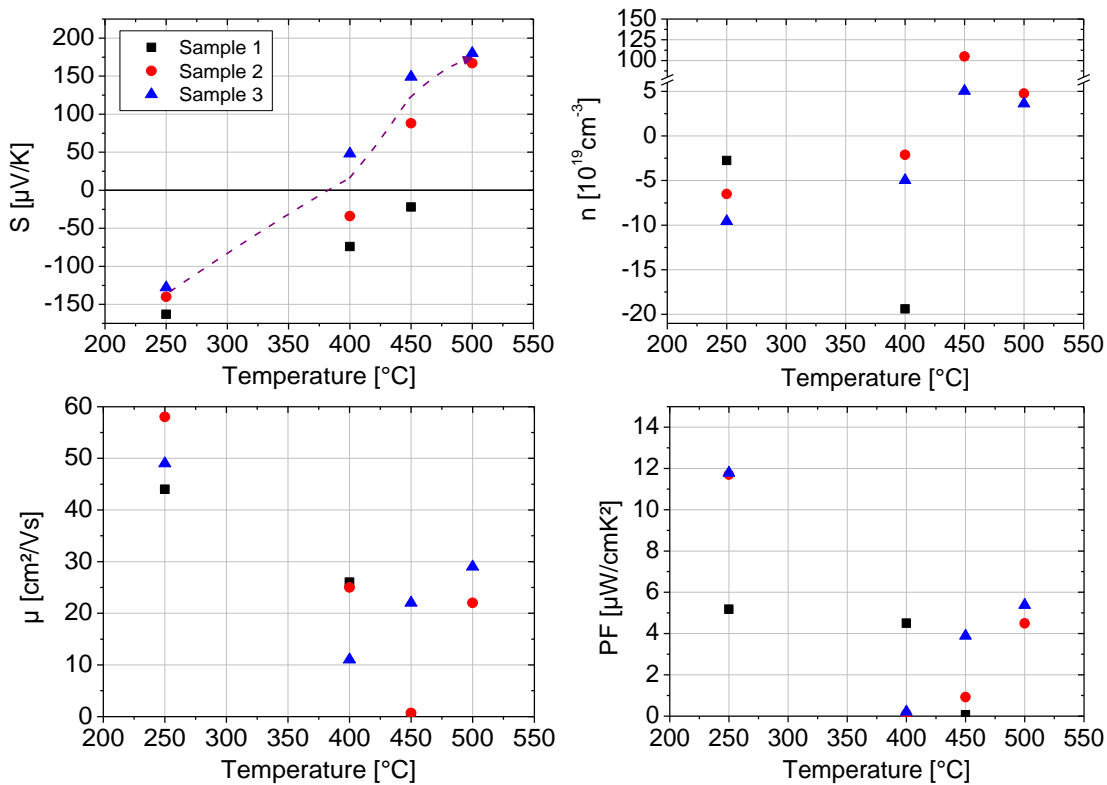


Figure 5.17 Electrical Properties of Bi₂Te₃ in dependence on annealing temperature. Black square: Sample 1, red circle: Sample 2, blue triangle: Sample 3. Purple dashed line: Eyeguide for S of samples 2 and 3. Note that due to compensation effects in the mixed conduction regime at 400–450 °C the determination of n and μ is unreliable, see section 6.2.1 for details. A negative sign of n indicates electron conduction.

Finally, it is noted that unfortunately the method cannot be used to overcome the compensation problems in nanoalloyed multilayers since the necessary temperature of 500 °C is far beyond the stability limit of these ML (section 6.2.1).

5.6 Conclusions

In summary, the nanoalloying method has been shown to yield Bi_2Te_3 and Sb_2Te_3 thin films with good thermoelectric properties and stoichiometry control. Crystal formation was found to start at a temperature as low as ~ 100 °C, enabling the use of temperature-sensitive substrates during compound fabrication. Changing the element initial layer thickness and deposition pattern provides a novel method to influence the film texture while altering the Te content in the samples provides a way to influence the electrical properties. Very high deposition rates can be applied without a degradation in transport properties.

Nanoalloyed Sb_2Te_3 films exhibit very high charge carrier mobilities (~ 400 cm^2/Vs) and high power factors (~ 30 $\mu\text{W}/\text{cmK}^2$). Thus, it could be shown that Sb_2Te_3 thin films are suitable for thermoelectric devices, in contrast to bulk materials. A value for the thermal conductivity as low as 0.4 W/mK was determined for the Bi_2Te_3 sample with a quintuple deposition pattern. However, TEM experiments revealed the presence of an oxidized Bi-rich “electron blocking phase” in nanoalloyed Bi_2Te_3 films.

For films isothermally annealed at temperatures of 250 °C under Te atmosphere, a defect chemistry clearly different from bulk material grown from the melt was observed. For Bi_2Te_3 , only n-type samples were obtained regardless of Te content. A new two-zone annealing procedure under controlled Te atmosphere was applied for as-grown Bi_2Te_3 films, allowing to adjust the film composition. It was found that the transport properties, majority carrier type and defect structure (concentration of hole-generating Bi_{Te} antisite defects) strongly depend on annealing temperature. With a sufficient annealing temperature, p-type Bi_2Te_3 films can be fabricated. This is in qualitative accordance with defect structure models that predict a strong dependence of defect chemistry, e.g. carrier concentration on compound formation temperature.

6 Bi₂Te₃ / Sb₂Te₃ superlattice thin films grown with a MBE setup by nanoalloying

For the fabrication of the nanoalloyed SLs, the quintuple pattern shown in section 5.1 was used for each partial layer of Bi₂Te₃ and Sb₂Te₃. The 1 nm pattern was repeated until the desired thickness was reached for each binary partial layer. All films were grown on BaF₂ if not otherwise indicated. Annealing times were always 2 h for the samples shown in this section.

6.1 Structural properties

6.1.1 Composition and structure

SL stacks with ratios of Sb₂Te₃ to Bi₂Te₃ ranging from 1:1 to 7:1 were fabricated and characterized. The compositions and nominal compound layer thicknesses of the samples are given in Table 6.1. The nominal compositions expected from the ratios of the compound layer thicknesses are in good agreement with the actual sample compositions determined by EDX. Deviations may be caused due to the overlap between the L-lines of Sb and Te which introduces an error if the actual composition deviates from the (Bi_{0.2}Sb_{0.8})₂Te₃ calibration standard used and due to the fact that the samples have a multilayered structure in contrast to the homogeneous calibration standard used (4.3.2).

Table 6.1. Structural properties of SLs. Units as previously defined in Table 5.1. *d*-Sb₂Te₃ and *d*-Bi₂Te₃ are single compound layer thicknesses in nm. *c*_{Bi} and *c*_{Sb} are element concentrations determined by EDX in at. %.

Ratio Sb ₂ Te ₃ : Bi ₂ Te ₃	<i>d</i> -Sb ₂ Te ₃	<i>d</i> -Bi ₂ Te ₃	<i>N</i> _{per}	<i>c</i> _{Bi}	<i>c</i> _{Sb}	<i>c</i> _{Te}	<i>d</i>
1 : 1	9	9	56	18.2	21.8	60.0	0.98
3 : 1	9	3	83	9.2	31.3	59.5	1.02
5 : 1	15	3	56	6.4	33.5	59.1	1.03
6 : 1	18	3	48	4.7	33.9	61.4	1.10
7 : 1	21	3	42	4.2	34.5	61.3	1.09

XRD patterns taken of the 1:1 SL, Figure 6.1, show a polycrystalline structure with a well-expressed degree of texture along the c-axis like the Sb₂Te₃ binary samples (section 5.1.2), however there is a significant amount of grains with other orientations, the most prominent being the (10.10)-reflex at ~ 38.0°. In the as grown state, the structure appears amorphous or very small-crystalline. The presence of the (10.10) and (00.15) compound reflexes indicates that the compound formation takes place already during deposition on the cold substrate. Grain growth for increasing exposition temperature is indicated by a sharpening of the reflexes. Neither after annealing at 150 °C nor 250 °C any trace of satellite reflexes that indicate the presence of a ML structure could be observed. This is attributed to the limited crystalline quality of the SL and the diffuse boundaries between the binary constituents. Experiments with sputtered films showed that a much larger degree of c-texture and thermal stability is required in order to be able to observe signs of SL satellites (section 7.6.1).

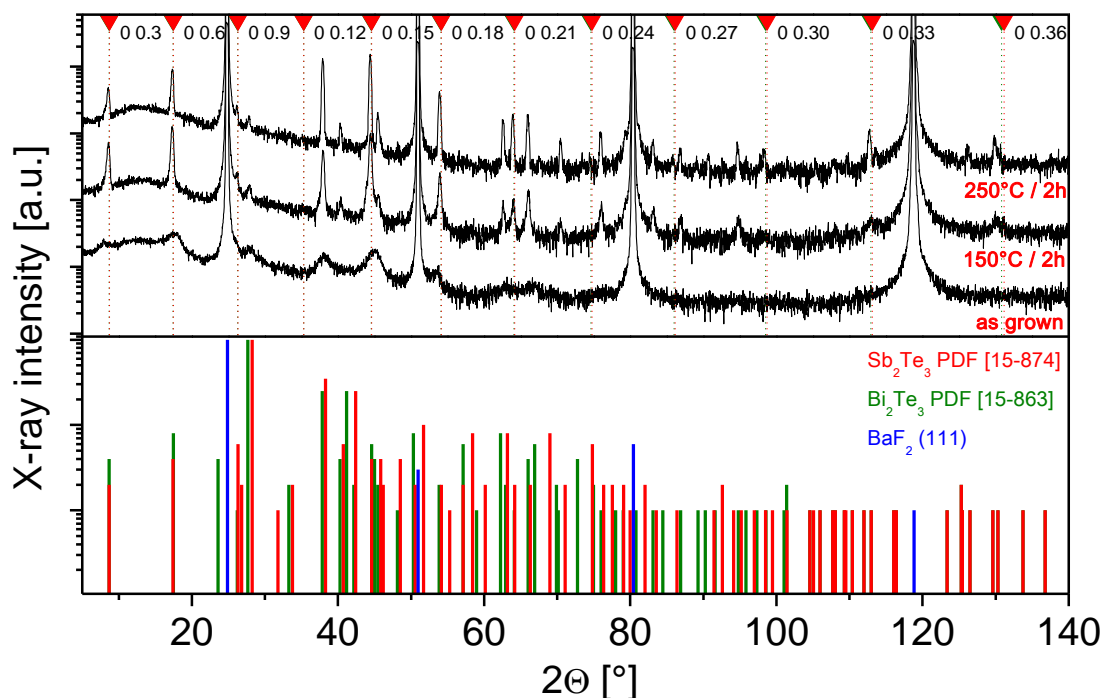


Figure 6.1 XRD pattern of the 1:1 SL in dependence of annealing temperature. Calculated (00.l)-reflections are indicated by dashed lines. For comparison, a powder diffractogram (JCPDS database) is shown as vertical bars below the acquired patterns.

The SEM cross sections were similar for all thin films shown in this work and are exemplarily shown for the 1:1 SL. In the as grown state, the film had an amorphous appearance with no grains distinctly visible. After annealing at 150 °C, the formation of small grains was evident. Annealing at 250 °C produced distinctly larger grains.

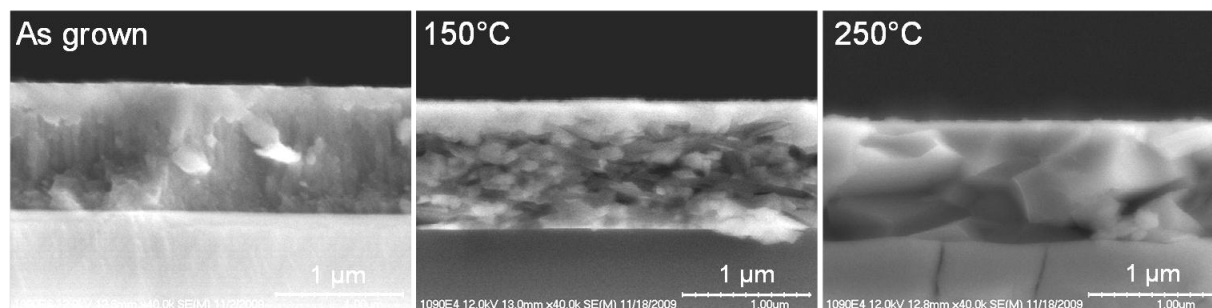


Figure 6.2 SEM cross sections of 1:1 SL samples. SLs with other ratios exhibited an analogous appearance.

6.1.2 Thermal stability

The stability of the multilayer nanostructuring can be evaluated using a variety of methods. For high crystalline quality films, the standard way to verify a periodic SL structure is to look for SL satellite reflexes corresponding to the SL period. However, this was not possible for the polycrystalline nanoalloyed MBE-grown films as discussed above, thus alternative complementary methods had to be used. On very smooth nanoalloyed thin films the stability of the ML structure can be readily evaluated with SIMS depth profiling (section 4.3.4). The amplitude of the element signal “oscillations” for a multilayered structure decreases for a stronger degree of interdiffusion. However, if the films are slightly rough and the single compound layers are wavy (see Figure 6.4), the element ions tend to get mixed even if the actual layer only consists of one single element, smearing out the depth profile and suggesting that no ML structure is present where there actually is one. For this reason, the stability was also evaluated by SEM and STEM imaging.

Generally, the multilayer structure was evident in the smoothed SIMS depth profiles (Figure 6.3) for all samples in the as grown state and annealed at 150 °C. At 250 °C, the ML structure is quite smeared out and hardly visible, if at all. An example is shown for the 1:1 SL. As expected, the signals of Bi and Sb follow a periodic pattern. Corresponding to the layer structure of the 1:1 SL, the period length is 18 nm. The Bi and Sb pattern are complementary, i.e. a Bi-dip is always present when there is a Sb peak. For all ratios of $\text{Sb}_2\text{Te}_3:\text{Bi}_2\text{Te}_3$, the period length observed by SIMS corresponded to the nominal values.

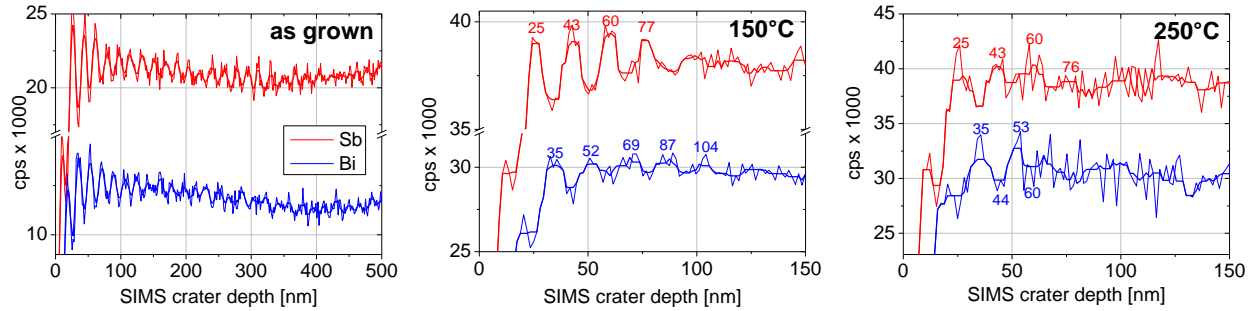


Figure 6.3 SIMS depth profiles of the 1:1 SL (Sb ion signal = red, Bi ion signal = blue, signal smoothing applied). Numbers indicate peaks and dips.

Very similar experiments [128] were reported by the group of D.C. Johnson on $\text{Bi}_2\text{Te}_3 / \text{Sb}_2\text{Te}_3$ SL films deposited by thermal evaporation with the MER method. The period length was between 6 and 12 nm. Even though a very high degree of *c*-orientation was evident, SIMS depth profiling revealed that also these SLs exhibited significant interdiffusion of Bi and Sb in the amorphous precursor state.

To further study interdiffusion phenomena, (S)TEM and HRTEM studies were carried out on the 1:1 SL in the as-grown state and after ex- and in-situ annealing, see Figure 6.4. As grown-images revealed a significant degree of waviness (i.e. roughness) of the ML structure. During annealing, compound formation of Bi_2Te_3 and Sb_2Te_3 from the deposited element stacks took place, accompanied by temperature-driven interdiffusion of Bi and Sb. The STEM cross sections micrographs demonstrated that the grain sizes are larger for higher annealing temperatures. Interestingly, the SL structure exhibited a discontinuous or “patchy” distribution in the annealed state, meaning that it was visible just within a part of the cross section. After annealing at 150 °C the SL structure seemed to remain stable inside the core of the respective grains but degraded near the grain boundaries owing to the fact that diffusion in solids was generally enhanced at or near grain boundaries which is demonstrated clearly by the images taken after in-situ annealing at 250 °C. Furthermore, the SL structure did not remain stable in all of the grains. It is assumed that the degree of interdiffusion depends on the relation of the direction of the multilayer stacking to the direction of the *c*-axis for each individual grain since diffusion in $\text{V}_2\text{-VI}_3$ materials is by orders of magnitudes smaller in the direction parallel to the *c*-axis than perpendicular to it (section 3.1 [64]). Consequently, if the layers are stacked in a sequence parallel to the *c*-axis, temperature-driven interdiffusion should be relatively weak which was confirmed by the high thermal stability of epitaxial, exclusively *c*-oriented material grown by MOCVD and MBE (section 9.2). Since every grain had a different orientation, the relative orientation of stacking direction to the *c*-axis varied for each grain, leading to a different stability of the SL structure. For ex-situ annealing at 150 °C, the sizes of the domains where the SL structure remained observable varied between ~ 50 - 400 nm which corresponded to the grain sizes observed. While after annealing ex-situ at 150°C the nanostructure could, in comparison, still be seen relatively well, ex-situ annealing at 250 °C yielded a SL structure that was smeared out to a large extent. Only in a few regions of the cross section the SL structure was still visible, mainly in the core region of the larger grains. The analysis of a large crystallite by HRTEM after in-situ anneal at 250 °C and simulation showed a good match of the reflections with the metrics of homogeneous $(\text{Bi}_{0.5}\text{Sb}_{0.5})_2\text{Te}_3$.

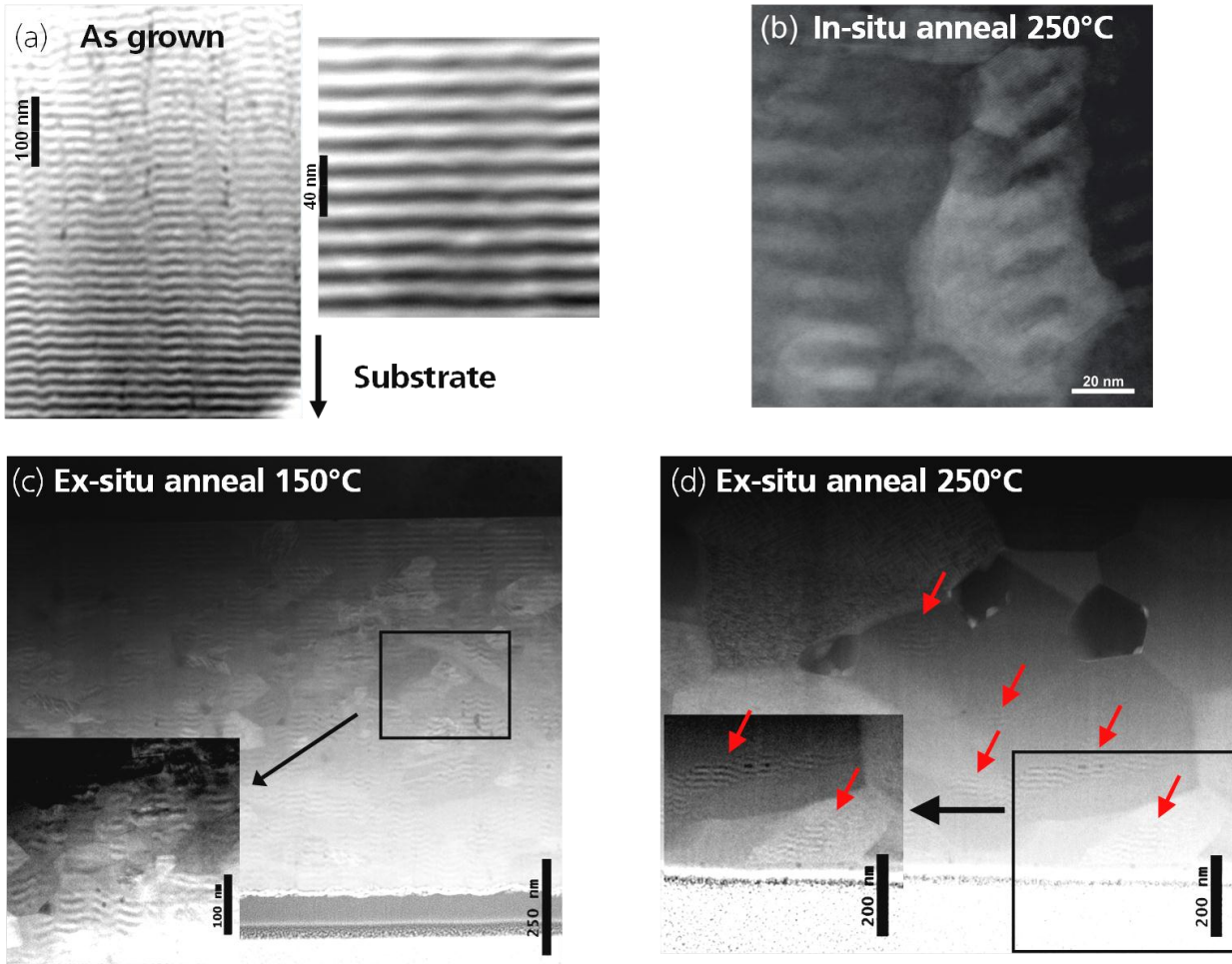


Figure 6.4 Results of HAADF-STEM studies on 1:1 SLs [171]. a) As grown state. b) Cross-section after in-situ anneal at 250 °C, nicely showing enhanced interdiffusion at grain boundaries. c) Cross-section after ex-situ anneal at 150 °C / 2 h. d) Cross-section after ex-situ anneal at 250 °C / 2 h.

As a supplement to the obtained results, the thermal stability of the ML structure was studied by SEM on the craters sputtered into the thin films during SIMS depth profiling (Figure 6.5). If the SIMS depth profiles are unclear due to single layer roughness or waviness, this method can be used to get an impression of the quality of the ML stacking. The walls of the SIMS craters have a slope with a very small tilt angle. When viewed from above, the single binary layers with a thickness d_l in the nm range appear with a thickness d_v of a few μm and can be observed with relatively low magnifications. Note that this experiment only gives qualitative information about the ML structure since the slope of the crater is not constant. The information gained from this experiment was in agreement with the experimental results of SIMS and (S)TEM analysis, i.e. the ML structure in total was relatively weakly expressed after annealing at 150 °C, particularly compared to sputtered or epitaxial SLs (see next chapters).

Due to the relatively weakly expressed ML structure already at relatively large period lengths of ~ 18 nm, no SLs with smaller period lengths were synthesized by the nanoalloying method since the chance of them “surviving” the annealing treatment was deemed very small.

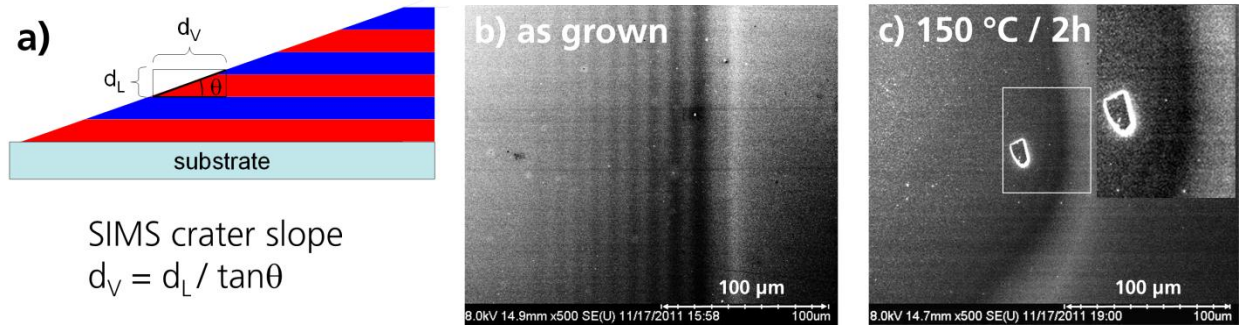


Figure 6.5 Observation of the ML structure by SEM. a) Due to the slope of the SIMS crater, the layers appear to be spaced apart much farther than the actual layer thickness and an imaging at the microscale is possible. b+c) Image of SIMS crater in the as grown and ex-situ annealed state.

6.2 Transport properties

6.2.1 Electrical properties

Figure 6.6 shows S , n , μ and σ of the nanoalloyed SLs in dependence of the $\text{Sb}_2\text{Te}_3:\text{Bi}_2\text{Te}_3$ single layer thickness ratio. For some ratios, more than one sample was characterized, demonstrating the good reproducibility of transport properties. For annealing at 250 °C, no significant difference between Si/SiO_2 and BaF_2 substrates was observable.

Particularly the electrical properties of the 1:1 SL showed unusual features and poor thermoelectric properties. n was reported as positive while the Seebeck coefficients were low and reported as negative. There are strong indications that this can be attributed to layer compensation effects since nanoalloyed Bi_2Te_3 was always found to be n-type at the used annealing temperatures while Sb_2Te_3 always showed p-type conduction (see section 5.2). If there is mixed conduction in a layer system and if the hole mobility μ_p ($\sim 200\text{-}400 \text{ cm}^2/\text{Vs}$ for the given element composition) is clearly larger than the electron mobility μ_n ($\sim 50\text{-}80 \text{ cm}^2/\text{Vs}$), the Hall coefficient R_H as defined in equation 4.10 may become positive despite electrons being the majority carrier type ($n > p$). Additionally, n cannot be derived correctly from R_H by eq. 4.11 in the case of mixed conduction and will be reported as too large. As n reported for the 1:1 SLs is most likely not correct, the same applies to the mobility μ which was calculated by $\mu = \sigma/en$ and is thus reported as too low. Actually, the carrier mobility at 150 °C annealing was very much (factor of 3 for all ratios of $\text{Sb}_2\text{Te}_3:\text{Bi}_2\text{Te}_3$) lower than at 250 °C which is assumed not only to be caused by a smaller grain size but also by compensation effects that disappeared during homogenization. Note that such a small μ for 150 °C annealing temperature compared to 250 °C was not observed on compensation-free sputtered SLs (see section 7.2). Finally, the total electrical conductivity of the films was low since the real number of carriers actually participating in charge transport was most likely very low due to the compensation effects (see also section 2.1.1.2). Additionally, p/n – junctions may be formed between n- Bi_2Te_3 and p- Sb_2Te_3 , resulting in a high resistance of the SL stack.

The Seebeck coefficient should be reduced according to eq. 2.17 for a stack of mixed conducting layers. Indeed, at 150 °C annealing for all ratios $\text{Sb}_2\text{Te}_3 : \text{Bi}_2\text{Te}_3$ the Seebeck coefficients were significantly lower than at 250 °C although the carrier concentration was also lower in the films annealed at 150 °C, contradicting the normally observed reciprocal relation. It is instructive to compare experimentally determined S in dependence of n to calculated values from the BTE-based model described in section 2.1.1.1, eq. 2.6 for one-band conduction, parabolic bands, acoustic scattering ($s=-1/2$), the integral form for n (left side of eq. 2.3) and m_d values for the solid solution $(\text{Bi}_{1-x}\text{Sb}_x)_2\text{Te}_3$ from Table 3.3 as shown in in Figure 6.7. Evidently, the strongly interdiffused samples annealed at 250 °C could be described in good approximation (non-systematic deviation of $\leq 15\text{-}20 \%$ to calculations) with a model for homogeneous solid solutions, indicating a loss of the ML structure while the experimental S of the samples annealed at 150 °C systematically fell below the calculated values by as much as $\sim 22\text{-}70 \%$, indicating that a multilayered structure still is present in the samples at that temperature.

A drastic improvement of S , μ , σ and the PF (Figure 6.9) could be achieved by increasing the $\text{Sb}_2\text{Te}_3 : \text{Bi}_2\text{Te}_3$ ratio and simultaneously reducing the thickness of the Bi_2Te_3 layer. Interdiffusion led to a mixing

of the partial layers to $(\text{Bi}_{1-x}\text{Sb}_x)_2\text{Te}_3$. For increasing ratios of Sb_2Te_3 : Bi_2Te_3 an increasing part of the films consisted of $(\text{Bi}_{1-x}\text{Sb}_x)_2\text{Te}_3$ with $x > 0.5$ and became p-conducting, reducing compensation effects.

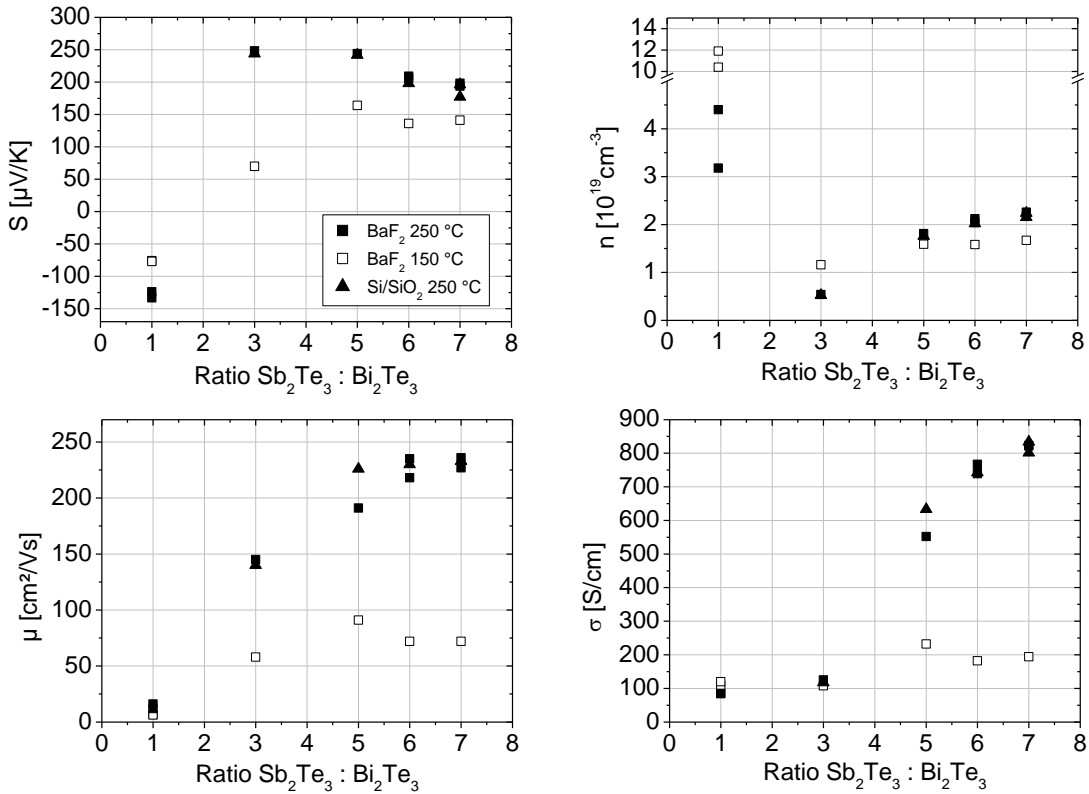


Figure 6.6 Transport properties of nanoalloyed MBE SLs with different ratios of Sb_2Te_3 : Bi_2Te_3 . Squares: BaF₂ substrate, full: 250 °C annealing, empty: 150 °C annealing. Full triangles: Si/SiO₂ substrate. Error bars were omitted for clarity.

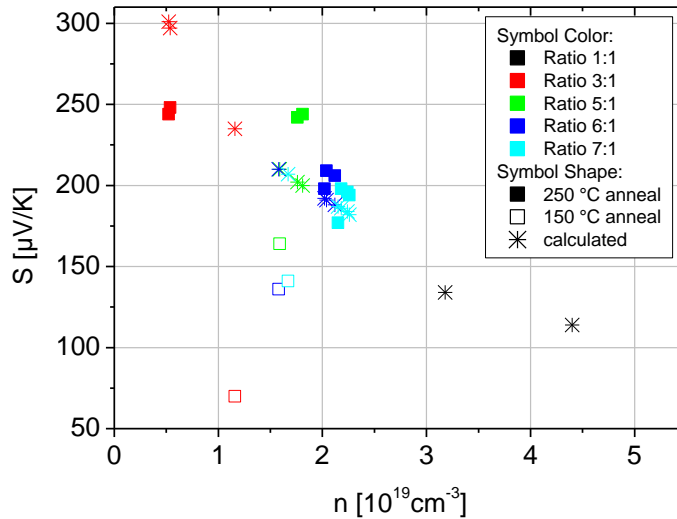


Figure 6.7 S vs. n for nanoalloyed MBE SLs with different ratios of Sb_2Te_3 : Bi_2Te_3 . Stars: Calculated data (see text). Squares: Experimental data. Full symbols: 250 °C annealing, empty symbols: 150 °C annealing. Colors: see key.

The results obtained here are relevant with regard to the results presented by R. Venkatasubramanian mentioned in section 3.5.2. Analogous to the results obtained with nanoalloyed binary films it appears that only n-type Bi_2Te_3 was obtained by the MOCVD method used for the fabrication of the SLs [117]. Despite of this, no compensation problems were ever reported. It is reckoned that the consideration of compensation effects might have lead to the decision to create “asymmetric” MLs with ratios of Sb_2Te_3 : Bi_2Te_3 different from 1:1. For these structures, high Seebeck coefficients were attained which was explained by the “ordered alloy concept”, see discussion in section 3.5.2 and Figure 6.8. In addition to

this concept, it is well possible that also interdiffusion plays a big role in the transport properties of the high-ZT MOCVD films, consisting of 5 nm of Sb_2Te_3 on only 1 nm of Bi_2Te_3 . From the only TEM images presented for the high-ZT SLs [60], interdiffusion of Sb into Bi_2Te_3 cannot be ruled out. In the same work, XPS studies on a single < 5 nm Sb_2Te_3 layer grown on a Bi_2Te_3 layer are presented which show only a negligible amount of Bi in the Sb_2Te_3 layer. This indicates a high stability against thermal interdiffusion but does not necessarily imply that the more extreme and opposite case is also true, e.g. that there is no interdiffusion of Sb into a Bi_2Te_3 layer with a thickness of only 1 nm.

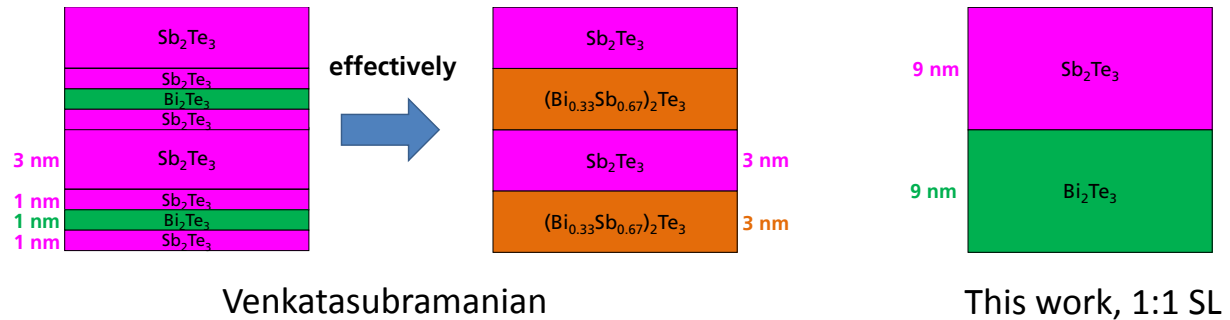


Figure 6.8 Left: Schematic representation for the SL structure presented by Venkatasubramanian. The stacking of Sb_2Te_3 on Bi_2Te_3 with a Bi_2Te_3 thickness of only 1 nm is supposed to lead to an “ordered alloy” [46] of p-type $(\text{Bi}_{0.33}\text{Sb}_{0.67})_2\text{Te}_3$ and thus eliminate compensation effects. Right: Layer structure for the 1:1 SLs presented in this work.

6.2.2 Thermal conductivity

As evident from Figure 6.9, although high PF could be obtained an efficient reduction of the thermal conductivity has not been achieved by the multilayer 2D nanostructuring. For all ratios of $\text{Sb}_2\text{Te}_3:\text{Bi}_2\text{Te}_3$, the total and estimated lattice thermal conductivity of the SL structures was **not lower** than that of both binary compounds that were created with the same deposition pattern as the SLs, in contrast to the data reported on the MOCVD SLs [57]. Instead, λ and λ_l just varied between the values of the binary compounds (see section 5.2). Additionally for the 1:1 and 3:1 SL, although the ML structure was clearly more pronounced in the sample annealed at 150 °C, the thermal conductivity was not lower than that of the sample heated at 250 °C.

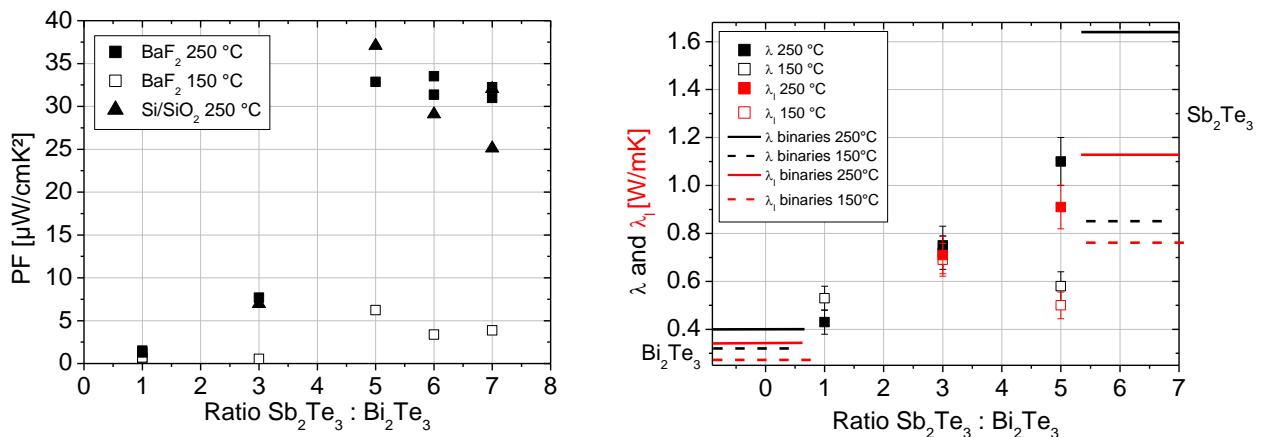


Figure 6.9 PF of nanoalloyed $\text{Bi}_2\text{Te}_3\text{-Sb}_2\text{Te}_3$ SLs deposited by MBE for different ratios of $\text{Sb}_2\text{Te}_3:\text{Bi}_2\text{Te}_3$. (error bars were omitted for clarity). Right: Thermal conductivities of SLs together with binaries (sample sets BT-Q and ST-Q, chapter 5) Triangles: Film on Si/SiO_2 substrates, squares: BaF_2 substrates. Full data points: 250 °C annealing, empty points: 150 °C annealing. Full lines: Binaries, 250 °C annealing. Dashed lines: Binaries, 150 °C annealing. Black / red: Total / lattice thermal conductivity.

Altogether, the ML-type nanostructure appeared to have no clearly observable effect on the thermal conductivity. This phenomenon can be explained by the particular situation of a superlattice structure superimposed on a nanocrystalline material. Qualitatively, it can be inferred from Matthiessen's rule (section 2.1.2) that multiple scattering effects are not directly cumulative and adding a weak multilayer-induced phonon scattering to significantly pronounced grain-boundary scattering (see e.g. section 7.3) should not significantly influence the total relaxation time. A deeper analysis requires considering the particular effects of nanostructures on the phonon spectrum: A nanocrystalline structure causing pronounced boundary scattering leads to a cutoff of the low-frequency range of the phonon spectrum (see Figure 2.5) while the SL structure is believed to affect the low-frequency range, too (2.1.2.1). Thus, it can be concluded that qualitatively, the cutoff-effect on phonon frequencies, i.e. the reducing effect on thermal conductivity by adding a SL structure to an already nanocrystalline material, should not be very strong. If additionally the layered structure is "softened out" as demonstrated here, its cutoff-effect should be reduced even further. A more pronounced reduction of thermal conductivity was possible by SL structures with a better definition, specifically epitaxial SLs (section 9.2).

The cross-plane ZT can be roughly determined by making similar assumptions as described in section 7.5. With an electrical conductivity anisotropy factor of 1 – 3.3, a ZT of 0.3 – 0.9 was estimated.

As a note, the shown λ_l was calculated from λ as follows: The Lorentz numbers were calculated as described in section 2.1.1.1 on the base of the BTE formalism with effective DOS masses as given in Table 3.3 for the SLs and Sb_2Te_3 and for Bi_2Te_3 from [11-p.118]. For the calculation of the electronic part of the thermal conductivity λ_{el} by eq. 2.5, the electrical conductivity σ_{cross} in cross-plane direction was estimated from σ_{in} by estimating the electrical conductivity anisotropy factor. This factor was estimated from bulk material data, i.e. 4 and 3.9 for Bi_2Te_3 and Sb_2Te_3 and the weighted values of 2.9 (ratio 5:1) and 3 (ratio from $(\text{Bi}_{0.2}\text{Sb}_{0.8})_2\text{Te}_3$ (2.6) and Sb_2Te_3 (3.9) [90]). All anisotropy factors were divided by 2 as an approximation due to the not strongly expressed c-texture of the films.

6.3 Conclusions

Polycrystalline Bi_2Te_3 / Sb_2Te_3 SLs with different ratios of $\text{Sb}_2\text{Te}_3:\text{Bi}_2\text{Te}_3$ and period lengths were fabricated by nanoalloying with a MBE setup. Clearly, interdiffusion had a strong impact on transport properties. Structural analysis by SIMS, SEM and TEM revealed that the ML structure was only weakly expressed, especially after annealing at 250 °C. The low stability could be traced back to the polycrystallinity and crystal orientation of the grown material, the degree of c-texture was not strongly expressed.

An efficient reduction of thermal conductivity by the SL structure was apparently not achieved. Taking into account the phonon spectrum, it was concluded that the scattering effect on the phonons by the weakly expressed SL structure was small compared to the scattering caused by the polycrystalline structure.

As expected from the exclusive electron conduction in nanoalloyed Bi_2Te_3 and hole conduction in Sb_2Te_3 , for some SL films strong carrier compensation effects were found to adversely affect SL transport properties. These effects were interconnected to the $\text{Sb}_2\text{Te}_3:\text{Bi}_2\text{Te}_3$ ratio and the quality of the SL structure. Choosing a high ratio and an annealing temperature of 250°C led to high power factors of ~30-40 $\mu\text{W}/\text{cm}^2\text{K}^2$. A ZT of 0.3 - 0.9 was estimated for the SLs.

7 Sputtered p-type Sb_2Te_3 / $(\text{Bi,Sb})_2\text{Te}_3$ multilayer systems grown by nanoalloying

The structural stability and thermoelectric properties of the SLs presented in chapter 6 were afflicted by significant interdiffusion and carrier compensation effects. During growth in the MBE system, the beam fluxes were observed to drift (see section 4.1.3.2), which is suspected to adversely affect the formation of well-oriented crystallites. In contrast to the effusion cell drift, the drift in sputtering rate takes place on a much larger time scale, i.e. was more constant during a single growth run.

Consequently, in order to improve the degree of c-orientation and layer homogeneity, it was decided to use sputtering to deposit the element thin films and change the deposition patterns (Figure 7.1). Moreover, in order to exclude compensation effects, it was decided to deposit the p-type compound $(\text{Bi,Sb})_2\text{Te}_3$ instead of Bi_2Te_3 . For all films, Si/SiO_2 wafers were used as substrates.

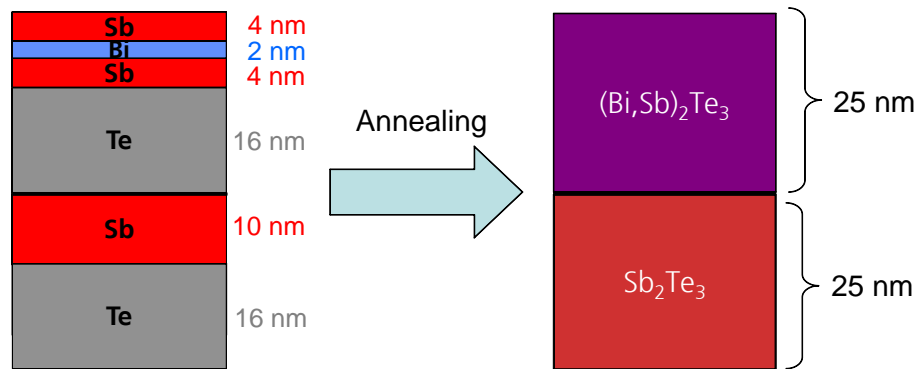


Figure 7.1 Deposition patterns used for the sputtered thin films shown in this chapter. Each film shown consists of 30 periods of this pattern, yielding a total film thickness of $\sim 1.5 \mu\text{m}$.

In the annealing experiments, five different combinations of annealing temperatures and times were used: $150^\circ\text{C} / 2 \text{ h}$, $250^\circ\text{C} / 2 \text{ h}$, $250^\circ\text{C} / 24 \text{ h}$, $300^\circ\text{C} / 2 \text{ h}$ and $350^\circ\text{C} / 2 \text{ h}$.

7.1 Structural properties

The compositions of the thin films were analysed using EDX, cf. Figure 7.2. Small fluctuations in the element concentrations are due to the measurement uncertainty. More pronounced variations of the composition are observed at higher annealing temperatures (e.g. for 350°C), where matrix effects caused by the thin film changing from a layered to a more homogeneous structure and the increasing film roughness were introduced. The actual Te content was slightly lower than the intended 59.5 - 60 at. % due to a sputtering rate drift of Te.

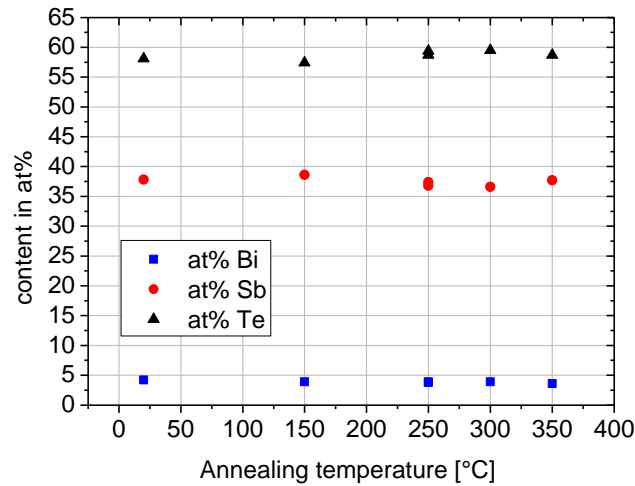


Figure 7.2 Composition of the thin films in the as deposited state and after annealing at different temperatures.

The SIMS depth profiles shown in Figure 7.3 are very even and homogeneous throughout the whole thickness of the SL, indicating a high structural quality of the nanoscale multilayer structure. As expected from the deposition pattern used the profiles follow a complementary pattern, i.e., every Bi peak is accompanied by a Sb dip at the same position. The period of the Bi “oscillation” corresponds very closely to the nominal period length of 50 nm. The intensity of the oscillations decreases continuously for higher temperatures. The SIMS profiles of the sample heated at 300 °C exhibit less pronounced oscillations indicating a significant degradation of the ML structure by interdiffusion. At 350 °C the ML structure appears completely lost and the corresponding SIMS depth profile (not shown here) consists of flat lines for the ion signals of all elements.

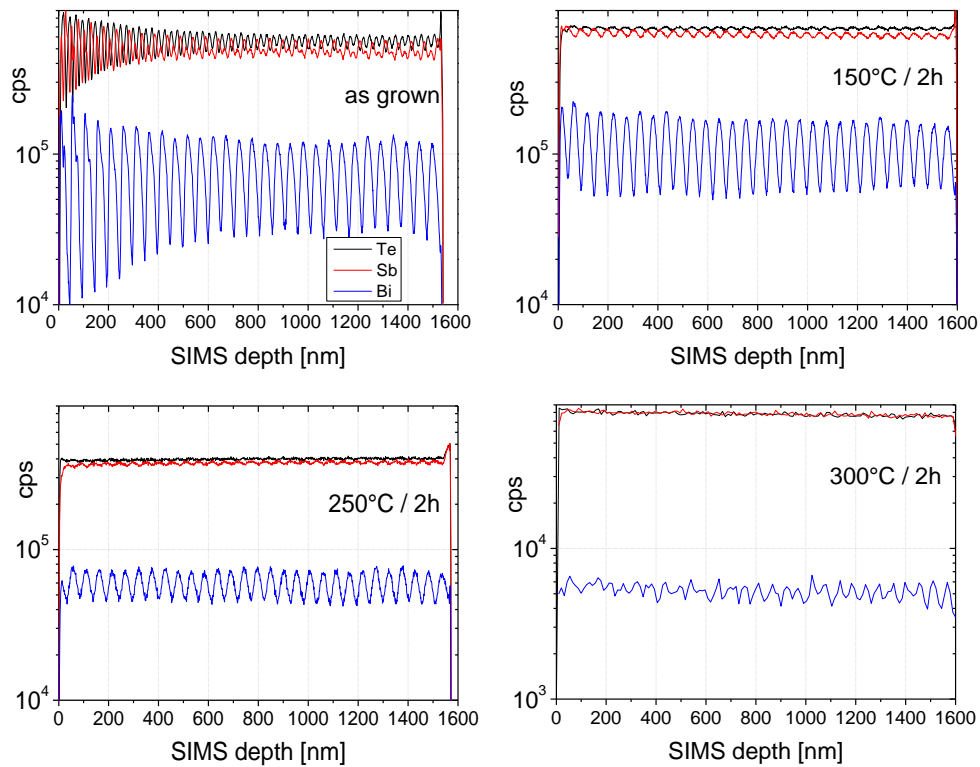


Figure 7.3 SIMS depth profiles of the SLs annealed at different temperatures. At 300 °C, the SL is significantly smeared out due to interdiffusion. Black: Te, red: Sb, blue: Bi.

A closer inspection of the depth profiles in the as deposited state and after annealing at 150 °C/2 h (Figure 7.4) confirms that the reaction path from the initial element layer stack in the as grown state to the compound stack follows the path suggested by Figure 7.1. In the as deposited state, the Sb-rich areas and the Te layers have a spacing of 25 nm. The different Sb contents in these areas are also reflected in the profiles. After compound formation, the distance between blocks with the same Sb and Te content (i.e. the distance between two Sb_2Te_3 or $(\text{Bi,Sb})_2\text{Te}_3$ blocks) increases to 50 nm. The separation distance between Bi-rich areas remains at 50 nm before and after compound formation.

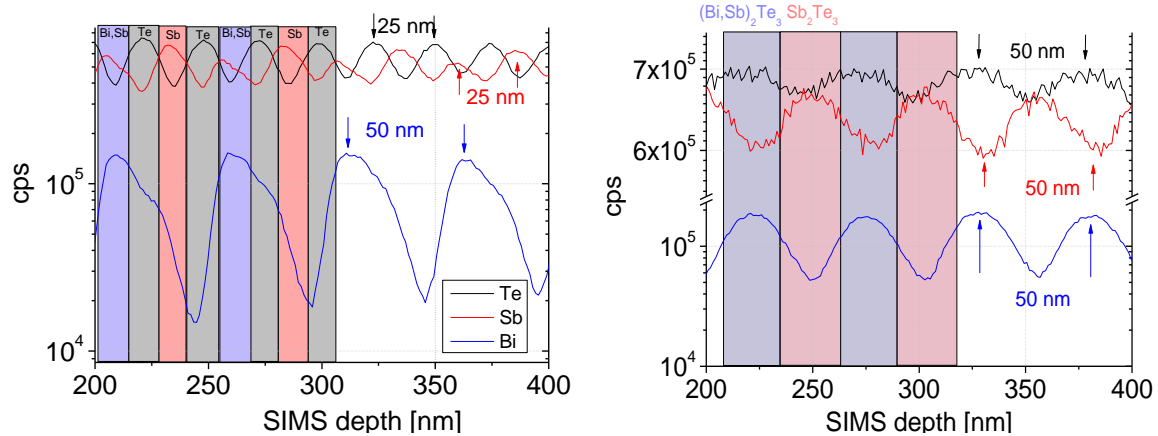


Figure 7.4 Detailed view of the SIMS depth profiles in the as-deposited state (left) and after annealing at 150 °C for 2 h (right). The periodicity of the Sb and Te ion signal increases from 25 nm to 50 nm after the annealing process.

SEM cross-section images taken along the cleaving edge of the films in slow-scan mode are given in Figure 7.5. As already shown in section 5.1.1, the grains exhibit a typical hexagonal platelet-like shape as described e.g. in [165]. This can be best observed in the thin film annealed at 350 °C that shows the largest grains. The fact that the hexagonal platelets that make up the grains are oriented perpendicularly to the growth direction indicates that the thin films are strongly textured with $[00.]$ parallel to the growth direction of the films. The atomic number dependent contrast (Z -contrast) of the back scattered electron (BSE) image taken in the as deposited state shows Bi-rich areas as bright lines with a spacing of 50 nm. The smoothness of the films is preserved up to an annealing temperature of 300 °C (not shown in Figure 7.5, roughness corresponds to thin film annealed at 250 °C). The grain size (i.e. also the crystallite size as inferred from Rietveld refinements) increases drastically when increasing the annealing temperature from 300 to 350 °C. Additionally, the films become very rough and porous, indicating recrystallization with pillar shaped crystal growth induced by the onset of bulk diffusion. A similar morphology of films, i.e. a high roughness and formation of pillar-shaped grains was observed for MOCVD Bi_2Te_3 thin films grown at the same temperature [60].

For films as deposited and annealed at 150 °C / 2 h, 250 °C / 2 h, 250 °C / 24 h, 300 °C / 2 h and 350 °C / 2 h the total film thickness was determined from cross-sections as 1.62, 1.72, 1.65, 1.61, 1.72 and 1.65 μm respectively. For the rough thin film annealed at 350 °C, the thickness was estimated by averaging several values measured at different positions of the film.

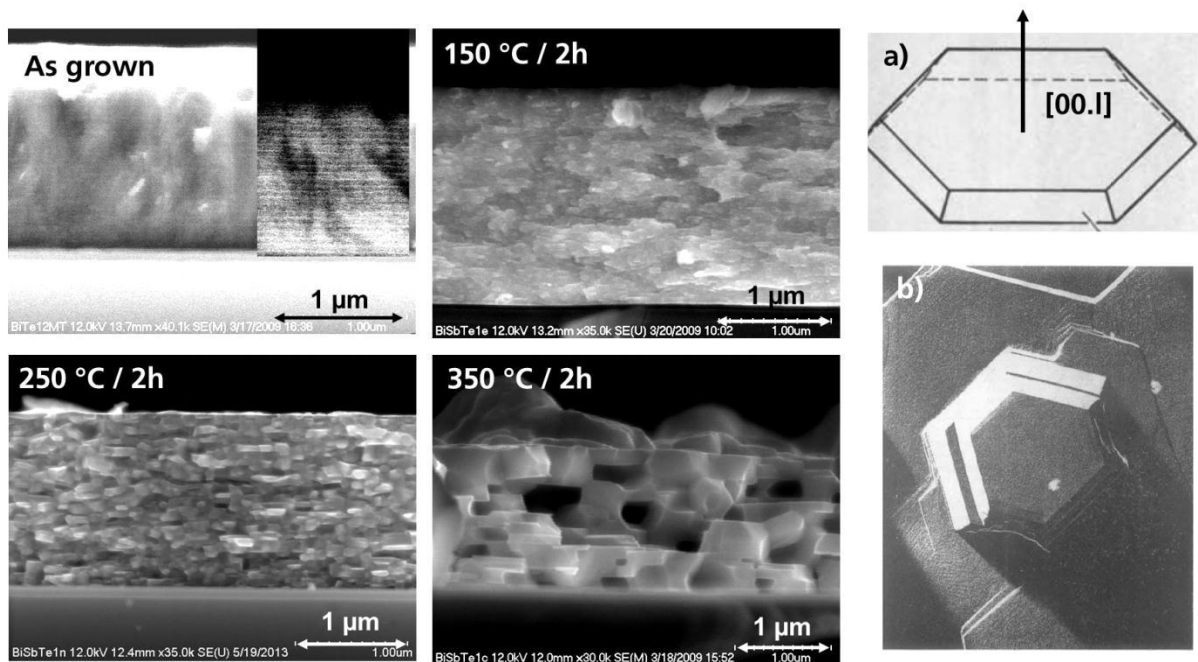


Figure 7.5 Left: SEM cross-sections of the SLs for different annealing temperatures. In the cross-section image of the thin film in the as deposited state, a BSE image is shown in the inset. Note that the exact film thicknesses can not be extracted from the slow-scan images shown in this figure due to image distortions caused by charging effects. Right: a) Drawing of hexagonal crystallites. b) SEM images of sputtered Bi_2Te_3 films, substrate temperature 400 °C [165]. It is noted that the films deposited by nanoalloying are much smoother than the films reported in [165], so the grains cannot be seen in top view with SEM on the films shown in this work.

In the as deposited state, the XRD patterns for the films (Figure 7.6) show very broad reflections that can be assigned to very small grained or amorphous elemental constituents Bi, Sb and Te or the compound phase (reflections near the (00.24) and (00.27) reflections). After annealing, a very pronounced *c*-texture is prominent for all annealing temperatures by strong intensities (00.*l*), in accordance with the morphology observed in the SEM images. Reflections corresponding to other crystallite orientations are weak and scarce. The X-ray intensity is high even for high-order *c*-reflections like e.g. (00.33). Grain growth at increasing annealing temperatures is indicated by a narrowing of the reflections. In Figure 7.6, the degree of *c*-texture can be readily evaluated by comparing the ratios of the intensities of the (00.*l*)- reflexes to the other reflexes. A monotonous decrease of this ratio is observed for increasing annealing temperatures, i.e. the pronounced *c*-texture remains stable and even gets stronger for higher annealing temperatures.

Rietveld refinements on the XRD data for the sample annealed at 150 °C, 250 °C and 350 °C (Figure 7.7, plots for 250 °C omitted) show a reasonable fit for the samples annealed at lower temperatures, i.e. 150 °C and 250 °C. The intensity could not be modeled correctly for the sample annealed at 350 °C due to the very high level of preferred orientation which is at the limits of what the Rietveld analysis method can be applied to, given that it is designed for the analysis of powder data. The patterns show different levels of diffuse scattering beneath the sharp Bragg peaks for samples annealed at temperatures of 150 and 250 °C, indicating the presence of defects that can only be eliminated at 350 °C.

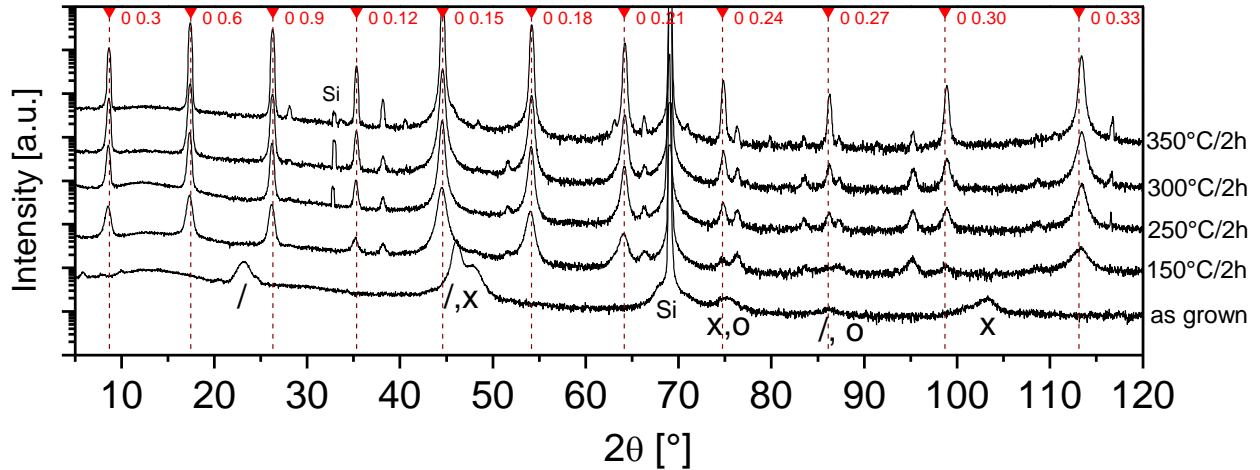


Figure 7.6 XRD patterns of the nanoalloyed SLs for different annealing temperatures. The positions and indices of the reflections (00.*l*) of Sb_2Te_3 are specified for comparison with the XRD data. A very strong degree of *c*-texture is evident. In the as grown state, broad reflections are evident that can be assigned to the elements or the compound phase. Reflex positions: *x* = Bi, *l* = Te, *o* = Sb.

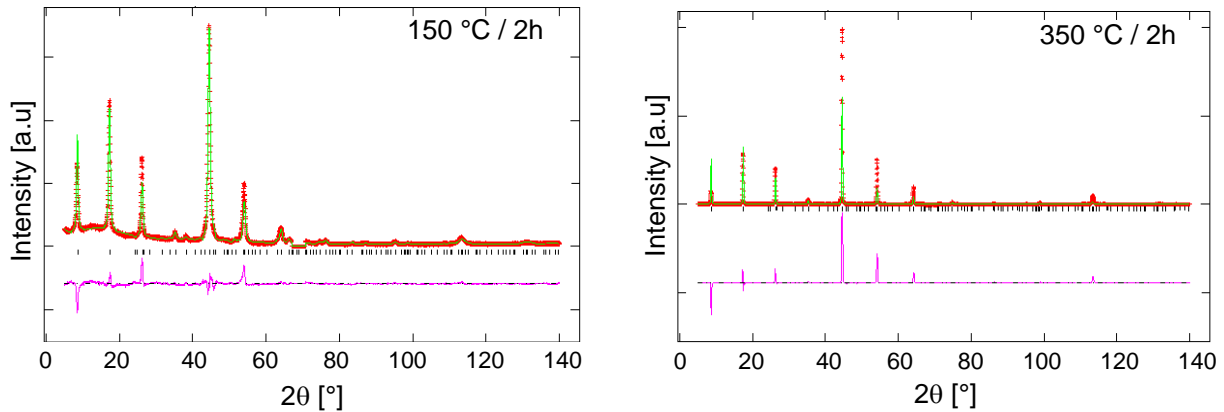


Figure 7.7 Plots of Rietveld-fitted XRD profiles for samples with 50 nm period length annealed at 150 °C and 350 °C.

The average crystallite size was calculated from the refined peak profile parameter L_x (section 4.3.1.2). The refinement results give crystallite sizes of 26, 64, 65, 221 nm at 150, 250, 300 and 350 °C, respectively and confirm that besides grain size also the degree of *c*-texture increases with annealing temperature (details given in [172]). The average crystallite size appears considerably smaller than for MBE-deposited binary compounds also annealed at 250 °C, shown in section 5.1, however the film texture has to be taken into account in this consideration. On the strongly textured sputtered SLs, almost only *c*-reflexes are observed. It also appears that the grains are flat (Figure 7.5 and Figure 7.15), i.e. the dimension in *c*-direction is smaller. In contrast, the binaries show a clearly lower degree of orientation and the grains are not flat. From this it is assumed that the crystallites are larger in the crystalline directions observed in the XRD pattern.

7.2 Electrical properties

The electrical properties of the SLs are given in Figure 7.8 and Figure 7.9. Two samples were analysed for each annealing temperature.

The film annealed at 350 °C had a rough and porous structure (Figure 7.5). The thickness value obtained by averaging over the cross section was used to calculate σ and μ from the Hall-van-der-Pauw measurements. However, it is generally questionable if the Van-der-Pauw method with its idealizations [137] can be applied accurately to rough and porous samples. For this reason, the electrical values, though following the expected trend are to be treated with caution, especially when comparing them to

the ones obtained on the smooth films annealed at lower temperatures. Before annealing, the SLs have rather (semi)metallic properties, i.e., a low S and a high n . This behaviour can be explained on the basis of the XRD results that clearly demonstrate that the as deposited film contains a mixture of elements and traces of V_2VI_3 compounds. After annealing, n drops sharply to $3\text{-}5 \times 10^{19} \text{ cm}^{-3}$ for all annealing temperatures while S ranges from ~ 150 to $\sim 190 \mu\text{V/K}$. The carrier mobility increases monotonously for an increasing annealing temperature, which can be explained with the grain growth and also the stronger degree of c -orientation of the films since for the examined compounds the highest μ are obtained perpendicular to the c -axis (section 3.3). Extending the annealing time from 2 h to 24 h leads to a significant increase of μ resulting in a high PF . In comparison, increasing the annealing temperature from 250 to 300 °C seems to have a stronger effect on μ and PF which can be explained by grain growth following Ostwald ripening (section 4.1.1).

The Seebeck coefficient in dependence of annealing temperature follows a characteristic parabolic trend that was apparent in all sputtered nanoalloyed films (see also the n-type films presented in chapter 8). At 150 °C, strongly expressed diffuse scattering (Figure 7.7) indicates a significant number of unspecified defects in the films. It is possible that a part of these defects is electrically active, generates charge carriers and lowers S . At 250 °C, diffuse scattering is noticeably reduced and S increases. For higher annealing temperatures and thus larger grain sizes, S decreases again. An explanation may be the effect of grain boundaries. Experiments on nanocrystalline PbTe [173] and Bi_2Te_3 [174] showed that S decreases with larger grain sizes. For PbTe , an energy filtering effect (see section 2.2.1) is proposed. The grain boundaries are theorized to act as a sort of filter for low-energy electrons and thus increase S [173].

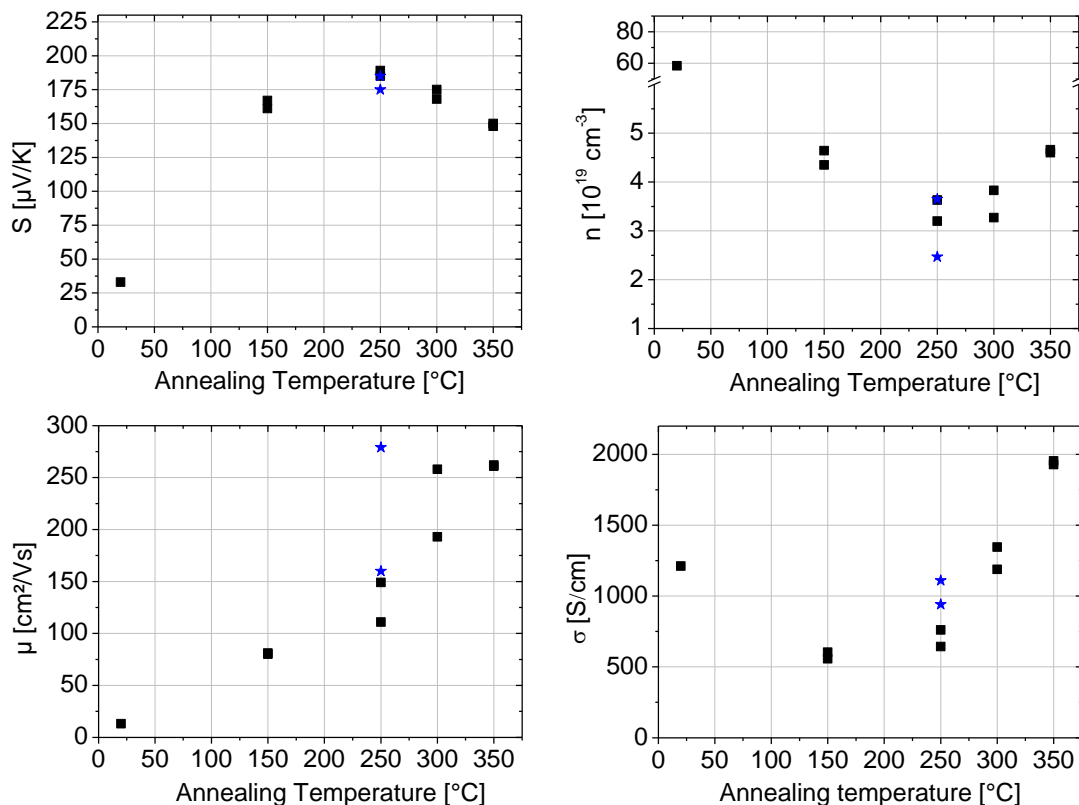


Figure 7.8 Electrical properties as function of annealing temperature. Black squares: 2 h annealing time. Blue stars: 24 h annealing time. Error bars were omitted for clarity.

Additionally, a Pisarenko plot (description see section 5.2, actual plot not shown here) was carried out. All data points were found to be on one Pisarenko line, confirming that only one compound, i.e. the V_2VI_3 phase as already seen in the XRD data is contributing to carrier transport.

7.3 Power factor and thermal conductivity

Overall, power factors of more than $40 \mu\text{W}/\text{cmK}^2$ could be achieved (Figure 7.9), exceeding the best values reported for p-type sputtered material that is similar in composition but homogeneous (maximum *PF* of $39 \mu\text{W}/\text{cmK}^2$, see Table 3.4 in section 3.4). The obtained *PF* were even comparable to bulk single crystals of $(\text{Bi}_{0.2}\text{Sb}_{0.8})_2\text{Te}_3$ ($37\text{-}51 \mu\text{W}/\text{cmK}^2$, measured along the basal plane [90]). Further attempts were made to improve the electrical properties by adjusting the stoichiometry to stoichiometric proportions, i.e. near the composition of 40:60 for (Bi/Sb):Te. It was found that the properties of the films strongly depend on the composition of the deposited material (Table 7.1). The deviation from the stoichiometric composition induces crystal defects (e.g. antistructure defects as described in section 3.3) and thus affects the transport properties, predominantly the charge carrier concentration and -mobility. The highest charge carrier mobility is obtained for sample 3, which can be seen as near stoichiometric taking into account the measurement uncertainty of ~ 0.5 at. %. Compared to sample 2 (properties shown in Figure 7.8 and Figure 7.9), the *PF* increased by 25 %. If this increase is extrapolated to higher annealing temperatures, power factors of nearly $50 \mu\text{W}/\text{cmK}^2$ could be possible. This assumption seems to be justified since for similar nanoalloyed MBE films with the same nominal composition, power factors of $52 \mu\text{W}/\text{cmK}^2$ were reported for an annealing treatment at 350°C [175].

Table 7.1 Electrical properties of nanoalloyed SLs with slightly different Te contents annealed at 250°C for 2 hours. Units as previously defined in Table 5.1. c_{Bi} and c_{Sb} are element concentrations determined by EDX in at. %.

Sample No.	c_{Bi}	c_{Sb}	c_{Te}	d	μ	n	σ	S	<i>PF</i>
1	4.8	38.6	56.7	0.82	82	6.5×10^{19}	850	136	16
2	3.9	37.4	58.7	1.65	149	3.2×10^{19}	761	189	27
3	4.3	36.1	59.6	0.85	228	3.2×10^{19}	1160	172	34

The cross-plane thermal conductivity of the thin films was determined by TDTR. The results are shown in Figure 7.9. Due to the very high roughness of the film annealed at 350°C no TDTR measurement was possible. The unannealed film had a relatively high thermal conductivity due to the large electrical conductivity of the elemental constituents. Similarly as described in section 6.2.2, for the annealed films λ_l was calculated with λ_{el} that was calculated from σ assuming an anisotropy factor of 3.3 (average value of bulk, see section 7.5) and the Lorentz number of bulk, calculated as described in section 2.1.1.1 on the base of the BTE formalism.

As expected, the thermal conductivity increases with higher annealing temperature due to the increased grain size, which also has a positive effect on the electrical conductivity. The cross-plane thermal conductivities of the *c*-oriented SLs are generally lower than that of comparable bulk single crystals of $(\text{Bi}_{0.2}\text{Sb}_{0.8})_2\text{Te}_3$ ($\sim 0.7 \text{ W/mK}$) or Sb_2Te_3 ($0.9 - 1.4 \text{ W/mK}$) measured parallel to the *c*-axis [90]. A reference homogeneous sample of $(\text{Bi}_{0.2}\text{Sb}_{0.8})_2\text{Te}_3$ annealed at 200°C for 2 h also shows a reduced thermal conductivity compared to bulk material.

From the available data, it can be concluded that there are two effects that reduce the thermal conductivity of the SLs compared to bulk material:

1.) There is a general reduction of thermal conductivity due to the polycrystalline nature of the thin films. Already in previous works on V_2VI_3 materials, a smaller grain size was found to correlate with a lower value for the thermal conductivity. For Bi_2Te_3 , a reduction of $\sim 25 - 45\%$ was found in comparison to single crystalline material [38,39], details see section 8.2.2. Related results were given for a *c*-oriented polycrystalline film of $(\text{Bi}_{0.25}\text{Sb}_{0.75})_2\text{Te}_3$ on mica by Boikov et al. [37] who reported a thermal conductivity reduction of 15 % when comparing an unannealed film with more grain boundaries to an annealed film, details see section 2.1.2.1.

2.) The nanostructuring should also affect the thermal conductivity. The film annealed at 150°C , which after annealing has the most perfect or best defined ML structure according to the SIMS depth profiles clearly shows the lowest total and lattice thermal conductivity of all SL films (Figure 7.9, right). In

comparison to its components Sb_2Te_3 and $(\text{Bi}_{0.2}\text{Sb}_{0.8})_2\text{Te}_3$ annealed at the same temperature, λ and λ_l appear slightly lower, yet the difference does not exceed the measurement uncertainty. In comparison to the predictions of the Debye-Callaway model for homogeneous $(\text{Bi,Sb})_2\text{Te}_3$ (section 2.1.2.1 [38], grain sizes taken from Rietveld refinement), the measured values for λ_l are generally lower. Remarkably, λ_l of the film annealed at 150 °C falls below the DC model for a homogeneous alloy by 30 %, while the values of the more homogenized films annealed at 250 and 300 °C are only lower by 10 - 20 %.

To conclude, it appears that the ML structure indeed has a slight, albeit hardly measurable influence on thermal conductivity in contrast to the MBE-deposited nanoalloyed SLs shown in section 6.2.2 and the n-type sputtered SLs shown in chapter 8 where no clear effect could be observed. It is noted that further evidence on the effect of 2D nanostructuring on thermal conductivity for nanoalloyed material is shown in section 7.6. A (lattice) thermal conductivity of (0.26) 0.40 W/mK that is clearly lower than that of both SL components can be achieved by reducing the period length of the sputtered SLs. *However, it must be noted that due to interdiffusion effects at higher annealing temperature it was not possible to combine a 2D-nanostructure-related low thermal conductivity with a high power factor – this is a **key point** to achieve high ZT values with SL structures as demonstrated on the MOCVD-grown films [8].*

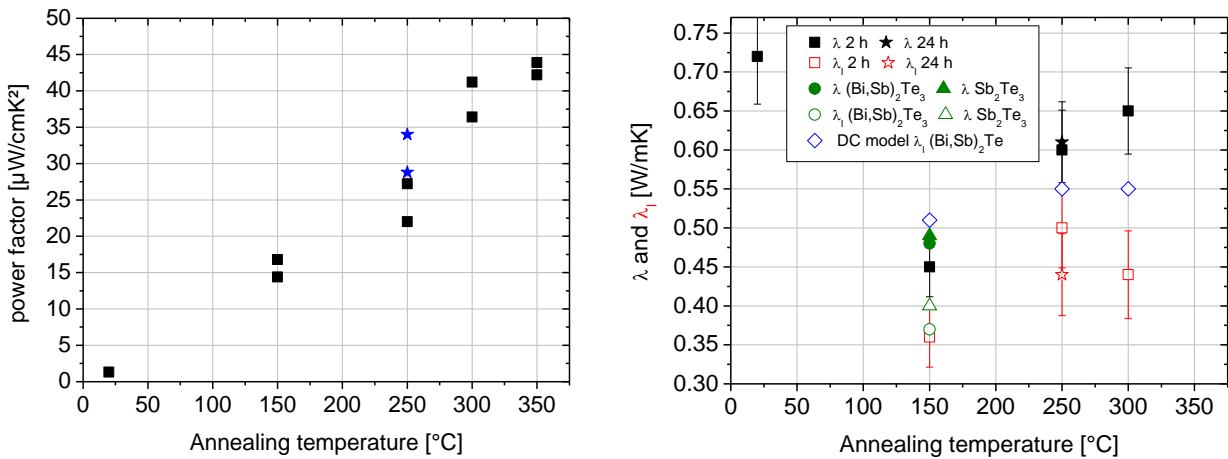


Figure 7.9 Left: Power factors as function of annealing temperature. Black squares: 2 h annealing time, blue stars: 24 h annealing time. Error bars were omitted for clarity. Right: Cross-plane total (full symbols) and lattice (empty symbols) thermal conductivity λ and λ_l as function of annealing temperature. Squares: SL, 2 h annealing. Stars: SL, 24 h annealing. Green circle: SL component $(\text{Bi}_{0.2}\text{Sb}_{0.8})_2\text{Te}_3$. Green triangle: SL component Sb_2Te_3 . Blue diamonds: Prediction of λ_l by Debye-Callaway model (section 2.1.2.1 [38]). Error bars of binaries (same size as error bars of SLs) were omitted for clarity

7.4 Upscaling of film thickness and cross-plane measurement of electrical conductivity

For a mass fabrication of sputtered thin films, the question whether the film thickness can be upscaled is a very important one since efficient microscale thermoelectric devices need film thicknesses of at least several 10 μm [176]. For this reason the film thickness of the nanoalloyed films was upscaled to 18 μm . The experiments were carried out on BaF_2 substrates due to the low mismatch of thermal expansion coefficient with the film that becomes relevant at high film thicknesses. The sputtering times required for this thickness were ca. 50 h. Due to the high requirements on the process stability, deposition required considerable preparation and surveillance of the sputtering process (see also section 4.1.4).

For the films, critical points to be clarified were the preservation of the ML structure in spite of the the long sputtering times and the ion-impact induced film heating during sputtering. SEM cross-sections on unannealed films (Figure 7.10) with a thickness of $\sim 18 \mu\text{m}$ revealed that the nanoscale ML structure could be sustained throughout the whole thickness of the films and that, just as in the thinner films, an annealing at 250 °C for 2 h lead to a complete crystallization. A slight roughness in the element layer pattern was caused by the formation of Te droplets as described in section 4.1.4.4.

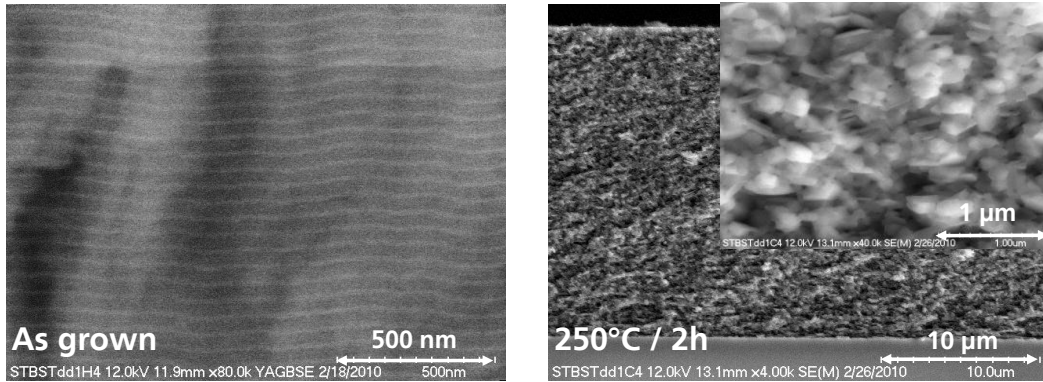


Figure 7.10 SEM cross sections of SLs with $\sim 18 \mu\text{m}$ thickness, BSE image. Left: As grown. The ML structure is clearly visible. Right: After annealing at $250 \text{ }^\circ\text{C}$ for 2 h. The whole film has crystallized and is still relatively smooth. The inset shows the grain structure in higher magnification.

The transport properties of a reference film with a thickness of $0.85 \mu\text{m}$ deposited with the same deposition parameters, sample 3 in Table 7.1, were nearly identical to that of the $\sim 18 \mu\text{m}$ thick film, showing together with the structural properties that the SL fabrication process can be upscaled and leads to very well reproducible film properties.

7.4.1 Electrical cross-plane conductivity measurements on thick films

First measurements or rather estimations of the cross-plane electrical conductivity were carried out on the films at the laboratory of Ali Shakouri, University of Santa Cruz, California using the quadratic pillar structure shown in Figure 7.11. The samples were annealed at $250 \text{ }^\circ\text{C}$ for 24 hours and then prepared in cooperation with Micropelt GmbH using Inductive Coupled Plasma etching. The process parameters as well as the metals used as contacts are confidential. The current was applied and the voltage taken between the Bi cap layer, serving as (nominally) equipotential contact pad and the layer “metal 1”, serving as back contact. A total of four measurements were carried out on pillars with side lengths of $70 \mu\text{m}$ and $80 \mu\text{m}$. Due to the high thickness ($d \sim 20 \mu\text{m}$) of the films, well measurable resistances R_p in the range of $40\text{-}50 \text{ m}\Omega$ were obtained. The contacts were ohmic as evident from the linear voltage / current relation. The contact resistance for the material combination was estimated to be around $1 \text{ m}\Omega$ and thus was negligible. The cross-plane conductivities σ_c were obtained by $\sigma_c = d/(AR_p)$ with A as pillar footprint. The obtained average of the four measurements was 725 S/cm .

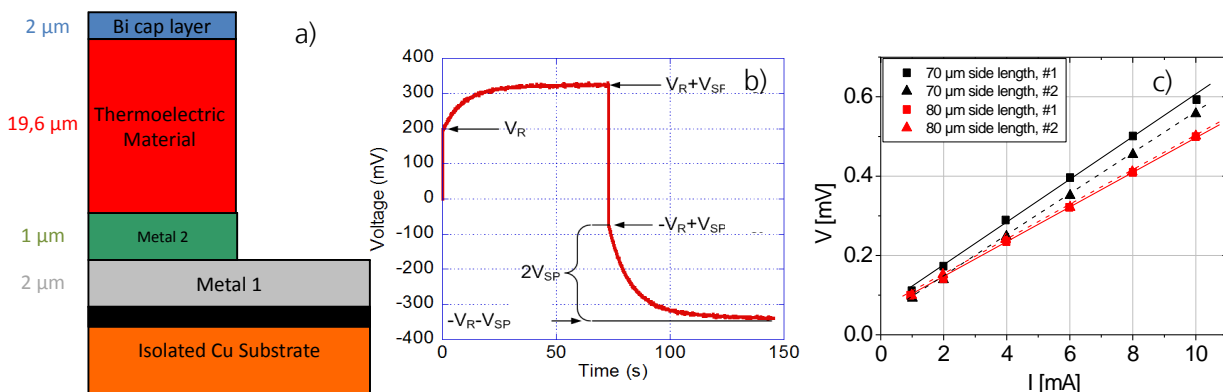


Figure 7.11 a) Fabricated pillar structure used for the measurement of cross-plane electrical conductivity. b) Exemplaric voltage transient observed during measurement on bulk Bi_2Te_3 [177]. c) Voltage / current lines on different pillars ($70 \mu\text{m}$ and $80 \mu\text{m}$ side length), showing that an ohmic contact was established.

However, thermoelectric effects have to be taken into consideration. When a current is applied to the pillar structure, the Peltier effect leads to a temperature gradient between top and bottom of the pillar. Through the gradient, a Seebeck voltage V_{SP} is generated that is superimposed on the ohmic part of the

voltage V_R which is used to determine the pillar resistance R_p (Figure 7.11 and ref. [178]). V_{SP} rises gradually, with the rise time being proportional to sample thickness. Due to the extremely fast voltage signal rise time in the range of few ms on the thin films, it was not possible to separate the two voltage components with the measurement equipment currently available, so the total voltage $V_{tot} = V_R + V_{SP}$ had to be used to calculate R .

There is a considerable error when calculating σ_c from this R . According to Harman, the ratio of V_{SP} to V_R is directly proportional to the ZT value, e.g. $ZT = V_{SP} / V_R$ [179]. Figure 7.11 shows as an example a recorded voltage transient for bulk Bi_2Te_3 ($ZT \sim 0.6$) with a voltage overestimation of $\sim 60\%$ and thus a conductivity underestimation by $\sim 40\%$ if V_{tot} is taken instead of V_R . The error in the examined films should be qualitatively similar. Furthermore, it is not fully clear how good the top Bi layer fulfills its idealized role as an equipotential contact pad with negligible resistivity. Nevertheless, the obtained value can serve as a first estimate. Currently, extensive works are underway to assemble a measurement setup and sample structuring technique that can be applied to determine V_R and thus the conductivity accurately, however this is beyond the scope of this thesis.

7.5 Estimation of ZT

To obtain or estimate the ZT value, the electrical data obtained in in-plane direction (in this case, perpendicular to the c -axis) must be appropriately combined with the data for the thermal conductivity obtained in cross-plane direction (parallel to the c -axis) taking into account the anisotropy of the transport properties in the examined materials. Until now, only little is known about the anisotropy of the Seebeck coefficient for SL thin films in the examined material system. Hence, a basic assumption is made that S is isotropic, similar to bulk $(\text{Bi}_{0.2}\text{Sb}_{0.8})_2\text{Te}_3$ that exhibits a S anisotropy of only $\sim 3\text{-}13\%$ [90]. Then, ZT can be estimated as follows:

1.) Concerning the electrical conductivity, one of the reasons that Venkatasubramanian's SL has reached very high ZT values was the elimination of the electrical conductivity anisotropy [8]. Assuming that this is also the case for the sputtered SL thin films annealed at $300\text{ }^\circ\text{C}$, a cross-plane value for ZT of ~ 1.9 is obtained being unusually high for sputtered thin films and being able to compete with the values presented by Venkatasubramanian.

2.) Another estimation can be made based on the assumption that the conductivity anisotropy factor corresponds to bulk values of ~ 3.3 , being an average of the anisotropy factor for Sb_2Te_3 of ~ 3.9 for comparable material and of $(\text{Bi}_{0.2}\text{Sb}_{0.8})_2\text{Te}_3$ of ~ 2.6 [90]. Using this average anisotropy factor ZT is reduced to ~ 0.6 , which is still a good value for sputtered nanocrystalline thin films (see Table 3.4).

3.) The correct value of ZT is expected to be between the two values given in 1. and 2. Using the estimated cross-plane electrical conductivity of $\sigma_c = 725\text{ S/cm}$, the cross-plane $\lambda = 0.6\text{ W/mK}$ and in-plane $S = 165\text{ } \mu\text{V/K}$, a ZT value of 1 can be estimated. This is to be considered a lower limit for ZT since σ_c is underestimated by up to 50% as described above. In this case of underestimation, a value of 2 would be the upper limit. A more accurate definition of the cross-plane ZT for the thin films requires the determination of the Seebeck coefficient and electrical conductivity in cross-plane direction. Further efforts are under way to enable this type of sophisticated characterization.

In conclusion, evidence is that ZT should be in the range of **1-1.9**, which is a very good value for (sputtered) thin films (see also Table 3.4).

The reduction in thermal conductivity necessary for this high value was achieved by nanocrystallinity rather than through a SL type nanostructure. A ZT of 1.4, i.e. within the range of values for the sputtered SLs obtained here was also reported by Boikov et al. on polycrystalline p-type material, see section 2.1.2.1. Recent calculations for $\text{Bi}_2\text{Te}_3 / \text{Sb}_2\text{Te}_3$ SLs (section 2.2.1.1) give a maximum ZT value of 0.9-1.3 which is also comparable to the estimated values for the sputtered SLs.

7.6 Reduction of period length

According to literature, a reduced period length (PL) should result in a lower thermal conductivity (i.e. potentially improved thermoelectric performance) as proposed in previous work, see e.g. 2.2.2. In order to verify this, the PL of the system was reduced by halving and quartering the initial element layer thicknesses given in Figure 7.1, resulting in a multilayer PL of 25 nm and 12.5 nm. In order to ascertain a weak interdiffusion of the SL structuring, annealing was only carried out at 150 °C for 2 h.

7.6.1 Structural properties

According to first experiments with sputtered nanoalloyed thin films [163], the degree of *c*-orientation should be more pronounced when reducing the element layer thickness in the deposition pattern. Indeed, the film with the smallest PL was almost exclusively *c*-oriented already after annealing at 150 °C with almost no reflections except the (00.*l*) series observed (Figure 7.12). To the best of our knowledge, the films presented here show the highest degree of *c*-orientation ever obtained for sputtered V₂VI₃ thin films.

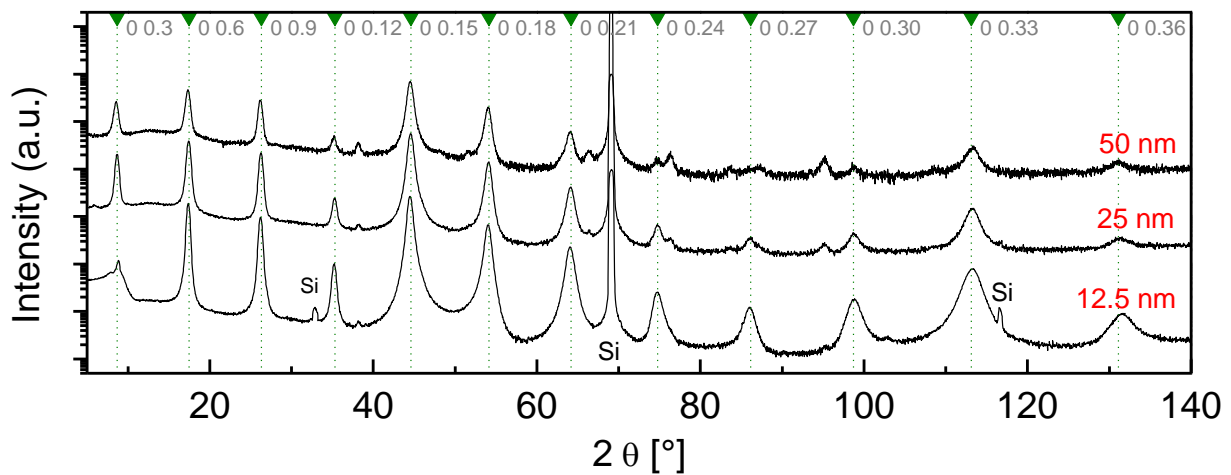


Figure 7.12 XRD patterns of nanoalloyed SLs with reduced PLs of 25 and 12.5 nm. The positions of the (00.*l*) reflections of Sb₂Te₃ are indicated together with the respective indices.

In additional SIMS depth profile analysis of the SL with nominally 12.5 nm PL, the ML structure is clearly present throughout the whole thin film even at this small SL dimension (Figure 7.13). High-resolution XRD analysis of the (00.6) and (00.9) lattice reflexes reveals weak SL reflexes in the form of peak shoulders. Their position closely matches the diffraction angles calculated for the SL satellites (eq. 4.22) with the corresponding PL. At the position of a peak, the slope shows a local minimum. Therefore, to better indicate the position of the shoulders the first derivative is also plotted. To the best of our knowledge, this is the first report of SL satellites observed on sputtered V₂VI₃ thin films.

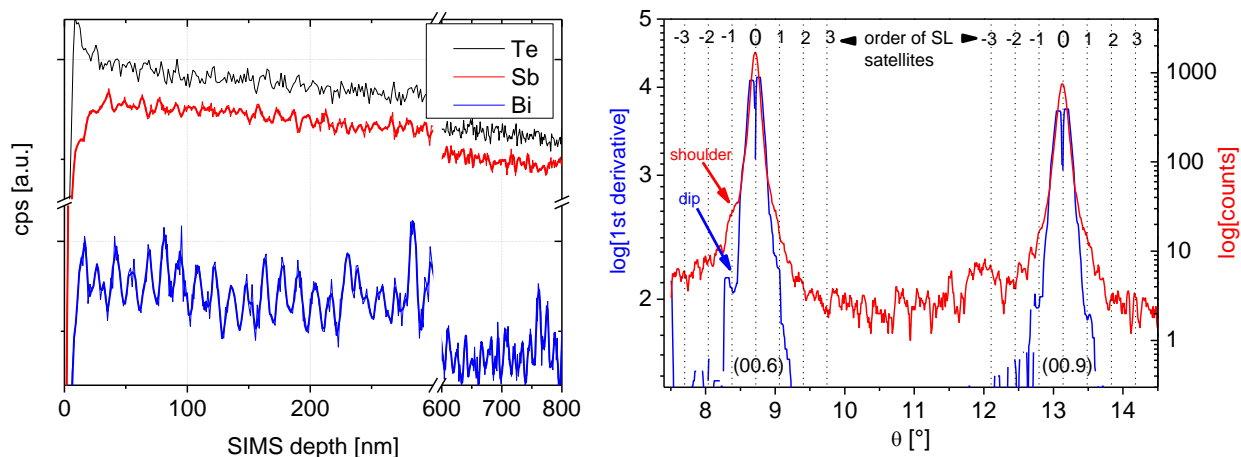


Figure 7.13 Left: SIMS depth profile of low-periodic SL, the spacing of the dips and peaks corresponds to the nominal PL of 12.5 nm. Slight signal smoothing is applied (thick lines). Right: HRXRD analysis of the (00.6) and (00.9) reflexes in the same SL, showing satellite shoulders. Additionally, the first derivative exhibits local minima at the shoulder diffraction angles.

SEM images (Figure 7.14) indicate that the 25 nm – film exhibits a grain structure similar to the 50 nm film (Figure 7.5) with slightly larger grains and that the grains of the 12.5 nm film exhibit a significantly larger size parallel to the film plane. The XRD patterns exhibit sharper and more intense reflexes with decreasing PL. The width of the (00.9) reflex decreases from 0.55° to 0.5° to 0.47° when going from 50 to 25 to 12.5 nm, i.e. the crystallite size in c-direction ranges from 14-17 nm according to eq. 4.21.

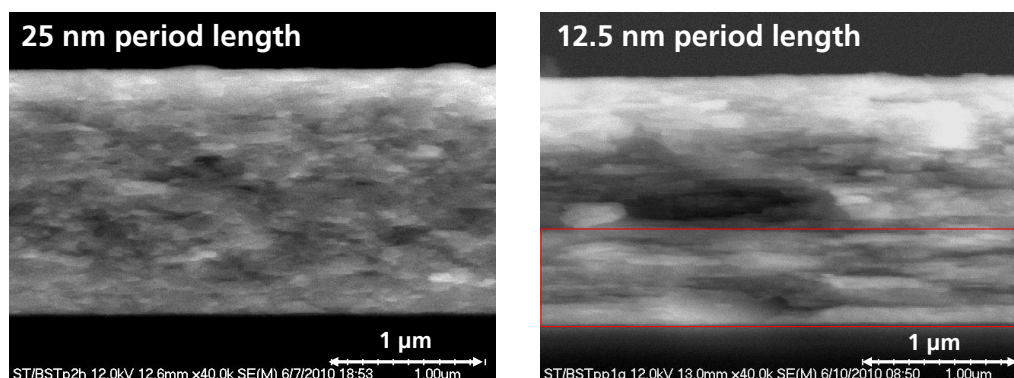


Figure 7.14 SEM images of SLs with a PL of 25 and 12.5 nm, showing large grains for the latter.

A STEM image, Figure 7.15, displays the high quality of the ML structure with a remarkably smooth layer structure that is evident through virtually all the sample area analysed, in strong contrast to the “spot-like” remainders of the ML structure in MBE-deposited SLs shown in section 6.1.2. As anticipated, the stronger c-orientation clearly results in a higher stability of the ML structure against interdiffusion. The crystallites are flat (as already suggested by the SEM analysis) with a length of ~ 50 -150 nm parallel to the film plane and ~ 20 -40 nm perpendicular to it. Their basal plane is mostly parallel to the substrate plane, i.e. the element layers in the deposition pattern (see SAED pattern). A slight tilt is evident by a weak splitting of the (00. l) related diffraction spots. The SAED pattern shows a superposition of at least three zones ([11.0],[21.0],[31.0]), indicating rotational disorder of the crystallites.

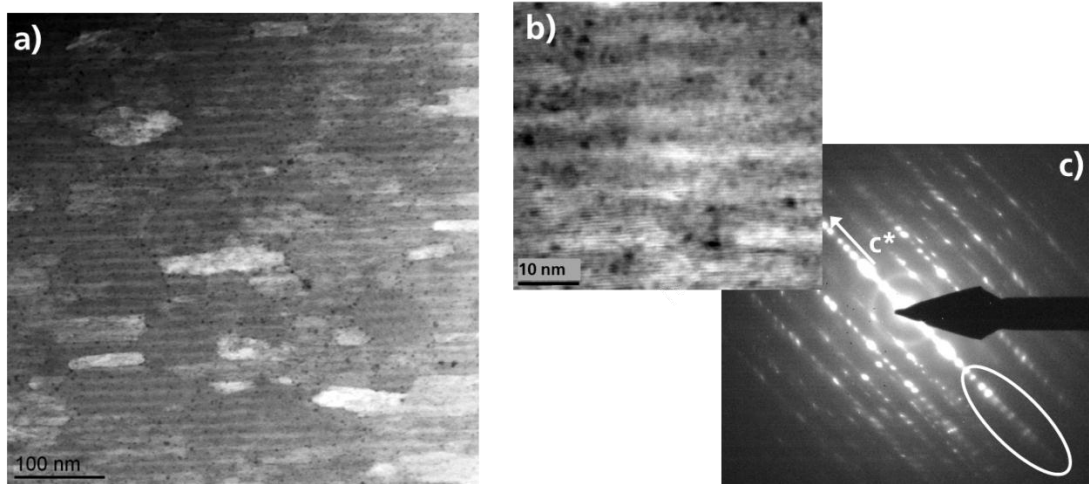


Figure 7.15 STEM images of sputtered SLs with reduced PL. a) Overview, showing the consistency and high smoothness of the ML structure. b) Detailed image of the SLs with higher magnification. c) SAED pattern showing a superposition of different zones and a slight grain tilt, indicated by a weak splitting of the diffraction spots belonging to the (00.l) reflexes (white oval).

7.6.2 Transport properties

The transport properties of SLs with different PLs are shown in Figure 7.16. The most prominent trend is an increase of carrier mobility with decreasing PL in accordance with the stronger c-orientation and higher grain size in in-plane direction as described in the preceding section.

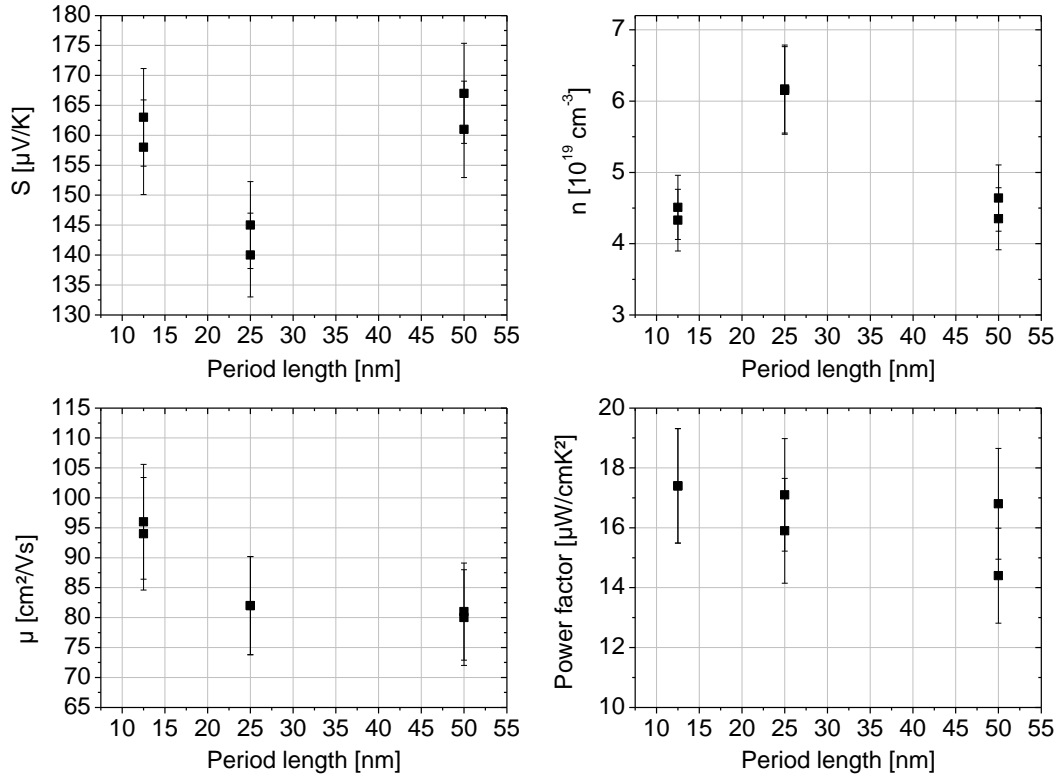


Figure 7.16 Electrical properties of SLs with different PLs in comparison. For each run, 2 samples were analysed.

λ was measured and λ_l calculated as already described in section 7.3. The main goal of reducing the thermal conductivity by the SL structure could be partially reached. There clearly is a reduction of (lattice) total thermal conductivity when going from 50 to 25 nm PL. The λ_l of 0.26 W/mK is as low as the lowest λ_l reported for the MOCVD-grown SLs (0.22 W/mK [8]), however the PF is again clearly lower. Due to the well-defined SL structure, apparently a reduction of λ_l by the 2D SL structure is possible despite the already strong reduction by the nanocrystallinity. However, no further reduction was observed when reducing the PL further (Figure 7.17).

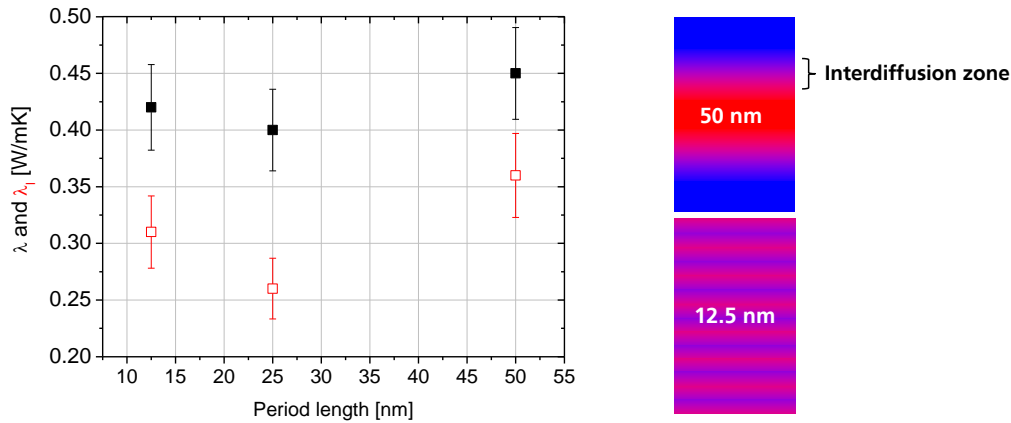


Figure 7.17 Left: λ (black full squares) and λ_l (red empty squares) of SLs with reduced PL. Right: Schematic of SLs with different PL, assuming equal diffusion lengths or interdiffusion zones. A loss of “material contrast” or homogenization is evident as illustrated by the coloration.

Two competing effects are supposed to be at work when reducing the PL: An increase of phonon scattering with lower PL and a simultaneous reduction of material contrast, i.e. a homogenization due to interdiffusion that is present even for perfectly c -oriented films since a significant amount of interdiffusion already takes place in the (partially) amorphous precursor state, see section 6.1.1. Assuming that the diffusion length or interdiffusion zone at the same annealing temperature is equal, samples with lower dimensionality will exhibit a higher level of “relative intermixing” (as illustrated in Figure 7.17 with colors) and the whole system becomes more and more similar to a homogeneous alloy. This assumption is supported by the SIMS depth profiles that show a reduced oscillation amplitude of the Bi signal. The ratio of peak to dip intensity decreases from 3.5 to 2 and 1.6 at PLs of 50, 25 and 12.5 nm, respectively. Possibly, the two mentioned effects cancel out each other so that no effective reduction of thermal conductivity occurs. Lastly, the grain size in the 12.5 nm film is apparently bigger than that of the other films (Figure 7.14). It is possible that this increase in grain size has led to an increase in λ that superimposes a small reduction by the reduction of the PL.

7.7 Conclusions

Nanoalloyed p-type Sb_2Te_3 / $(\text{Bi,Sb})_2\text{Te}_3$ SL films (period length of 50 nm) with very strongly expressed c -orientation and high smoothness were fabricated by sputtering. The SL films yielded low $\lambda \sim 0.45 - 0.65$ W/mK and very high $PF > 40 \mu\text{W}/\text{cmK}^2$ comparable to single crystalline bulk materials, with potential for further improvement. A ZT between 1.0 (conservative estimation) and 1.9 (optimistic assumptions) was estimated. The film thickness could be upscaled to $\sim 18 \mu\text{m}$ while the properties could be maintained, opening a path for an application of the technique to actual device mass-fabrication.

The SL structure was well-expressed up to annealing temperatures of 300°C , but increasingly smeared out at higher temperatures. A small effect of the SL structure on lattice thermal conductivity was observed, however it appeared rather small compared to the effects of the nanocrystallinity. After lowering the period length, an exclusive c -orientation was observed and the SL structure was so well-expressed that SL satellite reflexes were observed on sputtered V_2VI_3 thin films for the first time. A very low λ of 0.4 W/mK ($\lambda_l = 0.26$ W/mK) was found when going to a PL of 25 nm.

8 Sputtered n-type Bi_2Te_3 / $(\text{Bi,Sb})_2\text{Te}_3$ multilayer systems grown by nanoalloying

Böttner et al. have shown that the nanoalloying process can be applied to create n-type Bi_2Te_3 / $\text{Bi}_2(\text{Se,Te})_3$ – SLs by sputtering [163]. The obtained thin films were strongly c-oriented and showed power factors of around $20 \mu\text{W}/\text{cmK}^2$. However, as also experienced during this work the sputtering of Se can cause several problems due to its low melting point and thermal conductivity combined with very high vapor pressure. Se deposition is also a problem in thermal evaporation methods since Se is known to evaporate in the form of Se_x ($x \geq 2$) molecules with poor chemical reactivity, necessitating the use of a cost-intensive cracker cell [180]. For these reasons, an alternative n-type SL system was developed where the $\text{Bi}_2(\text{Se,Te})_3$ layer was replaced with n-type $(\text{Bi,Sb})_2\text{Te}_3$, Figure 8.1.

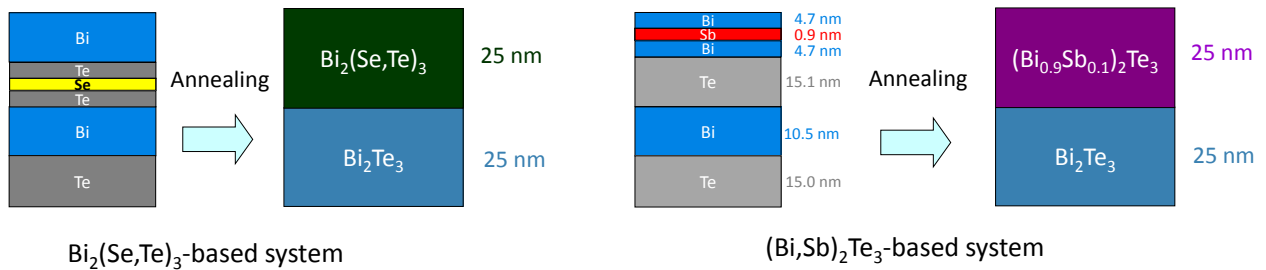


Figure 8.1 Left: $\text{Bi}_2(\text{Se,Te})_3$ – based SL system examined in [163]. Right: n-type $(\text{Bi}_{1-x}\text{Sb}_x)_2\text{Te}_3$ – based system examined in this work. The shown pattern was repeated 30 times to give a total thin film thickness of $\sim 1.5 \mu\text{m}$.

8.1 Optimization of Sb-content in $(\text{Bi,Sb})_2\text{Te}_3$

The optimal Sb-content in $(\text{Bi}_{1-x}\text{Sb}_x)_2\text{Te}_3$ for the SL films had to be determined. On one hand, the reduction of thermal conductivity is expected to be more pronounced for higher Sb-contents. On the other hand, $(\text{Bi}_{1-x}\text{Sb}_x)_2\text{Te}_3$ bulk samples tend towards p-type conduction for higher Sb contents x . However, it had previously been found that the defect chemistry and transport properties of $(\text{Bi}_{1-x}\text{Sb}_x)_2\text{Te}_3$ thin films differ remarkably from that of bulk materials, (see e.g. section 5.2) so that previous results from bulk materials could not be transferred to thin films. Consequently, to determine the optimum Sb content three nanoalloyed homogeneous films of $(\text{Bi}_{1-x}\text{Sb}_x)_2\text{Te}_3$ with $x = 0.05, 0.1, 0.2$ were examined. The measurement of the element concentrations by EDX proved to be problematic since there is a strong overlap of the Sb and Te peaks in the spectrum and no element calibration standard was available for low Sb concentrations. Therefore, the Sb fraction was extrapolated from experiments with EDX concentration measurements with alloys of Sb+Bi. The determined Te content of the films ranged between 59.4 and 60 at. %. The electrical transport properties in dependence x are given in Figure 8.2.

Compared to the bulk material, the carrier mobility for the examined material compositions close to Bi_2Te_3 is significantly lower. The inferiority of μ compared to bulk material was already observed for binary nanoalloyed and epitaxial Bi_2Te_3 films grown with an MBE setup, section 5.2.1 and Table 3.4. The decrease in charge carrier mobility with increasing Sb content can be explained by alloy scattering of the charge carriers. The decrease of mobility does not exactly follow the linear trend reported for bulk materials (section 2.1.1.3). Interestingly, for $x = 0.05$ and 0.10 , the Seebeck coefficient increases slightly (in conformance with reports from literature, section 3.3) while the charge carrier concentration remains constant, yielding an increased PF . For $x = 0.2$, there is a sharp drop in n while S remains constant which may be explained by the introduction of first holes as charge carriers with larger Sb contents that compensate with the electrons. As a consequence of the low charge carrier concentration, the power factor drops significantly.

Obviously, a Sb content of $x = 0.1$ offers the best compromise between sufficiently high element contrast and good electrical properties. Thus, $(\text{Bi}_{0.9}\text{Sb}_{0.1})_2\text{Te}_3$ was used in the SL systems.

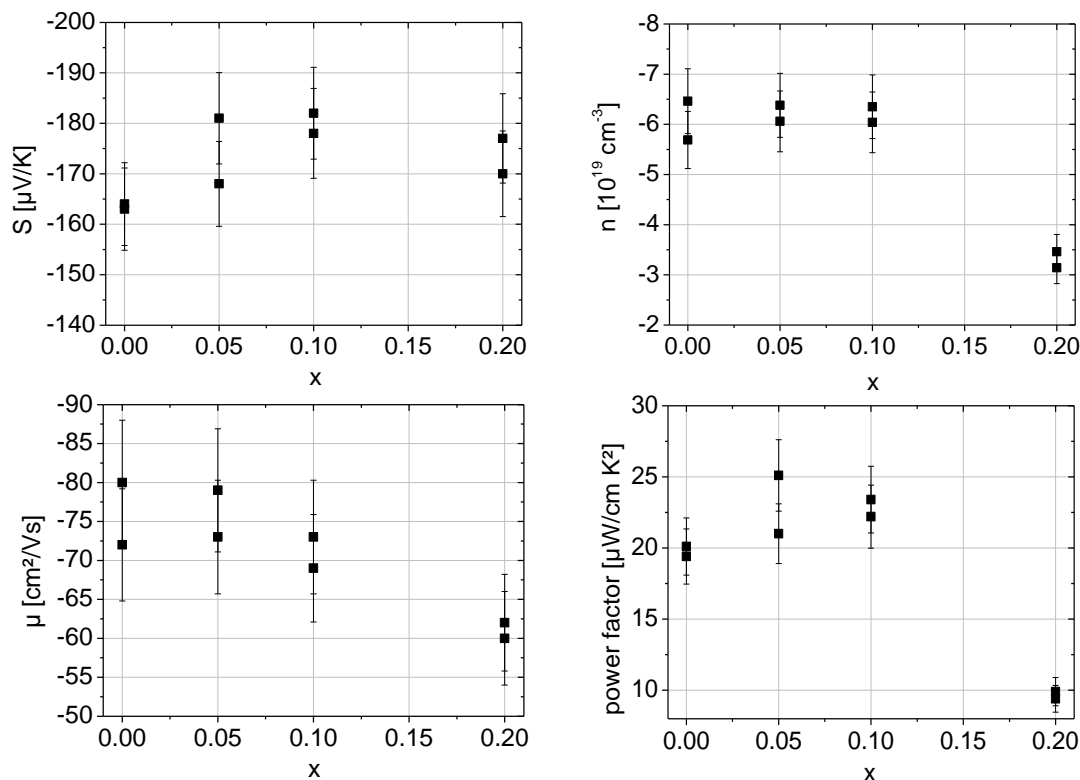


Figure 8.2 Electrical properties of $(\text{Bi}_{1-x}\text{Sb}_x)_2\text{Te}_3$ in dependence on Sb content x after annealing for 2 hours at 250 °C. To verify reproducibility and consistency of the results, two samples from each growth run were analysed. A negative sign of n indicates electron conduction.

8.2 Bi_2Te_3 / $(\text{Bi},\text{Sb})_2\text{Te}_3$ – SL systems

8.2.1 Structural characterization

The Bi_2Te_3 / $(\text{Bi}_{0.9}\text{Sb}_{0.1})_2\text{Te}_3$ SLs were annealed at 150, 200, 225, and 250 °C for 2 hours. The determined Te contents of the annealed films ranged from ~ 59.1–60.3 at. %. This measurement is not completely reliable due to Sb and Te peak overlap in EDX and the absence of an appropriate calibration standard with similar matrix properties. SEM cross-sections of the as-grown and annealed films are shown in Figure 8.3. The thin films become slightly rough during sputtering and are covered with spherical bumps with a diameter of ~ 500 nm and a height of ~ 100 nm. These bumps gradually appear in sputtered Bi-rich layer systems after the total thin film thickness exceeds ca. 800 nm. The appearance of the bumps is due to the roughness of sputtered Bi as shown in section 4.1.4.3. During deposition, the roughness caused by Bi gradually adds up and leads to a roughening of the total layer system. In the as-grown state, BSE imaging clearly reveals a multilayered structure with a spacing of 25 nm for the Bi-rich areas and a period length of 50 nm as intended (Figure 8.3, top left). After annealing platelet-like grains appeared which are preferably aligned parallel to each other. Such morphology was found as a characteristic feature on similar p-type nanoalloyed films (chapter 7), demonstrating a strong c -axis orientation of the films. The grain sizes increase with annealing temperature. At an annealing temperature of 250 °C, additional hill-like structures with a height of several 100 nm begin to appear that mark the onset of recrystallization processes due to increasing bulk diffusion. Similar to p-type SLs, a further increase of annealing temperature would lead to very rough thin films with holes, unsuitable for device fabrication (Figure 7.5). The degradation of thin film morphology was observed in a homogeneous thin film of $(\text{Bi}_{0.9}\text{Sb}_{0.1})_2\text{Te}_3$ that was annealed at 300 °C (not shown here).

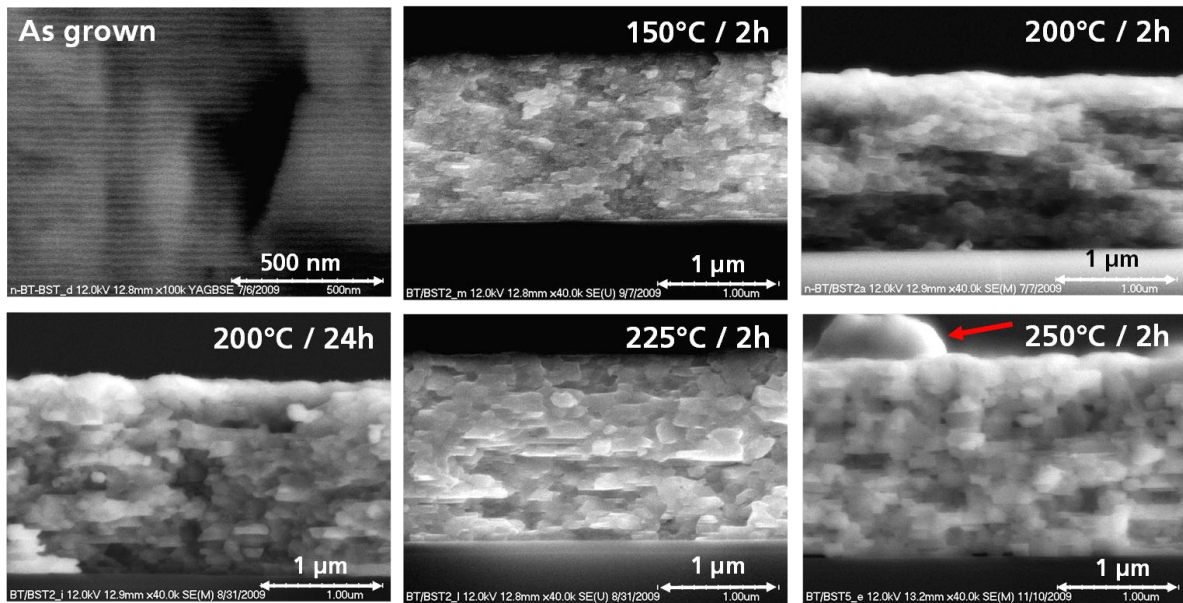


Figure 8.3 SEM cross-sections of Bi₂Te₃/(Bi_{0.9}Sb_{0.1})₂Te₃ SLs in as-grown and annealed state for different annealing temperatures. The as grown image is a back scattered electron image. Images for 150 °C and 225 °C are shown as secondary-electron-only image for a better resolution of the individual grains and for demonstration of grain growth. The grain size increases with annealing temperature and starting at 250 °C, the film roughness increases significantly, i.e. additional flat and large hill-like structures appear (red arrow).

Figure 8.4 shows XRD patterns for samples annealed at three temperatures and in the as grown state. Already for the as-grown sample broad reflections of the compound phase can be observed. Additional broad reflections arise from amorphous or not fully crystallized material. For the annealed samples pronounced reflections of the (00.*l*) type beside weak (*hk.l*) reflections are detected. The sharpening and increasing intensity of the (00.*l*) reflections with increasing annealing temperature indicates larger grain sizes in agreement with the SEM images.

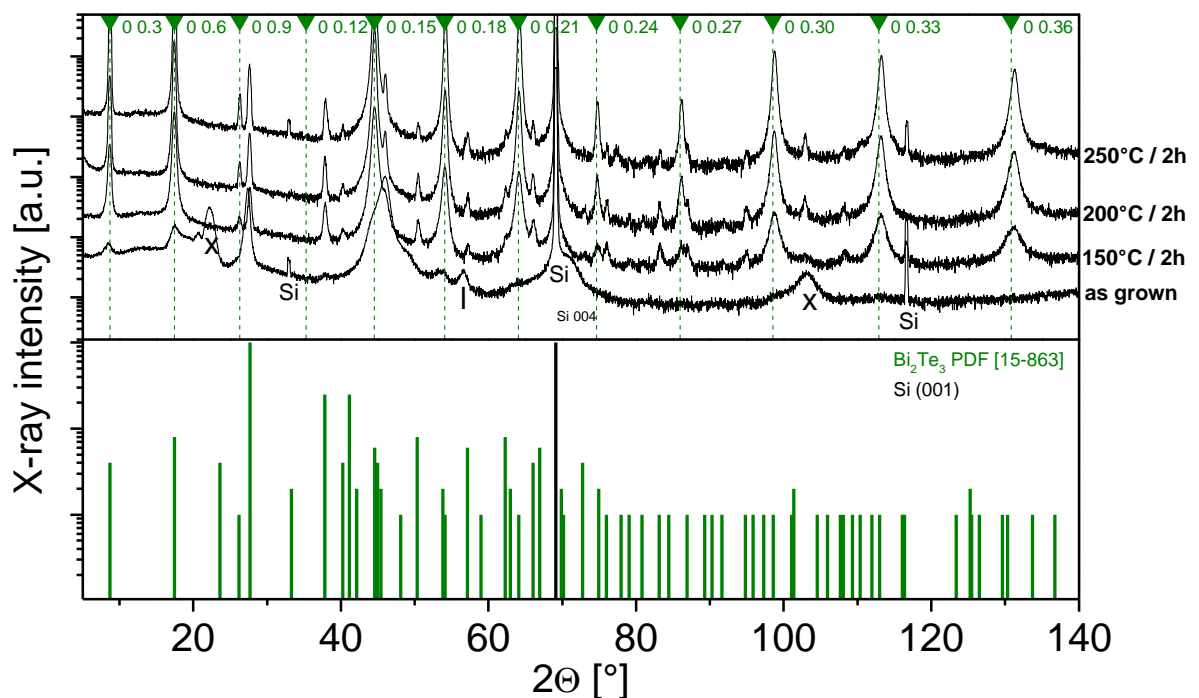


Figure 8.4 $\theta - 2\theta$ scan of Bi₂Te₃/(Bi_{0.9}Sb_{0.1})₂Te₃ – SLs, logarithmic intensity scaling. From top to bottom: 250, 200, 150 °C, and as grown. (00.*l*) – reflections of Bi₂Te₃ are indicated by dashed lines. For comparison, a powder diffractogram (JCPDS database) is shown as vertical bars below the experimental patterns. X = Bi, I = Te.

Rietveld analysis was carried out on the XRD patterns recorded for the samples annealed at 150, 200, 250 °C, yielding crystallite sizes of 38, 86 and 124 nm, respectively (more details on the refinement are given in [181]). All data could be fitted to a rhombohedral unit cell with the space group $R\bar{3}m$.

The characterization of the ML structure via SIMS depth profiling proved to be difficult since the thin films exhibited considerable roughness as mentioned above and consequently, the mass spectrometer signals for the different ions were noisy. For the SIMS analysis, a modified layer system was deposited where the sequence of the metal/chalcogen layers was inverted so that the thin film growth started with Bi instead of Te. The films deposited with the inverted deposition pattern exhibited less roughness, allowing a better evaluation of the ML structure. However, XRD patterns showed that there was a much less defined c-texture than for the original sequence, so the SIMS profiles (Sb ion signals), shown in Figure 8.5, give only a lower limit for the thermal stability of the ML structure. After annealing at 250 °C, there is no clear proof that a ML structure is still present. At 200 °C, the thin film definitely shows a chemical segregation of Sb, and therefore the stability of the SLs is considered to be stable up to that temperature.

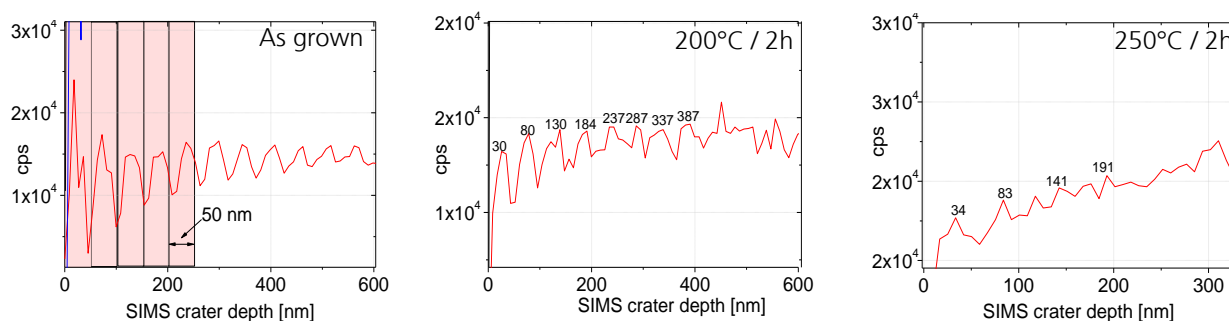


Figure 8.5 SIMS depth profiles of $\text{Bi}_2\text{Te}_3 / (\text{Bi}_{0.9}\text{Sb}_{0.1})_2\text{Te}_3$ – SLs with modified stacking sequence annealed for 2 h at different temperatures. The Sb ion signal is plotted versus the crater depth. Numbers indicate the peak positions. The spacing between the peaks corresponds to a SL period length of 50 nm.

Overall, the chemical segregation appears significantly less defined than for similarly grown, nanoalloyed sputtered p-type $\text{Sb}_2\text{Te}_3 / (\text{Bi}_{0.2}\text{Sb}_{0.8})_2\text{Te}_3$ SL films (section 7.1) and was not observed throughout the whole film. SEM images of the SIMS crater support this assumption as shown in Figure 8.6: At 150 °C annealing temperature, only very faint indication of the SL structure was observed, while the SL was clearly observed in the p-type films annealed at 250 °C. We assume that this is predominantly a consequence of the lower degree of c-texture compared to the p-type samples. It is also possible that the diffusion coefficient of Sb in Bi_2Te_3 is higher than that of Bi in Sb_2Te_3 , however due to a lack of literature data on this subject this cannot be verified.

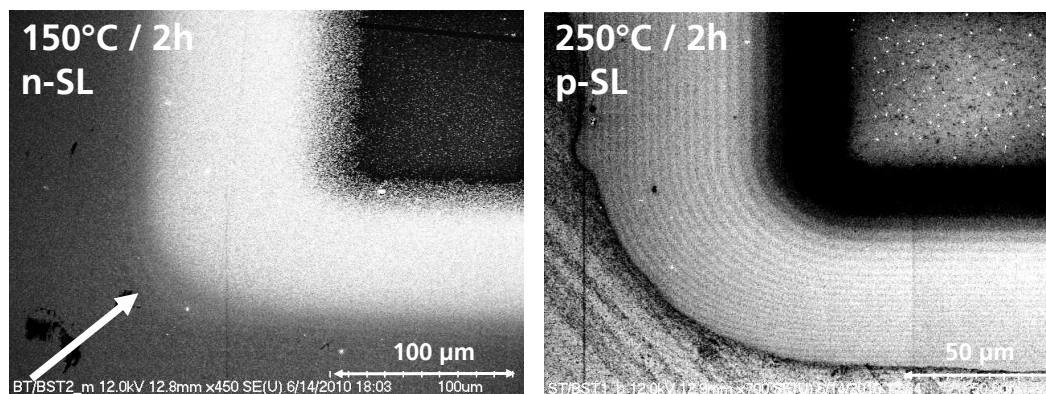


Figure 8.6 SEM images of SIMS craters of n-type $\text{Bi}_2\text{Te}_3 / (\text{Bi}_{0.9}\text{Sb}_{0.1})_2\text{Te}_3$ and a p-type $\text{Sb}_2\text{Te}_3 / (\text{Bi}_{0.2}\text{Sb}_{0.8})_2\text{Te}_3$ SL (section 7.1). In spite of the lower annealing temperature, the ML structure in the n-type SLs (only faint traces visible, see white arrow) appears only weakly expressed in comparison to the p-type SL that could be observed throughout the entire film.

8.2.2 Transport properties

In Figure 8.7, the electrical properties of the SLs are shown and compared to the results of the sputtered Bi₂Te₃ / Bi₂(Se,Te)₃ – SLs [163]. As already observed on nanoalloyed binaries (section 5.3), the as-grown film has metallic characteristics (low S and μ , high n) due to the presence of pure Bi layers (see XRD patterns). The dependence of electrical properties on annealing temperature is analogous to the p-type SLs shown in section 7.2 and 7.3. With increasing grain size, μ improves for higher annealing temperatures and S follows a parabolic trend. A high maximum S of ~ -190 $\mu\text{V/K}$ was achieved.

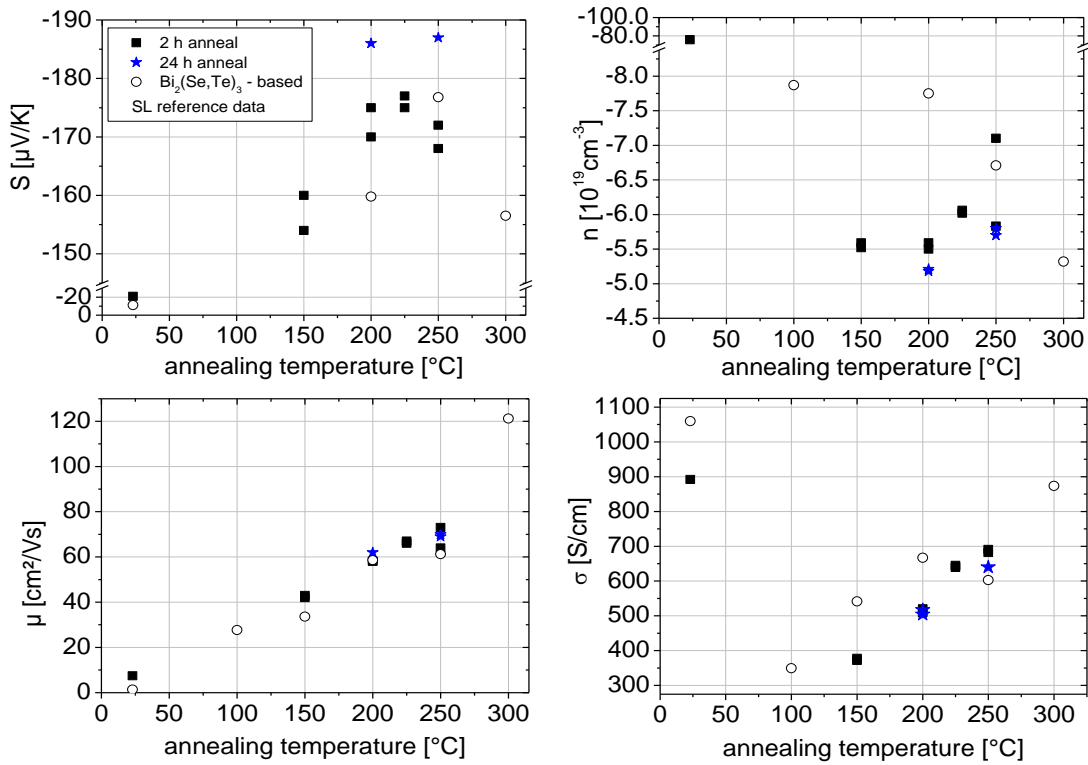


Figure 8.7 Electrical transport properties of Bi₂Te₃ / (Bi_{0.9}Sb_{0.1})₂Te₃ – SLs annealed at different temperatures. Full squares: Thin films from this work, annealed for 2 h. Blue stars: Thin films from this work, annealed for 12 h (250 °C) and 24 h (200 °C). Black empty circles: Bi₂Te₃ / Bi₂(Se,Te)₃ – SLs [163] with a similar period length of 45 nm, annealed for 2 h. Note the broken axis in the top graphs. Error bars omitted for clarity. A negative sign of n indicates electron conduction.

Generally, a longer annealing time leads to a higher power factor as seen in Figure 8.8. With an annealing time of 2 h, power factors of ~ 20 $\mu\text{W}/\text{cmK}^2$ can be attained. Increasing the annealing time to 12 h offers the possibility to gain another small increase in power factor up to 22 $\mu\text{W}/\text{cmK}^2$. This is among the highest values reported for n-conducting Bi₂Te₃-based sputtered thin films (see Table 3.4), however, the texture of the deposited material also has to be taken into account when comparing different values. Another very important point is that the SL system Bi₂Te₃ / (Bi_{0.9}Sb_{0.1})₂Te₃ can compete with similarly textured Bi₂Te₃ / Bi₂(Se,Te)₃ SLs in terms of electrical properties while being significantly easier to sputter due to the substitution of problematic Se by Sb.

The cross-plane thermal conductivity at room temperature was determined with the TDTR method in dependence of the annealing temperature, Figure 8.8. For the annealed films, the shown λ_l was estimated from λ in a similar manner as shown in section 6.2.2 and 7.3, i.e. by assuming 1.) the Lorenz number for Bi₂Te₃ (Figure 2.2) and 2.) an electrical conductivity anisotropy factor of 4 (value for Bi₂Te₃ [90]). Due to the roughness of the films the estimated measurement uncertainty is higher than for smooth films and is around 11-20 %. The homogeneous films serving for comparison were prepared with the Bi₂Te₃ and (Bi_{1-x}Sb_x)₂Te₃ partial pattern from the SL deposition pattern.

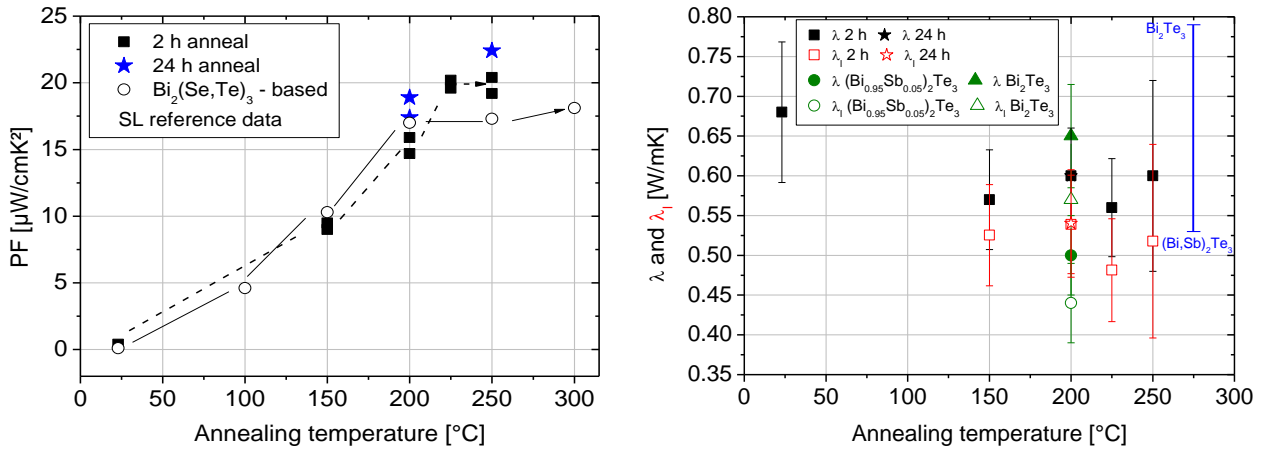


Figure 8.8 Left: PF of Bi_2Te_3 / $(\text{Bi}_{0.9}\text{Sb}_{0.1})_2\text{Te}_3$ – SLs versus annealing temperature. Dashed line: Eyeguide. Right: Cross-plane total and lattice thermal conductivity λ and λ_l as function of annealing temperature. Black full squares: SL, 2 h annealing. Black star: SL, 24 h annealing (at 200°C , not visible since value is identical to the one after 2 h annealing). Green circle: Homogeneous film of $(\text{Bi}_{0.95}\text{Sb}_{0.05})_2\text{Te}_3$. Green triangle: Homogeneous film of Bi_2Te_3 . Blue bar: Range of λ_l as predicted by Debye-Callaway model. Grain sizes L of the films in this work were taken from the Rietveld refinement (values given in section 8.2.1). Empty data points: λ_l corresponding to the λ value given by the filled data point.

The cross-plane thermal conductivity of the strongly c -axis oriented homogeneous thin film of Bi_2Te_3 is significantly lower than that of comparable single crystalline bulk Bi_2Te_3 ($\lambda \sim 1 \text{ W}/\text{mK}$ along the c -axis [90]). This reduction is due to the polycrystalline nature of the material. Analogously, in previous works a smaller grain size was also found to correlate with a lower value for λ (section 2.1.2.1, [39][38]). Thermal conductivities of 0.55 - 0.75 W/mK for polycrystalline Bi_2Te_3 with a grain size from 30 - 100 nm were reported in agreement with the value for Bi_2Te_3 measured here.

Figure 8.8 reveals three characteristic features that indicate that the ML nanostructuring has no measurable effect on thermal conductivity within the measurement uncertainty limits.

- 1.) λ and λ_l of the SL at any annealing temperature are not lower than the average thermal conductivities of comparable homogeneous compounds Bi_2Te_3 and $(\text{Bi}_{0.95}\text{Sb}_{0.05})_2\text{Te}_3$.
- 2.) There is also no minimum in λ and λ_l at 150°C where the SL is still relatively well preserved.
- 3.) The λ_l of the films are comparable to values given by a Debye-Callaway (DC) model for homogeneous films of Bi_2Te_3 and $(\text{Bi},\text{Sb})_2\text{Te}_3$, section 2.1.2.1. From the model, a lower boundary for λ_l of 0.53 W/mK is obtained for $(\text{Bi},\text{Sb})_2\text{Te}_3$ with a grain size $L = 38 \text{ nm}$ and an upper boundary of 0.79 W/mK is obtained for Bi_2Te_3 with $L = 124 \text{ nm}$. The $\text{Bi}_2\text{Te}_3/(\text{Bi}_{0.9}\text{Sb}_{0.1})_2\text{Te}_3$ – SLs are “weakly alloyed” with low contents of Sb and fall between a binary and the modelled alloy. Thus, it is sensible to compare them to the range given by each of these two λ_l s as indicated in the figure. Evidently, the measured λ_l of the SL films are only slightly below this range, meaning that they are compatible to model predictions for homogeneous films. We note that also for homogeneous $(\text{Bi},\text{Sb})_2\text{Te}_3$ films, lower λ and consequently λ_l than anticipated from the model were observed in the reference.

The absence of any measurable reduction in λ and λ_l is not surprising since, at a period length of 50 nm, already for the p-type Sb_2Te_3 / $(\text{Bi}_{0.2}\text{Sb}_{0.8})_2\text{Te}_3$ SLs the observed reduction of the thermal conductivity was very small, if at all measurable (section 7.3). A plausible explanation for the weak effect was proposed in section 6.2.2 for MBE-grown SLs. Grain boundary scattering and ML nanostructuring act on the same phonon frequency range. Thus, it is possible that λ is so strongly reduced by the nanocrystalline structure that it cannot be further reduced by the, in the case of n-type SLs, weakly expressed ML-type 2D nanostructuring that is smeared out and has a low material contrast.

8.3 Conclusions

In this chapter, sputtered nanoalloyed n-type homogeneous compound films of Bi_2Te_3 and $(\text{Bi,Sb})_2\text{Te}_3$ and SL films were investigated. It was shown that n-type sputtered $(\text{Bi,Sb})_2\text{Te}_3$ could be used to replace $\text{Bi}_2(\text{Te,Se})_3$ layers, thus avoiding the use of Se targets which is of significant practical importance since these targets are difficult to handle. Power factors of 22-25 $\mu\text{W}/\text{cmK}^2$ that are very high for sputtered n-type material were obtained for optimized Sb content, i.e. for $(\text{Bi}_{0.9}\text{Sb}_{0.1})_2\text{Te}_3$. Relatively smooth films could be obtained for an annealing temperature of up to 225 °C.

Furthermore, a symmetric $\text{Bi}_2\text{Te}_3 / (\text{Bi}_{0.9}\text{Sb}_{0.1})_2\text{Te}_3$ SL with a period length of 50 nm was synthesized using different annealing temperatures. A distinct c-orientation of the sputtered layers was evident. SIMS depth profiles revealed that the ML structure was present up to an annealing temperature of 200 °C. High Seebeck coefficients of up to $\sim -190 \mu\text{V}/\text{K}$ were achieved. A relatively high maximum power factor of 22 $\mu\text{W}/\text{cmK}^2$ could be attained after annealing at 250 °C for 12 h. Cross-plane thermal conductivities were in the range of 0.55 to 0.6 W/mK. The thermal conductivity was generally reduced due to the nanocrystallinity of the material, however, there seemed to be no measurable reduction of the thermal conductivity by the SL-type 2D nanostructuring.

9 Epitaxial Bi₂Te₃ / Sb₂Te₃ binary thin films and superlattices

9.1 Binary thin films

For the growth of Bi₂Te₃ / Sb₂Te₃ SLs it was necessary to find an appropriate growth temperature and beam flux ratio that allowed

- 1.) to uphold the SL structure, i.e. keep temperature-driven interdiffusion at levels as low as possible and
- 2.) to grow both binary compounds as a smooth film with good transport properties.

In this work, it was aimed to select Te:Bi/Sb ratios and thus growth temperatures low enough to satisfy point 1.) and high enough to satisfy point 2). The task was significantly aggravated by the fact that the actual temperature of the substrate surface is different for each vacuum system and varies depending on substrate holder material, thickness, chamber design etc. In most cases, the temperature sensing device is located close to the heaters that are located *behind* the substrate holder, thus the surface temperature of the substrate that sits *on top* of the substrate holder is generally lower than the temperature measured at that point. The majority of authors does not give details how and where exactly the substrate temperature was measured. A transfer of reported growth parameters directly to the setup used in this work was therefore not possible. However, the used Te:Bi/Sb ratio allowed qualitative inference concerning the used temperature used since, inevitably, in general a higher temperature must be chosen for higher Te:Bi/Sb ratios since otherwise no stoichiometric film results.

9.1.1 Bi₂Te₃

Bi₂Te₃ thin films were synthesized using the same MBE system that was used in previous works by Nurnus et al. [42][100]. The detailed properties of the films were described in detail in the refs. and will not be further discussed here. After the previous works, the MBE system substrate holder including thermocouple was rebuilt due to a mechanical defect, leading to a change in the relation of the substrate temperature measured by the thermocouple to the actual substrate temperature. Thus, the process parameters (heater temperatures) given in [42-p.59ff] could not be applied. For the current experiments, a growth temperature of 350 °C and cell pressures of 2.9×10^{-7} and 2.0×10^{-7} (flux ratio ~ 3:2) Torr for were chosen for Te and Bi, respectively. Zou [111][112], Charles [130], George [182] et al. all used a ratio of $\geq 2:1$ at different growth temperatures. Nurnus chose a ratio of 12:5 [100]. Despite the Te:Bi ratio being lower than typically reported in literature, the parameters used in this work yielded stoichiometric smooth epitaxial films with very good structural and electrical properties. The mobility of $\mu = 80 - 90 \text{ cm}^2/\text{Vs}$ at $n = 1.4 - 1.6 \times 10^{20} \text{ cm}^{-3}$ even exceeds the values $\mu = 50 \text{ cm}^2/\text{Vs}$ at $n = 1.0 \times 10^{20} \text{ cm}^{-3}$ [100] reported by Nurnus on the same substrate type. Corresponding to the previous experiments and the reports on MOCVD films [117], the deposited Bi₂Te₃ was always n-type. The growth rate of Bi₂Te₃ films deposited with the mentioned parameters was 9.8 nm/min.

9.1.2 Sb₂Te₃

Parameters for growing high-quality epitaxial Sb₂Te₃ on the used system were unknown at the start of this work. In order to achieve suitable process parameters without having to examine too many combinations of effusion cell fluxes and substrate temperatures, the following optimization procedure to quickly find the optimum deposition temperature was applied:

- 1.) A deliberately low Te/Sb flux ratio was chosen in order to be able to work with comparatively low substrate temperatures. Typical ratios found in literature are high since attention was paid to optimizing the properties of the homogeneous binary films rather than trying to synthesize stable low-periodic SL stacks. As a starting point, the effusion cell fluxes were adapted from the successful growth of epitaxial Bi₂Te₃, i.e. a flux ratio of 3:2 was used. In contrast to this, Chien used a Te:Sb ration of 2:1 [183], Kim [102] used 1.8-4.3:1 and Cho [103] even 3.4-5.5:1 for Sb-rich (Bi,Sb)₂Te₃.
- 2.) For the chosen flux ratio of 3:2, the substrate temperature was varied between 330 and 370 °C, resulting in Te-rich films. At 330, 350 and 370 °C the Te contents were 65.2, 63.0 and 61.5 at. % Te,

respectively. Parallel experiments showed that high quality Bi_2Te_3 films could be grown at a temperature of 350 °C so this temperature was also chosen for the final optimization of the Sb_2Te_3 films in order to “unite” them to a superlattice with Bi_2Te_3 .

3.) To eliminate the mentioned residual Te excess, the beam fluxes were adapted using eq. 4.6. At a growth temperature of 350 °C a Te/Sb flux ratio of 1.2-1.3:1 was found to yield stoichiometric films. The growth rate of Sb_2Te_3 films deposited with the mentioned parameters was 6.9 nm/min.

9.1.2.1 Structural properties

The structural properties of the three films grown at 330, 350 and 370 °C were examined. XRD patterns showed a near perfect c-orientation of all films (Figure 9.1). Minor reflexes of which most correspond to other crystal planes of Sb_2Te_3 were evident, however the majority of these reflexes are only observable at 370 °C and do not exceed a peak height ratio of 100 – 1000 to the neighboring (00.l) reflexes. As expected due to the slight Te excess in the films, besides pure Sb_2Te_3 reflexes there are further reflexes that can be assigned to both Sb_2Te_3 and Te or Te only.

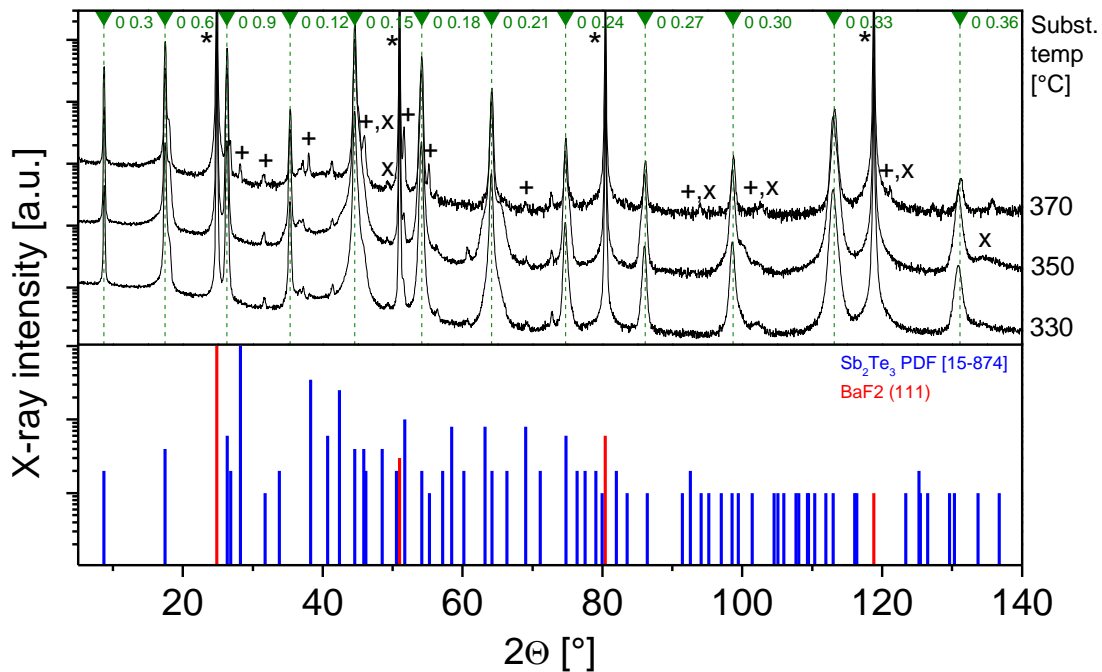


Figure 9.1 XRD pattern of epitaxially grown Sb_2Te_3 for different growth temperatures. * = substrate reflexes. + = reflexes belonging to Sb_2Te_3 with orientations different from (00.l), x = reflexes of Te.

SEM imaging confirmed that the films were smooth up to a deposition temperature of 350 °C. The typical layered structure already observed on the Bi_2Te_3 films [42-p.62] is also evident here. At 370 °C, the growth mode abruptly changed to a three dimensional growth mode. A change to islandic growth at higher substrate temperatures was also described in [60].

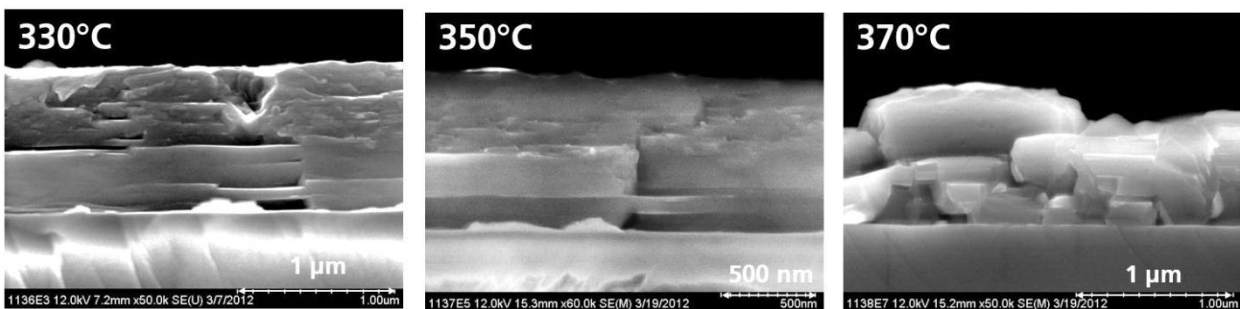


Figure 9.2 SEM cross sections of epitaxially grown Sb_2Te_3 for different growth temperatures.

XRD pole figures (Figure 9.3 a) reveal a three-fold symmetry and rotationally ordered growth. However, a small degree of rotational twinning, i.e. the existence of secondary crystallites with the same (00.) orientation but rotated by a fixed angle of 60° towards the primary crystallites is evident. Analogous twinning was also recently reported by Wang and Uher for MBE-grown Sb_2Te_3 ([97], unpublished data) and earlier for MBE-grown Bi_2Te_3 by Nurnus et al. [42-p.69,184]. The integral intensity ratio of main to twinned phase is roughly 20:1 (Figure 9.3 b). The twinning also becomes evident in the surface topology that could be observed especially well on the roughest films grown at 370°C (Figure 9.3 c). From a comparison of the ϕ -scan of Sb_2Te_3 to that of BaF_2 (not shown in the figure), an epitaxial relation analogous to the relation reported for Bi_2Te_3 on BaF_2 [42-p.69] was found.

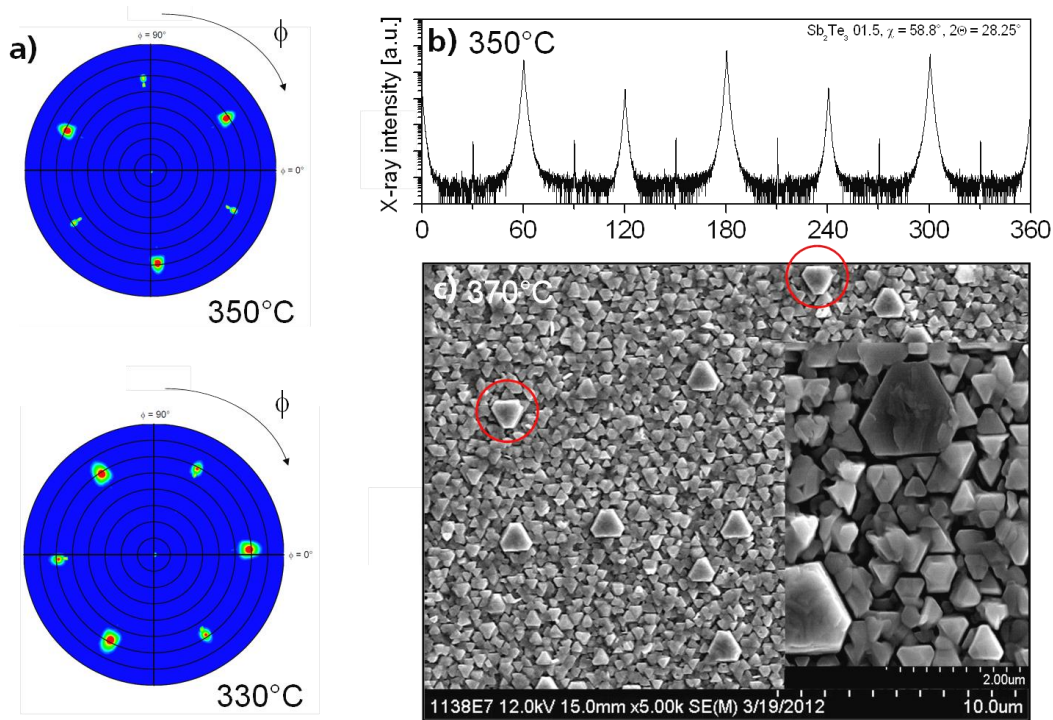


Figure 9.3 a) Pole figures of Sb_2Te_3 , 2θ was set to 28.25° , corresponding to the (01.5) reflex. The range of χ was $0 - 80^\circ$. Intensity is color coded, going from blue (lowest) over green to yellow to red (highest). b) Corresponding ϕ -scan carried out at $\chi = 58.8^\circ$ and $2\theta = 28.25^\circ$. c) SEM surface image of rough sample grown at 370°C , illustrating that the secondary phase consists of crystallites rotated by 60° towards the primary phase (red circles).

9.1.2.2 Electrical properties

The dependences of μ , n and S on Te content are given in Figure 9.4. and can be best observed on the films grown at 350°C (eyeguide). The behaviour is generally very similar to the nanoalloyed films (section 5.2.2), i.e. there is a quite drastic change when the Te content exceeds 60 at. %. The chosen low-temperature, low-flux ratio growth parameters yielded carrier mobilities reaching almost $500\text{ cm}^2/\text{Vs}$ which is to the author's knowledge among the best values reported (Table 3.4) and is not much lower than the highest carrier mobility of $680\text{ cm}^2/\text{Vs}$ recently reported by Wang and Uher ([65], growth temperature also 350°C).

The PF s are, remarkably, lower than that of the nanoalloyed polycrystalline films due to a different relation of S and n . For Seebeck coefficients of $120\text{-}140\text{ }\mu\text{V}/\text{K}$, the carrier concentration is regularly around or above $2.5 \times 10^{19}\text{ cm}^{-3}$ (Figure 5.10) while it is clearly lower for the epitaxial films. In turn, this also means that S is higher for the same n . Two possible reasons for this can be found:

1.) Effects of crystal texture. Nanoalloyed Sb_2Te_3 (section 5.1.2) has a significant proportion of grains with their c -axis not perpendicular to the measurement direction, which is parallel to the film plane. It follows that in contrast to the strictly c -textured epitaxial films, the measured transport properties of the nanoalloyed films are also influenced by the crystal properties parallel to the c -axis. Finally, it is known

that for the same n , S is higher in c-direction in Sb_2Te_3 (Table 3.2), explaining the lower Seebeck coefficients of epitaxial films towards nanoalloyed films.

2.) Effects of grain boundaries: In the nanoalloyed films, polycrystallinity can enhance S by grain boundary scattering, causing electron-filtering effects (details in section 7.2).

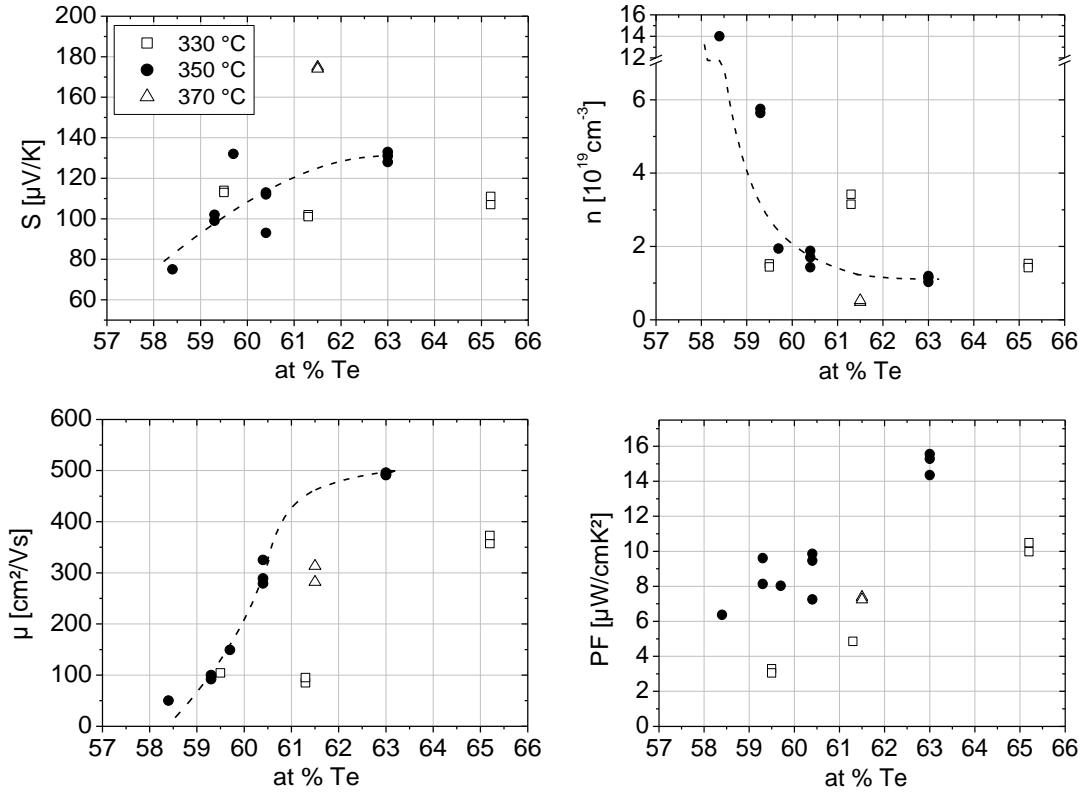


Figure 9.4 Electrical properties of epitaxially grown Sb_2Te_3 films as function of Te content. Symbols: See key in S vs. n plot. Dashed line: Eyeguide for dependence on Te content at 350 °C. Multiple samples of each growth run (e.g. Te content) were analysed to confirm reproducibility. Error bars omitted for clarity.

The electrical conductivity does not follow a clear trend with Te concentration. Similarly to the nanoalloyed films, the Pisarenko plot shows a different S/n relation for Te-rich and Te-deficient films (Figure 9.5).

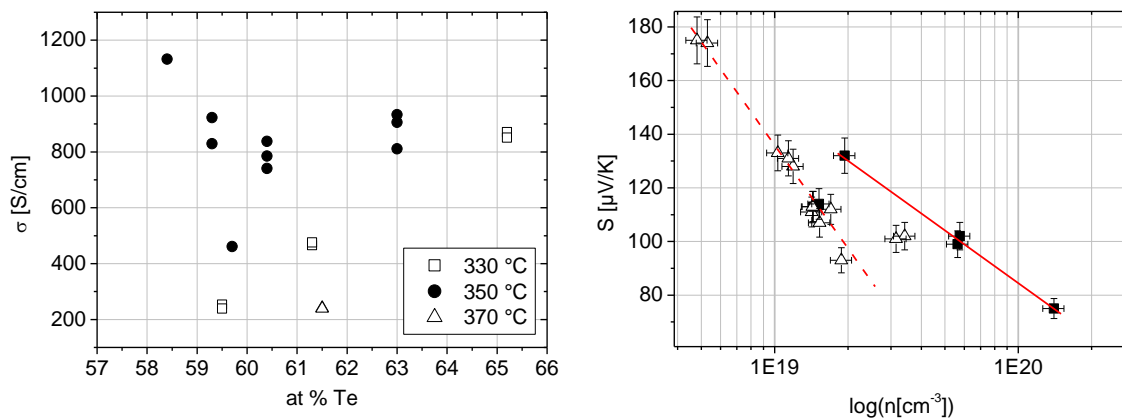


Figure 9.5 Left: Electrical conductivity of epitaxial Sb_2Te_3 films as function of Te content for different growth temperatures. Error bars omitted for clarity. Right: Pisarenko plot. The S/n relation is different for samples with Te excess (empty triangles, dashed line) and Te deficiency (full squares, full line).

9.2 Bi₂Te₃ / Sb₂Te₃ superlattices

SL structures with different period lengths and compositions were deposited and characterized. The determined optimal growth temperature of 350 °C (section 9.1) was used. Structural and transport properties are listed in Table 9.1 and will be discussed in the following sections. Special focus was put on the SLs with 6 nm period length (thickness of Sb₂Te₃ / Bi₂Te₃ 5 / 1 nm) since the record ZT value of 2.4 was reached with this SL dimension.

Table 9.1 Characteristic structural and transport properties of fabricated SLs. Units as previously defined in Table 5.1. Carrier concentration n in units of 10^{19} cm^{-3} . $d\text{-Sb}_2\text{Te}_3$ and $d\text{-Bi}_2\text{Te}_3$ are single compound layer thicknesses in nm. c_{Bi} and c_{Sb} are element concentrations determined by EDX in at. %. Values for 5 / 1 nm SLs are shaded in red. A negative sign of n indicates that electron conduction was determined from Hall-van-der-Pauw measurements.

Sample	$d\text{-Sb}_2\text{Te}_3$	$d\text{-Bi}_2\text{Te}_3$	N_{per}	c_{Bi}	c_{Sb}	c_{Te}	d	μ	n	σ	S	PF	λ
1	9	9	56	17.8	22.7	59.5	1.08	-4	-75	478	-42	0.8	0.51
2	5	1	166	5.8	34.2	60.0	0.96	46	4.2	368	121	5.4	0.6
3	5	1	166	6.0	33.9	60.1	1.02	43	4.1	284	80	1.8	
4	5	1	166	5.6	32.1	62.3	1.03	59	2.7	254	65	1.1	
5	5	1	166	5.7	34.3	60.0	1.00	59	3.9	363	127	5.9	
6	15	3	56	5.9	35.0	59.1	0.93	61	5.7	549	111	6.8	0.63
7	6	6	83	17.8	21.5	60.7	0.95	-28	-8.2	372	-75	2.1	0.50

9.2.1 Structural characterization

9.2.1.1 XRD analysis and SEM cross sections

Cross sections in Figure 9.6 show a smooth sample surface, a layered structure typical for strongly textured V_2VI_3 material and a sharply defined multilayered structure. Small bumps that can be associated with a slight Te excess are evident on sample 4.

A XRD analysis revealed a monocrystalline structure, an exclusive c-orientation of the films and consequently a much better definition of the SL structure compared to nanoalloyed films. In Figure 9.6, XRD patterns of samples 5, 7 and 6 with different PLs are compared. PLs of 6.0, 11.8, and 18.6 nm were determined from the patterns, showing a good agreement to the nominal values of 6, 12 and 18 nm.

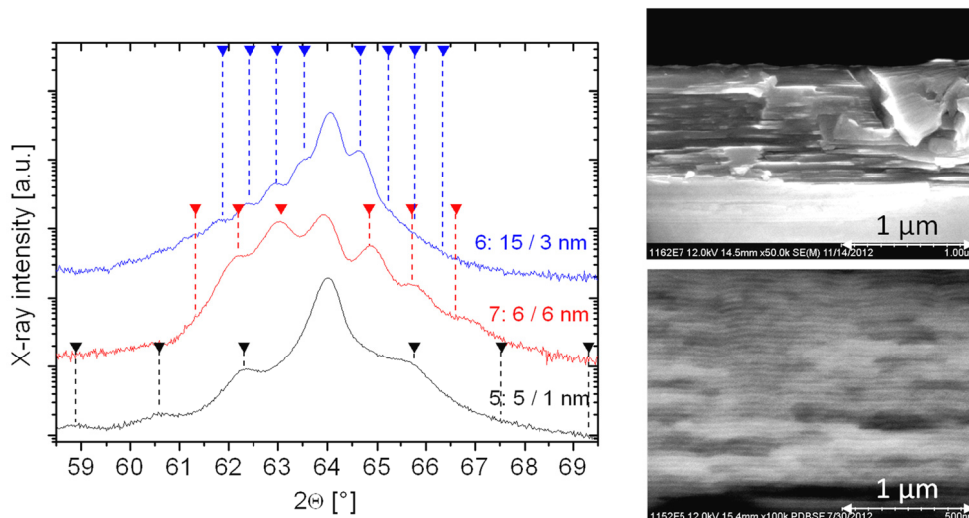


Figure 9.6 Left: XRD patterns of samples 5, 6 and 7 in the vicinity of the (00.21) reflex. Nominal satellite reflex positions according to the determined PLs are indicated by symbols and dashed lines. Black: Sample 5, blue: sample 6, red: sample 7. Right: SEM cross sections of sample 6 (top) and BSE image of sample 1 (PL of 18 nm, bottom).

Results on SLs with 6 nm period length

The results of the XRD analysis of samples 2 and 4 in grazing incidence geometry are shown in Figure 9.7. Both samples show clearly distinguishable SL satellites, indicating a very sharp definition of the SL structure. In sample 4, the SL satellites appear significantly more intense. The reason for that may be the slight Te excess. Experiments aiming at a clarification of this phenomenon are under way, however during this work it could not be clarified how exactly the sample composition can influence SL stability. Due to the large number of satellite reflexes, a convenient indexing convention which is commonly used by the group of D.C Johnson [123] was applied. The reflexes are considered as Bragg reflexes of the SL and not of the crystal lattice. By this convention, every sixth SL Bragg reflex coincides with a (00.*l*) reflex (*l*=3,6,9..) of the crystal lattice, provided that the SL period corresponds to a multiple of the lattice constant *c* (~ 3.05 nm). For an assumed period length of 6.12 nm, the nominal positions of all SL-related reflexes were calculated using eq. 4.19 and showed a good agreement with measured reflex positions (Figure 9.7). Evidently, sample 2 has a similar PL as sample 4. In the recording of the XRD pattern it was tried to exclude substrate reflexes as much as possible. It is noted that the position of some reflexes was not fully clear either due to low intensity or remaining substrate reflexes superpositioning the SL reflexes.

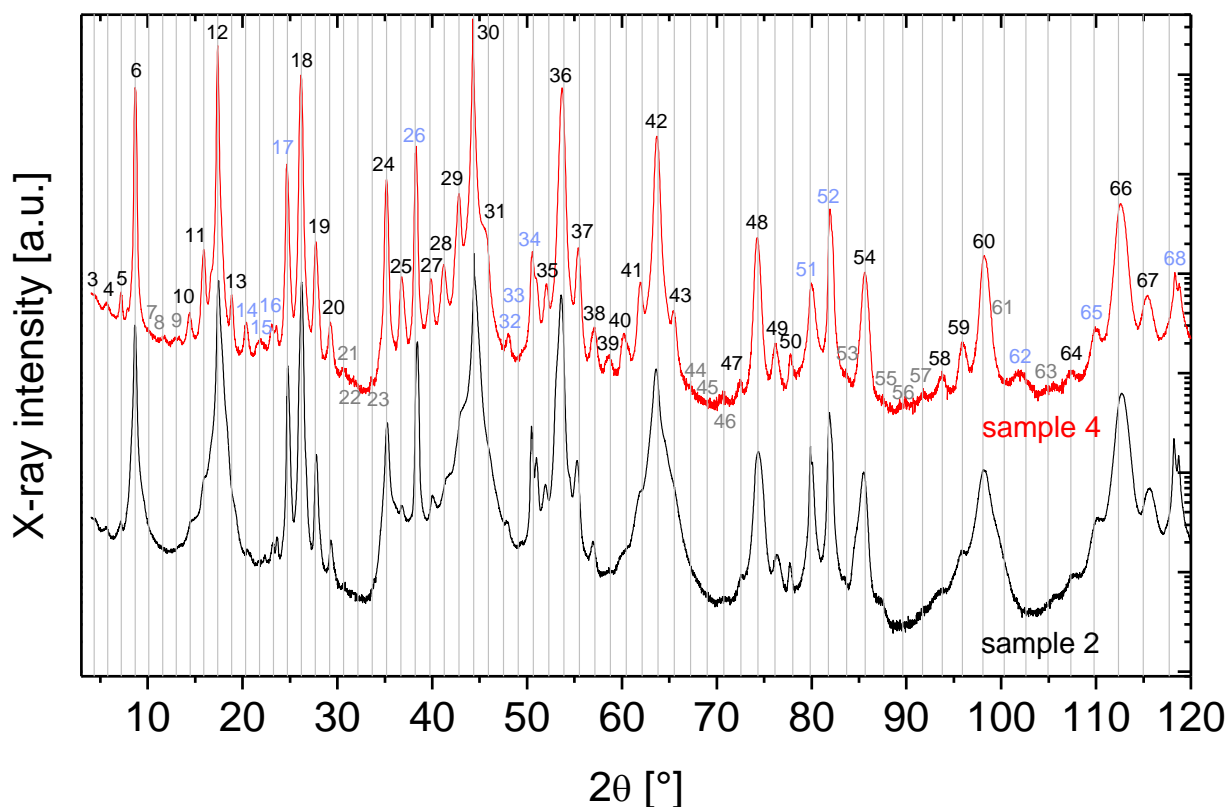


Figure 9.7 XRD pattern of samples 2 and 4 (intensity given in logarithmic scale). Sample 4 shows very well expressed satellite reflexes that are indexed as described in the text. Grey lines correspond to satellite positions calculated for a PL of 6.12 nm. Some satellite position were not fully clear due to low intensity (grey) or overlap of BaF_2 substrate reflexes (light blue).

9.2.1.2 (S)TEM analysis

HAADF-HRSTEM images (Figure 9.8 c and f) impressively demonstrate the extremely sharp, almost atomically abrupt definition of the SL structures. We note that this is the first reported reproduction of such low-periodic sharp SL structures since the works of Venkatasubramanian. The Bi_2Te_3 / Sb_2Te_3 compound films appear clearly separated and EDX line scans display a clear chemical modulation. Furthermore, the layers exhibit a slight long-range bending and localized kink-like strong bending which was not reported for analogous MOCVD-deposited SLs [60]. However, superlattice bending was also

reported for n-type Bi₂Te₃ / Bi₂(Se,Te)₃ SLs grown on the same MBE system [168]. Two types of bending were identified in the previous work: A long range bending mainly due to film and layer roughness and localized kink-like strong bending caused by threading dislocations. Additionally, the presence of regions where the SL structure was strongly weakened was also associated with the dislocations. Since the lattice mismatch of substrate and film is 2.7 % for Sb₂Te₃ and 0.1 % for Bi₂Te₃ (Table 3.1), i.e. even larger than for the Bi₂Te₃ / Bi₂(Se,Te)₃ SLs, it is reasonable to believe that equal or more dislocations are present in the p-type SLs and cause a similar or even greater bending. Also in the p-type SLs the structure appears predominantly weakened in the vicinity to the strongly bent regions.

HAADF-HRSTEM imaging of the region around the bending reveals a staircase-like structure of the Bi₂Te₃-layers in relation to the c-axis. Interdiffusion along the preferred a-axis can easily take place, indicating that the strongly bent regions act as centres for temperature-driven interdiffusion (see further experiments in section 9.2.3.1).

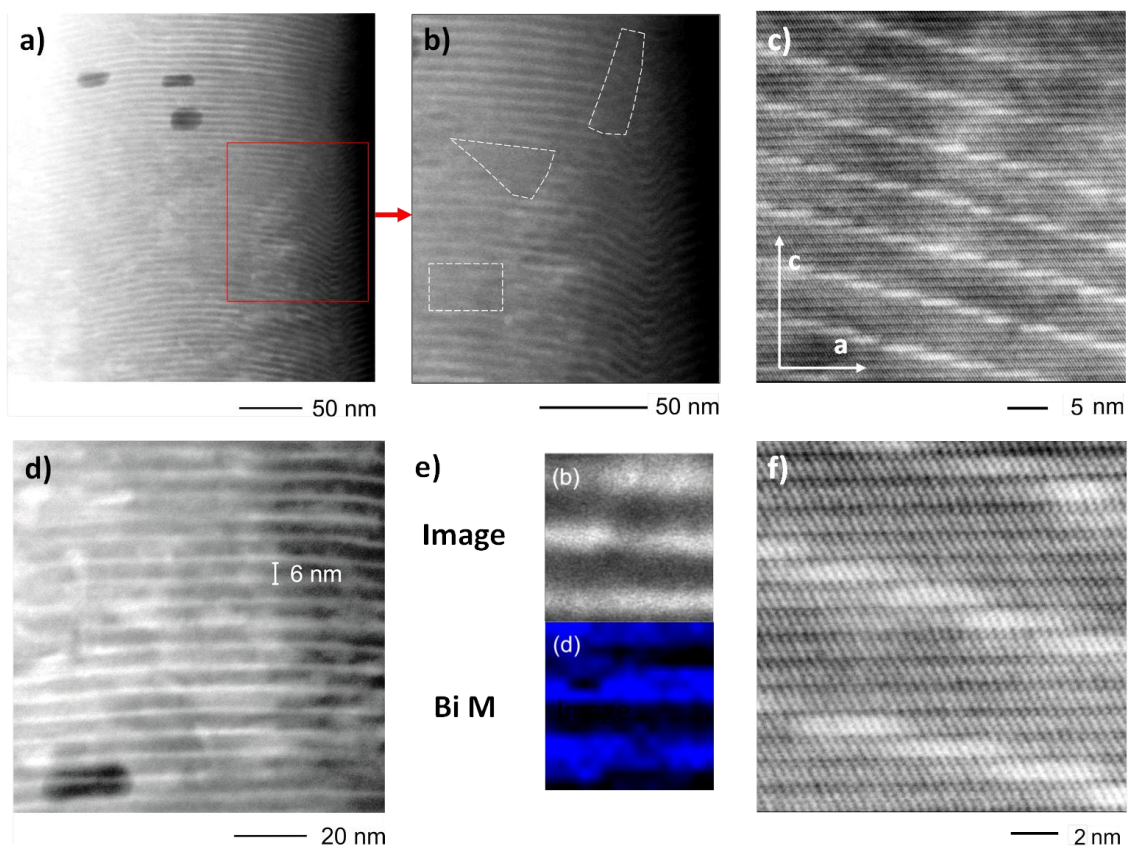


Figure 9.8 STEM images of SL cross section. Bi-containing regions appear as bright lines. All images taken from cross-sections of sample 2 except for c and f (sample 4). a) HAADF-STEM image. b) Enlarged section of "a". The dashed line indicates areas with a weakened SL structure. c) Magnified HAADF-HRSTEM image around SL bending, demonstrating a staircase-like structure. d) Further magnified HAADF-STEM image around SL bending. e) EDX elemental map, Bi M signal. f) Further magnified HAADF-HRSTEM image of "c".

Apart from the imperfections associated with the layer bending, the film appeared to exhibit very high "single-crystalline" like quality. No evidence of grain boundaries and rotational disordering of the grains was found during the STEM analysis on sample 2. However, since twinning was found in the binaries (section 9.1.2.1), it is likely that this type of defect also exists in the SLs and was not found during the first TEM analysis.

A further analysis of the film/substrate interface was carried out, confirming the epitaxial, rotationally ordered film growth (SAED patterns not shown). The patterns revealed an epitaxial relation as already found for analogously grown Bi₂Te₃ by Nurnus [42-p.69]. The (11.0) plane of the V₂VI₃ film is parallel to the (011) plane of BaF₂.

9.2.2 Transport properties

9.2.2.1 Electrical properties

The transport properties of the SL films grown at 350 °C are given in Table 9.1. In contrast to the very high Seebeck coefficients of $\sim 200\text{--}270 \mu\text{V} / \text{K}$ and carrier mobilities up to $\sim 600 \text{ cm}^2/\text{Vs}$ that were reported for the MOCVD-grown SLs (section 3.5.2) all MBE-grown SLs did not exceed $\sim 120 \mu\text{V}/\text{K}$ and $\sim 60 \text{ cm}^2/\text{Vs}$. Consequently, the PF s are also far lower than reported for the MOCVD-grown SLs. The low S and low μ can clearly be traced back to carrier compensation effects as already discussed in sections 2.1.1.2 and 6.2.1. The interfaces between $n\text{-Bi}_2\text{Te}_3$ and $p\text{-Sb}_2\text{Te}_3$ are much more sharply defined than for nanoalloyed SLs (chapter 6) and no interdiffusion and formation of Sb-rich $(\text{Bi,Sb})_2\text{Te}_3$ compounds with high S and μ takes place – thus changing the $\text{Sb}_2\text{Te}_3:\text{Bi}_2\text{Te}_3$ to up to 5:1 did not bring an improvement in contrast to the nanoalloyed SLs.

9.2.2.2 Thermal conductivity

Cross-plane thermal conductivities were determined by TDTR and are shown in Figure 9.9. The data are compared to lattice thermal conductivities published for the MOCVD-grown SLs and Sb_2Te_3 (Figure 2.9, [57]). For this purpose, λ_l was estimated by using cross-plane electrical conductivities calculated from in-plane values by assuming the same anisotropy values for the electrical conductivity as published for the MOCVD-grown SL of the respective period (Figure 3.6 or Figure 1 in [8]). In the corresponding works, the Lorenz number of metals ($2.45 \times 10^{-8} \text{ V}^2/\text{K}^2$) is used to calculate λ_l which is certainly not exactly valid in the carrier concentration range of $10^{19} - 10^{20} \text{ cm}^{-3}$. Therefore, in addition to the Lorenz number for metals as a better approximation also the Lorenz number calculated for homogeneous $(\text{Bi,Sb})_2\text{Te}_3$ (section 2.1.1.1) used here to calculate λ_l . However, the two different Lorenz numbers do not yield significantly different results for λ_l .

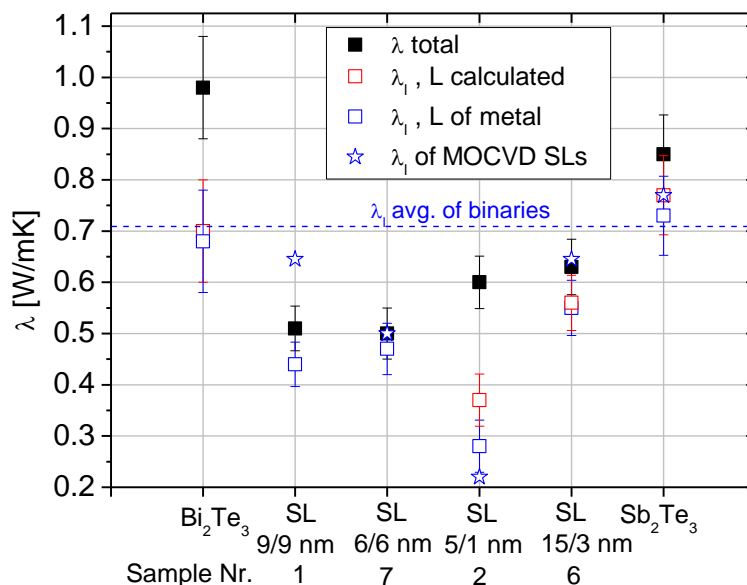


Figure 9.9 Total (black filled squares) and lattice thermal conductivities of MBE-grown epitaxial SLs for calculated (red empty squares) and metal (blue empty squares) Lorenz numbers L . λ_l of MOCVD-grown SLs and Sb_2Te_3 [57] (blue stars) are also given. Dashed line: average thermal conductivity of Bi_2Te_3 and Sb_2Te_3 .

Two main conclusions can be drawn:

1.) The reported significant reduction of both λ and λ_l compared to the binary constituents of the SLs could clearly be confirmed. A reduction can be seen for all PLs while the lowest PL of 6 nm yields the most pronounced reduction of roughly 60 %. Since the epitaxial SLs have a monocrystalline character, the reduction in thermal conductivity can now clearly be attributed to the SL structure and not nanocrystallinity as in the nanoalloyed films shown in the preceding chapters.

2.) For most of the examined PLs the determined λ_l are in good agreement to the published values for MOCVD films [57], particularly when considering that the used growth and measurement methods are technically different (3ω for MOCVD, TDTR for MBE). The obtained value of $\lambda_l = 0.28$ W/mK for 6 nm PL corresponds well to the previously published value of 0.22 W/mK if a scattering of 10 % between the measured total thermal conductivities due to measurement uncertainty is taken into account.

9.2.3 Thermal stability of SLs with 6 nm period length

In this section the stability of SLs with a PL of 6 nm under thermal treatment is discussed. Note that the thermal treatments described here (XRD, SRX, annealing system) are taking place ex-situ. The temperatures measured in these processes correspond well to actual sample temperatures in contrast to in-situ temperature measurement in the MBE system during growth that systematically reports a higher temperature than present at the sample surface (see preface of section 9.1,p.111). For this reason, growth and post-deposition temperatures cannot be compared directly.

9.2.3.1 Structural analysis by temperature-dependent XRD and (S)TEM

XRD patterns of sample 2 were recorded in dependence on temperature (Figure 9.10) around the (00.9) reflex where the SL satellites were well visible. Each temperature was held for 1 hour and the experiment was carried out under Helium atmosphere. Patterns recorded at 50 °C and 100 °C are omitted since they are identical to the pattern at 150 °C.

First indications of interdiffusion can be found at 250 °C. The second order SL satellite (SL-2) vanishes, indicating a loss of long-range order that is likely associated with the loss of atomic sharpness that was observed in the pristine SLs (Figure 9.8). At 375 °C, a significant loss in intensity of the first satellite reflex is evident, indicating the beginning loss of the SL nanostructure. At 400 °C, all reflexes corresponding to a SL structure are absent from the XRD pattern. Additionally, broad extra reflexes such as the (01.5) reflex at roughly 28.1° appear, indicating the onset of recrystallization processes and a change in crystallite orientation. It is noted that the appearance of such reflexes seems to depend on the annealing environment since such recrystallisation processes were not apparent for isothermal annealing experiments at 400 °C (section 9.2.3.3).

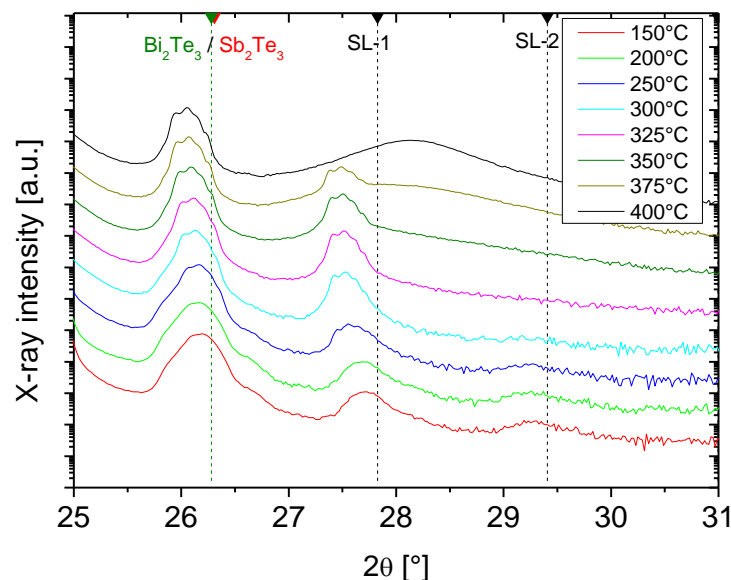


Figure 9.10 XRD pattern around (00.9) reflex in dependence on temperature. A reflex shift due to thermal lattice expansion is evident, room-temperature positions are marked with dashed lines. SL-1 and SL-2 are satellite reflexes of the first and second order.

Furthermore, cross-section HAADF-STEM images for different temperatures were taken of an area where pronounced layer bending was evident, Figure 9.11. Each temperature was held for 30 minutes. As already observed on p-type and n-type pristine SLs (sect. 9.2.1.2), also for the temperature-dependent experiments a similar correlation between layer “slope” and interdiffusion is evident. Layers with a strong tilt appear prone to strong interdiffusion while (near-)horizontally aligned layers are relatively stable. In conformance with XRD results, at 250 to 300 °C there seems to be some loss of SL sharpness as indicated by a subtle broadening of the Bi_2Te_3 containing layers. At 360 °C, the ML structure begins to get erased completely in some regions. It is noted that the onset of bulk diffusion at roughly this temperature is assumed from experiments with similar nanoalloyed films (development of roughness and pillar-like structure, section 7.1). At 400 °C large proportions of the SL are clearly lost while at 450 °C, all nanostructuring is gone. We note that, starting at 400 °C, the films started to evaporate in the vacuum environment of the sample holder, complicating analysis and image acquisition at and above this temperature

The TEM results are generally in agreement with the XRD analysis. While XRD patterns show no SL structure at 400 °C, remnants of the nanostructure are still visible at this temperature in the cross section. This is most likely due to the shorter temperature holding time in the TEM analysis and the tendency of the SL satellites to vanish easily if the SL structure loses sharpness (as was observed on nanoalloyed films).

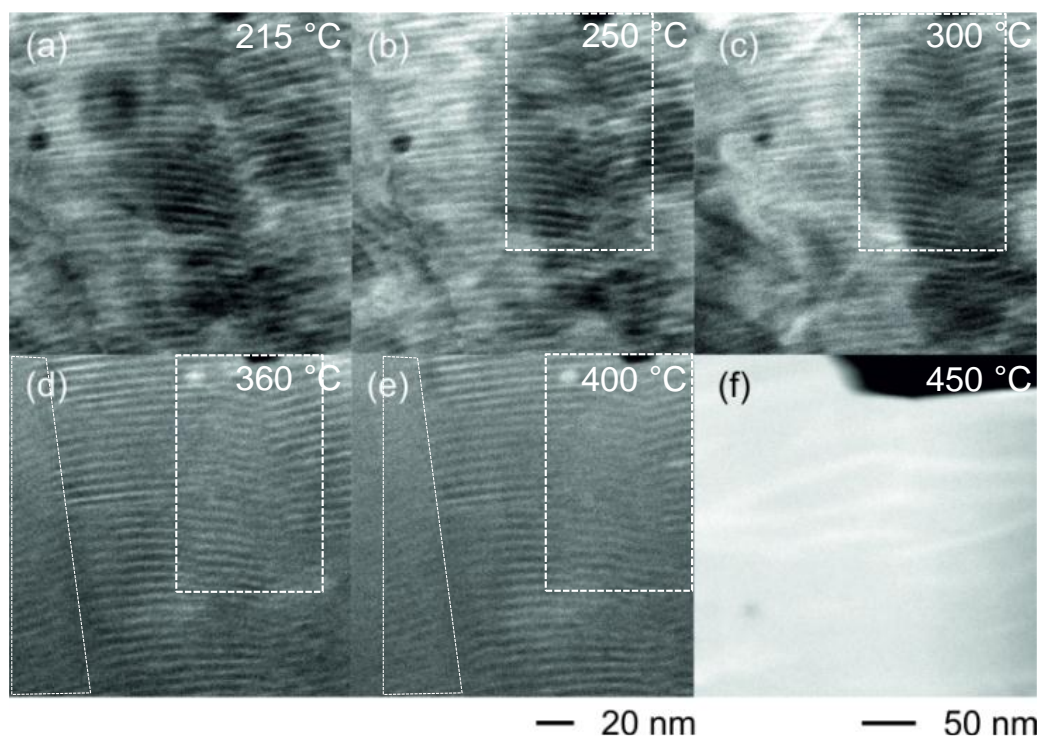


Figure 9.11 Cross-section HAADF-STEM images of area with pronounced bending, sample 2. Images taken in dependence on temperature demonstrate the progress of interdiffusion. Note that slight image drifting occurred during the analysis. Areas indicated by dashed lines serve for comparison of equal section.

9.2.3.2 Transport properties in dependence on temperature

Increasing the growth temperature to 400 °C resulted in an increase of S and μ , indicating a reduction of the compensation effects (Table 3.2). However, increasing the deposition temperature lead to drastically increasing re-evaporation as indicated by the pronounced shrinkage in film thickness, putting a limit to this type of experiment.

Measuring the sample properties ex-situ after deposition proved to be a more flexible approach. The Seebeck coefficient of sample 4 was recorded in dependence on temperature using the SRX setup (Figure 9.12). After the first heating cycle ending at 342 °C and the subsequent cooldown, the Seebeck coefficient at room temperature increased significantly and was almost twice as high as before the heat

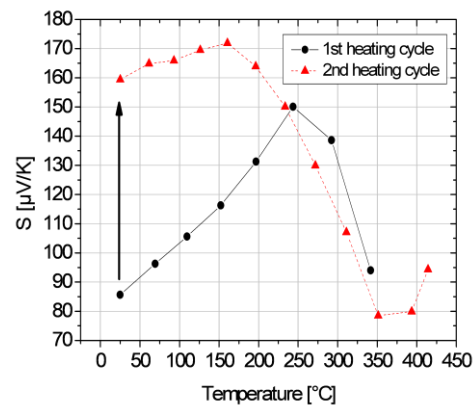
treatment. Apparently, compensation effects have been strongly reduced and there are hints for interdiffusion, turning the 5nm/1nm Sb₂Te₃/Bi₂Te₃ SL at least partially into a p-type solid solution with the composition (Bi_{0.16}Sb_{0.84})₂Te₃. Indeed, the S of 160 $\mu\text{V/K}$ corresponds very well to the values of ~ 160 $\mu\text{V/K}$ reported for a bulk solid solution with this composition (Figure 3.5,[122]).

To conclude, the experiment indicates that significant interdiffusion has taken place below or at 340 $^{\circ}\text{C}$, which corresponds to TEM images that indicate the beginning of interdiffusion of the Bi₂Te₃ layers at 250-300 $^{\circ}\text{C}$. However, with this kind of experiment it is hard to track down exactly the onset of interdiffusion that should be noticeable by an increase in the Seebeck coefficient since it is masked by other effects not related to interdiffusion: Firstly an increase of S due to the shift of the Fermi level out of the valence band to the middle of the band gap and then a decrease most likely due to the onset of intrinsic conduction also influence the measurement.

Table 9.2 Transport properties of SLs in dependence on substrate temperature T_{sub} [$^{\circ}\text{C}$]. Units as previously defined in Table 5.1. Carrier concentration n in units of 10^{19} cm^{-3} .

Figure 9.12 Seebeck coefficient in dependence on temperature for ex-situ heating using the SRX system. A significant increase of the Seebeck coefficient is evident after the first heating cycle (arrow).

T_{sub}	c_{Bi}	c_{Sb}	c_{Te}	d	μ	n	σ	S	PF
350	18	22.5	59.5	1.03	59	2.7	254	65	1.1
400	6.0	34.2	59.8	0.84	150	2.1	515	153	12.1
425	-	-	-	0.08	-	-	-	-	-



9.2.3.3 Electrical properties after ex-situ isothermal annealing

Two sets of samples with a composition analogous to samples 2 and 4 (1 nm Bi₂Te₃ / 5 nm Sb₂Te₃) were grown for annealing experiments. The isothermal annealing was carried out under nitrogen atmosphere at 400 $^{\circ}\text{C}$ for 2 hours in the annealing system shown in section 4.1.5.1.

Table 9.3 Transport properties of SLs with 6 nm period before and after annealing at 400 $^{\circ}\text{C}$. Units as previously defined in Table 5.1. Carrier concentration n in units of 10^{19} cm^{-3} . Lattice thermal conductivity estimation as described in section 9.2.2.2 with calculated Lorenz number.

As grown										After annealing										
c_{Bi}	c_{Sb}	c_{Te}	d	μ	n	σ	S	PF	$\frac{\lambda}{\lambda_l}$	c_{Bi}	c_{Sb}	c_{Te}	d	μ	n	σ	S	PF	$\frac{\lambda}{\lambda_l}$	
5.5	32.1	62.4	1.02	80	1.7	212	92	1.8	-	6.0	34.6	59.4	0.86	235	7.3	2756	129	45.9	1.4	
5.7	34.3	60.0	1.00	59	4.0	380	129	6.3	0.73 0.50	5.9	34.7	59.4	1.03	182	10.7	3108	97	29.2	1.4	
																				0.81
																				0.68

In the XRD patterns of annealed films only lattice (00 l) reflexes were evident while satellite reflexes were completely absent, proving that most or all of the SL structure is lost and the compound (Bi_{0.16}Sb_{0.84})₂Te₃ has formed. The change in transport properties is obvious. The S/n relationship and μ change drastically, indicating the reduction of carrier compensation effects. As a result of the changes, the PF s increase massively to values usually observed on single crystalline alloys (Table 3.2). Notably, S remains quite low – it can be presumed that this is caused by the nonoptimized annealing environment, resulting in

significant Te loss. Further improvement is likely possible by optimized annealing conditions, e.g. by using a powdered diffusion source of the same composition.

The increasing PF is accompanied by a significant increase in both total and lattice thermal conductivity. The total thermal conductivity even exceeds that of epitaxial binaries and is in the region of single-crystalline bulk material, i.e. between that of $(\text{Bi}_{0.2}\text{Sb}_{0.8})_2\text{Te}_3$ (0.7-0.9 W/mK) and Sb_2Te_3 (0.9-1.6 W/mK) [90]. It may be presumed that the temperature-dependent SL interdiffusion is accompanied by general annealing effects on the crystal lattice, enhancing transport properties somewhat.

9.3 Conclusions

In this chapter, results on binaries and Bi_2Te_3 / Sb_2Te_3 SLs deposited epitaxially on (111)- BaF_2 substrates by MBE were shown. All films were fully textured and exhibited a very high crystalline quality with mostly ordered growth.

Binaries with good electrical properties were deposited. A low carrier concentration $< 2 \times 10^{19} \text{ cm}^{-3}$ and a very high carrier mobility of $\sim 500 \text{ cm}^2/\text{Vs}$ for epitaxial Sb_2Te_3 were determined.

Epitaxial Bi_2Te_3 / Sb_2Te_3 SLs with period lengths as small as 6 nm were proven to be thermally stable, confirming the results reported by Venkatasubramanian. Very well expressed satellite reflexes in XRD analysis and (HR)STEM imaging confirmed an extremely sharp definition of the SL structure. A reduction of thermal conductivity (i.e. a lattice thermal conductivity reduction by up to $\sim 60\%$ compared to the binary compounds) was clearly evident which could be attributed to the SL structure and not, as in the nanoalloyed films, to the nanocrystallinity of the material.

A clear difference, however, was evident for the electrical properties. Much lower Seebeck coefficients and carrier mobilities than reported for MOCVD-grown SLs were observed, owing to compensation effects. In conclusion, it remains unclear how the high S in the MOCVD-grown SLs could be reached or rather how the supposedly unavoidable compensation effects (it was stated in one of the previous works that only n- Bi_2Te_3 could be obtained in the growth experiments with MOCVD [117]) could be circumvented.

Three possible mechanisms could be responsible:

Ordered alloy: Venkatasubramanian proposes the formation of an “ordered alloy” ([46], see section 3.5.2 and 6.2.1) corresponding to p-type Sb-rich $(\text{Bi,Sb})_2\text{Te}_3$. To investigate this phenomenon, a total of six samples with the layer sequence 5 nm Sb_2Te_3 / 1 nm Bi_2Te_3 was deposited with slightly varying period lengths and Te contents (the properties of three of these samples are given in Table 9.1). However, for no sample the purported effects of an ordered alloy formation could be reproduced here and, consequently, μ , S and the PF s remained low.

Doping: A p-doping of the Bi_2Te_3 films, either intentional by introducing foreign dopands such as group IV elements or unintentional by remaining carbon-based residues of the organic-based MOCVD growth. However, none of this was reported in any of Venkatasubramanian’s works.

Interdiffusion: Finally, the possibility of slight interdiffusion transforming the only 1 nm thin Bi_2Te_3 layer into p-type $(\text{Bi,Sb})_2\text{Te}_3$ has to be taken into account. To shed some light on this point, the properties of annealed epitaxial SLs were analyzed. After annealing at 400 °C a loss of the SL structure, a very high carrier mobility, an improved Seebeck/charge carrier ratio and thus a massively improved PF of $45 \mu\text{W}/\text{cmK}^2$ was evident, however at the prize of a significantly increased thermal conductivity. The path to a high ZT may be to achieve a narrowly defined degree of slight interdiffusion that provides good electrical properties and *simultaneously* a low thermal conductivity. It is possible that a process window that fulfills both these conditions was found by Venkatasubramanian during the MOCVD growth experiments. It is also possible that interdiffusion may have been caused by the growth mode of the films which, despite the assumptions of the author, is likely not epitaxial in the common sense (see section 3.5.1). Rotational crystalline disorder may be present in the films, allowing for slight defect-enhanced interdiffusion not present in truly epitaxially grown material.

List of acronyms and symbols

Acronyms

(HA)ADF	(High angle) annular dark field	MOCVD	Metal organic chemical vapor deposition
BEP	Beam equivalent pressure	(M)QW	(Multi) quantum well
BF	Bright field	PF	Power factor
BFM	Beam flux monitor	PGEC	Phonon glass electron crystal
BSE	Back scattered electron	PL	Period length
BTE	Boltzmann transport equation	PLD	Pulsed laser deposition
BZ	Brillouin zone	SAED	Selected area electron diffraction pattern
COP	Coefficient of performance	SE	Secondary electron
DC	Debye Callaway	SEM	Scanning electron microscopy
DF	Dark field	SIMS	Secondary ion mass spectroscopy
DOS	Density of states	SL	Superlattice
EDX	Energy-dispersive X-ray analysis	TDTR	Time domain thermal reflectance
FIB	Focused ion beam	(HR)TEM	(High resolution) transmission electron microscopy
HF	High frequency	STEM	Scanning transmission electron microscopy
HWE	Hot wall epitaxy	THM	Traveling heater method
MBE	Molecular beam epitaxy	TZM	Thornton zone model
MER	Method of elemental reactants	XRD	X-ray diffraction
MFP	Mean free path	XRR	X-ray reflectometry
ML	Multilayer		

Symbols

A	Area	d_{sl}	Superlattice period length
A	Material specific constant in effusion cell pressure (section 4.1.3.2)	d_t	Thermal penetration depth
A_e	Orifice area of effusion cell	d_z	Thickness of layer of element Z
A_s	Sample surface area	$\Delta\bar{T}_s$	Weighted average of the temperature distribution on surface
A_0	Amplitude of absorbed heat	$\Delta\bar{T}_f$	Steady-state temperature rise in thin film
a	(Cubic) lattice constant	$\Delta\bar{T}_{tot}$	Total steady-state temperature rise
a_h, a_c	Hexagonal and cubic lattice constant	E	Energy
α	Thermal expansion coefficient	E_A	Activation energy
B_U, B_l, B_N	Prefactors for phononic relaxation times in Debye-Callaway model	E_C	Energy of lower edge of conduction band
B	Magnetic field strength (section 4.2.1)	E_F	Fermi energy
B	Material specific constant in effusion cell pressure (section 4.1.3.2)	E_G	Width of band gap
β_T	Thomson coefficient	E_n	Quantized energy level of electron in infinite quantum well
C	Constant in Pisarenko relation	E_{xy}	Continuous energy of electron in infinite quantum well
C	Current Te content (in section 4.1.2)	e	Electron charge
C_{BEP}	Variable in effusion cell pressure fit	F_z	Fermi integral
c	Hexagonal lattice constant	F	Possible degrees of freedom
c_v	Specific heat per unit volume	F_H	Prefactor in Hall measurement
D	Desired content of element (in section 4.1.2)	f	Electron distribution in non-equilibrium
D_t	Thermal diffusivity	f_0	Fermi-Dirac distribution in equilibrium
d	Thickness or size	ϕ	Coefficient of performance
d_A, d_B	For multilayer system: Thickness of layer A and B, also thickness of quantum well / barrier	$\phi_n(z)$	Wave functions for localized electrons in quantum well
d_{BST}	Thickness of layer of compound $(Bi_{1-x}Sb_x)_2Te_3$	ϕ_c	Coefficient of performance in a Carnot cycle
d_{hkl}	Distance between two lattice planes with Miller index (hkl)	G	Reciprocal lattice vector
d_n	Thickness of n-th layer	Γ_e	Effusion rate
		γ	Parameter containing σ, λ and S

LIST OF ACRONYMS AND SYMBOLS

H	Heaviside function	n	Charge carrier concentration
\hbar	Planck constant	n_i	Intrinsic carrier concentration
η, η^*	Efficiency (* = in an ideal quantum well)	n_{BiTe}	Antisite defect density
η_c	Carnot efficiency	n_{BST}	Number of moles of compound $(Bi_{1-x}Sb_x)_2Te_3$
η_{max}	Maximum efficiency of a thermogenerator	n_z	Number of moles of element Z
I	Electric current	P	Possible number of phases
I_B, I_0	Electric current in Hall measurement with / without magnetic field	PF	Power factor
$I_{\phi max}$	Current of maximum coefficient of performance of a thermocooler	PF_{11}, PF_{33}	Power factor perpendicular and parallel to c-axis
K	Number of components in Gibb's phase law in section 4.1.5.2	p	Specularity parameter
K	Scherrer constant in section 4.3.1.2	p	Grain size, obtained by Rietveld refinement (section 4.3.1.2)
K_i	Transport integrals	p_{BEP}	Beam equivalent pressure of effusion cell
k	Momentum	p_{eq}	Vapor pressure in equilibrium
k_B	Boltzmann constant	n_0, p_0	Charge carrier concentration prefactor as defined in eq. 2.3
k_x, k_y	Continuous momentum of electron in ideal quantum well	Π	Peltier coefficient
L	Lorentz number	Π_{AB}	Differential Peltier coefficient
$k_{ }$	Momentum component in x-y plane	\dot{Q}	Amount of heat exchanged per time (also cooling/heating power)
Lp	Period length	Q	Heat
l	Sample length in 4-point probe method	θ	Angle (mostly diffraction angle in XRD experiments)
l_{mfp}	Mean free path length	θ_D	Debye temperature
λ	Thermal conductivity	θ_m, θ_n	Superlattice reflexes at order m and n
λ_A, λ_B	Thermal conductivity of layer A and B	R	Electrical Resistance
λ_e	Electronic thermal conductivity	R_{am}	Interface reflectivity
λ_{el}	Electron wavelength	R_H	Hall coefficient
λ_l	Lattice thermal conductivity	R_l	Electrical load Resistance
λ_p	Phonon wavelength	R_{ref}	Reflection coefficient
λ_{XRD}	Wavelength of X-ray radiation	R_{th}	Thermoreflectivity
λ_l	Longitudinal phonon thermal conductivity	R_p	Pillar resistance
λ_T	Transversal phonon thermal conductivity	R(y)	Ratio $-V_{in}/V_{out}$ in dependence on parameter y
$\lambda_{V_2V_1}$	Thermal conductivity of V_2V_1 material	r	Position vector
$\lambda_{11}, \lambda_{33}$	Total thermal conductivity perpendicular and parallel to crystal c-axis.	r_{ac}	Ratio of acoustic impedances of two layers
M	Molecular weight (of atomic species)	ρ_{BST}	Density of compound $(Bi_{1-x}Sb_x)_2Te_3$
M_A	Mean atomic weight	ρ_{BT}	Density of Bi_2Te_3
M_{BST}	Molar mass of compound $(Bi_{1-x}Sb_x)_2Te_3$	ρ_{el}	Electrical resistivity
M_i	Atomic mass of i-th unit cell	ρ	Mass density
M_R	Ratio of load / generator resistance	ρ_{ST}	Density of Sb_2Te_3
M_Z	Molar mass of element Z	ρ_{gr}	Resistivity increase due to grain boundary scattering
\bar{M}	Average atomic mass of unit cells	ρ_z	Density of element Z
m	Order of SL reflex	$\rho(E)$	Energetic density of states
m_d	Density of states effective mass	S	Seebeck coefficient
m_z	Mole proportion of element Z	S_{AB}	Differential Seebeck coefficient
m_1, m_2, m_3	Effective masses along the crystal axes	S_A, S_B, S_C	For multilayer system: Seebeck coefficient of layer A,B and Seebeck coefficient of whole stack
$m_{ }$	Component of effective mass in x-y direction	S_i	Sensitivity of ratio V_{in}/V to other parameters
m^*	Effective mass	S_V	Total boundary surface per unit volume
μ	Charge carrier mobility	S_x	Seebeck coefficient of element x
μ_{BiTe}	Formation energy of antisite defect	S_y	Sensitivity of ratio $-V_{in}/V_{out}$ to parameter y
μ_i	Partial charge carrier mobility	S_d^{Al}	Sensitivity of ratio $-V_{in}/V_{out}$ to thermal conductivity of aluminum
μ_p, μ_n	Carrier mobility of holes and electrons	S_{λ}^{V-VI}	Sensitivity of ratio $-V_{in}/V_{out}$ to thermal conductivity of V_2V_1 material
μ_{tot}	Total charge carrier mobility	S_{11}, S_{33}	Seebeck coefficient perpendicular / parallel to crystal c-axis
μ_{11}, μ_{33}	Charge carrier mobility perpendicular and parallel to c-axis	s	Scattering parameter
N	Planck distribution	s_i	Uncertainty of other parameters in TDTR
N_A	Avogadro number		
N_N	Concentration of scatterers		
N_0	Initial source concentration		
$N(x,t)$	Atomic concentration in diffusion profile		
n	Order of SL reflex in section 4.3.1.1		

LIST OF ACRONYMS AND SYMBOLS

	measurement	V_{out}	Out-of-phase part of voltage measured by lock-in amplifier (TDTR)
S_d^{Al}	Uncertainty of thermal conductivity of aluminum	V_{sp}	Seebeck voltage generated by Peltier effect
S_λ^{V-VI}	Uncertainty of thermal conductivity of V_2V_3 material	V_0	Thermoelectric part of measured voltage
σ	Electrical conductivity	\mathbf{v}	Velocity
$\sigma_e(\beta)$	Electron scattering probability in Rutherford scattering	v_s	Speed of sound
$\sigma_A, \sigma_B, \sigma_C$	For multilayer system: electrical conductivity of layer A,B and conductivity of whole stack	v_A, v_B	Speed of sound in layer A and B
σ_{11}, σ_{33}	Electrical conductivity perpendicular and parallel to c-axis	W	Electric power
$\sigma(E)$	Differential electrical conductivity	w	Sample width in 4-point probe method
T	Temperature	$w_{FWHM}(2\theta)$	Full width at half maximum of reflex at angle 2θ
T_H, T_C	Hot and cold side temperature	w_0	$1/e^2$ radius of pump beam
T_m	Mean Temperature of T_H and T_C	ω	Angular frequency
T_M	Melting temperature	ω_{cut}	Low-frequency cutoff wavelength
t	Time	x	Integration variable in some equations, otherwise proportion of constituent, e.g in solid solutions
τ	Relaxation time	$\psi(\mathbf{r})$	Electron wave function
$\tau_R, \tau_N, \tau_C, \tau_U, \tau_I, \tau_B$	Relaxation times for resistive, normal, total, Umklapp, impurity and boundary scattering.	Z	Figure of merit of single material
τ_0	Relaxation time prefactor	Z	Atomic number (4.3.2)
U_H	Hall voltage	Z_A, Z_B	Acoustic impedance of material A and B
U_s	Voltage between copper wires in Seebeck measurement	z	Figure of merit of single material, afterwards replaced by Z
V	Voltage	ZT	Dimensionless figure of merit
$V(z)$	Well potential	$Z_C T$	Figure of merit of whole multilayer system
V_B	Barrier potential, i.e. depth of quantum well	$Z_{2D} T$	Figure of merit for idealized MQW system with strict 2D carrier confinement
V_{in}	In-phase part of voltage measured by lock-in amplifier (TDTR)	ZT_{11}, ZT_{33}	Figure of merit perpendicular / parallel to c-axis

List of figures and tables

Tables

Table 3.1 Relevant structural properties of thin film materials and used substrate materials.....	34
Table 3.2 Selected transport properties of Traveling Heater Method (THM)-grown and annealed binaries Bi_2Te_3 (n-type), Sb_2Te_3 and $(\text{Bi}_{0.2}\text{Sb}_{0.8})_2\text{Te}_3$	37
Table 3.3 Some effective DOS masses m_d for different x in p-type $(\text{Bi}_{1-x}\text{Sb}_x)_2\text{Te}_3$	38
Table 3.4 Properties overview of $(\text{Bi,Sb})_2\text{Te}_3$ alloy and binary thin films grown with different methods.....	40
Table 4.1 Material properties of elements and compounds used in this work.....	44
Table 4.2 Used MBE effusion cell parameters during growth.....	47
Table 4.3 Comparison of thermal conductivity values λ obtained with the TDTR and 3ω method for different nanoalloyed thin films.....	61
Table 5.1 Bi-Te samples: Nominal element initial layer thickness for deposition patterns shown in Figure 5.1, chemical composition and room-temperature in-plane transport properties after annealing at 250 °C for 2 hours.....	66
Table 5.2 Refined lattice parameters, orientation index from Rietveld analysis and the crystallite size of Bi-Te samples....	67
Table 5.3 Sb-Te samples: Nominal element initial layer thickness for deposition patterns shown in Figure 5.1, chemical composition and room temperature in-plane transport properties after annealing at 250 °C for 2 hours..	68
Table 5.4 Refined lattice parameters, orientation index from Rietveld analysis and the crystallite size of Sb-Te samples. .	69
Table 5.5 Electrical transport parameters of Bi_2Te_3 and Sb_2Te_3 films grown with increased deposition rate..	78
Table 6.1. Structural properties of nanoalloyed Bi_2Te_3 / Sb_2Te_3 SLs.	81
Table 7.1 Electrical properties of nanoalloyed Sb_2Te_3 / $(\text{Bi,Sb})_2\text{Te}_3$ SLs with slightly different Te contents annealed at 250 °C for 2 hours..	95
Table 9.1 Characteristic structural and transport properties of fabricated Bi_2Te_3 / Sb_2Te_3 SLs..	115
Table 9.2 Transport properties of Bi_2Te_3 / Sb_2Te_3 SLs in dependence on substrate temperature T_{sub} [°C].	121
Table 9.3 Transport properties of Bi_2Te_3 / Sb_2Te_3 SLs with 6 nm period length before and after annealing at 400 °C.	121

Figures

Figure 1.1 Applications of thermoelectricity. Images supplied by Micropelt GmbH and Fraunhofer IPM.	17
Figure 1.2 Thermocouple and unicouple..	18
Figure 1.3 Plot of plot of η_{max} vs. ZT_m (eq. 1.8) and current data for ZT of thermoelectric materials.	20
Figure 2.1 Interconnection of electrical conductivity, Seebeck coefficient, thermal conductivity and ZT on carrier concentration for Bi_2Te_3	21
Figure 2.2 Calculated Lorentz number L in dependence of n for $(\text{Bi}_{1-x}\text{Sb}_x)_2\text{Te}_3$	23
Figure 2.3 Calculated total carrier concentration n_{tot} in dependence of hole concentration p for Bi_2Te_3	24
Figure 2.4 Electron mobility in dependence of composition in the Bi_2Te_3 - Sb_2Te_3 system.	25
Figure 2.5 Schematic dependence of thermal conductivity on phonon frequency and lattice thermal conductivity of $(\text{Bi}_{0.25}\text{Sb}_{0.75})_2\text{Te}_3$ and Bi_2Te_3 for different substrates.....	27
Figure 2.6 Plot of thermal conductivity vs. grain size of Bi_2Te_3 and $(\text{Bi}_{0.5}\text{Sb}_{0.5})_2\text{Te}_3$ thin films.	27
Figure 2.7 Schematic of MQW structure and subbands in a single quantum well.	29
Figure 2.8 a) Calculated cross-plane Seebeck coefficient, power factors, variation of anisotropy ratio in $(\text{Bi}_2\text{Te}_3)_x(\text{Sb}_2\text{Te}_3)_{1-x}$ SLs.	30
Figure 2.9 TEM image of a SL with 60 Å (6 nm) period length and variation of lattice thermal conductivity with period length for Bi_2Te_3 / Sb_2Te_3 SLs together with model data.....	32
Figure 2.10 Coherent acoustic phonon signal for Bi_2Te_3 and a SL with 3nm Bi_2Te_3 / 3nm Sb_2Te_3 .	
Figure 3.1 Complete Bi_2Te_3 unit cell, hexagonal representation and detail image of one quintuple with interlayer spacings between the atomar layers, bond types are indicated.....	33
Figure 3.2 Crystal structure of BaF_2	34
Figure 3.3 a) Bi_2Te_3 phase diagram, homogeneity range of the Bi_2Te_3 phase and Sb_2Te_3 phase diagram.	35
Figure 3.4 a+c) Comparison of the connection of Seebeck coefficient and Te content, corresponding to the phase diagrams shown in Figure 3.3 and examples of phases of the homologous series $(\text{Bi}_2)_m(\text{Bi}_2\text{Te}_3)_n$ [76].....	35
Figure 3.5 Transport properties of $(\text{Bi}_{1-x}\text{Sb}_x)_2\text{Te}_3$ in dependence of x [122].	38

Figure 3.6 a) Mobility (=conductivity) anisotropy in symmetric SLs with different periods. b) Harman method: Voltage spike at $t=0 \mu\text{s}$, complicating the extraction of the “thermoelectric” part of the measured voltage. c) Scattering of data points used to determine ZT..... 42

Figure 4.1 Left: Schematic illustration of the nanoalloying process for a $\text{Bi}_2\text{Te}_3 / \text{Sb}_2\text{Te}_3$ SL and dependence of sticking coefficient on substrate temperature for Bi and Te 43

Figure 4.2 MBE setup EPI 930 by Veeco/Epi Inc..... 46

Figure 4.3 BEP in dependence of effusion cell temperature with fit after eq. 4.8.. 47

Figure 4.4 Cross sections of single element thin films.. 48

Figure 4.5 Principles of magnetron sputtering..... 49

Figure 4.6 Main sputtering chamber with targets inserted and screenshot of controlling software..... 50

Figure 4.7 Thornton Zone model for sputtered films..... 50

Figure 4.8 Surface morphology of sputtered element thin films... 51

Figure 4.9 Sputtering rate vs. power for the elements used in this work determined in calibration runs..... 52

Figure 4.10 a) Annealing system used in this work. The setup is also capable of two-zone annealing experiments. b) Schematic drawing of ampoule and furnace position for two-zone annealing. c) Heating / cooling curves for an annealing temperature of $250 \text{ }^\circ\text{C}$ 53

Figure 4.11 Partial pressure of Te and Bi_2Te_3 samples with different Te content versus temperature..... 54

Figure 4.12 Room temperature measurement setup for Seebeck coefficient and sample holder of SRX measurement setup (CAD drawing). 57

Figure 4.13 TDTR measurement principle.. 57

Figure 4.14 Time domain thermal reflectance measurement setup..... 58

Figure 5.1 Quintuple and bilayer pattern used to deposit the initial element layers for nanoalloyed Bi_2Te_3 and Sb_2Te_3 65

Figure 5.2 Diffraction patterns of annealed nanoalloyed Bi_2Te_3 film samples. 67

Figure 5.3 SEM cross sections of cleaving edge of nanoalloyed annealed Bi_2Te_3 samples. 68

Figure 5.4 Diffraction patterns of annealed nanoalloyed Sb_2Te_3 for different deposition patterns and element initial layer thicknesses after annealing. 69

Figure 5.5 TEM images of annealed nanoalloyed Sb_2Te_3 (left) and Bi_2Te_3 (right) grown with the quintuple pattern. 70

Figure 5.6 SEM images of annealed nanoalloyed Sb_2Te_3 cross sections..... 70

Figure 5.7 Electrical properties of nanoalloyed annealed Bi_2Te_3 in dependence of Te content. 71

Figure 5.8 and eq. 5.1 Antisite defect densities of Bi_2Te_3 and Sb_2Te_3 in dependence on temperature with relation used for calculation..... 72

Figure 5.9 TEM image of Bi-rich layers in a nanoalloyed Bi_2Te_3 thin film and Seebeck coefficient of Bi_2Te_3 in dependence of the logarithm of carrier concentration together with Pisarenko fit. 73

Figure 5.10 Electrical properties of nanoalloyed annealed Sb_2Te_3 films as function of Te content..... 74

Figure 5.11 Electrical conductivity in dependence on Te content of Sb_2Te_3 and Seebeck coefficient in dependence of the logarithm of carrier concentration together with Pisarenko fit. 75

Figure 5.12 Temperature resolved XRD patterns of Bi_2Te_3 (left) and Sb_2Te_3 (right), quintuple deposition pattern. 76

Figure 5.13 Room-temperature XRD patterns of Bi_2Te_3 (left) and Sb_2Te_3 (right), as grown and annealed, quintuple deposition pattern.. 76

Figure 5.14 Seebeck coefficient and electrical conductivity in dependence on temperature for as-grown Bi_2Te_3 and Sb_2Te_3 77

Figure 5.15: Cross sections of Bi_2Te_3 and Sb_2Te_3 films grown with increased deposition rate. 78

Figure 5.16 Te concentration of Bi_2Te_3 in dependence on annealing temperature and cross-section of sample 3 after annealing at $500 \text{ }^\circ\text{C} / 24 \text{ h}$ 78

Figure 5.17 Electrical Properties of Bi_2Te_3 in dependence on annealing temperature..... 79

Figure 6.1 XRD pattern of the 1:1 SL $\text{Bi}_2\text{Te}_3 / \text{Sb}_2\text{Te}_3$ SL in dependence of annealing temperature..... 82

Figure 6.2 SEM cross sections of 1:1 $\text{Bi}_2\text{Te}_3 / \text{Sb}_2\text{Te}_3$ SL samples..... 82

Figure 6.3 SIMS depth profiles of the 1:1 $\text{Bi}_2\text{Te}_3 / \text{Sb}_2\text{Te}_3$ SL..... 83

Figure 6.4 Results of HAADF-STEM studies, cross-sections of 1:1 $\text{Bi}_2\text{Te}_3 / \text{Sb}_2\text{Te}_3$ SLs as grown and annealed.. 84

Figure 6.5 Observation of the nanostructuring in $\text{Bi}_2\text{Te}_3 / \text{Sb}_2\text{Te}_3$ SLs by SEM on the SIMS crater..... 85

Figure 6.6 Transport properties of nanoalloyed MBE SLs with different ratios of $\text{Sb}_2\text{Te}_3:\text{Bi}_2\text{Te}_3$ 86

Figure 6.7 Calculated and experimental S vs. n relation for nanoalloyed MBE SLs with different ratios of $\text{Sb}_2\text{Te}_3:\text{Bi}_2\text{Te}_3$ 86

Figure 6.8 Schematic representation for the SL structure presented by Venkatasubramanian and layer structure for the 1:1 $\text{Bi}_2\text{Te}_3 / \text{Sb}_2\text{Te}_3$ SLs presented in this work..... 87

Figure 6.9 PF and thermal conductivities of nanoalloyed $\text{Bi}_2\text{Te}_3\text{-Sb}_2\text{Te}_3$ SLs deposited by MBE for different ratios of $\text{Sb}_2\text{Te}_3:\text{Bi}_2\text{Te}_3$ 87

Figure 7.1 Deposition patterns used for the sputtered thin films shown in the chapter. 89

Figure 7.2 Composition of the $\text{Sb}_2\text{Te}_3 / (\text{Bi,Sb})_2\text{Te}_3$ SLs in the as deposited state and after annealing at different temperatures..... 90

Figure 7.3 SIMS depth profiles of the $\text{Sb}_2\text{Te}_3 / (\text{Bi,Sb})_2\text{Te}_3$ SLs annealed at different temperatures. 90

Figure 7.4 Detailed view of the SIMS depth profiles of $\text{Sb}_2\text{Te}_3 / (\text{Bi,Sb})_2\text{Te}_3$ SLs in the as-deposited state and after annealing at 150 °C for 2 h (right).....	91
Figure 7.5 SEM cross-sections of the $\text{Sb}_2\text{Te}_3 / (\text{Bi,Sb})_2\text{Te}_3$ SLs for different annealing temperatures together with drawing of hexagonal crystallites and reference SEM images of sputtered Bi_2Te_3 films.	92
Figure 7.6 XRD patterns of the $\text{Sb}_2\text{Te}_3 / (\text{Bi,Sb})_2\text{Te}_3$ SLs.	93
Figure 7.7 Plots of Rietveld-fitted XRD profiles for SLs with 50 nm period length annealed at 150 °C and 350 °C.....	93
Figure 7.8 Electrical properties of $\text{Sb}_2\text{Te}_3 / (\text{Bi,Sb})_2\text{Te}_3$ SLs as function of annealing temperature.....	94
Figure 7.9 Left: Power factors, total and lattice thermal conductivity of $\text{Sb}_2\text{Te}_3 / (\text{Bi,Sb})_2\text{Te}_3$ SLs as function of annealing temperature.....	96
Figure 7.10 SEM cross sections (BSE image) of $\text{Sb}_2\text{Te}_3 / (\text{Bi,Sb})_2\text{Te}_3$ SLs with ~ 18 μm thickness as grown and after annealing at 250 °C for 2 h.....	97
Figure 7.11 a) Fabricated pillar structure used for the measurement of cross-plane electrical conductivity. b) Exemplaric voltage transient observed during measurement on bulk Bi_2Te_3 c) Voltage / current lines on different pillars (70 and 80 μm side length).....	97
Figure 7.12 XRD patterns of nanoalloyed SLs with reduced PLs of 25 and 12.5 nm.	99
Figure 7.13 SIMS depth profile of low-periodic SL and HRXRD analysis of the (00.6) and (00.9) reflexes in the same SL, showing satellite shoulders.....	100
Figure 7.14 SEM images of $\text{Sb}_2\text{Te}_3 / (\text{Bi,Sb})_2\text{Te}_3$ SLs with a PL of 25 and 12.5 nm.....	100
Figure 7.15 STEM images of sputtered $\text{Sb}_2\text{Te}_3 / (\text{Bi,Sb})_2\text{Te}_3$ SLs with reduced PL.	101
Figure 7.16 Electrical properties of $\text{Sb}_2\text{Te}_3 / (\text{Bi,Sb})_2\text{Te}_3$ SLs with different PLs in comparison.....	101
Figure 7.17 λ and λ_1 of $\text{Sb}_2\text{Te}_3 / (\text{Bi,Sb})_2\text{Te}_3$ SLs with reduced PL and schematic of SLs with different PL.....	102
Figure 8.1 $\text{Bi}_2(\text{Se},\text{Te})_3$ – based SL system examined previously and n-type $(\text{Bi}_{1-x}\text{Sb}_x)_2\text{Te}_3$ – based system examined in this work.....	103
Figure 8.2 Electrical properties of $(\text{Bi}_{1-x}\text{Sb}_x)_2\text{Te}_3$ in dependence on Sb content x after annealing for 2 hours at 250 °C...	104
Figure 8.3 SEM cross-sections of $\text{Bi}_2\text{Te}_3/(\text{Bi}_{0.9}\text{Sb}_{0.1})_2\text{Te}_3$ SLs in as-grown and annealed state for different annealing temperatures.	105
Figure 8.4 $\theta - 2\theta$ scan of $\text{Bi}_2\text{Te}_3/(\text{Bi}_{0.9}\text{Sb}_{0.1})_2\text{Te}_3$ – SLs for different annealing temperatures.....	105
Figure 8.5 SIMS depth profiles of $\text{Bi}_2\text{Te}_3/(\text{Bi}_{0.9}\text{Sb}_{0.1})_2\text{Te}_3$ – SLs with modified stacking sequence annealed for 2 h at different temperatures.....	106
Figure 8.6 SEM images of SIMS craters of n-type $\text{Bi}_2\text{Te}_3/(\text{Bi}_{0.9}\text{Sb}_{0.1})_2\text{Te}_3$ and a p-type $\text{Sb}_2\text{Te}_3 / (\text{Bi}_{0.2}\text{Sb}_{0.8})_2\text{Te}_3$ SL.	106
Figure 8.7 Electrical transport properties of $\text{Bi}_2\text{Te}_3 / (\text{Bi}_{0.9}\text{Sb}_{0.1})_2\text{Te}_3$ – SLs annealed at different temperatures.....	107
Figure 8.8 PF, total and lattice thermal conductivity of $\text{Bi}_2\text{Te}_3 / (\text{Bi}_{0.9}\text{Sb}_{0.1})_2\text{Te}_3$ – SLs versus annealing temperature.....	108
Figure 9.1 XRD pattern of epitaxially grown Sb_2Te_3 for different growth temperatures.....	112
Figure 9.2 SEM cross sections of epitaxially grown Sb_2Te_3 for different growth temperatures.....	112
Figure 9.3 Pole figures, ϕ -scan and SEM surface image of epitaxially grown Sb_2Te_3	113
Figure 9.4 Electrical properties of epitaxially grown Sb_2Te_3 films as function of Te content..	114
Figure 9.5 Electrical conductivity and Pisarenko plot of epitaxial Sb_2Te_3 films as function of Te content for different growth temperatures.	114
Figure 9.6 XRD patterns, SEM cross sections and BSE images of different epitaxial $\text{Bi}_2\text{Te}_3 / \text{Sb}_2\text{Te}_3$ SLs with different period lengths in the vicinity of the (00.21) reflex.	115
Figure 9.7 XRD pattern of epitaxial $\text{Bi}_2\text{Te}_3 / \text{Sb}_2\text{Te}_3$ SL samples with 6 nm period length, showing very well expressed satellite reflexes.....	116
Figure 9.8 Different HAADF-STEM cross-sections and an EDX elemental map of $\text{Bi}_2\text{Te}_3 / \text{Sb}_2\text{Te}_3$ SLs with 6 nm period length.	117
Figure 9.9 Total and lattice thermal conductivities of MBE-grown epitaxial $\text{Bi}_2\text{Te}_3 / \text{Sb}_2\text{Te}_3$ SLs.	118
Figure 9.10 XRD pattern of $\text{Bi}_2\text{Te}_3 / \text{Sb}_2\text{Te}_3$ SL with 6 nm period length around (00.9) reflex in dependence on temperature.....	119
Figure 9.11 Cross-section HAADF-STEM images of area with pronounced bending in $\text{Bi}_2\text{Te}_3 / \text{Sb}_2\text{Te}_3$ SL with 6 nm period length for different temperatures.	120
Figure 9.12 Seebeck coefficient of $\text{Bi}_2\text{Te}_3 / \text{Sb}_2\text{Te}_3$ SL with 6 nm period length in dependence on temperature for ex-situ heating.	121

List of publications

Publications in peer-reviewed journals as primary author:

- M. Winkler, J. D. König, S. Buller, U. Schürmann, L. Kienle, W. Bensch, H. Böttner, *Nanoalloyed Bi_2Te_3 and Sb_2Te_3 thin films and $\text{Bi}_2\text{Te}_3/\text{Sb}_2\text{Te}_3$ Multilayers*, MRS proceedings (spring meeting 2011, reviewed proceedings band), mrs11-1329-i10-15, 1329 (2011), doi:10.1557/opl.2011.1237. Parts of this work are shown in chapter 5 and 6.
- M. Winkler, X. Liu, J. D. König, L. Kirste, H. Böttner, W. Bensch, and L. Kienle, *Sputtered p-Type $\text{Sb}_2\text{Te}_3/(\text{Bi,Sb})_2\text{Te}_3$ Soft Superlattices Created by Nanoalloying*, J. Electron. Mater. 41, 1322 (2012). This work is shown in chapter 7 with additional results.
- M. Winkler, X. Liu, J. D. König, S. Buller, U. Schürmann, L. Kienle, W. Bensch, H. Böttner, *Electrical and structural properties of Bi_2Te_3 and Sb_2Te_3 thin films grown by the nanoalloying method with different deposition patterns and compositions*, J. Mater. Chem. 22, 11323 (2012). This work is shown in chapter 5.
- M. Winkler, X. Liu, U. Schürmann, J. D. König, L. Kienle, W. Bensch, H. Böttner, *Current status in fabrication, structural and transport property characterization and theoretical understanding of Bi_2Te_3 / Sb_2Te_3 superlattice systems*, Z. Anorg. Allg. Chem. 638, 2441 (2012). Parts of this work are shown in section 3.5.
- M. Winkler, X. Liu, A.-L. Hansen, J. D. König, W. Bensch, L. Kienle, H. Böttner, K. Bartholomé, *Sputtered n-type Bi_2Te_3 / $(\text{Bi,Sb})_2\text{Te}_3$ superlattice systems*, Nanothermoelectrics 1, 1-9 (2013), DOI: 10.2478/n-te-2013-0001. Parts of this work are shown in chapter 8.

Book chapters as primary author:

- M. Winkler, T. Dankwort, U. Schürmann, X. Liu, J.D. König, L. Kienle, W. Bensch, H. Böttner, *Fabrication and Comprehensive Structural and Transport Property Characterization of Nanoalloyed Nanostructured V_2VI_3 Thin Film Materials*, Book chapter in O. Eibl, K. Nielsch, N. Peranio, F. Völklein, *Thermoelectric Bi_2Te_3 Nanomaterials*, submitted in July 2014 and printing in progress. Parts of this work are shown in chapters 2, 3, 5, and 6.

Proposals:

- M. Winkler, U. Schürmann, L. Kienle, X. Liu, W. Bensch, J.D. König, H. Böttner: Follow-up project *Break and Beyond: Renewal proposal for a research grant within the Priority Program 1386 (SPP 1386) "Nanostructured Thermoelectric Materials: Theory, Model Systems, and Controlled Synthesis"*, second funding period. The proposal was accepted and funding was granted for another 36 months.

Publications in conference proceedings issues:

- M. Winkler, Jan D. König, S. Buller, U. Schürmann, L. Kienle, W. Bensch, H. Böttner, Proc. 8th European Conference on Thermoelectrics, Como, Italy, 19 (2010). Parts of this work are shown in chapter 5 and 6.
- M. Winkler, D. Ebling, H. Böttner, L. Kirste, Proc. 8th European Conference on Thermoelectrics, Como, Italy, 26 (2010). This work is shown in chapter 8 with additional results.
- M. Winkler, X. Liu, U. Schürmann, J. D. König, L. Kienle, W. Bensch, H. Böttner, *Nanostructured Thermoelectric Bi_2Te_3 / Sb_2Te_3 - based superlattice systems*, MRS Online Proceedings Library, Volume 1490, January 2013, mrsf12-1490-b13-02. Parts of this work are shown in section 2.2 and section 3.5.

Reports (Publicly accessible) :

- M. Winkler, BMBF-Verbundvorhaben Nanopelt: Implementierung nanoskaliger Schichten in thermoelektrischen Bauelementen auf alternativen Substraten, Abschlussbericht, Projektleiter: M. Winkler. Archived by the Technische Informationsbibliothek Universitätsbibliothek Hannover (TIBUB), <http://edok01.tib.uni-hannover.de/edoks/e01fb12/684423340.pdf> (24.01.2013)

Patents:

- M. Winkler, J. König, *Verfahren zum Herstellen einer elektrischen Kontaktschicht an einem mehrschichtigen, elektrischen Bauelement*, DE102014007890.6, submitted in May 2014.

Publications in peer-reviewed journals with contributions from the author of this work:

- J.D. König, M. Winkler, S. Buller, W. Bensch, U. Schürmann, L. Kienle, H. Böttner, *Bi₂Te₃-Sb₂Te₃ Superlattices Grown by Nanoalloying*, J. Electron. Mater. 40, 1266, (2011). Parts of this work are shown in chapter 5 and 6.
- U. Schürmann, M. Winkler, J. D. König, X. Liu, V. Duppel, W. Bensch, H. Böttner and L. Kienle, *In Situ TEM Investigations on Thermoelectric Bi₂Te₃/Sb₂Te₃ Multilayers*, Adv. Eng. Mater. 2012, 14, 139. Parts of this work are shown in chapter 6.
- N. Peranio, Z. Aabdin, W. Töllner, M. Winkler, J. König, O. Eibl, K. Nielsch, H. Böttner, *Low loss EELS and EFTEM study of Bi₂Te₃ based bulk and nanomaterials*, MRS Proceedings 1329, 2011, mrss11-1329-i10-21 doi:10.1557/opl.2011.1238.
- N. Peranio, M. Winkler, Z. Aabdin, J. König, H. Böttner, and O. Eibl, *Room temperature MBE deposition of Bi₂Te₃ and Sb₂Te₃ thin films with low charge carrier densities*; Phys. Status Solidi A, 289 (2012). Parts of this work are shown in section 5.2.
- Z. Aabdin, M. Winkler, D. Bessas, J. König, N. Peranio, O. Eibl, R. Hermann, and H. Böttner, *Sb₂Te₃ and Bi₂Te₃ Thin Films Grown by Molecular Beam Epitaxy at Room Temperature*; MRS Proceedings 1329, 2011, mrss11-1329-i04-04 doi:10.1557/opl.2011.1251.
- Z. Aabdin, N. Peranio, M. Winkler, D. Bessas, J. König, R.P Hermann, H. Böttner, and O. Eibl, *Sb₂Te₃ and Bi₂Te₃ thin films grown by room-temperature MBE*; J. Electron Mater. 41, 1493 (2012). Parts of this work are shown in section 5.2.
- N. Peranio, M. Winkler, D. Bessas, Z. Aabdin, J. König, H. Böttner, R.P. Hermann, O. Eibl, *Room-temperature MBE deposition, thermoelectric properties, and advanced structural characterization of binary Bi₂Te₃ and Sb₂Te₃ thin films*; J. Alloy Compd. 521, 163 (2012). Parts of this work are shown in section 5.2.
- Z. Aabdin, N. Peranio, O. Eibl, W. Töllner, K. Nielsch, D. Bessas, R.P. Hermann, M. Winkler, J. König, H. Böttner, V. Pacheco, J. Schmidt, A. Hashibon, and C. Elsässer, *Nanostructure, excitations, and thermoelectric properties of Bi₂Te₃ based nanomaterials*, J. Electron Mater. 41, 1792 (2012)
- N. F. Hinsche, B. Yu. Yavorsky, M. Gradhand, M. Czerner, M. Winkler, J.König, H. Böttner, I. Mertig, and P. Zahn, *Thermoelectric transport in Bi₂Te₃/Sb₂Te₃ superlattices*, Phys. Rev. B 86, 085323 (2012). Parts of this work are shown in section 2.2.1.1.

Other peer-reviewed publications with no direct relation to this thesis:

- J.D. König, M. Winkler, H. Böttner, *Transport Properties of Doped, Nanostructured IV–VI Epitaxial Films Grown by MBE*, J. Electron. Mater 38, 1418 (2009)
- M. Scholdt, H. Do, J. Lang, A. Gall, A. Colsmann, U. Lemmer, J.D. König, M. Winkler, H. Böttner, *Organic Semiconductors for Thermoelectric Applications*, J. Electron. Mater 39, 1589 (2010)

- J.D. König, M.D. Nielsen, Y. Gao, M. Winkler, A. Jacquot, H. Böttner, J.P. Heremans, *Titanium forms a resonant level in the conduction band of PbTe*, Phys. Rev. B 84, 205126 (2011)

The contents of this work were presented by the author as follows:

Invited talks:

- M. Winkler, Jan D. König, D. Ebling, H. Böttner, S. Buller, U. Schürmann, L. Kienle, W. Bensch, H. Böttner, L. Kirste, *Nanoalloying – An approach for creating thermoelectric compounds and nanostructured multilayers in the material group (Bi,Sb)₂Te₃*, 8th European Conference on Thermoelectrics, Como, Italy, 2010
- M. Winkler, M. Jäggle, X. Liu, J. D. König, H. Böttner, W. Bensch, L. Kienle, *Micro- and nanoscale thermoelectrics: An overview over basic concepts and recent advances*, SPIE Microtechnologies, Grenoble, France, 2013
- M. Winkler, J.D. König, M. Jäggle, H. Böttner, K. Bartholomé, *Thermoelektrik – Anwendungen, Messtechnik und Schichtherstellung*, V2013, Dresden, Germany, 2013
- M. Winkler, J.D. König, A.L. Hansen, T. Dankwort, H. Böttner, K. Bartholomé, W. Bensch, L. Kienle, *Stability, structure and properties of Sb₂Te₃-Bi₂Te₃ intergrowths and superlattices*, CIMTEC 6th Forum on New Materials, Montecatini, Italy, 2014

Regularly talks and posters:

- M. Winkler, J. D. König, H. Böttner, X. Liu, W. Bensch, T. Dankwort, U. Schürmann, L. Kienle, *Stability, structure and properties of Sb₂Te₃-Bi₂Te₃ intergrowths and superlattices*, 33rd International Conference on Thermoelectrics, Nashville, USA, 2014, talk
- M. Winkler, D. Ebling, H. Böttner, *Sputtered n-type soft superlattices based on Bi₂Te₃/(Bi,Sb)₂Te₃ created by nanoalloying*, 30th International Conference on Thermoelectrics, Traverse City, USA, 2011, talk
- M. Winkler, X. Liu, J. D. König, L. Kirste, H. Böttner, W. Bensch, and L. Kienle, *Sputtered p-type Sb₂Te₃ / (Bi,Sb)₂Te₃ soft superlattices created by nanoalloying*, 30th International Conference on Thermoelectrics, Traverse City, USA, 2011, poster
- M. Winkler, J. D. König, H. Böttner, X. Liu, W. Bensch, U. Schürmann, L. Kienle, *Sputtered p-type Sb₂Te₃/(Bi,Sb)₂Te₃ soft superlattices fabricated by nanoalloying with high structural and thermoelectric quality*, E-MRS spring meeting, Strasbourg, France, 2012, talk
- M. Winkler, H. Böttner, J. D. König, W. Bensch, X. Liu, L. Kienle, U. Schürmann, I. Mertig, P. Zahn, N.F. Hinsche, B.Y. Yavorsky, *“Break” - Reinvestigating the high ZT values reported for Bi₂Te₃ / Sb₂Te₃ superlattice structures*, E-MRS spring meeting, Strasbourg, France, 2012, poster
- M. Winkler, J. D. König, H. Böttner, U. Schürmann, T. Dankwort, L. Kienle, X. Liu, W. Bensch, *ZT and more – Fabrication and Characterization of nanoscale V₂VI₃ superlattice systems*, E-MRS spring meeting, Strasbourg, France, 2013, talk
- M. Winkler, J. D. König, H. Böttner, X. Liu, W. Bensch, U. Schürmann, L. Kienle, *Energy efficiency by nanoscale thermoelectric materials*, 16. Vortragstagung Materialchemie für Energie- und Ressourcennutzung, Darmstadt, Germany, 2012, talk
- Workshop “Thermoelectric Properties related to Nanostructure and Dimensionality in Bi₂Te₃ Nanomaterials”, Darmstadt, Germany, 2012, talk
- Workshop of the Graduiertenkolleg „Micro Energy Harvesting“, IMTEK Freiburg, Germany, 2010 and 2013, talk and poster

Acknowledgement

I'd like to thank the following persons for their contributions to this work:

- First and foremost Prof. Dr. Eibl for the supervision of this work and the scientific advice with clear instructions. I'd also like to thank for the pleasant and fruitful cooperation within the SPP1386 and further efforts such as the workshop on Bi₂Te₃ related materials in 2012.
- Prof. Dr. Reinhold Kleiner for the co-supervision of this work.
- Dr. Nicola Peranio, Institute for Applied Physics, Eberhard Karls Universität Tübingen for the TEM images shown in chapter 5, the pleasant cooperation, scientific discussions and the proofreading of this work.
- My former head of department Dr. Harald Böttner and group leader Dr. Jan König for acquiring the DFG and BMBF project that was used for the funding of this work (see below), for the fruitful cooperation and always helpful and welcome scientific advice and discussion.
- Our head, former head of institute and head of department, Prof. Karsten Buse, Prof. Elmar Wagner and Dr. Kilian Bartholomé for allowing me and my department to participate in the DFG Priority Program 1386 and thus making this work possible.
- Dr. Alexandre Jacquot for the 3ω measurements, the temperature-dependent Seebeck coefficient and conductivity measurements with the SRX setup and for scientific discussions.
- Dieter Rutsch, Uwe Vetter and Jan König for help with maintenance and technical advice for the sputtering system and MBE, Uwe Kruck and Julia Tetcau for carrying out the annealing and the maintenance of the annealing setup.
- Prof. David G. Cahill, University of Illinois, for setting up the TDTR measurement system in cooperation with Fraunhofer IPM and his very useful help interpreting and analyzing the TDTR data and advice operating the system.
- Dr. Ulrich Schürmann, Torben Dankwort and Prof. Lorenz Kienle, Synthesis and Real Structure, Institute for Materials Science, Christian-Albrechts-Universität zu Kiel, Germany for the TEM images shown in chapters 6,7,9. Dr. Xi Liu, Saskia Buller, Anna-Lena Hansen and Prof. Wolfgang Bensch, Institute of Inorganic Chemistry, Christian-Albrechts-Universität zu Kiel for the recorded XRD patterns and for the Rietveld refinements.
- Dr. Lutz Kirste, Theo Fuchs and Martin Grimm, Fraunhofer IAF, Freiburg for parts of the XRD patterns and for all SIMS depth profiles.
- Zhixi Bian, Philip Jackson and Prof. Ali Shakouri, University of Santa Cruz, California for carrying out the cross-plane conductivity measurements shown in section 7.4.
- David Johnson, University of Oregon for his professional advice and the possibility to use his lab CAMCOR and equipment for research on superlattice structure, and of course for the pleasant stay at our institute in Freiburg and his dinner invitations.
- All our partners of Project "Break" and "Break and Beyond" that I have not specifically mentioned for the very pleasant and fruitful cooperation.
- The members of Micropelt company for their useful advice on sputtering V₂VI₃ materials.

Finally, I'd like to thank my family for their neverending support and especially my parents for making studying possible for me. Many thanks go out to all my friends and my lovely girlfriend Annette for moral support and for the relaxation of internal stress (pun intended) during this thesis. Special thanks go to all my colleagues from Fraunhofer IPM and their great work, my department (T)ES and especially my room- and lunchmates for the pleasant (work) atmosphere.

Financial support by the German Research Foundation (DFG) within the Priority Program (Schwerpunktprogramm) 1386 "Nanostructured Thermoelectric Materials: Theory, Model Systems and Controlled Synthesis", Projects "Break" and "Break and Beyond", BO3099/1-1 and -2 and the Bundesministerium für Bildung und Forschung (BMBF) within the program frame "Werkstoffinnovationen für Industrie und Gesellschaft", funding program "Nanochance", 03X4506B, is gratefully acknowledged.

Bibliography

- [1] L. Anatyshuk, J. Stockhom, G. Pastorino, Proc. 8th European Conference on Thermoelectrics, Como, Italy, 15 (2010)
- [2] T.J. Seebeck, *Magnetische Polarisation der Metalle und Erze durch Temperaturdifferenz*, Chapter in *Abhandlungen der Königlichen Akademie der Wissenschaften zu Berlin*, p. 265 (1825), republished in *Ostwald's Klassiker der exakten Wissenschaften No. 70*, Verlag von Wilhelm Engelmann, Leipzig, 1895
- [3] A.F. Ioffe, *Semiconductor Thermoelements and Thermoelectric Cooling*, Infosearch Limited London, 1957. Translated from Russian Version and edited by H.J. Goldsmid.
- [4] E. Altenkirch, *Phys. Z.* 12, 920 (1911)
- [5] D.M. Rowe, *Modern thermoelectrics*, Holt, Rhinehart and Winston Ltd. (London), 1983
- [6] A.F. Joffe, L.S. Stil'bans, *Physical problems of thermoelectricity*, *Rep. Prog. Phys.* 22, 167 (1959)
- [7] L.D. Hicks, M.S. Dresselhaus, *Phys. Rev. B* 47, 12727 (1993)
- [8] R. Venkatasubramanian, E. Siivola, T. Colpitts & B. O'Quinn, *Nature* 413, 597 (2001)
- [9] Ch. Weißmantel, C. Hamann, *Grundlagen der Festkörperphysik*, VEB Deutscher Verlag der Wissenschaften, Berlin, 1979, Licensed reprint by Springer Verlag, Berlin Heidelberg New York, 1980
- [10] H.J. Goldsmid, *Thermoelectric refrigeration*, Plenum Press, New York, 1964
- [11] G.S. Nolas, J. Sharp, H.J. Goldsmid, *Thermoelectrics – Basic Principles and New Materials Developments*, Springer-Verlag, Berlin-Heidelberg, 2001
- [12] R. Pelster, R. Pieper, I. Hüttl, *PhyDid* 1/4, 10 (2005)
- [13] O. Yamashita, S. Sugihara, *J. Mater. Sci.* 40, 6439 (2005)
- [14] B. Poudel, Q. Hao, Y. Ma, Y. Lan, A. Minnich, B. Yu, C. Yan, D. Wang, A. Muto, D. Vashaee, X. Chen, J. Liu, M.S. Dresselhaus, G. Chen, Z. Ren, *Science Express* 320, 634 (2008)
- [15] J.R. Sootsman, D.Y. Chung, M.G. Kanatzidis, *Angew. Chem. Int. Ed.* 48, 8616 (2009)
- [16] G.J. Snyder, E.S. Toberer, *Nature Materials* 7, 105 (2008)
- [17] S. Sakurada, N. Shutoh, *Appl. Phys. Lett.* 86, 082105 (2005)
- [18] S.R. Culp, J.W. Simonson, S.J. Poon, V. Ponnambalam, J. Edwards, Terry M. Tritt, *Appl. Phys. Lett.* 93, 022105 (2008)
- [19] X. Tang, Q. Zhang, L. Chen, T. Goto, T. Hirai, *J. Appl. Phys.* 97, 093712 (2005)
- [20] V.K. Zaitsev, M.I. Fedorov, E.A. Gurieva, I.S. Eremin, P.P. Konstantinov, A. Yu. Samunin, M.V. Vedernikov, *Phys. Rev. B* 74, 045207 (2006)
- [21] M.I. Fedorov, V.K. Zaitsev, *Thermoelectrics of Transition Metal Silicides*, chapter in *CRC Handbook of Thermoelectrics (Ed. D.M. Rowe)*, CRC Press, Boca Raton, 2006, 31-1
- [22] G. J. Snyder, T. Caillat, *MRS Proc.* 793 (Fall Meeting 2003, Symposium S), 37 (2004)
- [23] A. Saramat, G. Svensson, A.E. Palmqvist, C. Stiewe, E. Mueller, *J. Appl. Phys.* 99, 023708 (2006)
- [24] N.L. Okamoto, K. Kishida, K. Tanaka, H. Inui, *J. Appl. Phys.* 100, 073504 (2006)
- [25] K. Biswas, J. He, I.D. Blum, C.-I Wu, T.P. Hogan, D.N. Seidman, V.P. Dravid, M.G. Kanatzidis, *Nature* 489, 414 (2012)
- [26] G.D. Mahan, *J. Appl. Phys.* 65, 1578 (1989)
- [27] G. Min, D.M. Rowe, *Appl. Phys. Lett.* 77, 860 (2000)

- [28] W. Demtröder, *Experimentalphysik 3 – Atome, Moleküle und Festkörper*, Springer-Verlag Berlin Heidelberg New York, 2nd edition 2000, corrected reprint 2004
- [29] H. Ibach, H. Lüth, *Festkörperphysik – Einführung in die Grundlagen*, Springer-Verlag, Berlin Heidelberg, 7th edition, 2009
- [30] A.F. Ioffe, *Physics of Semiconductors*, Infosearch Limited, London, 1960. Translation of *Fizika Poluprovodnikov*, Publishing House of the USSR Academy of Sciences, Moscow-Leningrad, 1957
- [31] M. Stordeur, M. Stölzer, H. Sobotta, V. Riede, Phys. Stat. Sol. (b) 150, 165 (1988)
- [32] H.J. Goldsmid, *Electronic refrigeration*, Pion Limited (London), 1986
- [33] P. Kwapulinski, J. Rasek, Z. Gierak, Phys. Stat. Sol. (a) 107, 299 (1988)
- [34] M. Asen-Palmer, K. Bartkowski, E. Gmelin, M. Cardona, A. P. Zhernov, A. V. Inyushkin, A. Taldenkov, V. I. Ozhogin, K. M. Itoh, and E. E. Haller, Phys. Rev. B 56, 9431 (1997)
- [35] D.T. Morelli, J.P. Heremans, G.A. Slack, Phys. Rev. B 66, 195304 (2002)
- [36] N. Savvides, H. Goldsmid, J. Phys. C: Solid State Physics 6, 1701 (1973)
- [37] Y.A. Boikov, B.M. Gol'tsman, V.A. Kutasov, Sov. Phys. Solid State 20, 757 (1978)
- [38] C. Chiritescu, C. Mortensen, D. G. Cahill, D. Johnson, and P. Zschack., J. Appl. Phys. 106, 073503 (2009)
- [39] M. Takashiri, S. Tanaka, K. Miyazaki, H. Tsukamoto, J. Alloy Compd. 490, L44 (2010)
- [40] P.J. Lin-Chung, T.L. Reinecke, Phys. Rev. B 51, 13244 (1995)
- [41] L.D. Hicks, T.C. Harman, X. Sun, M.S. Dresselhaus, Phys. Rev. B 53, R10493 (1996)
- [42] J. Nurnus, *Thermoelektrische Effekte in Übergittern und Multi-Quantentrog-Strukturen*, PhD. thesis, University of Freiburg, Department of Physics, Germany, 2001
- [43] D.A. Broido, T.L. Reinecke, Phys. Rev. B 51, 13797 (1995)
- [44] A. Shakouri, Proc. ICT 2005: 24th International Conference on Thermoelectrics, Clemson, USA, 495 (2005)
- [45] J.P. Heremans, Acta Physica Polonica A 108, 609 (2005)
- [46] R. Venkatasubramanian and T. S. Colpitts, Enhancement in Figure-of-Merit with Superlattice Structures for Thin-Film Thermoelectric Devices in Thermoelectric Materials, ed. by T. M. Tritt et al., MRS Symposia Proc. 478, Materials Research Society, Pittsburgh, 1997, p. 73.
- [47] N.F. Hinsche, B.Y. Yavorsky, I. Mertig, P. Zahn, Phys.Rev. B 84, 165214 (2011)
- [48] B.Y. Yavorsky, N.F. Hinsche, I.Mertig, P. Zahn, Phys. Rev. B 84, 165208 (2011)
- [49] N.F. Hinsche, B.Yu. Yavorsky, M. Gradhand, M. Czerner, M. Winkler, J. König, H. Böttner, I. Mertig, P. Zahn, Phys. Rev. B 86, 085323 (2012)
- [50] P. Hylgaard, G.D. Mahan, Phys. Rev. B 56, 10754 (1997)
- [51] S.Y. Ren, J.D. Dow, Phys.Rev.B 25, 3750 (1982)
- [52] M.N. Touzelbaev, P. Zhou, R. Venkatasubramanian, and K. E. Goodson, J. Appl. Phys. 90, 763 (2001)
- [53] F. Takahashi, Y. Hamada, T. Mori and I. Hatta, Jpn. J. Appl. Phys. 43, 8325 (2004)
- [54] S. Tamura, D.C. Hurley, J.P. Wolfe, Phys. Rev. B 38, 1427 (1988)
- [55] V. Narayanamurti, H.L. Störmer, M.A. Chin, A.C. Gossard, W. Wiegmann, Phys. Rev. Lett. 43, 2012 (1979)
- [56] G. Chen, Phys. Rev. B 57, 14958 (1998)

- [57] R. Venkatasubramanian, Phys. Rev. B 61, 3091 (2000)
- [58] D.S. Wiersma, P. Bartolini, A. Lagendijk, R. Righini, Nature 390, 671 (1997)
- [59] A.F. Ioffe, A.R. Regel, Prog. Semicond. 4, 237 (1960)
- [60] R. Venkatasubramanian, T. Colpitts, B. O'Quinn, M. Lamvik, N. El-Masry, Appl. Phys. Lett. 75, 1104 (1999)
- [61] A. Pattamatta, C.K. Madnia, Int. J. Heat. Mass. Tran. 52, 860 (2009)
- [62] Y. Wang, X. Xu, and R. Venkatasubramanian, Appl. Phys. Lett. 93, 113114 (2008)
- [63] Y. Wang, C. Liebig, X. Xu, and R. Venkatasubramanian, Appl. Phys. Lett 97, 083103 (2010)
- [64] H. Böttner, G. Chen, R. Venkatasubramanian, MRS Bulletin 31, 211 (2006)
- [65] G. Wang, L. Endicott, and C. Uher, Sci. Adv. Mater. 3, 539 (2011)
- [66] N.H. Abrikosov, V.F. Bankina, L.V. Poretskaya, L.E. Shelimova, E.V. Skudnova, Semiconducting II-VI, IV-VI, and V-VI Compounds, Plenum Press, New York, 1969, 165
- [67] S. Nakajima, J. Phys. Chem. Solids 24, 479 (1963)
- [68] T.L. Anderson, H.B. Krause, Acta Crystallogr. B30, 1307 (1974)
- [69] J.O. Barnes, J.A. Rayne, and R.W. Ure, Phys. Lett. A 46, 317 (1974)
- [70] X. Chen, H.D. Zhou, A. Kiswandhi, I. Miotkowski, Y.P. Chen, P.A. Sharma, A.L. Lima Sharma, M.A. Hekmaty, D. Smirnov, and Z. Jiang, Appl. Phys. Lett. 99, 261912 (2011)
- [71] H. Neumann, G. Kommichau, W. Schmitz, B. Schumann, J. Mater. Sci. Lett 5, 1131 (1986)
- [72] W.C. Haynes, CRC Handbook of Chemistry and Physics, 92nd edition, Taylor and Francis, 2011
- [73] B. El-Kareh, *Fundamentals of Semiconductor Processing Technologies*, Norwell, Kluwer Academic Publishers, 1995
- [74] Z. Huang, F. Zu, J. Chen, G. Ding, Intermetallics 18, 749 (2010)
- [75] R.F. Brebrick, J. Phys. Chem. Solids 30, 719 (1969)
- [76] J.W.G. Bos, H.W. Zandbergen, M.-H. Lee, N.P. Ong, R.J. Cava, Phys. Rev. B 75, 195203 (2007)
- [77] P. F. P. Poudeu, M. G. Kanatzidis, Chem. Comm. 21, 2672 (2005)
- [78] T. Caillat, M. Carle, D. Perrin, H. Scherrer and S. Scherrer, J. Phys. Chem. Solids 53, 227 (1992)
- [79] H. Scherrer, B.Hammou, J.P. Fleurial, S.Scherrer, Phys. Lett. A 130, 161 (1988)
- [80] G.R. Miller, C.-Y. Li, J. Phys. Chem. Solids 26, 173 (1965)
- [81] T. C. Harman, S. E. Miller, and H. L. Goeing, Bull. Amer. Phys. Soc. 30, 35 (1955).
- [82] P. Pecheur, G. Toussaint, J. Phys. Chem. Solids 55, 327 (1994)
- [83] F.A. Kröger, J. Phys. Chem. Solids 7, 276 (1958)
- [84] A. Hashibon, C. Elsässer, Phys. Rev. B 84, 144117 (2011)
- [85] N. Peranio, W. Winkler, M. Dürschnabel, J. König, O. Eibl, Adv. Funct. Mater. 23, 4969 (2013)
- [86] S. K. Mishra, S. Satpathy, and O. Jepsen, J. Phys.: Condens. Matter 9, 461 (1997)
- [87] B.Y. Yavorsky, N.F. Hinsche, I.Mertig, P. Zahn, Phys. Rev. B 84, 165208 (2011)
- [88] D.L. Greenaway, G. Harbecke, J. Phys. Chem Solids 26, 1585 (1965)
- [89] I.G. Austin, Proc. Phys. Soc. 76, 169 (1960)
- [90] H. Scherrer, S. Scherrer, *Bismuth Telluride, Antimony Telluride, and Their Solid Solutions, chapter in CRC Handbook of Thermoelectrics*, ed. D.M. Rowe, CRC press, Boca Raton, FL, 1995, ch. 19
- [91] C.B. Satterthwaite, R.W. Ure Jr., Phys. Rev. 108, 1164 (1957)

- [92] H.T. Langhammer, M. Stordeur, H. Sobotta, V. Riede, *Phys. Status Solidi B* 109, 673 (1982)
- [93] R. Jäschke, *Ann. Physik* 470, 106 (1965)
- [94] R. Martin-Lopez, H. Scherrer, *Solid State Commun.* 108, 285 (1998)
- [95] J. Nurnus, H. Böttner, H. Beyer, A. Lambrecht, *Proc. ICT99: 18th International Conference on Thermoelectrics*, Baltimore, USA, 696 (1999)
- [96] Personal communication with C. Uher during Workshop "Thermoelectric properties related to nanostructure and dimensionality in Bi₂Te₃ nanomaterials", GSI Darmstadt, 5.-6. July 2012
- [97] G. Wang, L. Endicott, C. Uher, *Growth and Characterization of Sb₂Te₃ Film on Al₂O₃ (0001) Substrates*, Talk on ICT 2011: 30th International Conference on Thermoelectrics, Traverse City, USA 2011
- [98] R. Venkatasubramanian, T. Colpitts, E. Watko, and J. Hutchby, *Proc. ICT 1996: 15th International Conference on Thermoelectrics*, Pasadena, USA, 454 (1996)
- [99] A. Boulouz, S. Chakraborty, A. Giani, F. Pascal Delannoy, A. Boyer, J. Schumann, *J. Appl. Phys.* 89, 5009 (2001)
- [100] J. Nurnus, H. Böttner, and A. Lambrecht, *Nanoscale Thermoelectrics*, chapter in *CRC Handbook of Thermoelectrics* (Ed. D.M. Rowe), CRC Press, Boca Raton, 2006, 48-1
- [101] S. Cho, Y. Kim, A. DiVenere, G.K. Wong, J.B. Ketterson, J.R. Meyer, *Appl. Phys. Lett.* 75, 1401 (1999)
- [102] Y. Kim, A. Di Venere, G.K.L. Wong, J.B. Ketterson, S. Cho, J. R. Meyer, *J. Appl. Phys.* 91, 715 (2002)
- [103] S. Cho, Y. Kim, J.B. Ketterson, *Appl. Phys. A* 79, 1729 (2004)
- [104] H. Böttner, J. Nurnus, A. Gavrikov, G. Kühner, M. Jägler, C. Künzel, D. Eberhard, G. Plescher, A. Schubert, K.-H. Schlereth, *J. Microelectromech. S.* 13, 414 (2004)
- [105] M. Stölzer, V. Bechstein, J. Meusel, *Proc. ICT 1997: 16th International Conference on Thermoelectrics*, Dresden, Germany, 93 (1997)
- [106] M. Stordeur, G. Willers, *Proc. ECT 2004: 2nd European Conference on Thermoelectrics*, Krakow, Poland, 12 (2004)
- [107] C.N. Liao, S.W. Kuo, *J. Vac. Sci. Technol. A* 23, 559 (2005)
- [108] A. Li Bassi, A. Bailini, C.S. Casari, F. Donati, A. Mantegazza, M. Passoni, V. Russo, C.E. Bottani, *J. Appl. Phys.* 105, 124307 (2009)
- [109] H. Obara, S. Higomo, M. Ohta, A. Yamamoto, K. Ueno, T. Iida, *Jpn. J. Appl. Phys.* 48, 085506 (2009)
- [110] L.W. da Silva, M. Kaviany, C. Uher, *J. Appl. Phys.* 97, 114903 (2005)
- [111] H. Zou, D.M. Rowe, G. Min, *J. Cryst. Growth* 222, 82 (2001)
- [112] H. Zou, D.M. Rowe, S.G.K. Williams, *Thin Solid Films* 408, 270 (2002)
- [113] L.M. Goncalves, C. Couto, P. Alpuim, A.G. Rolo, F. Völklein, J.H. Correia, *Thin Solid Films* 518, 2816 (2010)
- [114] C. Boulanger, *J. Electron. Mater.* 39, 1818 (2010)
- [115] C. Schumacher, *Pulsed Electrodeposited p- and n-Doped Chalcogenide Semiconductors for Thermoelectric Applications: From Films to Nanowires*, Ph.D. thesis at the University of Hamburg, Department of Physics, Germany, 2012
- [116] M. Winkler, X. Liu, U. Schürmann, J.D. König, L. Kienle, W. Bensch, H. Böttner, *Z. Anorg. Allg. Chem.* 638, 2441 (2012)

- [117] R. Venkatasubramanian, T. Colpitts, E. Watko, M. Lamvik, N. El-Masry, *J. Cryst. Growth* 170, 817 (1997)
- [118] H. Cui, I. Bhat, B. O'Quinn, R. Venkatasubramanian, *J. Electron. Mater.* 30, 1376 (2001)
- [119] J.D. König, M. Winkler, S. Buller, W. Bensch, U. Schürmann, L. Kienle, H. Böttner, *J. Electron. Mater.* 40, 1266 (2011)
- [120] M. Winkler, J. D. König, S. Buller, U. Schürmann, L. Kienle, W. Bensch, H. Böttner, *MRS Proc.* (spring meeting 2011) 1329, mrss11-1329-i10-15 (2011)
- [121] M. Winkler, Jan D. König, S. Buller, U. Schürmann, L. Kienle, W. Bensch, H. Böttner, *Proc. ECT 2010: 8th European Conference on Thermoelectrics, Como, Italy*, 19 (2010)
- [122] C.H. Champness, P.T. Chiang, P. Parker, *Can. J. Phys.* 43, 653 (1965)
- [123] D.C. Johnson, *Curr. Opin. Solid St. M.* 3, 159 (1998)
- [124] A. Mzerd, D. Sayah, J.C. Tedenac, A. Boyer, *J. Cryst. Growth* 140, 365 (1994)
- [125] L. Ratke, P.W. Voorhees, *Growth and Coarsening: Ostwald Ripening in Material Processing*, Springer-Verlag, 2002
- [126] F.R. Harris, S. Standridge, C. Feik, D.C. Johnson, *Angew. Chem. Int. Engl.* 42, 5295 (2003)
- [127] J.H. Yao, K.R. Elder, H. Guo, M. Grant, *Phys. Rev. B* 47, 14110 (1993)
- [128] C. Mortensen, R. Rostek, B. Schmid, D.C. Johnson, *Proc. ICT 2005: 24th International Conference on Thermoelectrics, Clemson, USA*, 261 (2005)
- [129] B.I. Boltaks, *Diffusion in Semiconductors*, Infosearch Limited London, 1963, translated from original title *Diffuziya v Poluprovodnikakh*
- [130] E. Charles, E. Groubert, A. Boyer, *J. Mat. Sci. Lett.* 7, 575 (1988)
- [131] M.A. Herman, H. Sitter, *Molecular Beam Epitaxy – Fundamentals and Current Status*, Springer Verlag, Berlin-Heidelberg, 1989
- [132] D. Khokhlov, *Lead Chalcogenides: Physics and Applications*, Taylor and Francis, New York, 2003
- [133] P.R. Norton, *The Molecular Beam Epitaxy Technique for PbSe-based Lead Chalcogenide Diode Lasers*, Ph.D. thesis at the University of Bath, England, 1986
- [134] C. Strondl, *Nanocomposite W-C:H diamond-like carbon coatings*, PhD thesis at the Rijksuniversiteit Groningen, Netherlands, 2007
- [135] R.V. Stuart, *Vacuum Technology, Thin Films, and Sputtering*, Academic Press, Inc, Orlando, 1983
- [136] J.A. Thornton, *J. Vac. Sci. Technol.* 11, 666 (1974)
- [137] L.J. van der Pauw, *Philips Research Reports* 13, 1 (1958)
- [138] D.K. Schroder, *Semiconductor Material and Device Characterization*, Wiley and Sons Inc., 2nd ed. 1998
- [139] S. Augustine, E. Mathai, *Semicond. Sci. Technol.* 18, 745 (2003)
- [140] Y.I. Ravich, B.A. Efimova, I.A. Smirnov, *Semiconducting Lead Chalcogenides*, Plenum Press, New York, 1970
- [141] O. Yamashita, H. Odahara, S. Tomiyoshi, *J. Mater. Sci.* 39, 5653 (2004)
- [142] A.T. Burkov, A. Heinrich, P.P. Konstantinov, T. Nakama, K. Yagasaki, *Meas. Sci. Technol.* 12, 264 (2001)
- [143] M. Stölzer, V. Bechstein, J. Meusel, *Proc. of the Fourth European Thermoelectric Society Workshop, Madrid*, 1998

- [144] O. Boffoué, A. Jacquot, A. Dauscher, B. Lenoir, M. Stölzer, *Rev. Sci. Instr.* 76, 053907 (2005)
- [145] D.G. Cahill, *Rev. Sci. Instr.* 75, 5119 (2004)
- [146] K. Kang, Y.K. Koh, C. Chiritescu, X. Zheng, and D.G. Cahill, *Rev. Sci. Instrum.* 79, 114901 (2008)
- [147] R.M. Costescu, M.A. Wall, D.G. Cahill, *Phys. Rev. B* 67, 054302 (2003)
- [148] S.T. Huxtable, D.G. Cahill, L.M. Phinney, *J. Appl. Phys.* 95, 2102 (2004)
- [149] C. Chiritescu, *Ultra Low Thermal Conductivity In Layered Disordered Crystalline Materials*, Ph.D. thesis in the Graduate College of the University of Illinois at Urbana-Champaign, 2010
- [150] D.G. Cahill, M. Katiyar, J. R. Abelson. *Phys. Rev. B* 50, 6077 (1994)
- [151] P. Cucka P, C.S. Barrett, *Acta Crystallogr.* 15, 865 (1962)
- [152] C.S. Barrett, P. Cucka, *Acta Crystallogr.* 16, 451 (1962)
- [153] P. Cherin, P. Unger, *Acta Crystallogr.* 23, 670 (1967)
- [154] A.L. Patterson, *Phys. Rev.* 56, 978 (1939)
- [155] M. Winkler, X. Liu, J. D. König, S. Buller, U. Schürmann, *J. Mater. Chem.* 22, 11323 (2012)
- [156] R.B. von Dreele, A.C. Larson, M. Lucan, *GSAS*, Neutron Scattering Centre, LANL, Los Alamos, 1995, NM 87545
- [157] A. Coelho, *TOPAS-Academic*, version 5 (Computer Software), Coelho Software, Brisbane, 2007
- [158] W.A. Dollase, *J. Appl. Cryst.* 19, 1986, 267
- [159] P.J. Suortti, *Appl. Cryst.* 5, 1972, 325
- [160] P. Schmidt, *Praxis der Rasterelektronenmikroskopie und Mikrobereichsanalyse*, Expert-Verlag, Mannheim-Renningen, 2004
- [161] D.B. Williams, C.B. Carter, *Transmission Electron Microscopy – A Textbook for Materials Science*, Springer Science+Business Media, LLC 1996, 2009 (Second Edition)
- [162] H. Beyer, *Thermoelektrische Effektivität von IV-VI Mehrfach-Quantentrog und Übergitter-Systemen*, Ph.D. thesis, Johannes Kepler University of Linz, Institute of Semiconductor and Solid State Physics, Austria, 2001
- [163] H. Böttner, A. Schubert, H. Kölbl, A. Gavrikov, A. Mahlke, J. Nurnus, *Proc. ICT04: 23rd International Conference on Thermoelectrics*, Adelaide, Australia, 114 (2004)
- [164] Z. Aabdin, N. Peranio, M. Winkler, D. Bessas, J. König, R. Hermann, H. Böttner, O. Eibl, *J. Electron. Mater.* 41, 1493 (2012)
- [165] M.H. Francombe, *Philos. Mag.* 10, 989 (1964)
- [166] N. Peranio, M. Winkler, D. Bessas, Z. Aabdin, J. König, H. Böttner, R.P. Hermann, O. Eibl, *J. Alloy. Compd.* 521, 163 (2012)
- [167] N. Peranio, M. Winkler, Z. Aabdin, J. König, H. Böttner, O. Eibl, *Phys. Status Solidi A* 209, 289 (2012)
- [168] N. Peranio, O. Eibl, J. Nurnus, *J. Appl. Phys.* 100, 114306 (2006)
- [169] Grosse, P.: *Die Festkörpereigenschaften von Tellur*, in: Springer Tracts in Modern Physics, Vol. 48, ed. by G. Höhler, Springer, Berlin-Heidelberg-New York 1969.
- [170] C.H. Champness, A.L. Kipling, *Can. J. Phys.* 44, 769 (1966)
- [171] U. Schürmann, M. Winkler, J.D. König, X. Liu, V. Duppel, W. Bensch, H. Böttner, L. Kienle, *Adv. Eng. Mater.* 14, 139 (2012)
- [172] M. Winkler, X. Liu, J. D. König, L. Kirste, H. Böttner, *J. Electron. Mater.* 41, 1322 (2012).
- [173] J. Martin, L. Wang, L. Chen, G.S. Nolas, *Phys. Rev. B* 79, 115311 (2009)

- [174] D-H. Kim, T. Mitani, *J. Alloy Compd.* 399, 14 (2005)
- [175] J.D. König, H. Böttner, J. Tomforde et al., *Proc. ICT2007: 26th International Conference on Thermoelectrics*, Jeju Island, Korea, 395 (2007)
- [176] J.-P. Fleurial, A. Borshchevsky, M.A. Ryan, W. Phillips, E. Kolawa, T. Kacisch, R. Ewell, *Proc 16th Int. Conf. Thermoelectrics*, Dresden, Germany, 641 (1997)
- [177] Personal communication with Z. Bian, P. Jackson, A. Shakouri, Quantum Electronics group, Jack Baskin School of Engineering, University of California, Santa Cruz
- [178] Z. Bian, Y. Zhang, H. Schmidt, A. Shakouri, *Proc. ICT 2005: 24th International Conference on Thermoelectrics*, Clemson, USA, 76 (2005)
- [179] T.C. Harman, *J. Appl. Phys.* 29, 1373 (1958)
- [180] L. Zhang, R. Hammond, M. Dolev, M. Liu, A. Palevski, A. Kapitulnik, *Appl. Phys. Lett.* 101, 153105 (2012)
- [181] M. Winkler, X. Liu, A.-L. Hansen, J. D. König, W. Bensch, L. Kienle, H. Böttner, K. Bartholomé, *Nanothermoelectrics* 1, 1-9 (2013), DOI: 10.2478/nte-2013-0001.
- [182] J. George, B. Pradeep, *Solid State Commun.* 56, 117 (1985)
- [183] Y.J. Chien, Z. Zhou, C. Uher, *J. Cryst. Growth* 283, 309 (2005)
- [184] J. Nurnus, C. Künzel, H. Beyer, A. Lambrecht, H. Böttner, A. Meier, M. Blumers, F. Völklein, N. Herres, *Proc. ICT 2000: 19th International Conference on Thermoelectrics*, Cardiff, UK, 236 (2000)

All values for physical constants such as electron mass etc. were taken from [28-p.1]